



HAL
open science

Superconductivity and Electronic correlations studied at the nanoscale

Christophe Brun

► **To cite this version:**

Christophe Brun. Superconductivity and Electronic correlations studied at the nanoscale. Condensed Matter [cond-mat]. Sorbonne Université, 2021. tel-03421022

HAL Id: tel-03421022

<https://hal.science/tel-03421022>

Submitted on 9 Nov 2021

HAL is a multi-disciplinary open access archive for the deposit and dissemination of scientific research documents, whether they are published or not. The documents may come from teaching and research institutions in France or abroad, or from public or private research centers.

L'archive ouverte pluridisciplinaire **HAL**, est destinée au dépôt et à la diffusion de documents scientifiques de niveau recherche, publiés ou non, émanant des établissements d'enseignement et de recherche français ou étrangers, des laboratoires publics ou privés.



Habilitation (HDR) Thesis

Christophe BRUN

Institut des Nanosciences de Paris

CNRS et Sorbonne Université campus Pierre et Marie Curie

Corridor 22-32 2nd floor, 75005 Paris, France

Tél. : (+33) 1 44 27 46 76, Email : christophe.brun@sorbonne-universite.fr

Born in Paris 08.03.1976, French, three children

<http://www.insp.jussieu.fr/-Spectroscopie-des-nouveaux-etats-.html>

Superconductivity and Electronic correlations studied at the nanoscale

Composition of the Jury

Sophie Guéron: Reviewer

CNRS Research director at LPS, Paris-Saclay University

Claude Chapelier: Reviewer

CEA Research director at INAC, Grenoble Alpes University

Frédéric Pierre: Reviewer

CNRS Research director at C2N, Paris-Saclay University

Teun Klapwijk: Examiner

Professor at Kavli Institute for Nanoscience, Delft Technical University

Benoit Douçot: President

CNRS Research director at LPTHE, Sorbonne University

Defended publicly on April 2, 2021 at Sorbonne University using on-line facilities

SUPERVISION OF MASTER, GRADUATE STUDENTS AND POSTDOCTORAL FELLOWS

2011 – 2020 Institute for Nanosciences of Paris, Sorbonne Université, France

Co-Supervision of 3 Postdocs: Alexandra Palacio-Morales (2018-2019) now Maître de Conférence at Université Paris-Saclay in France, Vasily Stolyarov (2013-2015) now research scientist at Moscow Institute of Physics and Technology in Russia, Vladimir Cherkez (2011-2013) now working in industry in France.

Co-Supervision/PhD advisor of 5 PhD students: Mehdi Torkzadeh (2019-present) Raphaël Leriche (2016-2019) now physics professor in high school, Danilo Longo (2015-2019) now in post-doc at Synchrotron Soleil on DEIMOS beamline, Gerbold Ménard (2013-2016) now post-doc at CEA-Saclay, Clémentine Carbillet (2011-2014) now working in industry in France.

Co-Advisor of 8 Master II students: Hector Abel (now in PhD thesis at University Paris-Saclay) Mehdi Torkzadeh (now PhD student with me), Tobias Bilgeri (now PhD at EPFL-Lausanne), Raphaël Leriche (see above), Quentin Berrahal (now PhD at Univ. Paris-Diderot), Matthieu Leclerc now working in industry, Gerbold Ménard (see above), Rémi Federicci (now working in industry in France).

The above-mentioned young people are all the ones I co-supervised and had the pleasure to work with in the last 9 years. I will present below in details their contribution to the research work and I will explain in what consisted my supervision. All the research activities I conducted and contributed to were carried out at the “Institut des Nanosciences de Paris” located in Sorbonne University on the “Pierre et Marie Curie campus”. The research work was performed in a wonderful, dynamic and evolving team called [“spectroscopy of novel quantum states team”](#). In the following introduction, I will describe first the research team and human context in which my research activities were undertaken. Then I will briefly describe the experimental apparatuses I worked with and/or I contributed to develop. Finally, I will present the 5 main research topics I put my energy into from 2011 to 2020.

Table of content

General introduction	4
Presentation of the research team and context	4
Presentation of the research apparatuses and environment.....	5
Presentation of the topics of research	8
Introduction to conventional superconductivity.....	8
Topic 1: Proximity effects in mesoscopic structures.....	12
A) Theoretical background	13
B) Experimental systems	16
C) S-N proximity effect to a 2D strongly disordered metal.....	17
D) Proximity effect between two superconductors.....	19
E) S-N-S network: revealing Josephson vortex cores.....	22
Topic 2: Effect of non-magnetic and magnetic disorder on superconductivity.....	25
A) Theoretical background	27
Case of weak non-magnetic disorder	27
Case of magnetic disorder.....	27
Beyond mean-field results	29
B) Suppressing superconductivity with non-magnetic disorder: effect of moderate and strong disorder.....	30
C) NbN thin film characterization	32
D) Origin of the emergent superconducting inhomogeneities in NbN thin films.....	33
E) Characterization of superconducting Pb monolayers.....	38
F) Weak disorder effects in superconducting Pb monolayers.....	39
G) Weak disorder effects induced by step edges in the vortex lattice of superconducting Pb monolayers.....	41
H) Mapping the wavefunction of the bound state of a single magnetic atom in a superconductor	43
I) Coupling between magnetic molecules and ultrathin super-conducting films: MnPc/Pb/Si(111).....	48
Topic 3: Topological superconductivity	55
A) General background.....	57
Brief account about topology in band theory in solid-state physics	57
Rashba spin-orbit coupling in a 2D electron gas	59
Superconducting pairing on a Rashba split band-structure.....	61
Signatures of Rashba SOC in the superconducting Pb/Si(111) monolayers	63
B) Evidence for 2D topological superconductivity.....	64
C) Evidence for Pairs of spatially separated Majorana excita-tions in 2D topological superconductors	67
Topic 4 and Research Project: electronic correlations and unconventional superconductivity	70
A) Electronic correlations and Mott physics in a single atomic plane.....	71
Introduction.....	71
Correlated metallic groundstate of the 1/3 monolayer Pb/Si(111) with strong spin-orbit coupling.....	74
Research Project: From Mott to superconductivity in a single atomic plane	81

B) Unconventional superconductivity in quasi-1D organic (TMTSF) ₂ ClO ₄	86
Introduction.....	86
Phase coexistence of spin-density wave and superconducting regions	89
Thanks	91
References	92
Acronyms used in the HDR thesis	94
Publication List.....	96
Invited Talks.....	101

General introduction

Presentation of the research team and context

Since I was hired by the CNRS in 2010, I integrated the Institute of Nanosciences of Paris (INSP) in October 2010 in the [“spectroscopy of novel quantum states team”](#) (SNEQ). The team consisted in three other CNRS researchers: Dimitri Roditchev, Tristan Cren, Yves Noat and a research Engineer François Debontridder. Because major renovations took place in the Jussieu campus during 2004-2010, the lab was set in Boucicaud campus. I thus joined the team for only few months in Boucicaud and we moved back from Boucicaud campus to Jussieu campus at the end of the year 2010. Installing our new lab after having moved all our equipment took us one year.

I am a specialist of electronic properties of materials presenting quantum effects. I study these electronic properties using an experimental technique called scanning tunneling microscopy/spectroscopy (STM/STS). One of the reason of my recruitment by CNRS in this research group was that D. Roditchev, F. Debontridder and T. Cren designed and built a homemade very-low temperature STM working entirely under UHV and strong magnetic field. This apparatus was state-of-the-art, unique in France and operational in 2007. Since my research project involved spectroscopic studies at the atomic scale of confined or low-dimensional superconducting systems, there was a strong scientific and technical adequacy between us. In 2011 our very-low temperature STM/STS experiment was working again installed in the new lab I contributed to set-up at INSP in Jussieu. I spent one year to become fully autonomous on this state-of-the-art experiment.

In the years 2012-2013, the context of our SNEQ team evolved since D. Roditchev left our group to become Professor at ESPCI and set a new lab there. Since 2013 our group is led by T. Cren. In 2016, our team was reinforced with the arrival of a half-time engineer, Pascal David. Since 2017 our team has grown with the arrival of Matteo Calandra (CNRS director of research), specialist of DFT calculations of 2D materials and electron-phonon coupling, Marie d'Angelo (associate Professor, MdC) specialist of ARPES and XPS spectroscopies on 2D materials, and Florent Pérez, specialist in electronic Raman spectroscopy at very low temperature and under strong magnetic field. Last but not least, Marie Hervé specialist of nanomagnetism studied by STM/STS techniques joined our group in 2019, hired as a CNRS scientist. These newcomers have strengthened our team in terms of techniques and topic complementarities. All these various people have also stimulated several collaborations and joint projects with my own research that I will present later.

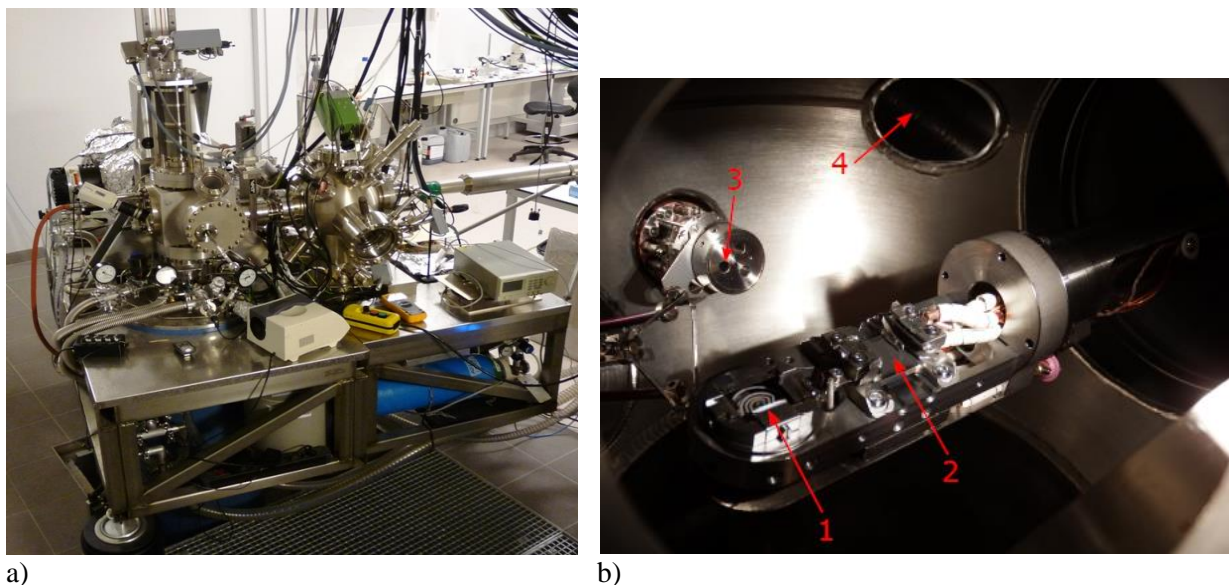
In this HDR thesis I will summarize about 9-10 years of research that I either personally carried out or directed, or to which I actively took part through joint projects with direct colleagues. My topics of research deal with the electronic properties of quantum materials and their nanostructures. This includes mostly superconducting and correlated systems. Through this period of time, I was also interested in several aspects of mesoscopic physics.

Using scanning tunneling microscopy (STM) and spectroscopy (STS), we access both the topography of the surface of the material under study and its local electronic energy-resolved properties, at the atomic scale. We thus obtain a real mapping of the local electronic density-of-states (LDOS) of a material for energies close to the Fermi energy, and we observe its evolution as a function of composition, nanostructuring, temperature,

or applied magnetic field. In some cases we can also carry out electronic transport measurements *in-situ*. State-of-the-art experiments are carried out under increasingly extreme conditions combining: ultrahigh vacuum (UHV, 10^{-11} mbar), very low temperature (down to 300 mK) and strong magnetic field (up to 10 Tesla). These stringent conditions are actually mandatory to study quantum physics using surface sensitive tools, since the LDOS of metallic/superconducting materials is highly dependent of the amount and nature of the impurities present in the material. Our samples are grown *in-situ* under UHV in a preparation chamber coupled to the microscope, or cleaved in this same chamber for bulk materials. A very strong point of our team is to develop and build our own experimental devices. This allows us to explore the quantum world in experimental conditions that are only beginning to be accessible to commercial devices.

Presentation of the research apparatuses and environment

In this subsection, I give some details about the experimental set-ups that were used and/or developed to conduct the following research projects.



a) *Figure 1. M3 experimental set-up. a) View of the entire system. Left chamber is the STM one. Right chamber is the preparation chamber. b) Close-up of devices located in the preparation chamber: 1 is the cold stage (the heater has a spiral shape), 2 double stage, 3 triple e-beam evaporator, 4 CF-40 tube enabling the connection of a modular autonomous chamber*

M3 ensemble: The state-of-the-art very-low temperature STM is called M3 and it is the experimental set-up on which most of the research presented below was done. Its conception is rather standard and follows the one of most surface physics instruments. It consists in three chambers: the load-lock chamber to introduce tips and samples, the preparation chamber and the STM chamber. Figure 1a presents the entire experimental ensemble. The preparation chamber has a base pressure in the 10^{-11} mbar range. It is equipped with a triple e-beam evaporator (Pb, Co and Sn), an Argon sputter gun to prepare metallic monocrystals, a LEED/Auger device enabling either low-energy electron diffraction or Auger spectroscopy of the studied materials. Several improvements were carried out on the preparation chamber. An alkali evaporator was installed. A commercial cryomanipulator was installed enabling to cool down the samples during their fabrication down to 100K with liquid nitrogen. This cryomanipulator is equipped with three sample stages: one “cold” stage (stage 1 on Fig. 1b) with counter-heating dedicated to sputtering or molecular beam epitaxy (MBE) growth of thin films or nanostructured samples, and a vertical double-stage (stage 2 on Fig. 1b) enabling to electrically contact samples for direct current heating or for performing electron bombardment from a W filament set on the bottom stage heating a sample located in the upper stage.

Another improvement consisted in the development of a modular autonomous UHV chamber dedicated to the evaporation of magnetic molecules (manganese and terbium Phtalocyanines: MnPc, TbPc₂). This chamber is seen in figure 2. It can be connected to any CF-40 flange and possess its own transfer arm and its own pumping system. It can thus be installed on any UHV system and can be carried for synchrotron experiment,

which we did at Soleil to perform X-ray circular magnetic dichroism experiment on the DEIMOS beamline (see Figure 3).

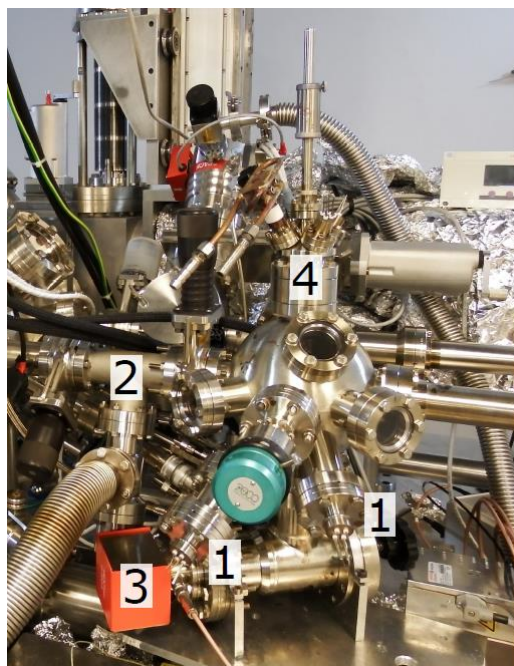


Figure 2. Modular autonomous chamber dedicated to the evaporation of magnetic molecules. On this photograph the chamber is mounted at the back of the preparation chamber seen in figure 1 and is connected to the CF-40 tube indicated by n°4 in figure 1b. 1) Two tubes containing each one an independent molecules crucible, each one having its own heating filament and thermocouple. 2) T-connecting tube for independent pumping and/or bake-out of the modular chamber. 3) Combined NEG and ion pump. 4) Cryogenic stage to receive the sample holder during the deposition of molecules.

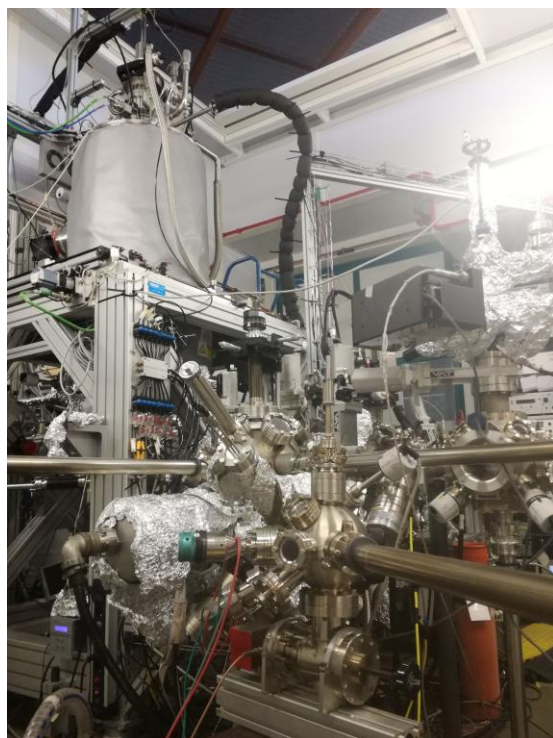


Figure 3. Modular chamber (dedicated to magnetic molecules deposition) presented in Fig.2 mounted on the UHV set-up of the DEIMOS beamline at synchrotron Soleil during a run from 20th to 27th of January 2020 in Saclay, France.

M2bis ensemble: A new instrument is currently being finalized in our group. Called M2bis, it is an STM/AFM operating under UHV with a vector magnetic field (1T horizontal, 3T vertical). This device is coupled to a preparation chamber under UHV. In 2015, this preparation chamber was put into service and the first samples could be prepared. The main challenge of this apparatus is that its cryogenic part does not consist in liquid baths, as usual in UHV scanning probe systems, but is a dry system controlled by a He pulse tube working in closed cycle. Getting rid of the mechanical and high-frequency noise induced by the pulse tube is thus an important issue. The STM/AFM head was designed, and the parts manufactured. A first head has already been assembled and tested. A large delay occurred in the set-up of this instrument due to various technical problems encountered on other set-ups and many delays induced by other technical developments. In addition, for priority reasons we decided to set-up a simpler third instrument dedicated to sample growth (description below) and to start the drawing of a RF-STM stick compatible with M3 existing cryostat (initiated by the recruitment of Marie Hervé). The final design and test of the STM/AFM should have been optimized in 2020. With the coronavirus pandemics, we are not sure that it will be fulfilled this year. Concerning this whole project, it has been launched by Tristan Cren, the drawings of the STM/AFM head being mainly from Dimitri Roditchev, further improved by François Debontridder and Pascal David. Assembly, implementation and tests of all kinds are led by François Debontridder, Pascal David, Tristan Cren and myself.

VT ensemble: Another new UHV ensemble dedicated to sample growth and optimization was set-up in the end of 2019-beginning of 2020 in our group, at the initiative of myself and Marie d'Angelo. The need of this apparatus is to enable spending time on searching for growth conditions of new samples. In the various complex projects that I will develop below, it became clear to us that not having such an ensemble tremendously increased the experimental load on M3. We thus made several investments to buy new equipment in order to benefit from a fully equipped and operational system. This ensemble is shown on Figure 4 and consists in three interconnected pieces: a load-lock chamber, a preparation chamber and a variable-temperature STM chamber. The preparation chamber is very similar to M3's one and shares with it identical elements such as a LEED/Auger device or a triple e-beam evaporator (filled with Sn, Co and Cu). In addition it is equipped with a retractable low temperature knudsen cell (filled with Pb at present), a silicon evaporator, and a precise scanning Ar+ ion-beam sputtering device with differential pumping. At present the manipulator of the preparation chamber is not a cryogenic one, but this will be developed in the group in the near future. The STM chamber is isolated from the preparation chamber by a gate valve and has its own pumping system (NEG+ion pump identical to the one indicated by N°3 on Fig.2). The STM is used only for topographic characterization of the fabricated samples but cannot be used for precise spectroscopy since the sample can be cooled to about 20K with liquid He but the STM tip is not thermalized with a well-defined thermostat. This system is fully operational since the end of January 2020.

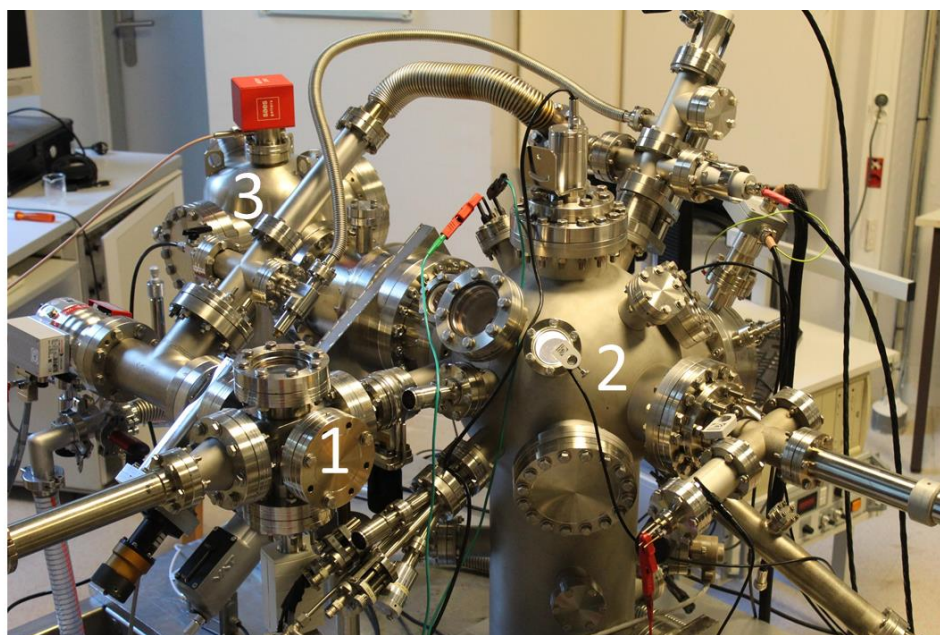


Figure 4. UHV ensemble dedicated to samples growth studies and their optimization. 1) indicates the load-lock chamber, 2) the preparation chamber and 3) the variable temperature STM chamber.

Presentation of the topics of research

I would like now to present the main research topics I worked on from 2011 to 2020 at the Institute of Nanosciences of Paris – located in Sorbonne University at Jussieu’s Pierre and Marie Curie campus in the “spectroscopy of novel quantum states” group. I decided to order these topics by scientific subjects, so that they don’t appear in chronological order. I chose as last topic the one that enables me to make a smooth transition to present one main aspect of my current and future research project. The first 3 topics deal with different types of studies related to conventional superconductivity. The 4th and 5th topics are linked to unconventional superconductivity, electronic correlations, and Mott physics. Here are the five topics:

- 1) Proximity effects in S-N, S-S and S-N-S mesoscopic structures
- 2) Effect of non-magnetic and magnetic disorder on conventional superconductivity
- 3) Topological superconductivity
- 4) Unconventional superconductivity in quasi-1D organic (TMTSF)₂ClO₄
- 5) Two-dimensional electronic correlations and Mott physics

There are other research topics on which I also worked actively for some years like the confinement of vortices in nanosized superconducting islands or multigap superconductivity in dichalcogenides materials like 2H-NbSe₂. Nevertheless, I chose to focus on the topics mentioned above for the sake of clarity and also because my input in these five projects was more important both in terms of research involvement, practicing, planning and supervision.

In the following of my HDR thesis, I will try to summarize in a pedagogical way the main scientific achievements that were obtained but I will also present the scientific context in which this work was done. I will also try to mention as honestly as possible what was my role in these works and specify in what consisted my supervision. This is not an easy task especially because nowadays with the increasing individualization of research there is a trend to force young individuals not to work in team in order for them to establish themselves as independent leaders. I feel against this trend that I find deleterious and against the French academic research system. As a consequence I always defended team work in our group that I find much more attractive, fun and more efficient. This point-of-view was also shared by my close permanent colleagues. I will also specify the type of funding that were obtained to help carrying out some of these projects and sustain the experimental developments that I mentioned before.

Introduction to conventional superconductivity

In the first two chapters we will be interested in superconducting proximity effects between a normal material and a superconductor or between two superconductors or in effects produced by non-magnetic and magnetic disorder on conventional superconductivity. We provide here basic concepts about conventional superconductivity that we will use to present our results. By conventional superconductivity we mean here a pairing mechanism mediated by an effective attractive interaction between electrons (through the electron-phonon coupling) such as in the original Bardeen-Cooper-Schrieffer (BCS) theory. We follow the presentation of Monique Combescot in [Combescot2015]. This attractive potential between electrons is meant to be weak (with respect to the Fermi energy ϵ_F) and in real space it is short range as a contact potential. It thus has the following form of an integral over the volume of the material:

$$H_{supra} = -V \iiint d^3\mathbf{r} \Psi_{r\uparrow}^\dagger \Psi_{r\downarrow}^\dagger \Psi_{r\downarrow} \Psi_{r\uparrow} \quad (0a)$$

where $\Psi_{r\uparrow}^\dagger = \sum_{\mathbf{k}} e^{-i\mathbf{k}\cdot\mathbf{r}} c_{\mathbf{k}\uparrow}^\dagger$ is the field operator creating an electron at location \mathbf{r} . $c_{\mathbf{k}\uparrow}^\dagger$ and $c_{\mathbf{k}\uparrow}$ are standard single-particle creation and annihilation operators for fermions of wavevector \mathbf{k} and spin \uparrow (with similar expressions for the down spin \downarrow). V is positive. Using the expressions for the Ψ 's and replacing in H_{supra} it gives

$$H_{supra} = -V \sum_{q\mathbf{k}_1\mathbf{k}_2} c_{\mathbf{k}_1+q\uparrow}^\dagger c_{\mathbf{k}_2-q\downarrow}^\dagger c_{\mathbf{k}_2\downarrow} c_{\mathbf{k}_1\uparrow} \quad (0b)$$

In the BCS approximation, it is assumed that the superconducting ground state consists of electron pairs of zero center of mass momentum to lower the kinetic energy. Thus only terms with $\mathbf{k}_1 + \mathbf{k}_2 = \mathbf{0}$ are kept in the Hamiltonian H_{supra} . This finally leads to the BCS coupling term:

$$H_{BCS} = -V \sum_{\mathbf{k}\mathbf{k}'} c_{\mathbf{k}'\uparrow}^\dagger c_{-\mathbf{k}'\downarrow}^\dagger c_{-\mathbf{k}\downarrow} c_{\mathbf{k}\uparrow} \quad (0c)$$

In the sum over \mathbf{k} and \mathbf{k}' are considered only the states such that $\epsilon_F - \omega_D \leq \epsilon_{\mathbf{k}} \leq \epsilon_F + \omega_D$ where the energy ω_D is a cut-off energy of the order of a phonon energy, typically comparable to the Debye energy of the material. Thus one sees that this attractive potential only couples the states that are close enough to the Fermi energy ϵ_F on the scale of ω_D but does not couple the states that are lower in energy. If one now writes $B_{\mathbf{k}}^\dagger = c_{\mathbf{k}\uparrow}^\dagger c_{-\mathbf{k}\downarrow}^\dagger$ which corresponds to the creation operator of an electron pair of time-reversed states, one sees that H_{BCS} can be written as $H_{BCS} = -V \sum_{\mathbf{k}\mathbf{k}'} B_{\mathbf{k}'}^\dagger B_{\mathbf{k}}$. One important peculiarity of this BCS potential underlined by Combescot and Shiau is that Cooper pairs interact only through the Pauli exclusion principle, thus allowing Cooper pairs to spatially overlap without breaking. This is in contrast for instance to delocalized excitons (so-called Wannier excitons) that dissociate upon overlapping with a sufficiently high density. Finally combining the standard Hamiltonian for a metal with the reduced BCS term, the Hamiltonian for a conventional superconductor takes the following form:

$$H = \sum_{\mathbf{k}\sigma} \epsilon_{\mathbf{k}} c_{\mathbf{k}\sigma}^\dagger c_{\mathbf{k}\sigma} - V \sum_{\mathbf{k}\mathbf{k}'} c_{\mathbf{k}'\uparrow}^\dagger c_{-\mathbf{k}'\downarrow}^\dagger c_{-\mathbf{k}\downarrow} c_{\mathbf{k}\uparrow}$$

Surprisingly this Hamiltonian belongs to the few ones in many-body physics that can be solved exactly. In particular in the canonical ensemble it was solved by Richardson and Gaudin. Historically it was solved in the grand canonical ensemble using various approaches that correspond to a mean-field approximation. As we will need some of these expressions in the following we recall here the main results. First we write

$$H - \mu N = \sum_{\mathbf{k}\sigma} (\epsilon_{\mathbf{k}} - \mu) c_{\mathbf{k}\sigma}^\dagger c_{\mathbf{k}\sigma} - V \sum_{\mathbf{k}\mathbf{k}'} c_{\mathbf{k}'\uparrow}^\dagger c_{-\mathbf{k}'\downarrow}^\dagger c_{-\mathbf{k}\downarrow} c_{\mathbf{k}\uparrow}$$

and set $\xi_{\mathbf{k}} = \epsilon_{\mathbf{k}} - \mu$. Then we use a mean-field approximation $H_{BCS} = H_{BCS}^{MF} + W$ where

$$H_{BCS}^{MF} = -V \sum_{\mathbf{k}\mathbf{k}'} \langle c_{\mathbf{k}'\uparrow}^\dagger c_{-\mathbf{k}'\downarrow}^\dagger \rangle c_{-\mathbf{k}\downarrow} c_{\mathbf{k}\uparrow} + c_{\mathbf{k}'\uparrow}^\dagger c_{-\mathbf{k}'\downarrow}^\dagger \langle c_{-\mathbf{k}\downarrow} c_{\mathbf{k}\uparrow} \rangle - \langle c_{\mathbf{k}'\uparrow}^\dagger c_{-\mathbf{k}'\downarrow}^\dagger \rangle \langle c_{-\mathbf{k}\downarrow} c_{\mathbf{k}\uparrow} \rangle$$

The term W can be neglected in the thermodynamic limit and setting

$$\Delta = V \sum_{\mathbf{k}} \langle c_{-\mathbf{k}\downarrow} c_{\mathbf{k}\uparrow} \rangle \quad (0)$$

one gets:

$$H - \mu N = \sum_{\mathbf{k}\sigma} \xi_{\mathbf{k}} c_{\mathbf{k}\sigma}^\dagger c_{\mathbf{k}\sigma} - \Delta \sum_{\mathbf{k}} c_{\mathbf{k}\uparrow}^\dagger c_{-\mathbf{k}\downarrow}^\dagger - \Delta^* \sum_{\mathbf{k}} c_{-\mathbf{k}\downarrow} c_{\mathbf{k}\uparrow} + \frac{|\Delta|^2}{V} \quad (1)$$

The averaged quantities such as $\langle c_{-\mathbf{k}\downarrow} c_{\mathbf{k}\uparrow} \rangle$ are meant either in the mean-field ground state at $T = 0$ or generalizing their statistical value at finite T . Using the spinor notation $\Psi_{\mathbf{k}}^\dagger = (c_{\mathbf{k}\uparrow}^\dagger \ c_{-\mathbf{k}\downarrow})$ and a 2×2 matrix form it gives

$$H - \mu N = \sum_{\mathbf{k}} \Psi_{\mathbf{k}}^\dagger \begin{bmatrix} \xi_{\mathbf{k}} & -\Delta \\ -\Delta^* & -\xi_{\mathbf{k}} \end{bmatrix} \Psi_{\mathbf{k}} + \xi_{\mathbf{k}} + \frac{|\Delta|^2}{V} \quad (2)$$

The solution to the mean-field BCS Hamiltonian is then given by diagonalizing the 2×2 matrix for instance using a Bogoliubov transformation which leads to the following expressions:

$$H - \mu N = \sum_{\mathbf{k}} (\xi_{\mathbf{k}} - E_{\mathbf{k}}) + \sum_{\mathbf{k}} E_{\mathbf{k}} (\gamma_{\mathbf{k}\uparrow}^\dagger \gamma_{\mathbf{k}\uparrow} + \gamma_{-\mathbf{k}\downarrow}^\dagger \gamma_{-\mathbf{k}\downarrow}) + \frac{|\Delta|^2}{V} \quad (3)$$

With $E_{\mathbf{k}} = +\sqrt{|\Delta|^2 + \xi_{\mathbf{k}}^2}$ and $\gamma_{\mathbf{k}\uparrow}^\dagger = u_{\mathbf{k}}^* c_{\mathbf{k}\uparrow}^\dagger - v_{\mathbf{k}}^* c_{-\mathbf{k}\downarrow}$ and $\gamma_{-\mathbf{k}\downarrow}^\dagger = u_{\mathbf{k}}^* c_{-\mathbf{k}\downarrow}^\dagger + v_{\mathbf{k}}^* c_{\mathbf{k}\uparrow}$ (3bis)

Using the condition that $\Delta^* \frac{v_{\mathbf{k}}}{u_{\mathbf{k}}} = E_{\mathbf{k}} - \xi_{\mathbf{k}}$ is a real positive number one can choose $u_{\mathbf{k}}$ to be real and positive and setting $\Delta = |\Delta| e^{i\varphi}$ where φ is the phase of the order parameter, this imposes that $v_{\mathbf{k}} = |v_{\mathbf{k}}| e^{i\varphi}$. One then finds $u_{\mathbf{k}} = \sqrt{\frac{1}{2} \left(1 + \frac{\xi_{\mathbf{k}}}{E_{\mathbf{k}}} \right)}$ and $|v_{\mathbf{k}}| = \sqrt{\frac{1}{2} \left(1 - \frac{\xi_{\mathbf{k}}}{E_{\mathbf{k}}} \right)}$.

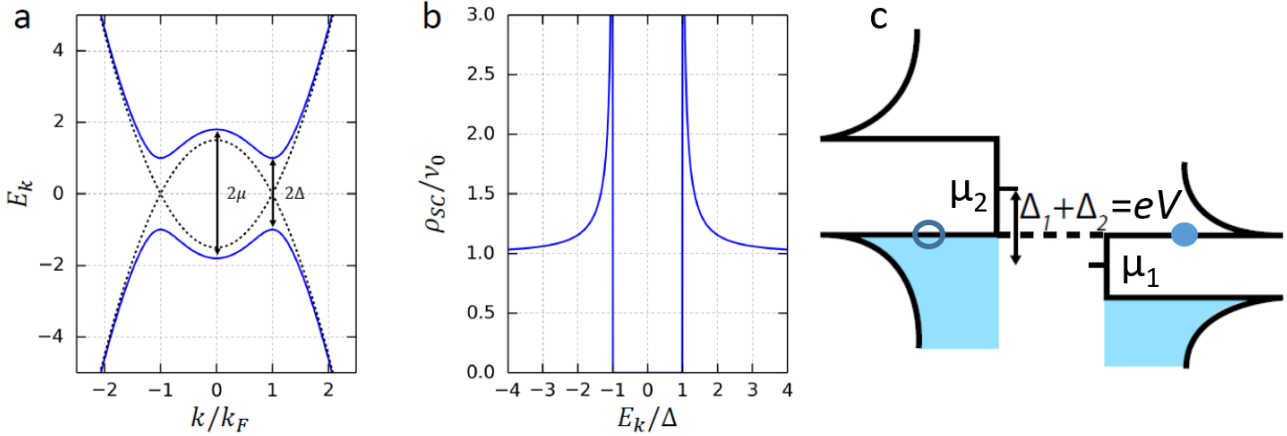


Figure 5. a) Elementary excitations $\pm E_k$ of a BCS superconductor in blue. In black dotted lines are shown the corresponding normal state electron-like (positive curvature) and hole-like (negative curvature) excitations. b) BCS density-of-states normalized by the one in the normal state as a function of excitation energy E_k divided by the gap Δ . c) Illustration of the ability of the semiconductor model to describe tunneling events of single electronic charges between two superconductors by horizontal transition conserving the energy between the hole excitation in 2 and the electron excitation in 1.

By looking at the expression (3) one sees that the sum of the first and last term represent a constant energy of the superconductor that differ from the one in the normal state by exactly the condensation energy. In the middle term of (3) is expressed the increase of energy from the BCS ground state through the action of the $\gamma_{\mathbf{k}\uparrow}^\dagger$ and $\gamma_{-\mathbf{k}\downarrow}^\dagger$ operators. These operators describe the elementary fermionic quasi-particle excitations and have all an energy $+E_k$. It is important to note that the indices $\mathbf{k}\uparrow$ and $-\mathbf{k}\downarrow$ of the γ^\dagger 's are meaningful and represent respectively the momentum and spin of the elementary excitation. Each elementary excitation involves simultaneous coherent excitations of an electron ($c_{\mathbf{k}\uparrow}^\dagger$ or $c_{-\mathbf{k}\downarrow}^\dagger$) and a hole ($c_{-\mathbf{k}\downarrow}$ or $c_{\mathbf{k}\uparrow}$) with a weight linked to u_k and $v_k = |v_k|e^{i\varphi}$, the phase factor between them being the phase φ of the superconductor. For each value of $+E_k$ there are 2 possible excitations: an electron-like with $+\xi_k$ and a hole-like with $-\xi_k$, having each themselves 2 possible \mathbf{k} values ($\mathbf{k}_F + \mathbf{q}$, $-\mathbf{k}_F - \mathbf{q}$) and ($\mathbf{k}_F - \mathbf{q}$, $-\mathbf{k}_F + \mathbf{q}$).

The BCS ground state can be written as $|\Psi_{BCS}\rangle = \prod_{\mathbf{k}}(u_{\mathbf{k}} + |v_{\mathbf{k}}|e^{i\varphi} c_{\mathbf{k}\uparrow}^\dagger c_{-\mathbf{k}\downarrow}^\dagger)|0\rangle$. It verifies $\gamma_{\mathbf{k}\uparrow}|\Psi_{BCS}\rangle = \gamma_{-\mathbf{k}\downarrow}|\Psi_{BCS}\rangle = 0$ so that this ground state corresponds to the vacuum state of the γ particles: i.e. there are no quasi-particle excitations in the BCS ground state. Furthermore this ground state does not correspond to a Bose condensation as is sometimes written or said. It corresponds to a coherent superposition of doubly empty and doubly occupied electronic states sharing all the same phase φ on an energy region of the order of few times $|\Delta|$. Nevertheless the attractive potential V that couples the electronic states of energy $\epsilon_{\mathbf{k}}$ acts over an energy scale $\epsilon_F - \omega_D \leq \epsilon_{\mathbf{k}} \leq \epsilon_F + \omega_D$ that is much larger than $|\Delta|$. In the BCS theory one finds that $|\Delta| = 2\hbar\omega_D e^{-\frac{1}{v_0V}}$. As seen in Fig.5a) and from the expression of E_k this corresponds to the energy gap existing in the superconductor for the smallest excitations energy for which $\pm\xi_k = 0$. However this quantity $|\Delta|$ does not correspond to the average binding energy of a single Cooper pair in the superconductor. This latter energy is $\epsilon_c = \hbar\omega_D e^{-\frac{1}{2v_0V}}$ which is half the binding energy found by Cooper for the single pair problem. One sees that because of the factor 2 in the exponential dependence $\epsilon_c \ll |\Delta|$. This means that creating a single excitation of energy $E_k = |\Delta|$ actually costs much more than unbinding a single pair. This is because when one breaks a pair, it corresponds to

$$\gamma_{\mathbf{k}\uparrow}^\dagger|\Psi_{BCS}\rangle = c_{\mathbf{k}\uparrow}^\dagger \prod_{p \neq \mathbf{k}} (u_p + |v_p|e^{i\varphi} c_{p\uparrow}^\dagger c_{-p\downarrow}^\dagger)|0\rangle$$

This process actually blocks the state \mathbf{k} because it puts with certainty a single electron in the state $\mathbf{k}\uparrow$ which prevents all other pairs to use this particular blocked \mathbf{k} state due to the Pauli principle. Let us note that here the total electron number is not conserved since the above expressions are given in the grand canonical ensemble. The density of states corresponding to the excited states E_k is given by the well-known formula

$\rho_{SC}(E) = v_0 \frac{|E|}{\sqrt{E^2 - |\Delta|^2}}$ represented on figure 5b and can be probed by tunneling experiment.

The reason for which we have represented in Figure 5a) negative excitations $-E_k$ symmetric to the positive ones is not clear up to now since all excitations considered up to now have positive energies $+E_k$ with respect to the BCS ground state. Nevertheless if one considers excitations where the number of particle changes, like in tunneling experiment where one electron of charge e tunnels from an electrode 2 (i.e. creates a hole in 2) to an electrode 1, considering negative excitation energies for holes becomes natural and is called the semiconductor model. This is very common in the literature. The justification is the following. When one deals with changing the number N of particles in the system one needs to reintroduce the chemical potential through a term like $+\mu N$. In this case, the energy E_{ek} needed to add a charge e to a superconductor is $E_{ek} = \mu + E_k > 0$ while the energy needed to create a hole in it is $E_{hk} = -\mu + E_k = -(\mu - E_k) < 0$. These expressions show that in tunneling events where charges are transferred one by one from the electrode 2 to the electrode 1 the total energy is conserved in each process so that one has $E_{ek}^1 + E_{hk}^2 = 0$. This leads to

$$\mu_1 + E_{k1} = \mu_2 - E_{k2} > 0 \quad (4)$$

This relation (4) is graphically illustrated in Fig. 5c) and corresponds to an horizontal transition between the two superconductors biased by $\mu_2 - \mu_1 = E_{k1} + E_{k2} = eV > 0$. Let us note also that from the expression (0) above:

$$\Delta = V \sum_{\mathbf{k}} \langle c_{-\mathbf{k}\downarrow} c_{\mathbf{k}\uparrow} \rangle = V \sum_{\mathbf{k}} u_{\mathbf{k}} v_{\mathbf{k}} (1 - 2f(E_{\mathbf{k}})) \quad (5)$$

It shows that the order parameter is expressed as the product of an attractive potential term V multiplied by a quantity (the sum over all \mathbf{k} terms) that can be interpreted as a pair amplitude of the superconductor. In the expression (5) $f(E_{\mathbf{k}})$ is the Fermi-Dirac function. Let us mention also that the characteristic length scale associated to the spatial variations of $|\Delta|$ is $\xi_0^{BCS} = \frac{\hbar v_F}{\Delta}$ where v_F is the electron Fermi velocity which gives also the characteristic size in real space of a Cooper pair.

From this introduction, we anticipate that the effects produced by non-magnetic and magnetic disorder on conventional superconductivity are very different in nature. The fundamental difference between these two types of disorder is that since Cooper pairs are coherent quantum superpositions of single-particle states made of two time-reversal conjugated eigenstates, i.e. having opposite momenta and spins ($\mathbf{k}\uparrow, -\mathbf{k}\downarrow$), a magnetic impurity breaks time-reversal symmetry while a non-magnetic one does not. As a consequence, a single magnetic atom induces locally so-called Yu-Shiba-Rusinov in-gap states inside the superconducting gap while a single non-magnetic impurity does not affect superconductivity. This very different behavior was first reported by Anderson and Abrikosov and Gor'kov [Anderson1959, AbriGork1961]. These arguments can be best understood from the Bogoliubov-de Gennes generalization in real space of the above Bogoliubov equations. When the material is not pure anymore but contains impurities or when the order parameter will vary spatially, for instance due to proximity effect to a normal metal as addressed below, the relations (1,2,3) above are more conveniently written in real space. Then we can reformulate the total Hamiltonian of the system using the single-particle creation/annihilation operators in real-space $\Psi_{r\uparrow} = \Psi(\mathbf{r}\uparrow) = \sum_{\mathbf{k}} e^{i\mathbf{k}\cdot\mathbf{r}} c_{\mathbf{k}\uparrow}$. Assuming as before a point interaction in real space between electrons leading to an attractive interaction, this leads to the following expression:

$$\mathcal{H}_{BdG} = \int \left\{ \sum_{\sigma} \Psi^{\dagger}(\mathbf{r}\sigma) \mathcal{H}_0 \Psi(\mathbf{r}\sigma) + \Delta(\mathbf{r}) \Psi^{\dagger}(\mathbf{r}\uparrow) \Psi^{\dagger}(\mathbf{r}\downarrow) + \Delta^*(\mathbf{r}) \Psi(\mathbf{r}\downarrow) \Psi(\mathbf{r}\uparrow) \right\} d\mathbf{r} \quad (6)$$

Where $\mathcal{H}_0(\mathbf{r}) = \left[\frac{1}{2m} (-i\hbar\nabla - e\mathbf{A})^2 + U(\mathbf{r}) - \mu \right]$ is the single-particle Hamiltonian taking into account the periodic crystal potential, possible non-magnetic disorder and the Hartree-Fock term of the point interaction between electrons. Here $\Delta(\mathbf{r}) = V \langle \Psi(\mathbf{r}\uparrow) \Psi(\mathbf{r}\downarrow) \rangle$. Since (6) is again quadratic in $(\Psi^{\dagger}(\mathbf{r}\uparrow) \Psi(\mathbf{r}\downarrow))$ it can be diagonalized in an orthonormal basis using $\gamma_{n\uparrow}$ and $\gamma_{n\downarrow}$ Bogoliubov operators as in (3bis), where n instead of \mathbf{k} indexes now the eigenstates of $\mathcal{H}_{BdG} = E_g + \sum_{n\sigma} E_n \gamma_{n\sigma}^{\dagger} \gamma_{n\sigma}$. This relation is the analogous of (3) above where E_g is the ground state energy and E_n is the excitation energy associated to $\gamma_{n\sigma}^{\dagger}$. The Ψ 's can be expressed as a function of the γ 's which gives:

$$\Psi(\mathbf{r}\uparrow) = \sum_n [\gamma_{n\uparrow} u_n(\mathbf{r}) - \gamma_{n\downarrow}^{\dagger} v_n^*(\mathbf{r})] \quad (7)$$

$$\Psi(\mathbf{r} \downarrow) = \sum_n [\gamma_{n\downarrow} u_n(\mathbf{r}) + \gamma_{n\uparrow}^\dagger v_n^*(\mathbf{r})] \quad (8)$$

The functions $u_n(\mathbf{r})$ and $v_n(\mathbf{r})$ are position dependent eigenfunctions to be determined by solving Schrödinger-like equations using the BdG Hamiltonian \mathcal{H}_{BdG} expressed in relation (6) above:

$$\begin{pmatrix} \mathcal{H}_0(\mathbf{r}) & \Delta(\mathbf{r}) \\ \Delta^*(\mathbf{r}) & -\mathcal{H}_0^*(\mathbf{r}) \end{pmatrix} \begin{pmatrix} u_n(\mathbf{r}) \\ v_n(\mathbf{r}) \end{pmatrix} = E_n \begin{pmatrix} u_n(\mathbf{r}) \\ v_n(\mathbf{r}) \end{pmatrix} \quad (9)$$

The gap verifies a self-consistency equation $\Delta(\mathbf{r}) = V \sum_n v_n^*(\mathbf{r}) u_n(\mathbf{r}) (1 - 2f(E_n))$ (9bis) which generalizes the relation (5).

We thus see that taking into account the effect of non-magnetic impurities in $\mathcal{H}_0(\mathbf{r})$ seem to lead to similar equations as in BCS theory above. Anderson has shown that it is true if $\Delta(\mathbf{r})$ can be assumed to be constant in the material [Anderson1959]. This latter condition is usually verified as soon as $k_F \ell_e \gg 1$ where k_F is the Fermi wavevector and ℓ_e the elastic electronic mean free path. Thus conventional superconductivity is generally very robust against non-magnetic disorder on one hand while it is very sensitive to magnetic disorder on the other hand. This much contrasted situation was the scientific origin of my motivation to study in details these two aspects by local scanning tunneling spectroscopy. Indeed as the zero-magnetic field natural length scale of superconductivity is its coherence length ξ_0 , which typically ranges at $T = 0$ K from few nm in highly disordered samples to several tens of nm in clean materials, local probes being capable of performing high-resolution spectroscopy at the atomic scale are very well suited for this type of study. While macroscopic probes such as magneto-transport or optical conductivity measurements can only grasp an overall and averaged behavior, local ones can probe the bound states or the inhomogeneities induced by any type of disorder at microscopic length scales relevant to superconductivity. This is precisely what I investigated in details in various systems and what I will present in the Topic 2. In the same spirit, local spectroscopic probes appear ideally suited to study lateral electronic contacts between various superconducting materials or between superconducting and metallic ones. This is what I will present now in the Topic 1.

Topic 1: Proximity effects in mesoscopic structures

This topic consists in studying at the atomic scale how superconducting correlations propagate between a superconductor (S) and another conducting material which can be a normal metal (N), another superconductor (S), etc. This subject was a part of my CNRS recruitment project which I wanted to realize by making a contact with a purely two-dimensional material: graphene. My colleagues Tristan Cren and Dimitri Roditchev had a common interest in these studies. Instead of using graphene, we first used the Pb/Si(111) system which has the main advantage of being an ultraclean system since it can be prepared entirely *in situ* using the molecular beam epitaxy (MBE) technique. This Pb/Si(111) system was independently studied by me for 3 years when I was a post-doc at EPFL-Lausanne in Switzerland and by Tristan and Dimitri at INSP. We thus had a clear common interest in such studies. I could contribute to three different studies by co-designing the following experiments:

- i) The S-N proximity effect between a single Pb nanocrystal forming the S part and a 2D disordered metal being the Pb wetting layer and forming the N part
- ii) A S-N-S network of Josephson junctions between Pb nanocrystals forming the S parts and a 2D disordered metal being the Pb wetting layer and forming the N part
- iii) The S-S proximity effect between two different superconductors: a single Pb nanocrystal having a large superconducting gap and a Pb monolayer having a small superconducting gap

For the works i) and ii) I co-supervised part of the experimental work of the PhD student **Lise Serrier-Garcia** (during 3 years). For ii) and iii) I co-supervised the experimental work of our **post-docs Vladimir Cherkez** (during 2 years), **Vasily Stolyarov** (during 2 years) and **master II student Gerbold Ménard** (during 4 months). In these 3 works my supervision mainly consisted in showing and helping these people getting the various appropriate samples, characterizing them using LEED, Auger spectroscopy and STM. I also taught them how measuring properly their local superconducting properties by STM/STS. I also introduced V.C. and G.M. to the physics of superconducting proximity effect. The theoretical modelling was done in

collaboration with a Spanish theoretician Juan-Carlos Cuevas. I also entirely supervised the writing of the master thesis of G.M. These works gave rise to several publications in which the people I co-supervised are written in bold:

- Scanning Tunneling Spectroscopy Study of the Proximity Effect in a Disordered Two-Dimensional Metal*
L. Serrier-Garcia, J.C. Cuevas, T. Cren, **C. Brun**, **V. Cherkez**, F. Debontridder, D. Fokin, F.S. Bergeret, and D. Roditchev, Phys. Rev. Lett. 110, 157003 (2013)
- Direct observation of Josephson vortex cores*
D. Roditchev, **C. Brun**, **L. Serrier-Garcia**, J.C. Cuevas, M. Milosevic, F. Debontridder, and T. Cren, Nature Physics 11, 332 (2015)
- Proximity Effect between two Superconductors Spatially Resolved by Scanning Tunneling Spectroscopy*
V. Cherkez, J.C. Cuevas, **C. Brun**, T. Cren, **G. Ménard**, F. Debontridder, **V. Stolyarov** and D. Roditchev, Phys. Rev. X 4, 011033 (2014)
- a book chapter: “*Proximity effect: a new insight from in-situ fabricated hybrid nanostructures*”, J.C. Cuevas, D. Roditchev, T. Cren, **C. Brun**, in The Oxford Handbook of Small Superconductors. First Edition. Edited by A.V. Narlikar Oxford University Press 2017.
- The PhD thesis of **Lise Serrier-Garcia** entitled “*Vortex confinés dans des nanostructures de Pb/Si(111) étudiés par microscopie à effet tunnel*” was defended in public the 17th of January 2014. Lise is now working in industry. The official PhD advisor was Dimitri Roditchev and the other co-supervisor was my colleague Tristan Cren. The main co-supervisor was Tristan Cren.

A) Theoretical background

Proximity effect means the propagation of superconducting correlations from a superconducting material to another material, being either a normal or a superconducting one. The appropriate microscopic description of proximity effect strongly depends on the amount of non-magnetic disorder in the materials under consideration. Nevertheless the microscopic process enabling to transfer an electron coming from a normal metal (N) to a superconductor (S) is unique and is called Andreev reflection.

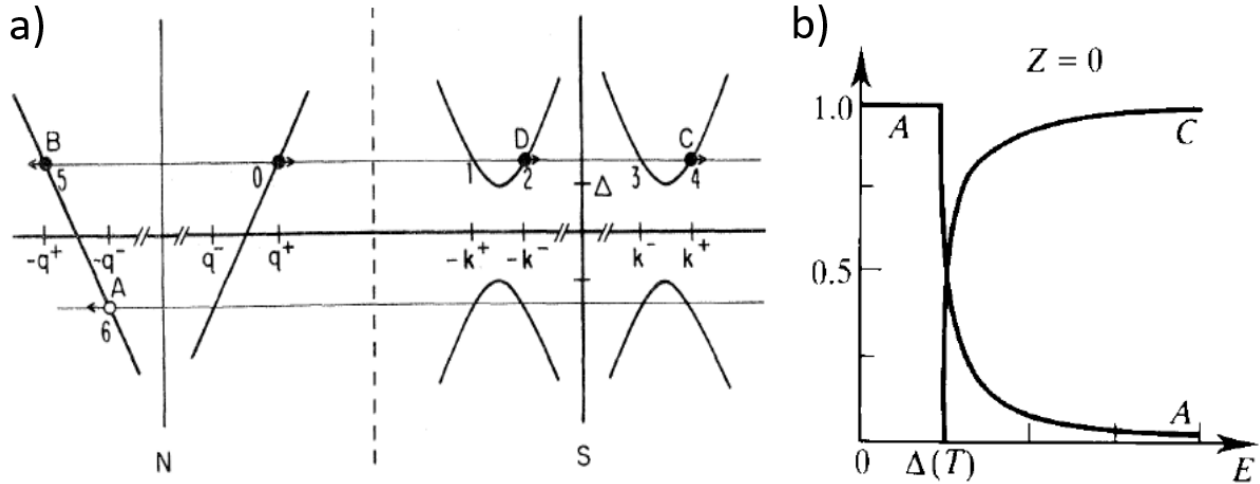


Figure 6. a) Graph representing the elementary quasi-particle excitations taking place in the Andreev reflection between a normal metal N and a superconductor S. Little arrows indicate the directions of the corresponding group velocities. b) When the interface between N and S is perfectly transparent ($Z=0$ case) and for matching band structure parameters between N and S, this graph shows the energy dependence of the hole amplitude $A(E)$ and transmitted quasi-electron amplitude $C(E)$. In this case $D(E)=B(E)=0$, the hole being perfectly reflected for $E \leq \Delta$.

The process associated to the Andreev reflection is illustrated in figure 6 along the N-S 1D interface from the seminal paper of Blonder-Tinkham-Klapwijk [BTK1982]. All possible elementary processes involving propagating quasi-particle states are indicated and can be expressed using the Bogoliubov-de Gennes approach written above in (6,7,8,9). An incoming electron 0 in N of wave vector \mathbf{q}^+ and energy $E_0 = \mu + E_{\mathbf{q}^+}$ propagating toward the superconductor can be transmitted in quasi-particles 2 and 4. This incoming particle

can also be reflected in N in the particle 5 if the barrier between N and S is not fully transparent. The surprise of the Andreev reflection is that when $E_{\mathbf{q}^+} < \Delta$, while there are no quasi-particle states in S below the gap, the incoming electron can nevertheless enter an evanescent state in S and is then reflected back in a hole, the quasi-particle 6, of momentum $-\mathbf{q}^-$ and energy $E_6 = -\mu + E_{-\mathbf{q}^-}$. When this happens, one has $E_0 = E_6 + 2\mu$, because in the whole process $E_{\mathbf{q}^+} = E_{-\mathbf{q}^-}$ so that a charge $2e$ is transferred in S during the Andreev reflection. In the case of a perfect interface and matching Fermi wavevectors ($|\mathbf{q}^+| \sim |\mathbf{q}^-| \sim |\mathbf{k}^+| \sim k_F$), figure 6b shows that the amplitudes D and B of particles 2 and 5 equals 0 while there is a perfect Andreev reflection for $E_{\mathbf{q}^+} \leq \Delta$ since $A = 1$. Its wavevector and group velocity are nearly opposite to incoming ones.

This Bogoliubov-de-Gennes approach is well adapted for ballistic materials where plane waves are eigenfunctions of $\mathcal{H}_0(\mathbf{r})$ defined in (6) in both N and S. In reality, many conventional superconductors and normal metals contain many non-magnetic impurities or enough disorder to be often in the diffusive limit. This means that:

$$\ell_e \ll \xi_0^{BCS} = \frac{\hbar v_F}{\Delta} \quad (10) \text{ also equivalent to } \Delta \frac{\tau_e}{\hbar} \sim k_B T_C \frac{\tau_e}{\hbar} = \frac{k_B T_C}{\frac{\hbar}{\tau_e}} \ll 1 \quad (10bis)$$

where $\ell_e = v_F \tau_e$. This condition expresses that many elastic scattering events will occur in a coherence volume and that the characteristic energy of superconductivity is much smaller than the energy associated to the ballistic motion. In this chapter, the studied diffusive materials will also typically verify

$$k_F \ell_e \gg 1 \quad (11)$$

implying that the non-magnetic disorder is not too strong and that we are far from Anderson localization. The concept of Anderson localization will be explained later in chapter 2. The consequences of conditions (10) and (11) is that the rapidly varying \mathbf{k} -dependent superconducting properties can be averaged out over the Fermi surface and integrated in \mathbf{k} so that atomic scale variations at the Fermi wavelength disappear. In addition, if the normal energy spectrum is linearized assuming isotropic Fermi velocity on the Fermi surface, the microscopic equations of superconductivity can be greatly simplified using an averaging procedure over the disorder distribution. Note that for diffusive superconductors, the coherence length is renormalized by scattering on defects and becomes smaller: one has $\xi_0 = b \sqrt{\xi_0^{BCS} \ell_e} = \sqrt{\frac{\hbar D}{\Delta}}$ where D is the diffusion coefficient of the electrons in S or N and is given by $D = \frac{1}{3} v_F \ell_e$ in 3D and $= \frac{1}{2} v_F \ell_e$ in 2D. b is a numerical constant of the order of 1.

The formalism best adapted to deal with out-of-equilibrium inhomogeneous superconductors, including magnetic or non-magnetic impurity scattering, inhomogeneous electron-phonon coupling, or electron-electron interactions, comes from the microscopic Gor'kov equations. These equations at equilibrium are equivalent to the ones (2) and (3) quoted above but are formulated using Green functions formalism. As this formalism naturally contains averages over the states of the system, it can efficiently handles statistical averaging over various types of disordered field and has been addressed by Eilenberger, Eliashberg, Larkin-Ovchinnikov, Usadel and others. As an experimentalist, I must say that I don't master this formalism which is quite advanced and highly technical. Nevertheless I understand how the Gor'kov equations can be established and simplified in the case of diffusive materials. This approach can be best simplified in the Usadel framework [Usadel1970], which takes an even simpler form in the thermodynamic equilibrium we are interested in here. The retarded Green function contains all information about the equilibrium properties. For instance at $T = 0$ the electronic retarded Green function is expressed as:

$$\mathcal{G}^R(\mathbf{r}, t | \mathbf{r}', t') = -i\theta(t - t') \langle \psi_H | \{ \psi_\sigma(\mathbf{r}, t), \psi_\sigma^\dagger(\mathbf{r}', t') \} | \psi_H \rangle$$

Where $\theta(t)$ is the Heaviside function, $\Psi_\sigma^\dagger(\mathbf{r}, t)$ is the Heisenberg representation of the $\Psi_\sigma^\dagger(\mathbf{r})$ defined above, $|\psi_H\rangle$ is the ground state and $\{\dots, \dots\}$ represents an anti-commutator. In a superconductor there occurs an electron-hole mixing as we have seen above. The natural basis is $\psi^\dagger = (\psi_\uparrow^\dagger(\mathbf{r}, t) \psi_\downarrow(\mathbf{r}, t))$ generalizing $\Psi_k^\dagger = (c_{k\uparrow}^\dagger c_{-k\downarrow})$ and the retarded Green function is generalized as follows by a 2×2 matrix indicated by a hat symbol:

$$\hat{\mathcal{G}}^R(\mathbf{r}, t | \mathbf{r}', t') = -i\theta(t - t') \hat{M}(\mathbf{r}, t | \mathbf{r}', t')$$

$$\text{where } \widehat{M}(\mathbf{r}, t | \mathbf{r}', t') = \begin{pmatrix} \langle \{\psi_{\uparrow}(\mathbf{r}, t), \psi_{\uparrow}^{\dagger}(\mathbf{r}', t')\} \rangle & \langle \{\psi_{\uparrow}(\mathbf{r}, t), \psi_{\downarrow}(\mathbf{r}', t')\} \rangle \\ -\langle \{\psi_{\downarrow}^{\dagger}(\mathbf{r}, t), \psi_{\uparrow}^{\dagger}(\mathbf{r}', t')\} \rangle & -\langle \{\psi_{\downarrow}^{\dagger}(\mathbf{r}, t), \psi_{\downarrow}(\mathbf{r}', t')\} \rangle \end{pmatrix}$$

Here all averages $\langle \ \rangle$ are taken over the ground state of the system at $T = 0$ or over a statistical average of the states of the system at finite temperature. One recognizes that the diagonal elements of \widehat{M} represent Green functions of the spin-up electrons and spin-down holes carrying information about the “normal” correlations in time and space. In view of previous relations (2) and (9), the off-diagonal elements of \widehat{M} are linked to superconducting correlations and represent the amplitudes for removing or adding an electron pair to the system at various positions and times. Using Usadel simplifications mentioned above leads to an isotropic Green function: $\widehat{G}^R(\mathbf{r}, t - t') = -i\theta(t - t')\langle \widehat{M}(\mathbf{r}, t | \mathbf{r}, t') \rangle_{\text{dis}}$ where $\langle \ \rangle_{\text{dis}}$ represents in fact several types of averages including the one on disorder and the thermal statistical one. Finally, one obtains the energy dependent retarded Green function $\widehat{G}^R(\mathbf{r}, E)$ by taking the Fourier transform of $\widehat{G}^R(\mathbf{r}, t - t')$ with respect to time: $\widehat{G}^R(\mathbf{r}, E) = \mathcal{F}[\widehat{G}^R(\mathbf{r}, t - t')]$. The matrix $\widehat{G}^R(\mathbf{r}, E)$ can be written as $\widehat{G}^R(\mathbf{r}, E) = \begin{pmatrix} g & f \\ f^{\dagger} & -g \end{pmatrix}$ and it satisfies the following compact diffusion equation:

$$\frac{\hbar D}{\pi} \nabla_r (\widehat{G}^R \nabla_r \widehat{G}^R) + [E \hat{\tau}_z + \widehat{\Delta}, \widehat{G}^R] + [\widehat{\Sigma}_{in} + \widehat{\Sigma}_{sf}, \widehat{G}^R] = 0 \quad (12)$$

Here D is the diffusion coefficient, ∇_r is the gauge-invariant gradient operator with respect to the space variable \mathbf{r} , $\hat{\tau}_z = \begin{pmatrix} 1 & 0 \\ 0 & -1 \end{pmatrix}$ is the Pauli matrix in electron-hole space, $[\dots, \dots]$ represents a commutator, $\widehat{\Delta} = \begin{pmatrix} 0 & \Delta(\mathbf{r}) \\ \Delta^*(\mathbf{r}) & 0 \end{pmatrix}$, $\widehat{\Sigma}_{in}$ and $\widehat{\Sigma}_{sf}$ represents terms describing inelastic interactions or spin-flip scattering. Here we take these two terms $\widehat{\Sigma}_{in} = \widehat{\Sigma}_{sf} = \widehat{0}$ since such processes will not be relevant in our case. $\widehat{G}^R(\mathbf{r}, E)$ satisfies normalization conditions: $(\widehat{G}^R)^2 = \widehat{1}$.

Through this simplified approach all relevant physical quantities are now space- and energy-dependent. In each particular situation one needs to solve numerically 2 coupled integro-differential equations verified by f and g which are complex numbers. The main difficulty comes from the fact that the order parameter $\Delta(\mathbf{r})$ has to be determined self-consistently through the following equation:

$$\Delta(\mathbf{r}) = v_0 V \int_{-\hbar\omega_D}^{\hbar\omega_D} \frac{dE}{2\pi} \text{Im}(f(\mathbf{r}, E)) \tanh \frac{E}{2k_B T} \quad (13)$$

where $v_0 V = \lambda$ is the electron-phonon coupling constant of the material and $\text{Im}(\dots)$ is the imaginary part. One sees that (13) is a generalization of (9bis) and (5), where $\Delta(\mathbf{r})$ can be chosen real when there is no phase difference across the junction. This relation exemplifies the fact that $\Delta(\mathbf{r}) = v_0 V(\mathbf{r})\mathcal{P}(\mathbf{r})$ is expressed as the product of pair potential $V(\mathbf{r})$, that can vary spatially, multiplied by a pair amplitude. In the low-disordered materials that we have studied here having $k_F \ell_e \gg 1$, $V(\mathbf{r})$ will have a step-like spatial dependence. For instance in a S-N junction $V(\mathbf{r}) = V > 0$ will be finite in S but $V(\mathbf{r}) = 0$ in N, while in a S₁-S₂ junction it will have two different values V_1 and V_2 in each superconductor. A physical quantity that manifests beautifully this space- and energy-dependence occurring in the proximity effect is the local density-of-states $\rho(\mathbf{r}, E)$. It is given by:

$$\rho(\mathbf{r}, E) = -\frac{1}{\pi} \text{Im}(g(\mathbf{r}, E)) \quad (14)$$

As we will see, its space- and energy-dependence will be so peculiar and rich that it will enables testing in great details the adequacy of the Usadel formalism to describe proximity effect. The Usadel equations have to be supplemented by boundary conditions expressing that deep into each material one recovers the reference Green functions for the normal metal or the superconductor. An additional condition comes into play at the interface between the two materials, characterizing how the spectral current density $\hat{\mathbf{j}}(\mathbf{r}, E) = \sigma_N \widehat{G}^R \nabla_r \widehat{G}^R$ should be conserved along the normal to the interface, where $\sigma_N = D e^2 v_0$ is the conductivity of each electrode in its normal state. This conservation of $\hat{\mathbf{j}}$ is written along z at position $\mathbf{r} = \mathbf{0}$:

$$\hat{j}_z(\mathbf{0}, E) = \sigma_{N_1} \hat{G}_1^R \nabla_r \hat{G}_1^R = \sigma_{N_2} \hat{G}_2^R \nabla_r \hat{G}_2^R = \frac{G_B}{S} [\hat{G}_1^R(\mathbf{0}, E), \hat{G}_2^R(\mathbf{0}, E)] \quad (15)$$

G_B is the interface conductance of the junction and S is the area of the junction. This condition implies continuity or discontinuity of the Green functions at the interface. For our work, the numerical implementation of the Usadel equations was carried out by Juan Carlos Cuevas from the Universidad Autonoma de Madrid, who is a specialist of theoretical mesoscopic superconductivity. As I said before this task is highly technical and I don't master it. The only thing I would like to add about it is that Juan Carlos used the Riccati parametrization for the Green function instead of the well-known $\theta - \varphi$, because it makes it easier to solve numerically the equations and has better physical grounds.

B) Experimental systems

For the three combined experimental-theoretical studies that I will present now, we have used the same couple substrate-nanostructured material: Pb grown on silicon, that has revealed to be quite versatile for our purpose. The substrate is a Si(111) piece of wafer, heavily or moderately n -doped with As donors. It is prepared by direct current heating to flash the sample many times above 1100°C, followed by a slow annealing between 900°C and 500°C. This whole procedure cleans the protective oxide layer, removes foreign atoms and makes the very well-known Si-7 × 7 surface reconstruction. A typical STM topography of the prepared substrate is shown in Fig.7c) emphasizing regular atomically flat terraces several hundreds of nm width, separated from one another by a step height of one Si atom. Then in a second step Pb atoms are evaporated from an e-beam evaporator onto the clean Si-7 × 7 surface to form the various desired normal or superconducting nanostructures. Because silicon has a large bandgap, becomes insulating below ~20-30 K, and does not alloy with Pb, it provides a perfect substrate for our mesoscopic nanostructures that does not induce inverse proximity effect.

In the studies C) and E) presented below, between 2 and 4 monolayers of Pb are evaporated on a substrate maintained at room temperature or slightly cooled above -50°C to lower Pb atom diffusion. Pb atoms form first a highly disordered wetting layer covering the entire silicon surface, whose structure is amorphous from diffraction experiments, and whose height is about 2-3 atom thick. This happens because Pb atoms saturate all dangling bonds of the Si surface atoms, but do not have enough energy to form a crystalline phase thus resulting in nanometer sized Pb clusters. Interestingly for us this amorphous Pb wetting layer remains normal and does not superconduct at 0.3 K. It furnishes the N part of our experiments. Additional Pb atoms deposited on the Pb wetting layer grow in forming single-crystal flat-top islands. These islands become superconducting between 5 and 6 K depending on their precise island thickness. They furnish our S part. This situation is schematically illustrated in Figure 7a). A sharp N-S interface is obtained with a very high transparency. The thickness of the S-N interface is the one of the wetting layer contacting the S island by its periphery. This case will be presented in C). By controlling the distance between two adjacent Pb islands (by changing the growth conditions) this fabrication process also enables to form an S-N-S lateral junction. This case will be presented in E).

In the study D) presented hereafter, we have used this Pb/Si(111) system to make a lateral junction between 2 superconductors S_1 and S_2 . This case is illustrated in Figure 7b). One of the superconductor S_1 is a single-crystal Pb island as above. The second superconductor is the wetting layer itself that has been transformed into a crystalline Pb monolayer by proper annealing at ~300 °C. This Pb crystalline monolayer also covers the entire Si surface. It has a complicated incommensurate structure [HupaloDevilStair2003] but is exactly one atom thick. This Pb crystalline monolayer becomes superconducting below about 2 K [Zhang2010] for optimal growth conditions and forms our S_2 electrode. A highly transparent S_1 - S_2 interface is provided by this fabrication process, whose thickness is exactly one atom high, because the whole growth process is carried out in 10^{-11} mbar pressure range ensuring excellent atomic contacts between atoms of the same chemical species, i.e. lead.

One could argue that ultrathin Pb islands or a single atom high Pb monolayer could depart significantly from a conventional BCS superconductor. In fact, to a first approximation this is not the case. Several groups have studied in details this issue that I have summarized in a review paper recently: see Brun, Cren and Roditchev Supercond. Sci. Technol. 30, 013003 (2017). Thus for what we are interested in this chapter, we can consider

that the various S electrodes are conventional superconductors but with an electron-phonon coupling term stronger than in the BCS weak coupling limit. This will nevertheless not affect significantly proximity effect and its theoretical description.

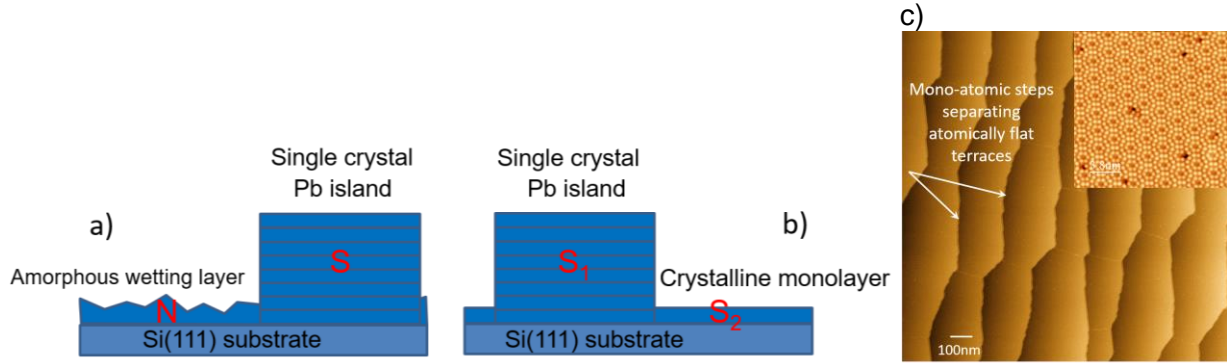


Figure 7. a) Sketch representing the S-N lateral junction formed in-situ between a single-crystal Pb island S and the surrounding normal amorphous wetting layer N. b) Sketch representing the S-S lateral junction formed in-situ between a single-crystal Pb island S_1 and the surrounding superconducting monolayer S_2 . c) Large scale topographic STM image of the Si- 7×7 reconstructed surface before Pb deposition. The insert shows a topography at smaller scale showing Si atoms and few atomic scale defects.

C) S-N proximity effect to a 2D strongly disordered metal

Let us first describe the various limits encountered in the S-N proximity effect before presenting our experimental results. For more clarity, we assume theoretically a S-N bilayer where S and N are stacked above each other along the x direction which indicates the direction of the junction. In the perpendicular (y, z) directions the materials are assumed infinite. The system is then invariant by translation in the (y, z) plane so that the problem is 1D along x . S is assumed semi-infinite along x . Although this geometry does not correspond to our lateral geometry described in Fig.7 above, it helps clarifying the expected results and does not change the qualitative picture. One then has two different cases:

- i) The length L of N along x (i.e. its thickness) is finite
- ii) The length L of N x is infinite

An energy-independent natural length scale that appears in this problem to characterize the superconducting

correlations in N is $\xi_N = \sqrt{\frac{\hbar D_N}{\Delta}}$ where D_N is the diffusion coefficient in N and Δ the superconducting energy gap of S far away from the S-N interface. We will discuss here only the so-called long junction cases where $L > (>) \xi_N$ which correspond to our experimental case. Also, we will neglect here inverse proximity in S which comes from the fact that in our real geometry $\sigma_S \gg \sigma_N$ and $v_{0S} \gg v_{0N}$. Finally, we have to consider the boundary condition (15) at the interface. It leads to a term $\frac{1}{r} = \left(\frac{G_B}{\sigma_{N2S}}\right)$ where G_B is the junction conductance and S the junction area. In order to estimate the value of r in the real geometry we assume that the transmission is carried out by N independent atomic channels of average transmission τ . This gives $G_B = G_0 N \tau$ where $G_0 = 2e^2/h$ is the conductance quantum per atomic channel. Since this transmission is atomically thin because it occurs towards a 2D metallic layer we assume that S can be written as $S = N \times 1 \times a^2$ where a is an effective lattice parameter per channel that we estimate by $a \approx 3 \text{ \AA}$. One finds $\sigma_{N2} = \frac{1}{d R_{N\Box}} \approx 6.7 \cdot 10^5 \Omega^{-1} \cdot \text{m}^{-1}$ where

$R_{N\Box} \approx 3 \text{ k}\Omega$ is taken from in-situ transport measurement [Pfen2002] and $d \approx 5 \text{ \AA}$. This leads to $r \approx \frac{2.6 \cdot 10^{-10}}{\tau}$.

The transmission τ is smaller than 1 but cannot be too small otherwise we would be in the tunnel regime and we could not observe any proximity effect. Thus one sees that in the regime we are interested in, one can safely assume $r = 0$, even if some estimated values that we used for a , d or $R_{N\Box}$ are not perfectly correct. Thus $r = 0$ implies the continuity of the Green functions on both sides of the interface.

Now that we have clarified the various boundary conditions of our Usadel equations let us go back to the case i). A natural energy scale associated to the length L is the Thouless energy $E_{Th} = \frac{\hbar D_N}{L^2}$. E_{Th} represents the

characteristic energy associated to the diffusive motion of the electrons to cross the entire N part which has a length L . This process takes a time τ_{Th} given by $L = \sqrt{D_N \tau_{Th}}$. Since we consider here junctions fulfilling $L > (>) \xi_N$ this leads to $E_{Th} < \Delta$. In this case the Usadel equations predict that a constant mini-gap Δ_g is induced everywhere in N which scales as E_{Th} and is given by $\Delta_g \approx 0.77 E_{Th}$. Thus Δ_g goes to 0 as $1/L^2$. At a distance x from the interface the LDOS $\rho(x, E)$ will be modified from the constant ν_{0N} DOS only in an energy interval given by $[-E_{Th}(x); E_{Th}(x)]$ where $E_{Th}(x) = \frac{\hbar D_N}{x^2}$. In other terms a quasi-particle excitation of energy E in N will propagate over a length $L_E = \sqrt{\frac{\hbar D_N}{E}}$. Now since in our S-N experiment we are interested in a situation where both S and N are semi-infinite, one needs to consider the case ii) above. In this case one has $\Delta_g = 0$ and at any energy $E \neq 0$ an excitation propagate over a length L_E . The expected $\rho(x, E)$ is represented in figure 8a) at various distances x from the interface expressed in unit of ξ_N . This regime has been first experimentally addressed by Sophie Guéron et al. in [Guéron1996] by probing the LDOS for three different distances L of a Cu-Al S-N contact. In practice at 0.3 K the phase coherence length is limited in our case by the thermal length $L_T = \sqrt{\hbar D_N / kT}$. This should lead to a flat LDOS above this length L_T . One important thing to note is that although a spectral gap Δ_g exists for finite L there is no finite order parameter induced in N since $V_N = 0$.

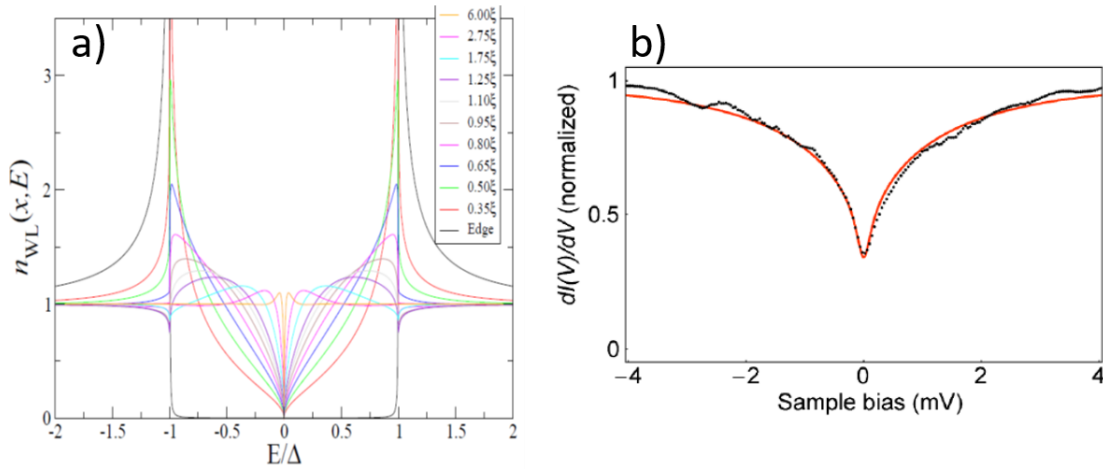


Figure 8. a) Local density-of-states $\rho(x, E)$, written here $n_{WL}(x, E)$, calculated from 1D Usadel equations for a semi-infinite S-N bilayer assuming $\Delta(0^-) = \Delta$ and negligible junction resistance. The various curves correspond to different distance x from the S-N interface (being at $x=0$) expressed in units of $\xi_N = \sqrt{\hbar D_N / \Delta}$. b) Black curve: reference $dI/dV(V)$ spectrum measured in N far away from S. Red curve: theoretical fit using the dynamical Coulomb blockade model assuming an Ohmic environment with $R=3.2$ k Ω and $C=80$ aF.

The experimental results are presented in Figure 9. The STM topography of the S-N system is seen in panel a) reflecting the situation presented in figure 7a) above. The total height of the Pb single-crystal island is 2.4 nm which corresponds to a thickness of 8 Pb atomic planes. The proximity effect measurements were carried out in the region indicated by the dashed rectangle over a length of about 70 nm. The experimental dI/dV spectra are presented in panel b). They evolve over a length of about 50 nm from a broadened BCS-like spectrum at the edge of the Pb island (i.e. $x = 0^-$) toward V-shaped spectra featuring a depressed DOS at E_F . Thus instead of recovering a flat DOS at E_F corresponding to a constant ν_{0N} , as shown in the theoretical figure 8a) for $x \geq 6\xi$, the characteristic excitation spectrum of the disordered Pb monolayer presents a depressed DOS at E_F . As we will see in details in chapter 2 later, this feature is characteristic of disordered metals presenting poor electronic screening due to large disorder and enhanced electron-electron repulsion.

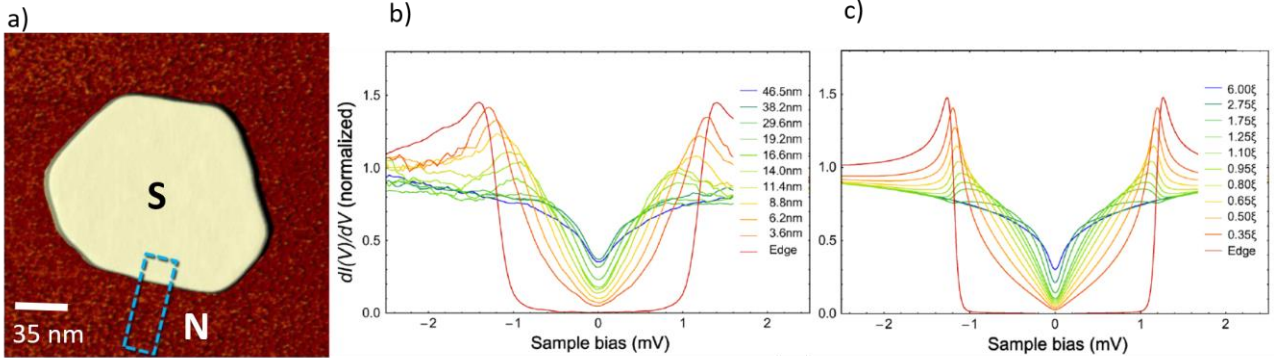


Figure 9. STM topography of the region of interest to study a S-N lateral proximity junction. S is a single-crystal Pb island of 8 atomic monolayers thickness (2.4 nm) and N is an atomically thin two-dimensional disordered Pb monolayer (average thickness between 4 and 6 Å). b) Experimental dI/dV spectra measured in the area indicated by the dashed rectangle in a) for various distance x from the interface. Each spectrum correspond to several laterally averaged dI/dV spectra over a width of about 15 nm parallel to the interface. c) Theoretical dI/dV spectra calculated from Usadel equations assuming a 1D geometry, no inverse proximity effect in S, negligible junction resistance and assuming for N a depleted V-shaped DOS spectrum.

A simple way of dealing with this non-constant DOS feature in N far away from S is to assume that the dynamical Coulomb blockade formalism can be applied [Ingold1992]. This actually works quite well and we used the simplest approximation, i.e. the Ohmic environment with an effective resistance R and capacitance C for the Pb monolayer. In this model the constant DOS ν_{0N} is convoluted by a $P(E)$ function that describes the probability that an electron loses energy during tunneling. Figure 8b) shows a reference spectrum measured in N on the Pb monolayer far away from S. One sees that the red curve from the dynamical Coulomb blockade model nicely fits the experimental one. Next, this $P(E)$ function is assumed to be homogeneous over all the N monolayer. The dI/dV spectra presented in figure 9c) are calculated by convoluting the LDOS $\rho(x, E)$ obtained from solving 1D Usadel equations with this established $P(E)$ function.

In order to implement the Usadel equations in our geometry, a lateral S-N'-N geometry is assumed, where S and N represent the unperturbed superconducting and normal reservoirs. One assumes $\Delta(0^-) = \Delta_S = 1.2$ meV. This explicitly neglects inverse proximity in S. This is justified because in our real geometry $\sigma_S \gg \sigma_N$ and $\nu_{0S} \gg \nu_{0N}$ due to the large difference in height and in amount of disorder in S and N. The length L of the N' part where proximity effect takes place is taken to be $L = 100\xi_N$. The boundary condition at the S-N' interface ($x = 0$) is expressed as above, but due to dimensionless position variable $\tilde{x} = x/L$, the factor r is multiplied by $1/L$ and becomes $r \approx \frac{1.7 \cdot 10^{-4}}{\tau}$. This shows that as considered above, for physical transmission τ of the order unity but not very small, one can assume $r = 0$. The N'-N interface is assumed to be perfect. One sees that the calculated dI/dV spectra presented in Fig.9c) reproduce very well the experimental ones in 9b). The only remaining parameter is $\xi_N = \sqrt{\hbar D_N / \Delta}$ which enables us to find $\xi_N = 15 \pm 3$ nm leading to $D_N \approx 4 \text{ cm}^2 \cdot \text{s}^{-1}$. A posteriori we can well justify why the Usadel theory could be applied assuming a 1D geometry:

- i) The lateral size of the island and monolayer are much larger than the characteristic length ξ_N so that our junction can be assumed to be invariant through a translation parallel to the S-N interface.
- ii) The height d_i of S and N verifies $d_i \ll \xi_N$.

We could achieve in this study a nice quantitative understanding of the S-N proximity effect in the interesting limit where N is a two-dimensional atomically thin disordered monolayer and thus where a good S-N electrical contact occurs through a junction whose thickness is between one and two atoms. This work was published in Serrier-Garcia *et al.* Phys. Rev. Lett. 110, 157003 (2013) and had a good impact. The only part that is treated here on a phenomenological basis is the use of dynamical Coulomb blockade to model the correlated normal state LDOS in N₂. We will present further works in chapter 2 that will enable improving on this issue.

D) Proximity effect between two superconductors

We consider two semi-infinite superconductors S_1 and S_2 with their own (Δ_1, T_{c1}, D_1) and (Δ_2, T_{c2}, D_2) parameters that are in good electrical contact. They verify $\Delta_2 < \Delta_1$. From the theoretical background developed above one expects that proximity effect will strongly affect the local DOS $\rho(\mathbf{r}, E)$ in the vicinity of the S_1 - S_2 interface. Since both superconductors are gapped for $T \ll T_{c1}, T_{c2}$, the largest changes in the LDOS $\rho(\mathbf{r}, E)$ should occur in the energy range around $\pm[\Delta_2, \Delta_1]$ and over length scales given by:

$$\xi_i = \sqrt{\frac{\hbar D_i}{\Delta_i}} \quad (16)$$

In our case the phase coherence length is most probably limited at $T = 0.3$ K by the thermal length $L_T = \sqrt{\frac{\hbar D}{k_B T}}$ which is about 140 nm for the superconducting monolayer S_2 . The experimental results at 0.3 K are presented in Fig. 10, where one sees in panel a) the STM topography of the studied S_1 - S_2 junction. The profile of height variations between S_1 and S_2 indicated by the dashed blue line is plotted in panel b). It shows that the atomically flat Pb island S_1 has a height of 7 ML (i.e. 7 Pb atomic planes) with respect to the Pb monolayer S_2 . Its total vertical height with respect to the Si(111) surface is thus 8 ML. It shows that the atomic contact between the monolayer and the island occurs through a one atom high line going along the S_1 - S_2 boundary.

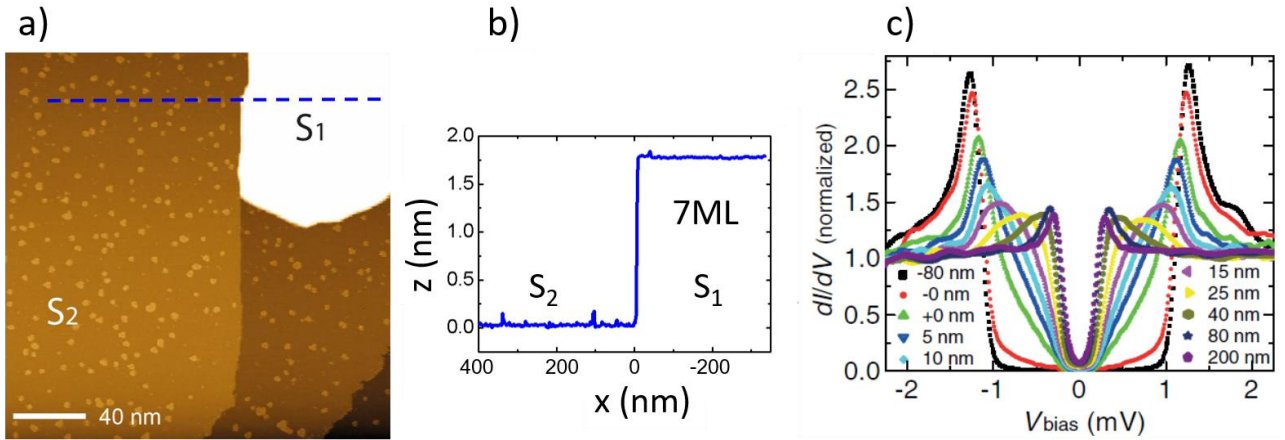


Figure 10. a) STM topography of the lateral junction. b) $z(x)$ topography profile along the blue dashed line shown in a) expressed in nm. c) Spatial evolution of the $dI/dV(V)$ spectra along the line shown in b). The $S_1 - S_2$ interface is located at $x = 0$ nm.

The panel c) shows the spatial evolution of the differential conductance spectra where 0 nm represents the S_1 - S_2 interface. Far away from the interface, the spectra in S_1 and S_2 are well described by the BCS theory enabling to extract $\Delta_1 = 1.20$ meV (at -80 nm) and $\Delta_2 = 0.23$ meV (at 200 nm). One sees that most of the qualitative changes in $\rho(\mathbf{r}, E)$ occur in S_2 between 0 and 80 nm, where one can nicely follow the coherence peaks that evolve from energy values close to Δ_1 at 0 to energy reaching Δ_2 at 80 nm. One notices as expected that in S_2 all spectra are gapped with a gap equal to Δ_2 . On the S_1 side, changes in $\rho(\mathbf{r}, E)$ are of much smaller amplitude. This asymmetry is due to the fact that the thickness of S_1 is 8 times larger than the one of S_2 , so that their conductances verify $\sigma_1 \gg \sigma_2$ and density-of-states $\nu_{01} \gg \nu_{02}$. The choice of not including any depairing parameter Γ_{in} or Γ_{sf} in the modelling led us to consider an effective temperature slightly higher than the bath temperature. It could have also been the other way round, but is not crucial here. The corresponding T_{ci} 's are taken equal to their fictitious BCS values $T_{c1} = 7.9$ K and $T_{c2} = 1.5$ K for self-consistency of the Usadel theory. These weak-coupling values are quantitatively different from the real T_{ci} 's, but this will not play an important role here as we will see.

The Usadel theory is applied assuming a 1D geometry because:

- i) The lateral size of the island and monolayer are much larger than the characteristic lengths ξ_i so that our junction can be assumed to be invariant through a translation parallel to the S_1 - S_2 interface.
- ii) The height d_i of each S_i verifies $d_i \ll \xi_i$.

The S_1 - S_2 real system is numerically implemented as an S_1 - S'_2 - S_2 system where S_1 at position -0 and S_2 at $L = 200$ nm have their equilibrium value conditions for the Green functions corresponding to $\Delta(-0) = \Delta_1$ and $\Delta(L) = \Delta_2$. S'_2 is the part of the superconducting monolayer of finite length L where proximity effect takes place. S'_2 is connected on both sides to unperturbed S_2 and S_1 . This assumes that inverse proximity effect does

not affect S_1 , which is not true strictly speaking but is a very small effect as seen from the spectra. As mentioned above this simplification comes from the large difference in the conductance and density-of-states between S_2 and S_1 . The boundary conditions (15) are implemented as follows: S'_2 - S_2 is assumed to be perfectly transparent while S_1 - S'_2 leads to a term $\frac{1}{r} = \left(\frac{G_B}{G_{N2}}\right)$ where G_B is the conductance of the junction between S_1 and S'_2 , and $G_{N2} = \sigma_2 S/L$ is the normal conductance of the central part S'_2 with S being the area of the junction. The fact that $1/L$ enters G_{N2} while only $\sigma_2 S$ is originally present in (15) is because numerically the real coordinate x in S'_2 is normalized with respect to L by considering the dimensionless coordinate $\tilde{x} = x/L$. Since the lateral junction physically consists in a line of N atoms of lattice parameter $a = 2.85 \text{ \AA}$ (the Pb lattice parameter) one has $S = Na^2$. On the other hand, in the simplest approximation G_B can be written $G_B = G_0 N \tau$ where $G_0 = 2e^2/h$ is the conductance quantum per atomic channel and τ is the average transmission per channel. Computing all numerical values and calculating σ_2 from the square resistance $\rho_{2\Box}$ value extracted from in-situ transport measurements $\rho_{2\Box} \sim 1 \text{ k}\Omega$ [Yamada2013] leads to:

$$r = \frac{\sigma_2 Na^2}{G_0 N L \tau} = \frac{1.8 \cdot 10^{-2}}{\tau} \quad (17)$$

This shows that even for a perfect average transmission per atomic channel $\tau = 1$ across the S_1 - S'_2 junction, a small discontinuity occurs across the interface between the Green functions because $r \neq 0$, which should show up in the local spectra. Figure 11a) shows the evolution of the 0.3 K spectra measured every nanometer. They are represented in a 2D color-conductance plot and can be compared to the theoretical ones plotted in panel 11b) for $r = 0.02$. The agreement is quite astonishing and a small discontinuity is indeed seen at $x = 0$. The panel c) enables to see better this discontinuity at $x = 0$ by showing with blue points the spatial dependence of the energy of the coherence peaks. The fit of this curve enables to extract $D_2 \approx 7 \text{ cm}^2 \cdot \text{s}^{-1}$ which sets the S_2 superconducting coherence length $\xi_2 = \sqrt{\frac{\hbar D_2}{\Delta_2}} \approx 46 \text{ nm}$. It also enables to appreciate that the self-consistency of the calculations is mandatory to extract the correct spatial dependence of $\rho(\mathbf{r}, E)$ and $\Delta(\mathbf{r})$ though the relation (13) (compare the red curves with and without self-consistency in panel c).

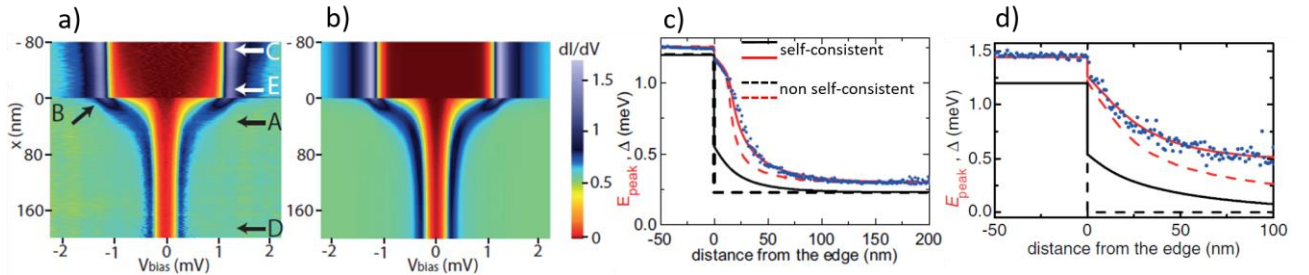


Figure 11. a) Spatial dependence of the $dI/dV(V)$ spectra measured at $T=0.3 \text{ K}$ along the S_1 - S_2 junction. The spectra are presented in a 2D color-coded plot where the scale of the normalized differential conductance is indicated next to the panel b). b) Same as in panel a) but showing the calculated $dI/dV(V)$ spectra from a 1D Usadel model. c) Blue dots represent the spatial dependence of the energy of the coherence peaks extracted from the experimental $dI/dV(V)$ spectra at $T=0.3 \text{ K}$. Red curves are the theoretical attempts to fit the experimental blue dots assuming or not self-consistency in the Usadel equations. d) Same quantities as in panel c) but at $T=2.05 \text{ K}$ above T_{c2} the critical temperature of S_2 . In panels c) and d) the black curves represent the calculated order parameter $\Delta(\mathbf{r})$ with or without self-consistency.

Furthermore our analysis reveals that a much increased local order parameter is induced close to the interface due to the stronger electron-phonon coupling constant $\lambda_1 = v_{01} V_1 > \lambda_2$ in S_1 (compare the black continuous curve in panel 11c) with the dashed curve). Indeed one reads $\Delta(+0) \approx 0.55 \text{ meV} > \Delta_2 = 0.23$, so that Δ is more than doubled. Interestingly this extra order parameter $\Delta(+0) - \Delta_2$ decreases exponentially with a characteristic length given by ξ_2 , as one expects in S_2 . Interestingly also, the value of ξ_2 found from the present analysis of the S_1 - S_2 proximity effect is in very good agreement with the size of a single superconducting vortex core in S_2 , presented later in **Topic2G** figure 24d), as it should be.

A similar spatial dependence was measured at $T = 2.05 \text{ K}$, which is above the critical temperature T_{c2} of S_2 . In principle, this regime should correspond to an S_1 - N_2 junction since S_2 is in its normal state. Naively, one could then expect a spatial dependence of the dI/dV spectra similar to the one presented in the previous part C) above but this time with a flat $\rho(\mathbf{r}, E)$ DOS in S_2 far from the interface, since it is a weakly disordered

system. This simple case of an S_1 - N_2 junction with $\lambda_2 = 0$ in N_2 corresponds to the $\rho(\mathbf{r}, E)$ LDOS plotted previously in Fig.8a) above. It implies zero induced spectral gap and zero order parameter in N_2 . However this statement is not correct, as we demonstrate here, because N_2 has a positive electron-phonon coupling constant $\lambda_2 > 0$ since it becomes superconducting below T_{c2} . In contrast, the self-consistency shows that the proximity to the superconductor S_1 induces a finite order parameter $\Delta_{T=2.05 K}(+0) \neq 0$ at the interface in N_2 . The value of $\Delta_{T=2.05 K}(+0)$ is close to the zero temperature value. The induced gap decays exponentially as $\Delta_{T=2.05 K}(+0)\exp(-\frac{x}{L_\Delta})$. Here L_Δ is a temperature-dependent length scaling as $1/\sqrt{T - T_{c2}}$ above T_{c2} . A panel similar to Fig.11c) is presented in Fig.11d) enabling to appreciate the quality of the fit of the experimental data and the spatial dependence of $\Delta_{T=2.05 K}(\mathbf{r})$. Note that the value of the discontinuity parameter $r = 0.02$ is kept unchanged in the whole analysis.

We could achieve in this study a nice quantitative understanding of the S_1 - S_2 proximity effect in the interesting limit where S_2 is a two-dimensional atomically thin crystalline monolayer. As a consequence a good S_1 - S_2 electrical contact occurs through a junction whose thickness is exactly one atom thick. Moreover, the S_1 - N_2 regime above T_{c2} with a positive λ_2 leading to a finite order parameter was never studied experimentally before. This work was published in Cherkez *et al.* Phys. Rev. X 4, 011033 (2014) and had a good impact.

E) S-N-S network: revealing Josephson vortex cores

Using the experimental system described in C) above, i.e. single-crystal Pb islands grown on top of a 2D highly disordered Pb monolayer, we managed to form S_i - N - S_j superconducting junctions by bringing Pb islands sufficiently close to each other. For finite length L of the N part superconducting correlations will propagate by proximity effect from one superconductor S_i to the second S_j if $L < L_\phi$ where L_ϕ is the phase coherence length in N. For us we have seen that in N, $L_\phi = \sqrt{\hbar D_N/kT} \approx 100$ nm at 0.3 K. We should thus make sure that the distance L between neighboring Pb islands is such that $L < 100$ nm. This is what we have realized experimentally as seen on the STM topography presented in figure 12a).

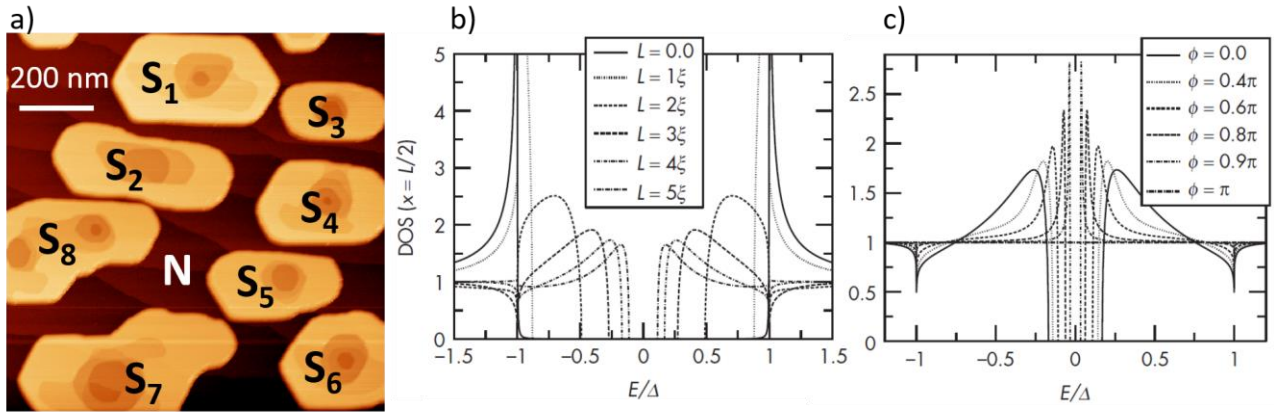


Figure 12. a) STM topography presenting a S-N-S network of $1 \times 1 \mu\text{m}^2$. It consists of superconducting junctions made of various single-crystal diffusive Pb islands (S_i in yellow) of height between 8 and 15 atomic monolayers in good electrical contact with an atomically thin disordered Pb monolayer (N in dark red). b) Theoretical calculations using 1D Usadel equations of the LDOS $\rho(x = L/2, E)$ computed in the middle of various S-N-S junctions of length L expressed in units of $\xi_N = \sqrt{\hbar D_N/\Delta}$. c) Similar theoretical calculations made for one S-N-S junction of length $L=4\xi_N$ for various phase differences ϕ between the two S parts.

Theoretically let us consider one single S-N-S junction of finite length $L < L_\phi$, located between $x = 0$ and $x = L$. Let us assume at both S-N interfaces the same boundary conditions as in paragraph C) above, i.e. negligible $r = G_N/G_B \approx 0$ parameter and absence of inverse proximity effect in both S electrodes: $\Delta(0^-) = \Delta(L^+) = \Delta_S = 1.2$ meV due to the large difference in conductance and density-of-states between S and N. In this case a constant mini-gap Δ_g is induced in N which value in the long-junction limit $L > (>) \xi_N$ equals $\Delta_g \approx 3.1 E_{Th} = 3.1 \hbar D_N/L^2$. The calculated LDOS in the middle of N at $x = L/2$ is plotted in Fig.12b) for various lengths L expressed as a function of ξ_N . Importantly a superconducting S-N-S junction is also a Josephson junction. In particular it was shown by Zhou et al. [Zhou1998] that applying a phase difference ϕ

between the two superconductors modulates the value of Δ_g . This behavior is seen in Fig.12c): at $\phi = 0$ Δ_g is maximum and progressively diminishes to completely close at $\phi = \pi$ where $\Delta_g = 0$. These theoretical predictions were confirmed by local STM/AFM measurements by H el ene le Sueur et al. [Lesueur2008] by probing the local LDOS of the S and N parts applying various constant phase differences across the junction. Our combined experimental and theoretical work enabled to go further and create phase gradients across the S-N-S junction, leading to the appearance of Josephson vortices in the N part that we could measure by local STS spectroscopy.

In the geometry of our experiment, shown in figure 12a), a simple way of creating phase gradients following the contour of each island is to apply a perpendicular magnetic field. This is illustrated in figure 13. Panel 13a) shows the $dI/dV(V = 0) \propto \rho(\mathbf{r}, E = 0)$ conductance map measured at 0.3 K on the whole area of interest in zero magnetic field. All S_i are homogeneously superconducting with their own $\Delta_{S_i}(\mathbf{r}) = \Delta_{S_i}$, corresponding to the dark blue color in the conductance map. In between neighboring islands like S_1 and S_2 one notices regions in N that have a bluish color as well, but lighter than in the S_i 's. Two of such regions J_1 and J_2 are indicated by a dashed rectangle for the S_1 -N- S_2 and S_4 -N- S_5 junctions. In all such proximity junction J_i a mini-gap Δ_{g_i} exists given by the length L_i of the S_i -N- S_j junction, as illustrated by the dI/dV spectrum measured in the middle of J_2 shown in the bottom inset of panel 13a). In applying a perpendicular magnetic field of 60 mT, the panel 13b) shows that the $dI/dV(V = 0) \propto \rho(\mathbf{r}, E = 0)$ conductance map (measured at 0.3 K) significantly changes with respect to the zero-field case. In particular Abrikosov vortices are induced in the largest Pb islands S_1, S_4, S_6, S_7 and S_8 as seen by their normal cores corresponding to light yellow conductance color. Since a single vortex in a conventional superconductor corresponds to a 2π phase singularity, there will be phase gradients created along these islands. In fact in all other islands carrying no vortices, there are also phase gradients because of the circulating Meissner currents, but these are not seen in the $dI/dV(V = 0)$ map. In addition, other changes of LDOS are also observed in several N parts of the junctions J_1 and J_2 . In particular a Josephson vortex has appeared in the middle of J_1 (corresponding to the yellow area surrounded by two bluish spots on its left and right) while another one is in the process of entering J_2 from the right. These Josephson vortices that appeared in N correspond to areas where the mini-gap Δ_{g_i} is destroyed locally. With respect to the properties of single S-N-S junctions presented above, this should imply that locally a gauge-invariant phase difference

$$\varphi^*(\mathbf{r}_1, \mathbf{r}_2) = \varphi(\mathbf{r}_2) - \varphi(\mathbf{r}_1) - \left(\frac{2e}{\hbar}\right) \int_{\mathbf{r}_1}^{\mathbf{r}_2} \vec{A}(\mathbf{r}) \cdot d\vec{r} = \pi \quad (18)$$

is established across opposite sides of S_1 and S_2 where a Josephson vortex set in between the positions \mathbf{r}_1 and \mathbf{r}_2 . Similarly bluish areas in N presenting a superconducting gap should correspond to situations where $\varphi^* = 0$. Thus our task was to derive a model enabling to draw these portraits of phase differences between neighboring islands to make a proper comparison with our experimental results.

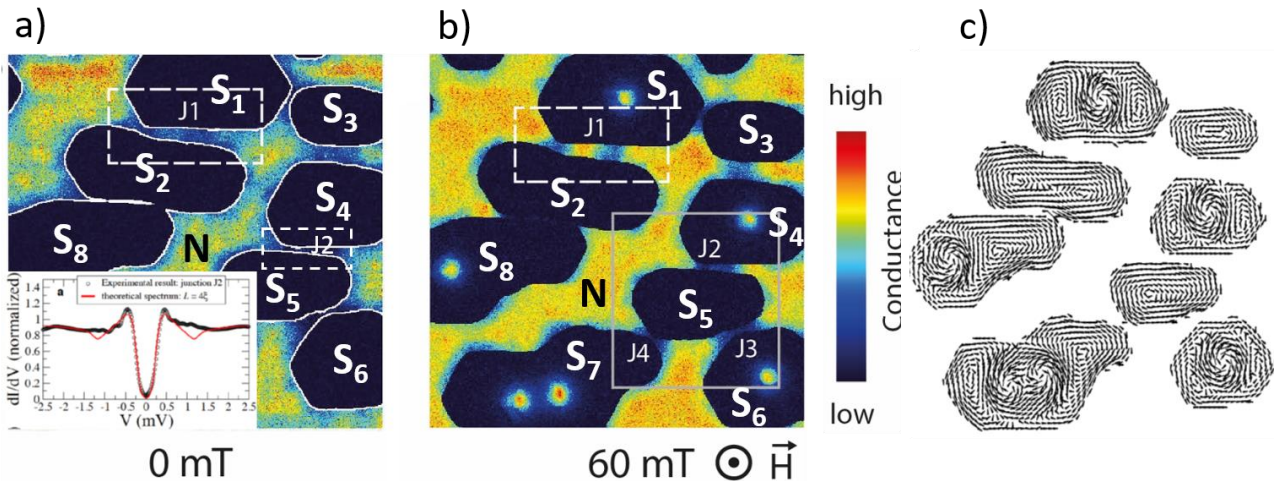


Figure 13. a) STS conductance map measured on the same area as the Fig12a), showing $dI/dV(V = 0) \propto \rho(\mathbf{r}, E = 0)$ measured at $T=0.3$ K and at zero magnetic field. The conductance scale axis is indicated next to the panel b). The inset presents an experimental dI/dV spectrum (black curve) measured in the middle of junction J_2 together with a fit using 1D Usadel equations (red curve). b) Same quantity as in a) but under a perpendicular magnetic field of 60 mT. Dark and blue areas indicate superconducting regions while yellow areas correspond to normal regions. c) Calculated superconducting current densities $\vec{J}_S(\mathbf{r})$ in each Pb islands for the applied perpendicular magnetic of field 60 mT presented in panel b). These calculations are

made by solving numerically Ginzburg-Landau equations assuming the real geometry of the islands.

Each diffusive superconducting island can be shown to carry a superconducting current density given by $\vec{j}_S(\mathbf{r}) = \rho_S(\mathbf{r})\vec{v}_S(\mathbf{r})$ where $\rho_S(\mathbf{r})$ is the local superfluid density and $\vec{v}_S(\mathbf{r}) = D_S[\vec{\nabla}\varphi(\mathbf{r}) - \frac{2e}{\hbar}\vec{A}(\mathbf{r})]$, $\vec{A}(\mathbf{r})$ being the vector potential associated to the magnetic field. Each $\vec{j}_S(\mathbf{r})$ portrait existing in each island should be gauge-invariant since it is a physical quantity directly linked to the locations of the Abrikosov vortices. Such quantities could in principle be calculated from 2D Usadel equations for each island and then for the whole S-N-S network to solve the full proximity network. Nevertheless the numerical complexity of such a task was beyond our capability at the time of this study. Improvements were presented later by other theoreticians [Amundsen2016]. We relied here on a simpler numerical method than solving the 2D Usadel equations for the real geometry. In order to get the theoretical $\vec{j}_S(\mathbf{r})$ and $\Delta(\mathbf{r})$ spatial distributions existing inside the S_i Pb islands corresponding to the one encountered in our experiment, we solved the 2D Ginzburg-Landau equations. These consist in two equations: one being a Schrödinger-like equation for the order parameter $\Delta(\mathbf{r})$, the second being an equation expressing the superconducting current density $\vec{j}_S(\mathbf{r})$ as a function of $\vec{A}(\mathbf{r})$. These equations are simpler because they are not energy dependent. Nevertheless they are physically correct at a mean-field level and have been shown by Gor'kov to result from microscopic BCS equations. These equations were solved numerically using finite-element methods by our colleague Milorad Milosevic from Antwerpen University who implemented a code enabling to incorporate the real geometry of our islands (in shape and height). The choice of the gauge was the symmetric one using $\vec{A}(\mathbf{r}) = \frac{1}{2}\vec{B} \times \vec{r}$, the center of the coordinates being taken at the center of the STM topography Fig.12a). Figure 13c) presents the calculated superconducting current density $\vec{j}_S(\mathbf{r})$ in each Pb island. One sees that the calculated locations of the Abrikosov vortices, where $\vec{j}_S(\mathbf{r})$ rotates on itself in the direction opposite to the Meissner currents, perfectly match the vortex positions observed in the experimental conductance map in panel 13b).

These computations enable us to have reliable gauge-invariant quantities corresponding to our physical experiment. Nevertheless in the Ginzburg-Landau calculations, the Pb islands remain uncoupled. Thus each phase portrait $\varphi_i(\mathbf{r})$ of the order parameter $\Delta_{S_i}(\mathbf{r}) = |\Delta_{S_i}(\mathbf{r})|e^{i\varphi_i(\mathbf{r})}$ for each island S_i is determined up to a constant arbitrary phase α_i . This gives 8 α_i independent parameters since there are 8 islands. In the real S-N-S network, all Pb islands are coupled two by two with each other through proximity links. Thus, at zero magnetic field and in equilibrium, 8 α_i values are set such that $\alpha_1 = \alpha_2 = \dots = \alpha_7 = \alpha_8$ in order to minimize the total energy of the S-N-S network and to avoid superconducting currents flowing from one island to another. This leaves free only one α_i parameter, say α_1 , all the other α_i being equal to α_1 . In finite magnetic field the situation is different. In principle at equilibrium one expects that no net Josephson current should circulate from one island to the next. Nevertheless, this latter condition does not prevent local superconducting currents from circulating in one direction or in the opposite one, in some local areas of the N part where $\varphi^*(\mathbf{r}_1, \mathbf{r}_2) \neq 0$ on both side of N, as is suggested by panels 13b) and 13c). Our analysis shows that in finite magnetic field each difference $\alpha_i - \alpha_j$ for each pair of proximity coupled Pb islands, has to be adjusted in order to give no net Josephson current for each S_i -N- S_j junction. Only this condition enabled us to reproduce correctly the complicated pattern of superconducting and normal areas seen by STS in each proximity S_i -N- S_j junction.

In order to connect the Ginzburg-Landau calculations to the superconducting correlations induced in N, we assumed a phenomenological superconducting amplitude parameter in N given by:

$$\rho(\mathbf{r}) = \sum_{i=1}^8 \int_{C_i} d\mathbf{r}_i e^{-\frac{r-r_i}{2\xi_N}} e^{i\left[\varphi(r_i) + \frac{2e}{\hbar} \int_{r_i}^r \vec{A}(r') \cdot d\mathbf{r}'\right]} \quad (19)$$

This parameter expresses the amount of local superconducting correlations $\rho(\mathbf{r})$ induced in N at position \mathbf{r} from the neighboring locations \mathbf{r}_i situated on all Pb islands' contours C_i . These contributions interfere because they are weighted like in (18) above using a gauge-invariant term (the term in brackets in the second complex exponential term of 19). This term explicitly takes into account the phase portraits established along the contour C_i of each island extracted from the Ginzburg-Landau calculations presented above. The first exponential term assumes that the superconducting correlations vanish exponentially with distance in N over a characteristic length ξ_N , which is consistent with what we have presented about the S-N proximity effect. The calculated 2D map of $\rho(\mathbf{r})$ is plotted in figure 14. The panel 14a) includes the optimization of the phase differences discussed above. It reproduces very well the experimental results of Fig13b), while the panel 14b) presents marked differences like in junction J_2 .

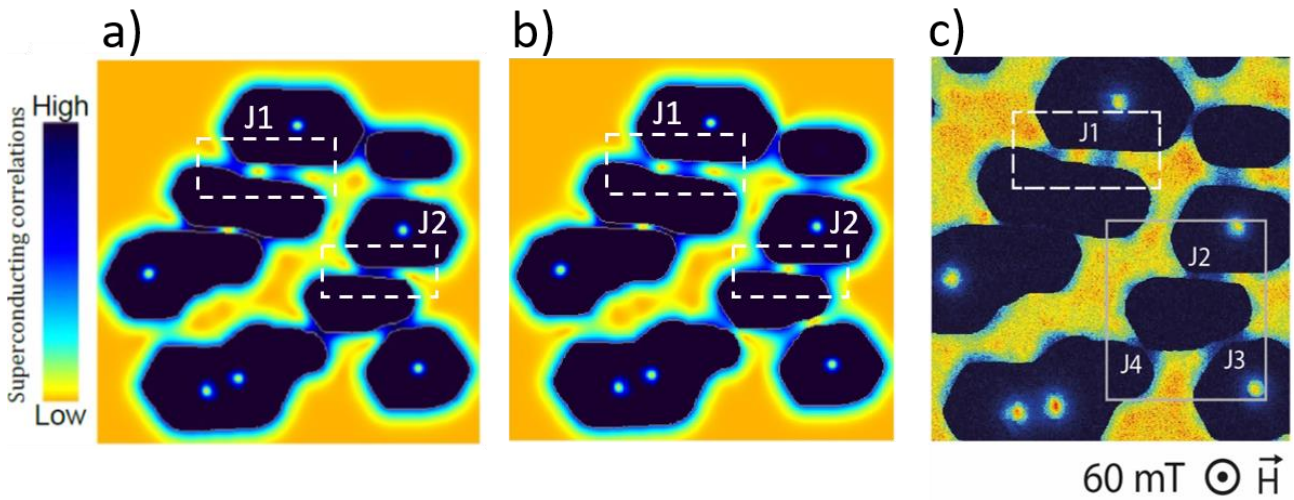


Figure 14. a) 2D map of the local superconducting correlations parameter $\varphi(\mathbf{r})$ obtained by optimizing all phase differences $\alpha_i - \alpha_j$ so that no net Josephson current circulates between two neighboring islands S_i and S_j . This map reproduces well the configuration in N measured by STS and presented in panel 13b) which is reproduced here in panel c). b) Same quantity as in a) but without optimization of the phase differences. In this case one sees that the configuration in junction J_2 for instance is different from the measured one and carries a net superconducting current. There are also other differences for other junctions.

Finally we see that our combined approach using numerical Ginzburg-Landau calculations for the real geometry of our S-N-S network, and a phenomenological superconducting amplitude parameter enabled to reach a very good understanding of our results. In addition we also would like to mention that our colleague Juan-Carlos Cuevas could provide and solve 2D Usadel equations for a single S_1 -N- S_2 junction assuming a perfect rectangular geometry and assuming either opposite superconducting currents running in the leads S_1 and S_2 or a perpendicular external magnetic field [Cuevas2007]. His results agree with the physical picture of Josephson vortices developed here. Our work was published in Roditchev *et al.* Nature Physics 11, 332 (2015) and had a good impact. This was the first time that effects produced by superconducting phase gradients could be revealed by local spectroscopy in proximity junctions showing in particular that Josephson vortices have normal cores in S-N-S junctions.

Topic 2: Effect of non-magnetic and magnetic disorder on superconductivity

This topic consists in studying at the atomic scale how non-magnetic disorder or impurities on one hand or isolated magnetic atoms or molecules on the other hand affect superconductivity. The subject dealing with the study of magnetic impurities in superconductors was a part of my recruitment CNRS project. My colleagues Yves Noat, Tristan Cren and Dimitri Roditchev had a common interest in these studies. The subject dealing with the study of the effects produced by non-magnetic disorder has two different directions. The first direction was already launched by my colleagues when I took part in it: studying the effect of weak and moderate disorder in NbN conventional superconducting thin films. In 2012, I launched the second direction: the study of the local superconducting properties of superconducting Pb monolayers grown on silicon substrate which revealed new weak-disorder effects. The subject dealing with the study of magnetic impurities has also two different directions. One direction was to study the effect of native magnetic atoms in the quasi-2D superconductor 2H-NbSe₂. This direction started in 2014 was initiated by test experiments that we performed in 2011 while calibrating STS measurements using superconducting vortices in 2H-NbSe₂. The second direction was to deposit intended controlled magnetic impurities on superconducting thin films. In collaboration with Tristan Cren and Nadine Witkowski we chose to deposit MnPc molecules on ultrathin Pb/Si(111) films. Our idea of choosing molecules instead of atoms was the easier possibility of manipulating them. To summarize, I will present here four different studies, two about the effects produced by non-magnetic disorder and two about the effects produced by magnetic impurities:

- i) Effects produced by weak and moderate non-magnetic disorder in polycrystalline NbN thin films

- ii) Weak non-magnetic disorder effects produced in a superconducting Pb monolayer
- iii) Mapping the wavefunction of the bound state of a single magnetic atom in a superconductor
- iv) Coupling between magnetic molecules and ultrathin superconducting films: MnPc/Pb/Si(111)

For the work (i) I **co-supervised the PhD thesis of Clémentine Carbillet** (during 3 years) and **2 post-docs Vladimir Cherkez** (during 2 years) and **Vasily Stolyarov** (during 2 years). I now continue to work on this topic, co-leading research activities with my colleague Tristan Cren. This activity was supported by the ANR [Superstripes](#) (ANR-15-CE30-0026) in which I was partner with Tristan and Dimitri. My supervision consisted first in teaching C. Carbillet and V. Cherkez the physics of disordered superconducting systems. I also supervised and planned detailed STM/STS experiments. I also helped them setting up the simultaneous electrical transport measurements in the STM head. I contacted and lead the discussion with our colleague theoreticians. I also completely supervised the writing of the PhD thesis of C. Carbillet whom I am co-advisor. V. Stolyarov wrote the labview program to interface the resistivity measurements. Most of the STS data analysis was done by my colleague T. Cren. Electronic transport measurements were supervised by our colleague Brigitte Léridon from ESPCI-Paris. This work gave rise to several publications in which the people I co-supervised are written in bold:

- a) *Unconventionnal superconductivity in ultrathin superconducting NbN films studied by scanning tunneling spectroscopy*
Y. Noat, **V. Cherkez**, **C. Brun**, T. Cren, **C. Carbillet**, F. Debontridder, , K. Ilin, M. Siegel, A. Semenov, H.-W. Hübers, D. Roditchev, Phys. Rev. B 88, 014503 (2013)
- b) *Confinement of superconducting fluctuations due to emergent electronic inhomogeneities*
C. Carbillet, S. Caprara, M. Grilli, **C. Brun**, T. Cren, F. Debontridder, B. Vignolle, W. Tabis, D. Demaille, L. Largeau, K. Ilin, M. Siegel, D. Roditchev, B. Leridon, Phys. Rev. B 93, 144509 (2016)
- c) *Spectroscopic evidence for strong correlations between local superconducting gap and local Altshuler-Aronov density-of-states suppression in ultrathin NbN films*
C. Carbillet, **V. Cherkez**, M.A. Skvortsov, M.V. Feigel'man, F. Debontridder, L.B. Ioffe, **V.S. Stolyarov**, K. Ilin, M. Siegel, D. Roditchev, T. Cren, **C. Brun**, Phys. Rev. B 102, 024504 (2020)
- d) The PhD thesis of Clémentine Carbillet entitled “*Nano-scale electronic inhomogeneities in ultrathin superconducting NbN*” was defended in public the 24th of October 2014. Clémentine is now working in industry. The official PhD advisor was Dimitri Roditchev and I was the main co-advisor with my colleagues Tristan Cren and Brigitte Léridon.

For the work (ii), I co-supervised the work of our **post-doc Vladimir Cherkez** (during 2 years). My supervision consisted in teaching how to prepare samples, carry proper STM/STS experiments, plan and design experiments. Most of the STS data analysis was done by my colleague Tristan Cren and a small part by myself. For this project that I launched, I performed most of the experiment myself before Vladimir arrived. These results enabled me to write and obtain a young ANR project in 2016: [RODESIS](#), superconductivity in a single atomic plane (ANR-16-CE30-0011). This work gave rise to several publications, including people I co-supervised in bold:

- a) *Remarkable effects of disorder on superconductivity of single atomic layers of lead on silicon*
C. Brun, T. Cren, **V. Cherkez**, F. Debontridder, S. Pons, L.B Ioffe, B.L. Altshuler, D. Fokin, M.C. Tringides, S. Bozhko, and D. Roditchev, Nature Physics 10, 444 (2014)
- b) *Review of 2D superconductivity: the ultimate case of epitaxial monolayers*
C. Brun, T. Cren, D. Roditchev, Supercond. Sci. Technol. 30, 013003 (2017)

For the work (iii), I co-supervised the work of our **PhD student Gerbold Ménard** (during 3 years) and master 2 students **Raphaël Leriche** (3 months) and **Mathieu Leclerc** (3 months). My supervision consisted mostly in teaching, planning and supervising the lab work with the STM/STS experiments, correcting the reports/PhD thesis. Most of the STS data analysis was done by Tristan Cren. Gerbold developed a Python program for the STS data analysis that I also implemented and improved further with him, so that we also analyzed all the STS data to cross-check with Tristan. This work was part of an ANR project [MISTRAL](#) (ANR-14-CE32-0021) where I was partner with my colleague Tristan. This work gave rise to several publications, including people I co-supervised in bold:

- a) *Coherent long-range magnetic bound states in a superconductor*
G. Ménard, S. Guissart, **C. Brun** S. Pons, **V.S. Stolyarov**, F. Debontridder, **M.V. Leclerc**, E. Janod, L. Cario, D. Roditchev, P. Simon, T. Cren, Nature Physics 11, 1013 (2015)

- b) *Yu-Shiba-Rusinov bound states versus topological edge states in Pb/Si(111)*
G.C. Ménard, C. Brun, R. Leriche, M. Trif, F. Debontridder, D. Demaille, D. Roditchev, P. Simon, T. Cren, Eur. Phys. J. Special Topics 227, 2303 (2019)
- c) The PhD thesis of **Gerbold Ménard** entitled “*2D superconductors perturbed by local magnetism: from Yu-Shiba-Rusinov bound states to Majorana quasiparticles*” was defended in public the 16th of September 2016. Gerbold Ménard is now post-doc at ESPCI-Paris with Nicolas Bergeal and Jérôme Lesueur. The official PhD advisor was Dimitri Roditchev. In practice the two main co-supervisors were myself and Tristan Cren.

For the work iv) this was the main part of the **PhD work of Danilo Longo** (during 4 years) that I entirely co-supervised and who defended his thesis in May 2019. This work was also a part of the **PhD thesis of Raphaël Leriche** that I also co-supervised. I also co-supervised **our Post-doc Alexandra Palacio-Morales** since February 2018 on these studies. My supervision with Danilo consisted in lab supervision, data analysis, and correcting of the PhD thesis. For Raphaël, since it was a smaller part of his PhD work, it was mostly lab supervision and scientific discussions. This work gave rise to several publications, including people I co-supervised in bold:

- a) *Surface Phase Nucleation of Lead Monoatomic Layers on Si (111) Induced by Manganese Phthalocyanine Molecules*
Danilo Longo, Marie-Laure Bocquet, Nicolás Lorente, Hervé Cruguel, François Debontridder, Sébastien Royer, Pascal David, **Alexandra Palacio-Morales**, Tristan Cren, Nadine Witkowski, Christophe Brun, Journal of Phys. Chem. C 124, 36 (2020)
- b) The PhD thesis of **Danilo Longo** entitled “*Engineering topological states in arrays of magnetic molecules in interaction with a 2D superconductor*” was defended in public the 13th of May 2019. Danilo Longo is now post-doc on the DEIMOS beamline at the synchrotron Soleil. The official PhD advisors were Tristan Cren and Nadine Witkowski. I was nevertheless the main co-advisor of his work.
- c) The PhD thesis of **Raphaël Leriche** entitled “*Electronic correlations in strong spin-orbit systems*” was defended in public the 1st of October 2019. Raphaël is now professor “agrégé” in physics in high school. The official PhD advisor was Tristan Cren. The other co-supervisor was myself.

A) Theoretical background

Case of weak non-magnetic disorder

As we have seen in the introductory part about BCS superconductivity, the BCS Hamiltonian is invariant by time-reversal symmetry which makes superconductivity very robust against non-magnetic disorder since the latter is time-reversal symmetric. Since it is written in real space, the Bogoliubov-de Gennes formalism (see equations 6,7,8 and 9 in the introduction) is more adapted to describe such effects. In particular a non-magnetic disorder or scattering potential is simply incorporated in $U(\mathbf{r})$ thus added to the periodic potential of the crystal. It is then simply integrated in $\mathcal{H}_0(\mathbf{r})$ as $\mathcal{H}_0(\mathbf{r}) = \left[\frac{1}{2m} (-i\hbar\nabla - e\mathbf{A})^2 + U(\mathbf{r}) - \mu \right] \cdot U(\mathbf{r})$ thus symmetrically affect the spin up and spin down of the electrons. Such a justification was early given by Anderson, Abrikosov and Gor'kov [Anderson1959, AbriGork1961] showing that superconductivity should be very weakly affected as soon as $k_F \ell_e \gg 1$, which criterion covers safely the diffusive regime of conventional superconductors that we have seen previously in the **Topic1** above.

Case of magnetic disorder

In contrast magnetic atoms were shown very early to destroy superconductivity very rapidly, typically for 1-3 % concentration. Since it was known that a magnetic field has a depairing effect on Cooper pairs, it was originally suspected that it would be the dipolar magnetic field associated to the local total magnetic moments

that would affect the coherent superposition of the Cooper pairs. In contrast, from the variations of T_c following the spin of the magnetic impurities, it was inferred that an exchange interaction between the local spin of the impurities and the spin of the electrons was the mechanism responsible for superconductivity suppression [Matthias1958]. Such a term corresponds to the following Hamiltonian:

$$\mathcal{H}_{mag-imp} = \sum_i \frac{JS}{2} (\Psi_{r_i\uparrow}^\dagger \Psi_{r_i\uparrow} - \Psi_{r_i\downarrow}^\dagger \Psi_{r_i\downarrow}) + K (\Psi_{r_i\uparrow}^\dagger \Psi_{r_i\uparrow} + \Psi_{r_i\downarrow}^\dagger \Psi_{r_i\downarrow}) \quad (20)$$

One sees that $\mathcal{H}_{mag-imp}$ contains two terms: a non-magnetic part affecting similarly both electron spins (the second term of 20) where K can be positive or negative. The first term of (20) describes an exchange interaction changing the energy of the up spins with respect to the down ones. The sign of J can be positive or negative depending on the microscopic exchange interaction (ferromagnetic for $J < 0$ and anti-ferromagnetic for $J > 0$). In the Hamiltonian (20) one assumes that there is a distribution of identical impurities all having a classical spin variable (thus large with respect to $1/2$) so that the spin \vec{S} of each impurity is treated classically. Furthermore one assumes for simplicity that all spins are oriented along $+z$ and located at various sites \mathbf{r}_i . If we don't assume that all impurity spins have the same orientation, a similar expression as (20) is obtained but with a term $J\vec{S}_i \cdot \vec{\sigma}/2$. In the case of the Hamiltonian (20) two very important results have been early obtained as a function of the unitary parameter μ which characterizes the strength of the magnetic impurity:

$$\mu = \frac{2\alpha}{1+\alpha^2} \quad (21)$$

Where

$$\alpha = (\pi\nu_0JS)^2 \quad (22)$$

and ν_0 is as before the DOS at ϵ_F .

- i) Strong magnetic impurity (corresponding to large $\mu \sim 1$). It has been shown by Yu, Shiba and Rusinov that a single magnetic impurity at position \mathbf{r}_i locally induces a bound state having an energy situated inside the spectral energy gap $[-\Delta; +\Delta]$ [Yu1965, Shiba1968, Rusinov1969]. Depending on the existence of possible harmonics of the Fourier transform of the scattering potential, multiplet of bound eigenstates can also exist. The energy E_0 of the bound state is given by:

$$E_0 = \Delta \frac{1-\alpha}{1+\alpha} \quad (23)$$

In the part **H**) below we will present an example of spatially resolved STS measurement of the bound state created by a single atomic impurity in the quasi-2D superconductor $2H\text{-NbSe}_2$.

- ii) Weak magnetic impurity (corresponding to small $\mu \rightarrow 0$ called Born scattering) [AbriGork1961]. In this case, a collection of independent weak scatterers with concentration n_S provokes depairing characterized by a parameter $\eta = \Gamma_S/\bar{\Delta} = \hbar/\tau_S\bar{\Delta}$ where τ_S can be seen as an effective spin flip time and $\bar{\Delta}$ is the average order parameter in presence of the magnetic impurities. In the equation $\eta = \Gamma_S/\bar{\Delta}$, $\bar{\Delta}$ has to be solved self-consistently for a fixed value of η . Γ_S is fixed independently. Abrikosov and Gor'kov have shown that $\eta = n_S\mu/(\pi\nu_0\bar{\Delta})$. Then all interesting physical quantity can be expressed as a function of η . For instance, the critical temperature T_c decreases linearly with η as:

$$k_B T_c(\eta) = k_B T_c(\eta = 0) - \frac{\pi\eta\bar{\Delta}}{4} \quad (24)$$

The original spectral gap existing in the DOS between $[-\Delta; +\Delta]$ for $\eta = 0$ moves to:

$$E_g(\eta) = \bar{\Delta} \left(1 - \eta^{\frac{2}{3}}\right)^{\frac{3}{2}} \quad (25)$$

The latter expressions show the well-known result of gapless superconductivity: the spectral gap vanishes when $\eta = 1$ while superconductivity still exists.

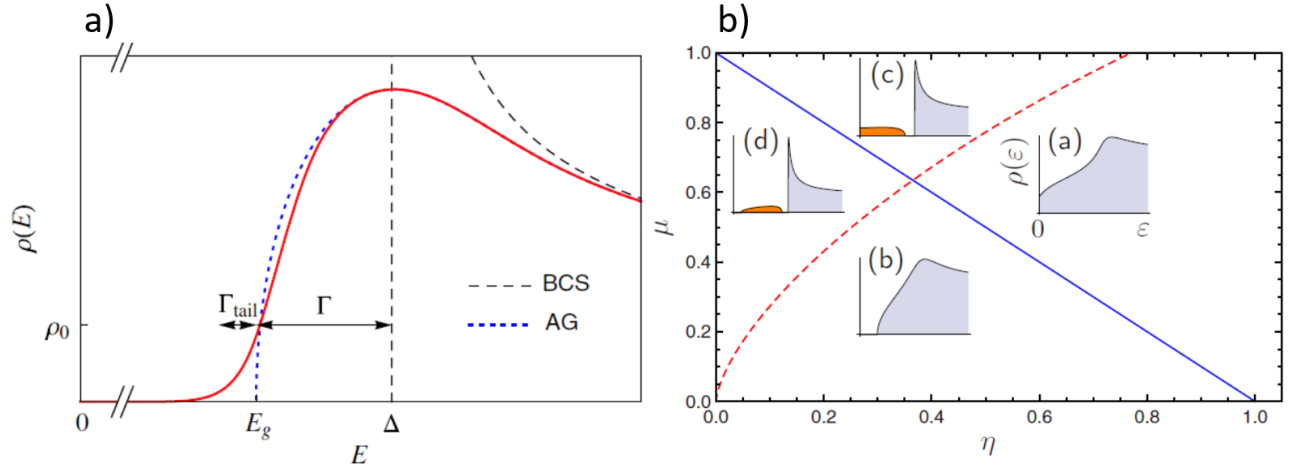


Figure 15. a) Average DOS calculations in the Abrikosov-Gor'kov model of magnetic impurities with $\mu \rightarrow 0$ (blue dotted curve). The dashed curve is the BCS result. The red curve corresponds to mesoscopic effects going beyond the mean-field behavior, showing that spatial fluctuations of the order parameter induce tail states localized in the regions where the local order parameter $\Delta(\mathbf{r})$ is smaller than the average value $\langle \Delta(\mathbf{r}) \rangle$. b) Qualitative behavior of the DOS as a function of the parameters μ and η . These figures are extracted from [Feigelman2012,Fominov2016].

The regime i) of strong coupling predicts the appearance of $\delta(E - E_0)$ in-gap states. For finite concentration of identical strong magnetic impurities, these states will start to overlap when the distance between the impurities $r_S = (1/n_S)^{1/3}$ will be smaller than the size of their bound state which is given by $L_0 = \xi_0(1 - E_0^2/\bar{\Delta}^2)^{-1/4}$. Then they will form a band around the energy E_0 . Qualitatively the DOS will look like the insets c) and d) presented in the Figure 15b), depending on whether the spectral gap E_g remains finite or is reduced to zero.

In the regime ii) the Abrikosov-Gorkov prediction of the average mean-field DOS corresponds to the blue dotted curve in panel 15a), which can be calculated using the Usadel equations (12) above with a depairing spin-flip parameter Γ_S . One sees that the original BCS DOS (black dashed curve) is strongly smeared out over an energy scale given by $\Gamma = \bar{\Delta} - E_g$. If now we consider that in the regime (ii) the strength μ of the impurities increases, it will lead to an impurity band merging to the continuum of excited states (see inset b in figure 15b). For even larger μ this will close completely the spectral gap E_g (see inset a in figure 15b).

Beyond mean-field results

Until now, we have explicitly considered mean-field cases where spatial fluctuations of the order parameter are neglected. Such spatial variations of $\Delta(\mathbf{r})$ will nevertheless certainly appear locally in real materials for various reasons. Originally the first attempt to describe such a situation was the one of Larkin and Ovchinnikov considering long-scale and short-scale variations (characteristic spatial variations longer or smaller than the superconducting coherence length) of the electron-phonon coupling constant $\lambda(\mathbf{r})$ [Larkin1971]. Other causes considered later can be the spatial variations of the non-magnetic potential [Lamacraft2000, Skvortsov2013] or of the magnetic potential [Fominov2016]. It has also been shown that including the effect of electron-electron repulsion enhancing spatial disorder effects in superconducting thin films strongly enhances mesoscopic effects [Feigelman2012]. Very fortunately for us the theoretical description of these various scenario leads to the following universal picture presented in figure 15a) where the DOS is represented by the red curve showing two main characteristics:

- iii) Short-scale non-magnetic disorder, whatever its microscopic origin, always reduce the spectral gap E_g with respect to the average order parameter value $\Delta = \langle \Delta(\mathbf{r}) \rangle$. The mean-field DOS $\rho(E)$ is then similar to the one corresponding to the Abrikosov-Gorkov model of weak magnetic scatterers.
- iv) A tail of sub-gap states Γ_{tail} exists broadening the mean-field DOSs $\rho(E)$. These states having $E < E_g$ correspond to quasiparticle states localized spatially in regions where the order

parameter $\Delta(\mathbf{r}) < \Delta = \langle \Delta(\mathbf{r}) \rangle$. They vanish exponentially as $\exp[-C\epsilon^\beta]$ with $\epsilon = E_g - E/\Gamma_{tail}$ and C and β are numerical factors depending on the model.

To be complete let us mention that the case of long-range variations of $\lambda(\mathbf{r})$, also first addressed in [Larkin1971], lead to the trivial result that a local BCS parameter exists corresponding to the local value of $\langle \lambda(\mathbf{r}) \rangle$.

B) Suppressing superconductivity with non-magnetic disorder: effect of moderate and strong disorder

Before presenting in part C) below our experimental results on NbN thin films, I would like to discuss here rather briefly, the various known mechanisms according to which superconductivity can be destroyed at large non-magnetic disorder potential. This field of condensed matter physics has as main topic the so-called “superconductor-insulator transition”. The main conclusion of all theoretical works is that beyond a critical disorder all conventional superconductors transit either to a metallic or to an insulating state [Gantmakher2010,Feigelman2010]. In some cases local superconducting correlations can survive in the insulator. There are basically three different mechanisms by which superconductivity can be destroyed:

- 1) **Coulomb blockade against superconductivity in Josephson junction arrays.** This scenario describes the case of a material that would physically consist of superconducting grains coupled to each other by low transparency insulating tunnel barriers. In this case one expects a competition between the charging energy E_C associated to each grain and the Josephson energy E_J enabling the coupling of superconductivity between two neighboring grains. The superconductor becomes insulating when $E_C > E_J$ with localized Cooper pairs. This model is not suited to describe materials that have a high-transparency tunnel barrier between the nanocrystallites constituting the thin films, such as the NbN thin films we have studied here.
- 2) **Suppression of superconductivity by Coulomb repulsion: the fermionic mechanism.** This scenario describes the case of a material that is “homogeneously” disordered: in contrast to the case 1) above there are no weak Josephson junctions. The essence of this scenario is that Coulomb repulsion between conducting electrons gets enhanced due to slow diffusion of electrons in highly disordered film. A general formulation of this situation going beyond perturbation theory could be put forward by Finkelstein [Finkelstein1987,Finkelstein1994]. It explicitly assumes that the main contribution to the reduction of the electron-phonon coupling constant comes from 2D electronic diffusion, i.e. $|\mathbf{k}|$ momenta such that $1/\xi \leq |\mathbf{k}| \leq 1/d$. We remind here that in a BCS superconductor the low-disorder critical temperature T_{C0} is given by $k_B T_{C0} = 1.14 \hbar \omega_D e^{-\frac{1}{\lambda_{BCS}}}$ where:

$$\lambda_{e-ph} = \lambda_{BCS} = \nu_0 V = \lambda_{phonons} - \frac{\lambda}{1 + \lambda \ln(\epsilon_F / \hbar \omega_D)} \quad (26)$$

In the BCS expression of the electron-phonon coupling constant λ_{BCS} the first term is the attractive part due to phonons and the second negative term is the repulsive part due to electron-electron repulsion known as Coulomb pseudopotential in western countries and Tolmachev logarithm in Russia. In the presence of increasing disorder, electrons interact through the Cooper channel which further reduces the total electron-phonon coupling constant (26). In this case the negative contribution in (26) becomes energy-dependent and for small energy transfer E , the total $e-ph$ coupling constant can be written as:

$$\lambda_{e-ph}(E) = \lambda_{BCS} - \frac{1}{12\pi g} \ln \frac{1}{E\tau} \quad (26bis)$$

where τ is the electronic elastic mean-scattering time and g the dimensionless film conductance $g = h/(2e^2 R_{\square})$. The renormalization group method enabled to show that T_C decreases when g diminishes according to the following formula:

$$\frac{k_B T_C \tau}{\hbar} = \left[\frac{\sqrt{8\pi g} - \ln\left(\frac{\hbar}{\tau k_B T_{C0}}\right)}{\sqrt{8\pi g} + \ln\left(\frac{\hbar}{\tau k_B T_{C0}}\right)} \right]^{\sqrt{2\pi g}} \quad (27)$$

As illustrated on figure 16a), this dependence (27) is nicely followed by the NbN ultrathin films we have studied. From (27) one finds that T_C vanishes at the critical conductance

$$g_{CF} = \left(\frac{1}{8\pi}\right) \ln^2\left(\frac{\hbar}{\tau k_B T_{C0}}\right) \quad (28)$$

Here T_{C0} is the critical temperature for low disorder. When superconductivity vanishes, the material becomes a poor metal because $g_{CF} \geq 1$. In this approach spatial fluctuations are neglected. By looking at the expression (26), one sees that spatial fluctuations of the film conductance $g(\mathbf{r})$ will lead to large spatial fluctuations of $\lambda(E, \mathbf{r})$ which in turn will strongly affect $T_C(\mathbf{r})$ and $\Delta(\mathbf{r})$. Thus upon g decreasing toward g_{CF} a more and more inhomogeneous superconducting material is expected. This scenario describes very well what occurs both macroscopically and locally in our NbN ultrathin films, as presented in figures 16b) and 16c). Our contribution to this issue is presented in detail in parts C) and D) below.

Finally, I would like to mention that a recent theoretical work points out the necessity of generalizing the Finkelstein approach in order to include all possible $|\mathbf{k}|$ momenta contribution to the correction of the electron-electron interaction constant (second term of 26bis) [Antonenko2020]. This leads to consider 3D electronic diffusion ($1/d \leq |\mathbf{k}| \leq 1/\ell_e$) and 3D ballistic contribution ($1/\ell_e \leq |\mathbf{k}| \leq k_F$). It is found that the ballistic contribution gives rise to the leading term:

$$\frac{\Delta T_C}{T_{C0}} = -\frac{\alpha}{k_F \ell_e} \quad (27bis)$$

where α is a material dependent parameter of the order of one. The comparison of the relation (27bis) or (27) to the experimental T_C versus $1/(k_F \ell_e)$ or reduced conductance $g \propto k_F^2 \ell_e d$ shows indeed that (27bis) is more general and appropriate to all films including 3D ones [Antonenko2020, Ivry2014].

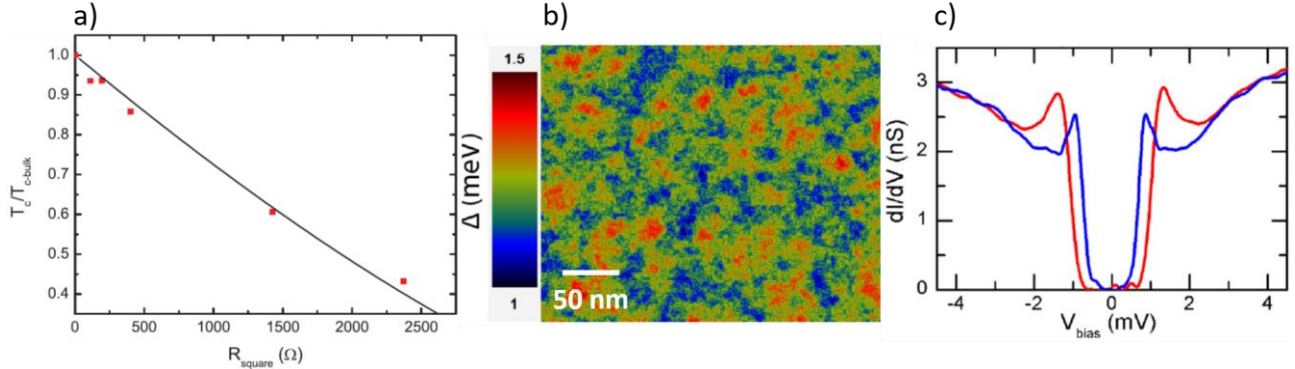


Figure 16. a) Reduction of the critical temperature T_C of NbN superconducting ultrathin films with increasing square resistance. b) Emergent granularity of the superconducting energy gap $\Delta(\mathbf{r})$ of a 2nm thick NbN film of $T_C \approx 0.25 T_{C\text{-bulk}}$ measured in a $300 \times 300 \text{ nm}^2$ area. Each point of the colored 2D map corresponds to a local value of $\Delta(\mathbf{r})$ varying between [1; 1.5] meV as indicated by the vertical scale. c) Selected dI/dV spectra corresponding to red (large gap) and blue (small gap) extrema patches in the gap map presented b).

- 3) Single-electron localization against superconductivity.** This last mechanism for superconductivity suppression relies on the localization of the wavefunction of single-electrons by the one-particle disorder potential. In this approach electron-electron interactions are neglected and the focus is set on the increasing disorder potential. In the part A) above in the paragraph entitled “Beyond mean-field results” we have described results that correspond to a regime from weak to moderate disorder. The electrons were treated as diffusive extended particles that can propagate through the material. When disorder further increases, strong localization will occur where the wavefunction of single-electrons will localize at various positions in the material. In this case the envelop $|\psi(\mathbf{r})|$ of their wavefunction

will decays exponentially from a point \mathbf{r}_0 in space as:

$$|\psi(\mathbf{r})| \propto \exp(-|\mathbf{r} - \mathbf{r}_0|/L_{loc}) \quad \text{where } L_{loc} \text{ is the localization length.}$$

A new energy scale δ_{Loc} appears due to this strong localization. It is given by:

$$\delta_{Loc} = \frac{1}{v_0 L_{loc}^3} \quad (29)$$

which gives the average energy spacing of the single-particle levels in the volume L_{loc}^3 where the electrons are localized. Then comparing δ_{Loc} with $k_B T_{C0}$ gives us the number of single-particle electron states in an energy interval $k_B T_{C0}$ (the characteristic energy scale of superconductivity). Early results concluded that conventional superconductivity should disappear when $\delta_{Loc} \approx k_B T_{C0}$ [Ma1985, Bulaevskii1985], i.e. when there is about one electronic level in the energy range Δ_0 . More recent work of Feigel'man and co-authors refined this condition and showed that in fact superconductivity survives when $k_B T_{C0} < \delta_{Loc} < \hbar\omega_D$ [Feigelman2010]. In this regime several new features appear due to two effects:

- i) The fractal nature of the electronic eigenfunctions in strong disorder.
- ii) A ‘‘parity gap’’, similar to the one put forward by Matveev and Larkin for ultrasmall superconducting grains [Matveev1998], develops in the material on an effective grain of volume L_{loc}^3 . It has recently been evidenced by STM/STS measurements in strongly disordered indium oxide films close to the insulating transition [Dubouchet2019].

C) NbN thin film characterization

We summarize here the main structural and electronic properties of the NbN films we have studied. They were grown at the Karlsruhe Institute of Technology by Kostia Ilin. The growth technique is magnetron sputtering in an Ar+N₂ atmosphere on sapphire substrates. This results in polycrystalline ultrathin films with single-crystal grain size of about 2-5 nm. As the thickness of the film varies, the T_c decreases regularly from the bulk NbN value $T_{c-bulk} \sim 16$ K for thicknesses d above 15 nm to about $T_c \approx T_{c-bulk}/4 \approx 4$ K at $d \approx 2$ nm, as illustrated on figure 17e). Below $d \approx 2$ nm the samples are usually not superconducting at 0.3 K and suggest an insulating behavior. One sees that the values of the square resistance of such films are in good agreement with the critical conductance g_{CF} given by the Finkelstein model in the formula (28) above: $g_{CF} \approx 1.25$ which leads to $R_{\square} \approx 10$ k Ω . Since these nitride films are stable in air, they are used in a number of applications such as single-photon detectors or bolometers. Our motivation was thus to study the local superconducting properties of such ‘‘real’’ films and investigate their emergent inhomogeneous character with increasing non-magnetic disorder. The increasing non-magnetic disorder is provided by the thickness reduction which reduces the diffusion coefficient D and density-of-states at the Fermi level v_0 .

Transmission electron microscopy measurements enable to see the individual nanocrystals, as seen in figure 17a), and to show that the films are covered by an ultrathin oxide layer of about 1 nm thickness as they are exposed to air. In order to study the thinnest films under good STM tunneling conditions and because they are sensitive to aging and thermal cycling, we introduced the samples in less than 48 hours in our STM set-up after their growth in Karlsruhe. Furthermore, in order to control their macroscopic superconducting state, the samples were contacted in a 4 point probe configuration with Al wire bonding, enabling to measure *in-situ* the sample electrical resistance in the STM head. This is illustrated in figure 17b) while the STM tip is approaching the NbN thin film. The sample holder was adapted to furnish 4 independent Cu electrical contacts seen in panels 17c) (front side) and 17c) (back side). These Cu pads get electrically connected to 4 gold covered springs in the STM head.

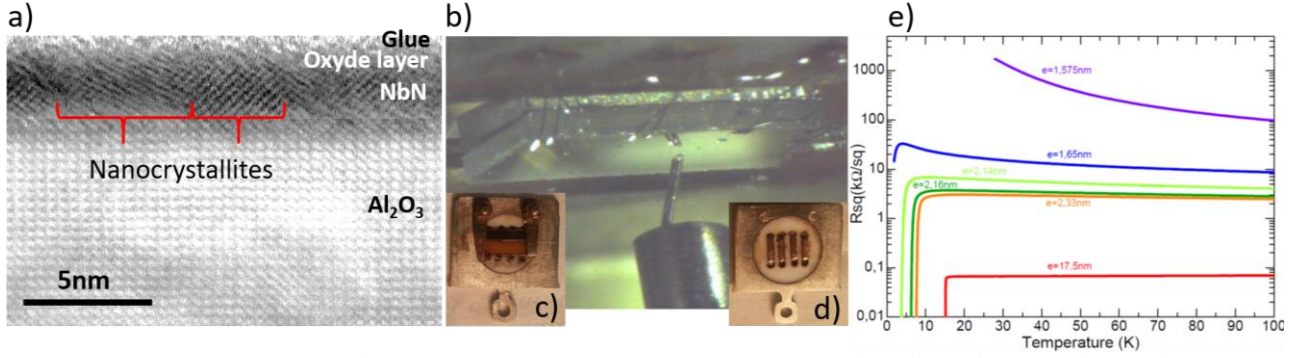


Figure 17. a) Transmission electron microscopy (TEM) image of an ultrathin NbN sample of about 2 nm thickness grown on sapphire. Nano-crystals constituting the film are visible, whose lateral size varies between 2 and 5 nm. The film is covered by an oxide layer of about 1 nm. b) Sample view contacted with 4-point Al wires for in situ resistivity measurements inside the STM head. Real STM tip is approaching from below. c) and d) Sample holder providing 4 independent electrical contacts seen from front and back side. e) Typical resistance curves of NbN thin films of various thicknesses measured as a function of temperature. Above 15 nm thickness T_c is close to 15 K and diminishes with the sample thickness to become zero below 2 nm.

Earlier longitudinal and Hall resistance measurements by our colleagues Ilin et al showed that for thicker films of about 15 nm thickness such that $T_c \approx T_{c-bulk} \sim 16$ K, the simple application of Drude formula:

$$k_F \ell_e = \hbar (3\pi^2)^{\frac{2}{3}} n_e^{-\frac{1}{3}} (e^2 \rho_n)^{-1} \quad (30)$$

leads to $k_F \ell_e \approx 6$ assuming a free electron mass [Semenov2009]. ρ_n is the film resistivity and n_e the electron density. This enables extracting $\ell_e \approx 1$ nm and $D \approx 0.6$ cm².s⁻¹. These values are fairly low indeed emphasizing that these films are highly disordered. When compared to the values of the same parameters obtained in the **Topic1** from proximity effect for the disordered and crystalline Pb monolayers, one sees that D is between 5 and 10 times smaller in NbN than in Pb. This enables explaining the unusual resistivity behavior seen in panel 17e): none of the films show a metallic behavior of a decreasing film's resistance with temperature. On the contrary the resistivity increases with reducing T as:

$$\rho_n(T) \propto \rho_0 \ln\left(\frac{\hbar/\tau}{k_B T}\right) \quad (31)$$

where τ is the electronic mean-free time associated to ℓ_e . The reason is that at 300 K the thermal coherence length $L_T = \sqrt{\frac{\hbar D}{k_B T}} \approx 1$ nm $\geq \ell_e$ using the low value of D given above. Thus due to the very diffusive behavior of these NbN thin films, quantum effects due to weak localization and electron-electron repulsion are readily observable all the way down from room temperature to low temperature, explaining the behavior given by the relation (31) above. My idea was then the following: according to the Finkelstein mechanism described above, the effects produced by electron diffusion due to disorder are enhanced by electron-electron repulsion which reduces the global T_c , as seen in Figure 16a). In agreement with the scenario proposed above in the section **B2**, is it possible to find a link between this reduction from the bulk T_c by the Finkelstein mechanism and the emergence of local superconducting inhomogeneities in NbN thin films? We succeeded to give a positive answer to this question. I present the results in the next section.

D) Origin of the emergent superconducting inhomogeneities in NbN thin films

My colleagues Yves Noat, Tristan Cren and Dimitri Roditchev showed that NbN thin films of thicknesses above 15 nm show rather homogeneous superconducting energy gap and LDOS properties. They have found that small superconducting energy gap inhomogeneities are already present at 8 nm thickness and further increase below this value [Noat2013]. Since in fact these superconducting inhomogeneities develop rather slowly with decreasing T_c below its bulk value, I proposed to investigate in details a film thickness for which the developed inhomogeneities at 300 mK are at least about 10% of the average energy gap value. For this purpose a film of nominal thickness $d \approx 2.16$ nm and $T_c = 3.8$ K $\approx \frac{T_{c-bulk}}{4}$ was chosen. Its resistance curve measured *in situ* as a function of temperature in the STM head is shown in figure 18a). It reaches a maximum

square resistance of about 7 k Ω at 10 K where two-dimensional thermal superconducting fluctuations begin. Phase fluctuations in fact dominate over amplitude fluctuations due to the reduced superfluid density in our disordered ultrathin film [LarkinVarlamov2005]. In our 2D situation $T_c = 3.8$ K corresponds to the Berezinskii-Kosterlitz-Thouless transition temperature. The mean-field transition temperature T_{c-MF} corresponds to $T_{c-MF} - T_c = 4Gi$ where the Ginzburg-Levanyuk parameter Gi is given by $Gi = \frac{e^2}{16\hbar} R_{\square} \approx 0.1$ and represents the reduced temperature interval $\Delta T/T_{c-MF}$ over which thermal amplitude fluctuations effects are visible [LarkinVarlamov2005]. This leads here to $T_{c-MF} \approx 1.7 T_c = 6.3$ K which is much larger than the real T_c .

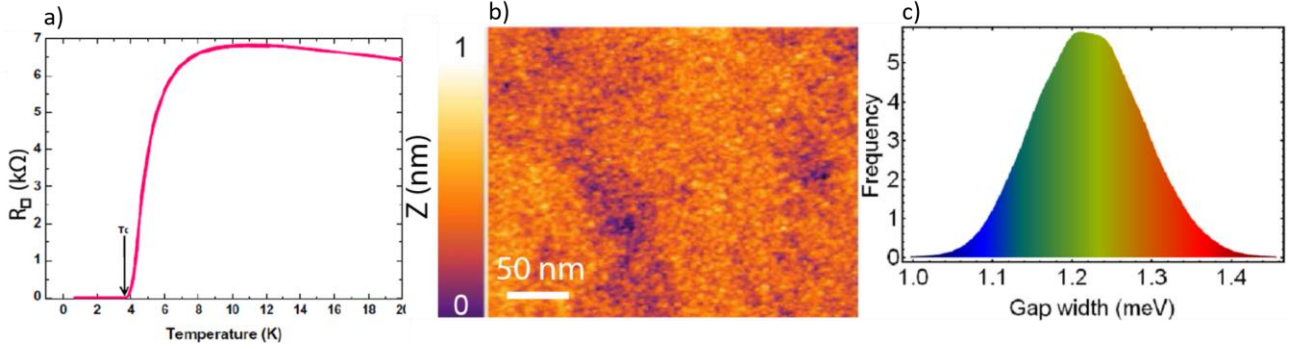


Figure 18. a) Resistance curve of a 2.16 nm thick NbN thin film grown on sapphire measured in situ inside the STM head. b) STM topography of the film showing its grainy structure. c) Statistical distribution of the local energy gap value measured by STS in area b). The corresponding local gap map is shown in figure 16b) and the representative dI/dV spectra of large and small gap values are presented in figure 16c).

A STM topography of a selected area of 300×300 nm² is seen in figure 18b). It shows a rather flat surface with a grainy structure whose grain size is in agreement with the size of the nanocrystals measured in TEM experiment and shown in figure 17a). Measured exactly on this region, the 2D local energy gap distribution $\Delta(\mathbf{r})$ is presented in figure 16b). The corresponding statistical distribution of $\Delta(\mathbf{r})$ is shown in figure 18c). The average gap value is $\langle \Delta(\mathbf{r}) \rangle \approx 1.22$ meV. The full width at half-maximum is $2\sigma_{\Delta} \approx 0.16$ meV. The correlation length l_{Δ} of $\Delta(\mathbf{r})$, which gives the typical size of the puddles of constant energy gap values in figure 16b), was extracted from the decay length of the autocorrelation function of $\Delta(\mathbf{r})$. This leads to $l_{\Delta} \approx 27$ nm. The 0 K superconducting coherence length $\xi \approx 5$ nm was extracted from high perpendicular magnetic field conductivity measurements that we performed at the high-magnetic field lab in Toulouse [Carbillet2016]. Thus one concludes that $l_{\Delta} \gg \xi$. Another important feature that we could establish is that there are no direct correlations between the spatial distribution of the energy gap $\Delta(\mathbf{r})$ and the STM topography $Z(\mathbf{r})$ reflecting the spatial distribution of the individual NbN nanocrystals. This means that there is no simple one to one correspondence between the geometrical arrangement of the nanocrystals and the energy gap distribution. This piece of information seems to be expected but was never presented before for such films. This result is shown in figure 19a) presenting the numerically calculated cross-correlation function $\rho_{cross\Delta;Z}(\mathbf{r})$ between $\Delta(\mathbf{r})$ and $Z(\mathbf{r})$. It is defined by:

$$\rho_{cross\Delta;Z}(\mathbf{r}) = \sum_{\mathbf{r}'} \frac{(\Delta(\mathbf{r}') - \langle \Delta(\mathbf{r}') \rangle)(Z(\mathbf{r}' - \mathbf{r}) - \langle Z(\mathbf{r}') \rangle)}{N\sigma_{\Delta}\sigma_Z} \quad (32)$$

where the sum is taken over N pixels indexed by \mathbf{r}' in each map and σ_{Δ} , σ_Z are the standard deviations of $\Delta(\mathbf{r})$, $Z(\mathbf{r})$ around their mean value. Nevertheless one sees that this cross-correlation is not completely zero everywhere, which would correspond to a uniform white color. There is a weak residual signal of the order of ± 0.1 at maximum (light red or light violet).

Let us now have a closer look at the individual dI/dV excitation spectra shown in figure 16c). The red and blue spectra in figure 16c) correspond respectively to the red and blue patches seen in figure 16b) representing larger and smaller local gap values. One notices that above the energy gap, the LDOS does not recover a flat value much below the one of the coherence peaks, as we had before in **Topic1** reflecting a BCS-like DOS like the one presented for example in figure 5b). In contrast the LDOS even increases above the value of the coherence peaks. In order to probe the energy dependence of the LDOS at energies much beyond the average gap value, we present the figure 19b). Interestingly, the LDOS is strongly V-shape and site-dependent. Such

a depleted DOS is characteristic of disordered metals with enhanced electron-electron repulsion, an effect first calculated by Altshuler and Aronov at a perturbative level [Altshuler1980,Altshuler1985].

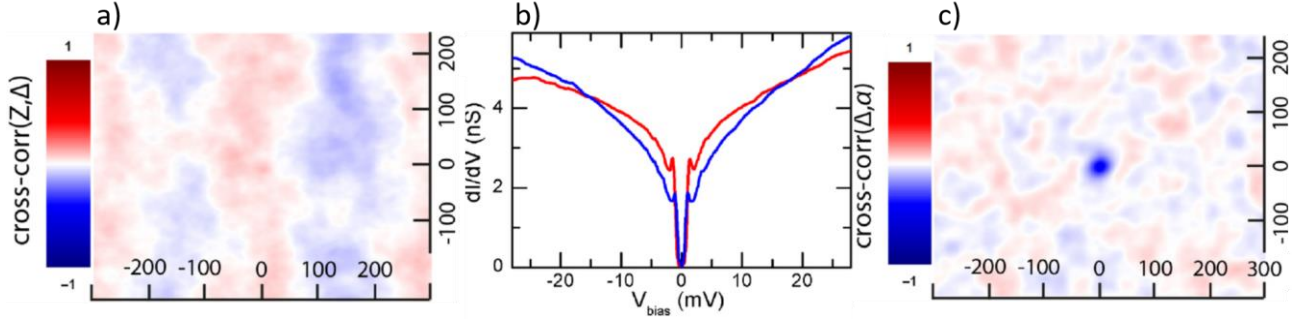


Figure 19. a) 2D color-coded map featuring the absence of spatial cross-correlations between the gap map $\Delta(\mathbf{r})$ and the STM topography $Z(\mathbf{r})$. b) Local dI/dV spectra measured at 0.3 K corresponding to energy gap values shown in figure 16c) but presented on a larger energy scale of about 25 times $\langle \Delta(\mathbf{r}) \rangle$. A strongly depleted V-shape LDOS is measured, whose shape changes with position. This is characteristic of strong electron-electron repulsion also called Altshuler-Aronov effect. c) 2D color-coded map showing a strong spatial cross-correlation between the gap map $\Delta(\mathbf{r})$ and the exponent map $\alpha(\mathbf{r})$ characterizing the strength of the Altshuler-Aronov effect.

We found experimentally that the energy dependence at site \mathbf{r} is well fitted by the simple relation:

$$\frac{dI}{dV}(V, \mathbf{r}) \propto bV^{\alpha(\mathbf{r})} \quad (32)$$

where b is a numerical constant and $\alpha(\mathbf{r})$ is a site-dependent exponent characterizing the strength of the Altshuler-Aronov depleted DOS. Figure 20a) shows an example of good fitting according to the relation (32) of 10 dI/dV spectra spaced by 3 nm from one another along a line starting at larger local gap value (bottom spectra) and ending at smaller gap value (top spectra). By performing a fit of each $dI/dV(V, \mathbf{r})$ single spectrum according to (32), we could extract the spatial distribution of the exponent $\alpha(\mathbf{r})$ over the whole area shown in figure 18b) (we do not show the $\alpha(\mathbf{r})$ map here, see figure 2 in [Carbillet2020]) where we simultaneously measured the 2D gap map $\Delta(\mathbf{r})$ presented in figure 16b). The values of $\alpha(\mathbf{r})$ are symmetrically distributed between 0.29 and 0.41 and the histogram is shown in figure 20b). We numerically computed the cross-correlation $\rho_{\text{cross}\Delta; \alpha}(\mathbf{r})$ between $\Delta(\mathbf{r})$ and $\alpha(\mathbf{r})$. The result is shown in panel 19c). In contrast to panel 19a), a strong anti cross-correlation is found, characterized by a small blue dot at the center $\mathbf{r} = \mathbf{0}$ of panel 19c). Its maximum value at $\mathbf{r} = \mathbf{0}$ is $\rho_{\text{cross}\Delta; \alpha}(\mathbf{r} = \mathbf{0}) = -0.55$. This means that the smaller is the local energy gap value $\Delta(\mathbf{r})$, the deeper is the depleted LDOS corresponding to a larger $\alpha(\mathbf{r})$. The radial decay of $\rho_{\text{cross}\Delta; \alpha}(\mathbf{r})$ is shown in figure 20c). It reveals that the correlation length of these anti-correlations is $l_{\text{cross}} \approx 25$ nm very close to $l_{\Delta} \approx 27$ nm, much larger than the superconducting coherence length $\xi \approx 5$ nm.

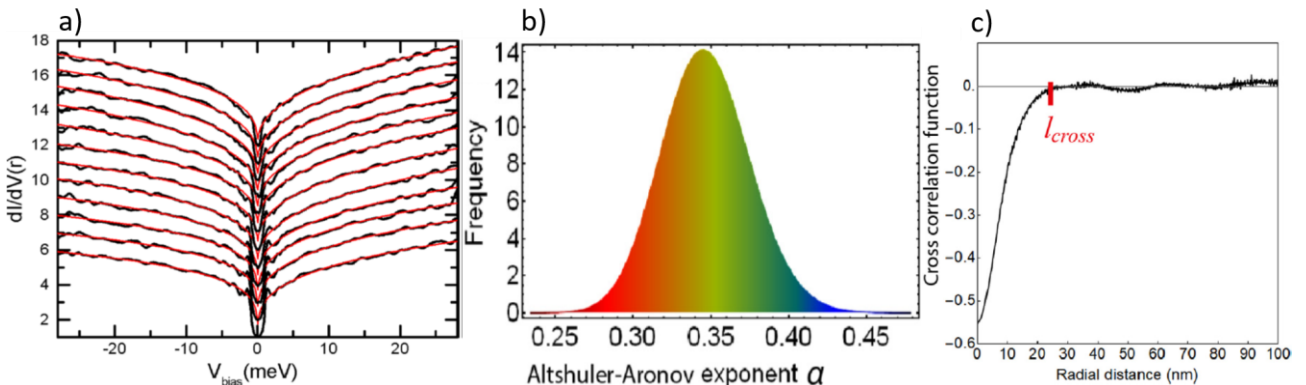


Figure 20. a) dI/dV spectra spaced by 3 nm measured in the area shown in figure 16b,18b along a line joining a puddle with larger local gap (bottom spectra) to a neighboring puddle having smaller gap value (top spectra). b) Statistical distribution of all $\alpha(\mathbf{r})$ values measured in the area shown in figure 16b,18b. c) Radial decay of the cross-correlation function $\rho_{\text{cross}\Delta; \alpha}(\mathbf{r})$ presented in panel 19c) between $\Delta(\mathbf{r})$ and $\alpha(\mathbf{r})$.

Our colleagues Mikhail Skvortsov and Mikhail Feigel'man worked out the theoretical modelling of our experimental results in order to furnish an almost quantitative interpretation. As we have seen before in **Topic1**, in a non-interacting metal the tunneling DOS probed by STS around the Fermi level E_F corresponds

to ν_0 the density-of-states which is usually constant for small energy excitation E and does not vary with position \mathbf{r} . In this case, one thus has:

$$\rho(\mathbf{r}, E) = \nu_0 \text{ for } E \ll \epsilon_F \quad (33)$$

In contrast, in a diffusive metal with electron-electron interaction, the tunneling DOS becomes energy dependent and can be written as:

$$\rho(E) = \nu_0 e^{-S(E)} \quad (34)$$

$$S(E) = 2 \frac{e^2}{h} \int_E^{\hbar/\tau} \frac{d\omega}{\omega} R(\omega) \quad (35)$$

where ν_0 is the bare DOS without interactions. $S(E)$ is an energy dependent quantity reflecting the fact that the interacting disordered metal cannot screen completely the charge of the incoming excitation probed by a tunneling experiment. In the relation (35), one sees that since $h/2e^2 = R_Q$ is the quantum resistance, there appears an energy-dependent spreading resistance $R(\omega)$. This spreading resistance $R(\omega)$ develops between two length scales: r_{in} and r_{out} . The diffusive length $r_{in} = \sqrt{\hbar D / \hbar \omega} = \sqrt{D/\omega}$, corresponds to the distance over which the excitation of energy $\hbar \omega$ can diffuse in the metal of diffusion coefficient D . The length r_{out} is associated to the spatial propagation of the electromagnetic field needed to screen out completely the charge of the excitation in the metal. It is here a much larger length. One has $r_{out} = \sqrt{D \omega_0 / \omega^2}$ where ω_0 is the metal plasma frequency. In our 2D geometry with square resistance R_{\square} , $R(\omega)$ is given by:

$$R(\omega) = \frac{R_{\square}}{2\pi} \ln \frac{r_{out}}{r_{in}} = \frac{R_{\square}}{4\pi} \ln \frac{\omega_0}{\omega} \quad (36)$$

Replacing in (35) this gives:

$$S(E) = \frac{R_{\square}}{4\pi R_Q} \ln^2 \frac{\hbar \omega_0}{E} - \ln^2 \omega_0 \tau \quad (37)$$

The expression (37) gives the full energy dependence of the DOS $\rho(E)$ through (34). The relevant energy range seen in figure 19b) for the depleted DOS due to the Altshuler-Aronov effect is such that in our case:

$$E \leq 30 \text{ meV} \ll \hbar/\tau \approx 0.33 \text{ eV} \quad (38)$$

justifying that all energies are well in the diffusive regime much below the energy scale $\hbar/\tau \approx 0.33 \text{ eV}$ associated to the ballistic regime. As a consequence, the second term in (37) is much smaller than the first one. Using $\hbar \omega_0 \approx 10 \text{ eV}$ from [Semenov2009], we find that $\rho(E)$ can be replaced to a very good approximation by a power law behavior:

$$\rho(E) \propto E^{\alpha(E)} \text{ where } \alpha(E) = -\frac{\partial S}{\partial \ln E} = \frac{R_{\square}}{2\pi R_Q} \ln \frac{\hbar \omega_0}{E} \quad (39)$$

Because of the very slow behavior of the logarithm in the energy range of interest, the relation (39) or the exact result (37) agree both very well with the experimental behavior presented in figure 19b). The relation (39) enables extracting the average exponent α using $\hbar \omega_0 \approx 10 \text{ eV}$, $R_{\square} \approx 7 \text{ k}\Omega$ (see figure 18a) and $E \approx 10 \text{ meV}$ which leads to $\alpha \approx 0.30$. This value is in very good agreement with the experimental range $0.29 \leq \alpha(\mathbf{r}) \leq 0.41$ and the experimental average value $\langle \alpha(\mathbf{r}) \rangle \approx 0.35$ (see panel 20b).

In the above theoretical picture, the interacting metal is assumed to homogeneously disordered without spatial variations of any relevant physical quantities. As experimentally we measured spatial variations of both $\alpha(\mathbf{r})$ and $\Delta(\mathbf{r})$, we need to introduce spatial fluctuations of the relevant physical quantities. The relations (37) and (39) suggest that the existence of local variations of the 2D resistivity R_{\square} in the form

$$R_{\square}(\mathbf{r}) = R_{\square} + \delta R_{\square}(\mathbf{r}) \quad (40)$$

where R_{\square} is the average square resistance, is the most natural hypothesis since α is proportional to R_{\square} but has a very weak dependence on other parameters like ω_0 or \hbar/τ due to the logarithm. This hypothesis is also physically justified by the Einstein relation between the resistivity $1/\sigma$ and the diffusion coefficient D and DOS ν_0 :

$$1/\sigma = D e^2 \nu_0 \quad (41)$$

The relation (40) indeed suggests that microscopically, local variations of resistivity might occur from inhomogeneities either in D or ν_0 or both. Assuming the relation (40) our colleagues Skvortsov and Feigel'man could generalize the calculations from (33) to (39) including inhomogeneities in the local square resistivity. This leads to a generalization of (39) as:

$$\alpha(E, \mathbf{r}) = \alpha(E) + \delta \alpha(E, \mathbf{r}) \quad (42)$$

$$\delta\alpha(E, \mathbf{r}) = \frac{\delta R_{\square}(\mathbf{r})}{2\pi R_Q} \ln \frac{E}{\hbar D/a^2} \quad (43)$$

where in (43) a is the correlation length of $\delta R_{\square}(\mathbf{r})$. Using the experimentally found values for $a = l_{\alpha} \approx 18$ nm (not shown here) and for the dispersion $\sigma_{\alpha} \approx 0.028$ (seen in figure 20b) one finds $\sigma_{\delta R_{\square}} \approx 1.1$ k Ω . This dispersion value of $\delta R_{\square}(\mathbf{r})$ seems quite reasonable since it represents 16% of R_{\square} .

The second step is to extend the Finkelstein model summarized briefly in part **B2** above which links the spatial variations of the local resistivity to the spatial variations of the order parameter. This is precisely a possibility that we have mentioned in part **B2**! This becomes very clear when one looks at the formula (26bis) and (27) showing that both the energy-dependent electron-phonon coupling constant $\lambda_{e-ph}(E)$ and the critical temperature T_c directly depends on the film's square conductivity g . Thus local variations of $g(\mathbf{r})=1/R_{\square}(\mathbf{r})$ on diffusive length scales given by $l_{\alpha} \approx 18$ nm, much larger than the superconducting coherence length $\xi \approx 5$ nm, are likely to be able to induce local variations in $\Delta(\mathbf{r})$. The proper generalization of the Finkelstein model corresponding to our situation leads to local gap variations $\delta\Delta(\mathbf{r})$ around the mean value $\langle\Delta(\mathbf{r})\rangle$ given by:

$$\frac{\delta\Delta(\mathbf{r})}{\langle\Delta(\mathbf{r})\rangle} = -\frac{\delta R_{\square}(\mathbf{r})}{6\pi R_Q} \ln^3 \frac{\hbar\omega_D}{\Delta_0} \quad (43)$$

where $\Delta_0 \approx 2.85$ meV is the energy gap value of clean (low disorder) NbN films. The Debye energy $\hbar\omega_D$ is not precisely known but is estimated to be 300 K. Injecting the value $\sigma_{\delta R_{\square}} \approx 1.1$ k Ω found above for $\delta R_{\square}(\mathbf{r})$ leads to $\sigma_{\Delta} \approx 0.074 \langle\Delta(\mathbf{r})\rangle$ whereas the experimental value is $\sigma_{\Delta} \approx 0.066 \langle\Delta(\mathbf{r})\rangle$ as seen from the histogram of $\Delta(\mathbf{r})$ in panel 18c). One sees that the agreement is quite good.

As a conclusion, our work enables to establish that in moderately disordered NbN ultrathin films local fluctuations of the film's resistivity lead to emergent inhomogeneous superconducting properties that can be quantified almost exactly through a local Finkelstein mechanism, thus a purely fermionic effect. We have also shown that these local resistivity variations can be quantified using local STS spectroscopy by fitting the depleted LDOS energy dependence around the Fermi energy. We can draw the following general conclusion: in a large class of conventional superconducting films where Δ and T_c concomitantly diminish through the Finkelstein mechanism due to enhanced electron-electron repulsion combined to disorder, there will appear emergent inhomogeneities in the superconducting properties induced by local inhomogeneities in the film resistivity. This conclusion could also be valid for other recently discovered 2D superconductors like monolayer or bilayer dichalcogenides, bilayer graphene or interface oxides. This is an important conclusion because most theoretical models addressing the development of superconducting inhomogeneities neglect electron-electron repulsion, focusing only on non-interacting disorder effect (see review [Feigelman2010] and [Ghosal1998],[Ghosal2001],[Ghosal 2011]). In addition, it would also be interesting to probe whether 3D diffusion and 3D ballistic regime are also relevant to our situation in order to get a quantitative agreement with our results. Indeed the theoretical work performed by our colleagues Skvortsov and Feigelman could be extended in view of their recent work in order to get a quantitative agreement for the local T_c variations [Antonenko2020]. We would like to mention that other groups reported the emergence of superconducting inhomogeneities by STM/STS in TiN, InO and NbN thin films [Sacepe2008, Sacepe2011, Chand2012, Kamlapure2013], but without presenting such high quality data as ours and without proposing this kind of detailed analysis.

I have presented here only part of our results. There remain several other interesting aspects. One of them concerns the local superconducting properties in perpendicular magnetic field. We have measured very peculiar vortex states and surprising excitation spectra at vortex cores suggesting that locally an insulating state might be induced by the magnetic field. This requires further studies. Another exciting aspect would be to investigate more disordered NbN films approaching the metallic or insulating transition. One could then probe whether the spectral gap E_g , measured by STS, strongly disconnects or not from the order parameter $\Delta \approx T_c$ as it was recently observed in indium oxide films [Dubouchet2019], due strongly developing bosonic effects leading to the appearance of a parity gap [Feigelman2015]. Our various works were published in [Noat et al. Phys. Rev. B 88, 014503 \(2013\)](#), [C. Carillet et al. Phys. Rev. B 93, 144509 \(2016\)](#) and [C. Carillet et al. Phys. Rev. B 102, 024504 \(2020\)](#).

E) Characterization of superconducting Pb monolayers

I launched this new topic in our group in 2012. My own interest was to investigate weak disorder effects on a 2D superconducting system consisting of a single layer of atoms. In some sense this is the thinnest one can reach for a two-dimensional superconductor since its thickness cannot be thinner than one atom height. With respect to the issues addressed above in NbN thin films, the situation here will be very different:

- First the amount of disorder will be much less: as seen in figure 21a) the square resistance before the superconducting transition is $R_{\square} \approx 1.3 \text{ k}\Omega \ll R_Q = h/2e^2 \approx 13 \text{ k}\Omega$. This suggests that in contrast to NbN ultrathin films we do not expect superconducting inhomogeneities for the Pb monolayer. This is confirmed by an estimation of the product $k_F \ell_e \geq 20$ for this system using STM and ARPES data (see our review [Brun2017]: $k_F \geq 1.4 \text{ \AA}^{-1}$ and $\ell_e \geq 3 - 4 \text{ nm}$).

- Second, since the film thickness d is only one atom, not only superconductivity is two-dimensional but the electron gas itself is also two-dimensional. One expects then differences with thin films that are two-dimensional with respect to superconductivity (i.e. $d < \xi$) but remain 3D with respect to the electron gas ($d > \lambda_F$). In particular one expects in such atomically thin superconductors that atomic steps will play an important role. We will see that this is indeed the case.

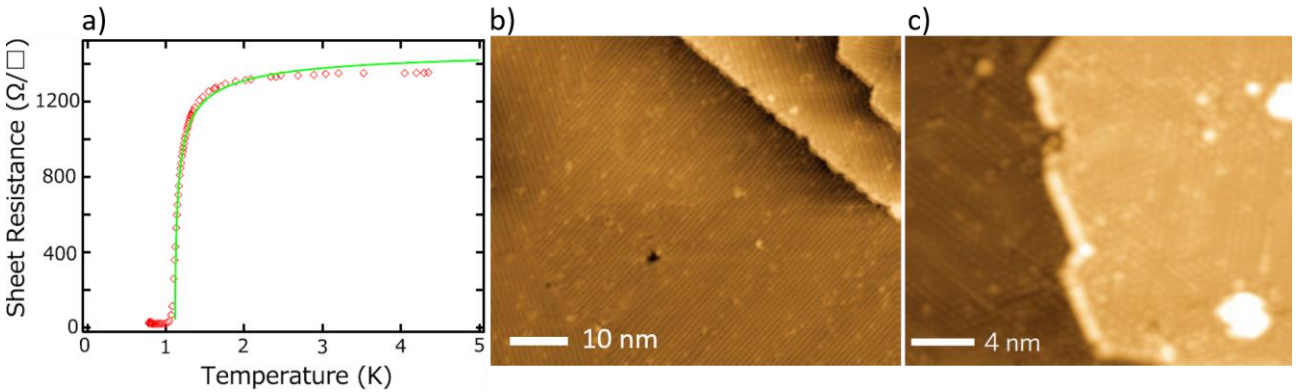


Figure 21. a) Square resistance as a function of temperature of the so-called “striped incommensurate” (SIC) superconducting Pb monolayer grown on Si(111). The 4-points measurements are performed in situ (not by us) [Yamada2013]. b) STM topography of the commensurate $\sqrt{7} \times \sqrt{3}$ -Pb/Si(111) phase featuring its anisotropic structure with lines of Pb atoms forming orientational domains rotated by 120° from each other. c) STM topography of the “striped incommensurate” (SIC) phase. It is locally triangular thus more isotropic.

Regarding the choice of an appropriate system, I learned in working with the Pb/Si(111) system that it is possible to grow a crystalline single atomic layer of Pb atoms on a reconstructed silicon Si(111)- 7×7 substrate. It was shown in 2010 that this system presents several dense superconducting phases built on an underlying 2D electron gas [Zhang2010, Brun2017]. Among them two phases are particularly interesting. One phase is less dense, has an exact coverage of 1.20 monolayer with respect to the underlying Si(111) surface, is anisotropic and forms a commensurate phase having the $\sqrt{7} \times \sqrt{3}$ reconstruction. A small scale STM topography is shown in figure 21b), enabling to see the lines of Pb atoms. Its T_c was reported to be 1.5 K and energy gap $\Delta \approx 0.27 \text{ meV}$ for the less disordered samples [Zhang2010]. The other phase is denser, has a coverage of ≈ 1.30 monolayer, is more isotropic but is incommensurate. It is denoted “striped incommensurate” in the literature and we will call it SIC for short in the following. It consists in small $\sqrt{3} \times \sqrt{3}$ triangular commensurate domain separated by $\sqrt{7} \times \sqrt{3}$ linear boundaries. A small scale STM topography is shown in figure 21c) and 22a). The larger scale image shown in figure 22e) enables appreciating better its domain structure. Its T_c was reported to be 1.8 K and energy gap $\Delta \approx 0.35 \text{ meV}$ for the less disordered samples [Zhang2010]. In both phases Zhang et al. reported a $\Delta(T)$ dependence in reasonable agreement with the BCS behavior.

Interestingly, this SIC phase is the same monolayer as the one we used in **Topic1 part D)** for studying the S-S proximity effect. We thus already know its diffusion coefficient $D \approx 7 \text{ cm}^2 \cdot \text{s}^{-1}$ and low-temperature coherence length $\xi \approx 50 \text{ nm}$ extracted from our proximity effect study. In the above presentation about proximity effect, we made simplifications and neglected small spectroscopic effects induced by weak-disorder that I will present now. Nevertheless, these effects are small as we will see and do not modify the whole picture presented before. Regarding the large scale morphology of both Pb/Si(111) monolayer samples,

we refer the reader to the previous figure 7b): when carefully prepared, the Pb atomic steps follow nicely the underlying single atomic steps of the silicon substrate. This shows that the samples basically consist in large atomically flat terraces of several hundreds of nanometers width separated by single atomic steps of one Pb atom height. We also want to mention another important point: as in both phases we have the presence of Pb atoms that are heavy there exists a strong spin-orbit coupling that will play a role and modify the superconducting coupling with respect to the BCS situation presented in the introduction. Nevertheless, the effect is not dramatic otherwise it would have been observed in the first study of Zhang et al [Zhang2010].

F) Weak disorder effects in superconducting Pb monolayers

We present in figure 22 the first main result induced by weak disorder on the SIC Pb monolayer. When measuring $dI/dV(V)$ conductance curves to probe the local excitation spectra we systematically observed rather large spatial fluctuations of the height of the coherence peaks. These variations are between 20% and 30% of the average peak height. The typical variations are presented in figure 22c) with a normal tip and in figure 22f) with a superconducting tip covered by Pb (which increases the spectroscopic energy resolution).

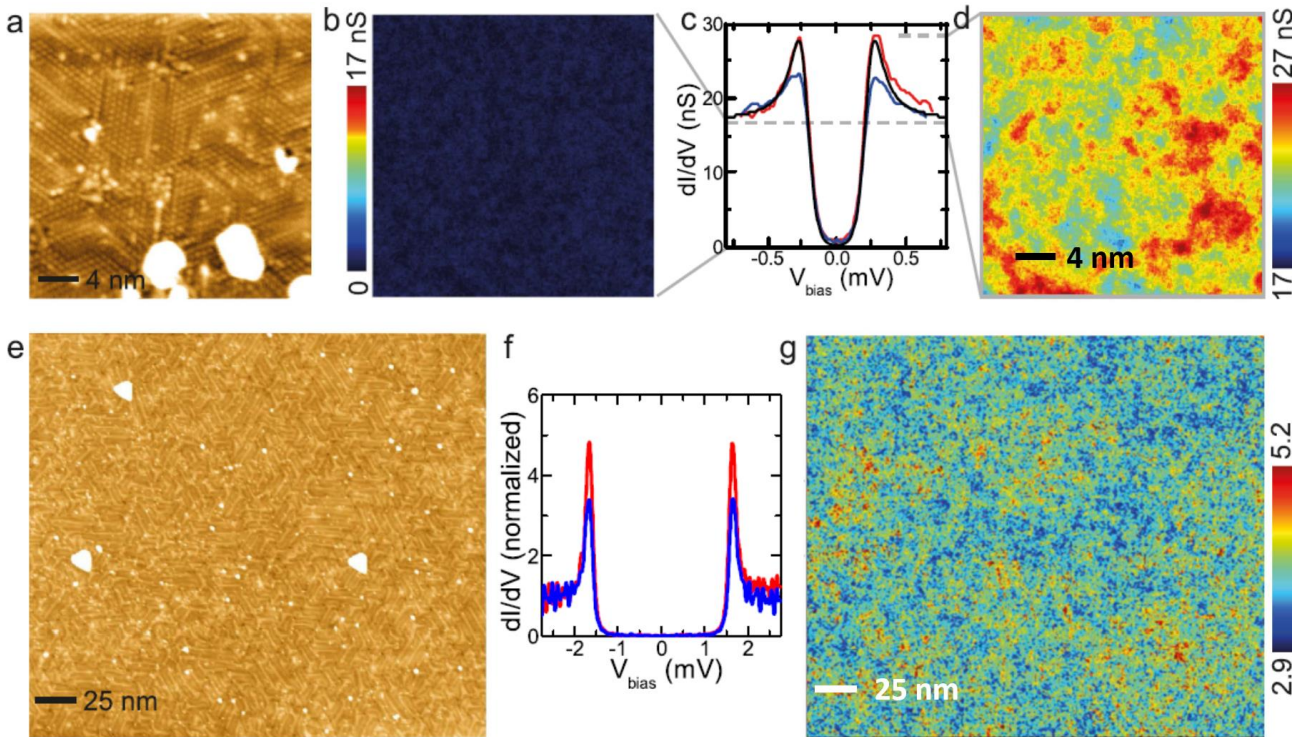


Figure 22. a) Small scale STM topography of the SIC phase showing its triangular atomic structure and its small domain size of 2-10 nm. b) $dI/dV(V = 0)$ zero-bias conductance map measured on area a) or e). c) Typical dI/dV spectra measured on area a) with a normal PtIr tip, showing variations in the height of the coherence peaks. Red and blue curves are experimental spectra, black curve is a BCS fit. d) $dI/dV(V = V_{peak})$ conductance map measured on area a) at the energy of the coherence peaks, showing the spatial distribution of the height of the coherence peaks. e) Larger scale STM topography of the SIC phase where a larger number of domains is seen. f) Same as c) but the dI/dV spectra are measured with a Pb superconducting tip whose energy gap is 1.3 meV. g) Same quantity as in d) but measured on the area e) with the Pb tip.

Let us note that the samples presented in panels 22a) and 22e) are different: the first sample is more disordered than the second one. Taking into account an energy gap for the tip $\Delta_{tip} \approx 1.30$ meV (characterized on thicker Pb islands), this leads to $\Delta_{SIC}^e \approx 0.35$ meV for the sample 22e) in good agreement with [Zhang2010] and $\Delta_{SIC}^a \approx 0.23$ meV for the sample 22a). The amazing result is that for both samples we do not measure at 0.3 K spatial variations of the energy gap, which remains constant over the monolayer, while simultaneously the spatial variations of the height of the coherence peaks occur on a length scale that is much smaller than $\xi \approx 50$ nm. Looking at the 2D conductance maps measured at the energy of the coherence peaks presented in panels 22d) and 22g), one sees that the size ℓ_{peak} of the puddles of constant peak height value is rather small

and is about few nanometers. Thus ℓ_{peak} seems quite comparable to the characteristic size of the nano-domains making the SIC, which is also similar to the elastic electron mean-free path ℓ_e in this Pb monolayer. Both these quantities can be estimated directly from STM measurements in various ways. ℓ_e can also be estimated from other macroscopic measured quantities using in-situ transport and ARPES. All techniques point to the same estimate $\ell_e \approx 3 - 8 \text{ nm} \ll \xi \approx 50 \text{ nm}$ [Brun2017]. A more advanced analysis, as I presented above for the NbN thin films, could be performed to provide a statistical distribution of the height of the peaks and a correlation length. This was not done by the time of this study, but could be done in the near future, since we are still working on this issue with our colleagues theoreticians Mikhail Skvortsov and Mikhail Feigel'man.

From the general theoretical background presented in the sections **Topic2A** and **Topic2B**, we have seen that the established models for various disorder mechanisms (disorder in the non-magnetic potential $U(\mathbf{r})$, in the pairing interaction $\lambda(\mathbf{r})$ or due to electron-electron interactions) all should lead to an LDOS broadening described by the Abrikosov-Gorkov theory modified by appropriate sub-gap tails states. Thus one sees that short-scale non-magnetic disorder effects are not expected to provoke variations in the excitation spectra at length scales smaller than ξ as we observe here in Pb monolayers. Nevertheless one should remind that in our introductory part about superconductivity we have explicitly mentioned the various assumptions that lead to the reduced BCS Hamiltonian. In particular the physically sound starting point that we have adopted was to consider a local interaction term between electrons written in real space as in equation (0a):

$$H_{supra} = -V \iiint d^3\mathbf{r} \Psi_{\mathbf{r}\uparrow}^\dagger \Psi_{\mathbf{r}\downarrow}^\dagger \Psi_{\mathbf{r}\downarrow} \Psi_{\mathbf{r}\uparrow} \quad (0a)$$

Such a term intrinsically generates many terms of the type:

$$\sum_{abcd} K_{abcd} c_{a\uparrow}^\dagger c_{b\downarrow}^\dagger c_{c\downarrow} c_{d\uparrow} \quad (0d)$$

where the indices \mathbf{a} are linked to the orbitals $|\mathbf{a}\rangle$ of energy $\epsilon_{\mathbf{a}}$ of the single-particle band Hamiltonian of the material in presence of disorder. In the BCS approximation, only the dominant term with $\mathbf{a} = \mathbf{b}$ and $\mathbf{c} = \mathbf{d}$ is kept, because the other ones such as (0d) are much smaller and the sum over the various eigenstates make them destructively interfere. Our colleagues theoreticians Lev Ioffe and Boris Altshuler proposed a toy model to explain our results taking into account explicitly the role of a non-BCS term of the type (0d) but considering only the leading term among these ones:

$$\sum_{ab} (K_{abbb} c_{a\uparrow}^\dagger c_{b\downarrow}^\dagger c_{b\downarrow} c_{b\uparrow} + K_{aaab} c_{a\uparrow}^\dagger c_{a\downarrow}^\dagger c_{a\downarrow} c_{b\uparrow}) \quad (0e)$$

Without going into more details, they assumed a model for a grain of size $L \gg \ell_e \gg \lambda_F$ verifying also $E_{Th} = \frac{\hbar D}{L^2} \gg \Delta \gg \delta$ where δ is the mean-level spacing in the grain. This implies that the dimensionless grain conductance verifies $g = G_{\square} h/2e^2 \gg 1$, as it is indeed the case for our monolayer superconductor. They found that a term such as given by (0e) will modify the BCS excitation energy $E_{\mathbf{a}} = \sqrt{\Delta^2 + (\epsilon_{\mathbf{a}} - \mu)^2}$ by mixing blocked states with unblocked ones. They found that this effect will lead both to broadening of the LDOS of the grain and to a shift of its spectral gap edge, everything being controlled by a small parameter γ given by:

$$\gamma \approx \frac{48\lambda^2 \delta^2}{\Delta^2} \ll 1 \quad (44)$$

It was then argued that one can go from the effective model for a grain to the one for a 2D material by using $\delta = \Delta/2g$. This leads to:

$$\gamma \approx \frac{12\lambda^2}{g^2} \ll 1 \quad (45)$$

Computing the range of expected values of γ for our film having $g \approx 10 - 30$ and assuming an electron-phonon coupling constant $\lambda \approx 1$ leads to $\gamma \approx 0.014 - 0.12$. Looking at the LDOS curves for various γ values predicted by this toy model is instructive. The results are plotted in figure 23. One sees that in practice the set of curves shown in panel 23a) are qualitatively similar to the Abrikosov-Gorkov ones. In particular the lower is the local conductance, the more rounded are the coherence peaks with a reduction of the spectral gap. Thus this simple model does not reflect perfectly our results since we do not detect a spectral gap reduction (up to our energetic resolution) while there is a clear coherence peak height variation. Also a correspondence that is not obvious is to link the very short scale variation observed in the experiment to physical variations of the film's local conductance. Such a behavior could be justified for highly disordered NbN thin films, as we demonstrated above in chapter **Topic2D**. Here the existence of an Altshuler-Aronov background is not

obvious and it is only a (very) small effect.

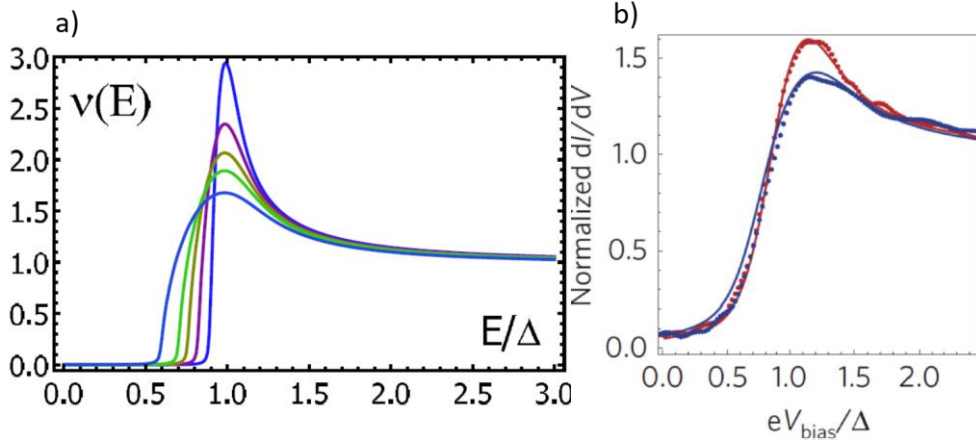


Figure 23. a) LDOS calculations for increasing values of the parameter g from $\gamma = 0.01$ (highest local conductance curve corresponding to the highest coherence peak) to $\gamma = 0.06$ (lowest local conductance curve, smallest coherence peak). b) Comparison between the calculated (continuous curves, red: $\gamma = 0.03$ and blue: $\gamma = 0.05$) and the normalized experimental $dI/dV(V)$ spectra (dotted curves, similar to the red and blue curves shown in figure 22c above).

We thus conclude that the theory needs further improvements. We are putting this forward with Mikhail Skvorstov and Mikhail Feigel'man. An additional aspect that might also play a role in this effect is the strong Rashba spin-orbit coupling and its possible variations at the local scale in particular when going from the $\sqrt{3} \times \sqrt{3}$ patches to the $\sqrt{7} \times \sqrt{3}$ boundaries. From an experimental point-of-view we thus plan to study similar physics in less heavy atomic monolayers using Al, In or Sn.

G) Weak disorder effects induced by step edges in the vortex lattice of superconducting Pb monolayers

We present now the second main result discovered in these superconducting monolayers. We have found a very different behavior of single atomic steps between the Pb-SIC monolayer and the Pb- $\sqrt{7} \times \sqrt{3}$ monolayer: they are highly transparent for the former and poorly transparent for the latter.

In the case of the Pb-SIC monolayer the atomic steps are highly transparent and connect electrically very well both adjacent terraces. We have inferred this both from zero-field dI/dV measurements (not shown here) and perpendicular magnetic field measurements. The magnetic field STS measurements are presented in the figure 24. Various $dI/dV(V = 0)$ conductance maps are shown, which enables to probe single vortices with high spatial resolution. For the Pb-SIC, we observe nice round (i.e. cylindrically symmetric) Abrikosov-like vortices as seen in panel 24a). The vortices are not preferentially pinned at step edges at low magnetic field (here $B = 0.04$ T). It has been previously shown by several groups that the half-width at half maximum of the radial cut of the zero-bias conductance through a single vortex corresponds to the superconducting coherence length [Cren2009]. Such a radial cut for the Pb-SIC is shown in panel 24d) leading to $\xi \approx 50$ nm in very good agreement with the value extracted previously from S-S proximity effect (see **Topic1D**). Such a deduction has been theoretically justified using 2D or 3D Usadel equations in a work of ours (not presented in this HDR thesis) studying proximity vortices in a Cu film deposited on a thicker Nb film [Stolyarov2018].

In contrast, in the Pb- $\sqrt{7} \times \sqrt{3}$ monolayer the atomic steps often present local regions with depressed superconducting gap on the upper terraces which are themselves electrically badly connected to the adjacent lower terrace (measurements at zero magnetic field not shown here, see Fig.20 in [Brun2014]). In such case, we thus observe a large discontinuity in the $dI/dV(V)$ spectra when going from the upper terrace to the lower one through the step edge. From our studies in **Topic1** about proximity effect and equation (15), we infer that the step transparency is low because the superconducting material is the same on the upper and lower terrace. This low step transparency is confirmed by perpendicular magnetic field measurements at $B = 0.04$ T seen in panel 24b). In this case one observes that for such applied field all vortices are pinned to step edges. This behavior is strikingly different from the one observed on the Pb-SIC monolayer (compare with panel

24a). Moreover, the individual vortices do not present a regular cylindrically symmetric shape. Some of them are elongated along the direction of the step edge. Interestingly Japanese colleagues have observed a similar behavior for the $\text{In}-\sqrt{7} \times \sqrt{3}$ monolayer [Yoshizawa2014], that has a structure similar to the one of $\text{Pb}-\sqrt{7} \times \sqrt{3}$. I presented their results on panel 24c). These characteristics point out to a different type of vortices than the circularly symmetric Abrikosov-like observed in panel 24a. We discuss this issue in the next paragraph.

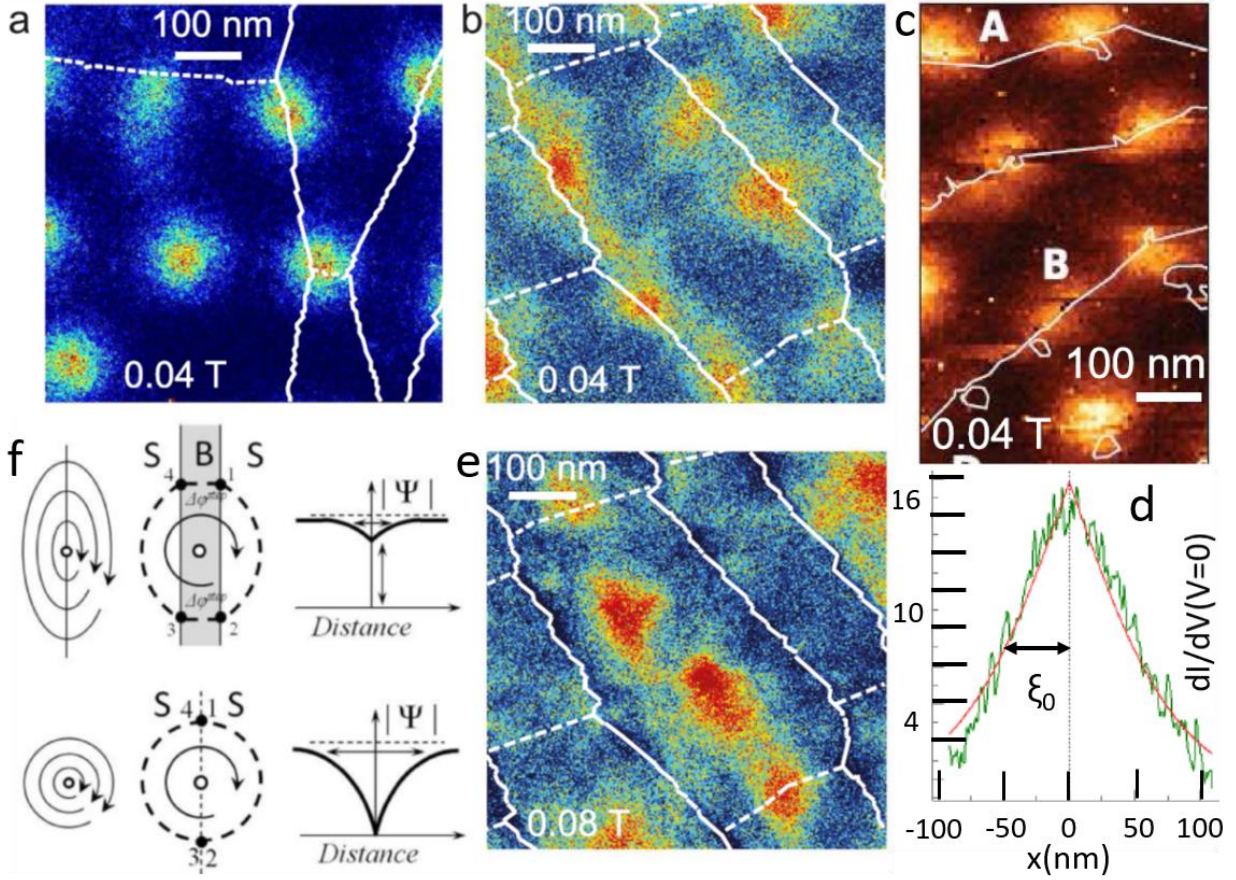


Figure 24. Vortices measured by STS in different superconducting monolayer superconductors. They are probed by $dI/dV(V=0)$ conductance maps at $T \ll T_C$. The scale bar is indicated. Single atomic steps are represented by continuous white lines. Dashed lines represent the underlying $\text{Si}-7 \times 7$ domain boundaries. The perpendicular magnetic field is indicated in the bottom left part of the maps. a) Pb -striped incommensurate (SIC) monolayer. b) and e) $\text{Pb}-\sqrt{7} \times \sqrt{3}$ monolayer. c) $\text{In}-\sqrt{7} \times \sqrt{3}$ monolayer. The Indium phase measurements are from [Yoshizawa2014] while the Lead ones are from [Brun2014]. d) Radial cut of the zero bias conductance of an Abrikosov vortex such as in panel a). f) Schematics explaining around a vortex: the flow of current density (left column), the evolution of the superconducting phase (middle column), the spatial distribution of the order parameter (right column) for an Abrikosov vortex (bottom three panels) and for a mixed Josephson-Abrikosov vortex (top three panels). Figure reproduced from [Brun2017].

For a perfectly transparent step edge, one has $\mathbf{j}_C^{\text{step}}(\mathbf{r}) = \mathbf{j}_C$ where \mathbf{j}_C is the critical current density in the interior of the terraces and $\mathbf{j}_C^{\text{step}}(\mathbf{r})$ is the critical current density along the step edge at location \mathbf{r} . In this situation the step does not behave as a Josephson junction and the profile of both the current lines and phase circulation are circularly symmetric around the 2π phase singularity of the Abrikosov-like vortex. The order parameter in this situation is zero exactly at the phase singularity where the critical current density is reached. This case is schematically shown in panel 24f bottom line. It corresponds to the Pb -SIC monolayer seen in panel in 24a).

In contrast, for a step behaving as a Josephson junction, one has $\mathbf{j}_C^{\text{step}}(\mathbf{r}) < \mathbf{j}_C$. In this case, the current density crossing the step edge $\mathbf{j}^{\text{step}}(\mathbf{r})$ is given by the Josephson relation $\mathbf{j}^{\text{step}}(\mathbf{r}) = \mathbf{j}_C^{\text{step}}(\mathbf{r}) \sin(\Delta\Phi^{\text{step}}(\mathbf{r}))$ where $\Delta\Phi^{\text{step}}(\mathbf{r})$ is the gauge-invariant finite phase drop occurring at point \mathbf{r} across the Josephson junction. In this situation the current lines around the phase singularity of the vortex will be elongated along the step edge by

a factor $j_c/j_c^{step}(\mathbf{r}) > 1$. This is schematically depicted by the top line in panel 24f. Near the vortex center the order parameter $\psi(\text{center})$ is reduced because the local current density is lower than the critical one j_c . It is given by:

$$|\psi(\text{center})| \approx \left[1 - \left(\frac{j_c}{j_c^{step}(\mathbf{r})} \right)^2 \right] |\psi_0| \quad (46)$$

where ψ_0 is the unperturbed order parameter inside the terrace. This situation corresponds to the vortices observed in both $\text{Pb}-\sqrt{7} \times \sqrt{3}$ and $\text{In}-\sqrt{7} \times \sqrt{3}$ seen in panels 24b and 24c. In practice it is observed that in agreement with the relation (46) such mixed Josephson-Abrikosov vortices indeed show an in-gap conductance lower than the one observed for Abrikosov-like vortices sitting inside terraces. Once the Josephson-Abrikosov vortices have saturated all step edges at low field, Abrikosov-like vortices enter the interior of the terraces at larger field (see panel 24e from which the dI/dV map shown in panel 24b was subtracted to make clearer where the new vortices sit). One notices that these additional vortices are not perfectly circular as in the panel 24a) of the Pb-SiC phase. They might move while scanning due to weak pinning, or due to thermal activated processes.

This work related to weak disorder effects in Pb superconducting monolayers presented in parts **Topic2E-F-G** has been published in two papers: one article [C. Brun et al. Nature Physics 10, 444 \(2014\)](#) and one review paper [C. Brun et al., Supercond. Sci. Technol. 30, 013003 \(2017\)](#). This research activity was very fruitful because we discovered many new interesting properties that were not reported previously. These results enabled me to write a young ANR project that I obtained in 2016: [Rodesis](#), entitled ‘‘superconductivity in a single atomic plane’’ (ANR-16-CE30-0011). This research topic is funded and pursued up to now. It aims at studying both the effect of non-magnetic and magnetic impurities on monolayer superconductors. This became the main part of the **PhD work of Danilo Longo** (during 4 years) that I entirely co-supervised and who defended his thesis in May 2019, and also part of the **PhD thesis of Raphaël Leriche**. I also co-supervised **our Post-doc Alexandra Palacio-Morales** since February 2018 on these studies. For the magnetic impurity studies we used magnetic molecules (MnPc) and designed/constructed a new UHV chamber dedicated to the evaporation of such molecules in a separate modular chamber that could be plugged on all preparation chambers of our STM set-ups (see figures 2 and 3 of the Introduction part). I will present these studies in section **Topic2I** below. Another very important development of this work is the study of topological superconductivity using Pb monolayer phases. This subject will be presented in the **Topic3** later.

H) Mapping the wavefunction of the bound state of a single magnetic atom in a superconductor

We now turn to the second part of this **Topic2** dealing with the effect of magnetic impurities on superconductors. As we have seen previously in the theoretical recap part **Topic2A**, a single magnetic atom is a pair-breaker for a conventional superconductor due to an exchange interaction between the impurity spin and the spin of the electrons of the superconductor. The early theoretical description by Yu, Shiba and Rusinov [Yu1965,Shiba1968,Rusinov1969] considered the simpler case but widely fulfilled of a large impurity spin that can be considered as a classical variable. We remind here the expression of the local interaction Hamiltonian at the site \mathbf{r}_i of the magnetic impurity (we presented it above in part **Topic2A**). We assume that the impurity spin \vec{S} is oriented along the $+z$ direction. It is given by the relation (20):

$$\mathcal{H}_{mag-imp}(\mathbf{r}_i) = \sum_i \frac{JS}{2} (\Psi_{r_i\uparrow}^\dagger \Psi_{r_i\uparrow} - \Psi_{r_i\downarrow}^\dagger \Psi_{r_i\downarrow}) + K (\Psi_{r_i\uparrow}^\dagger \Psi_{r_i\uparrow} + \Psi_{r_i\downarrow}^\dagger \Psi_{r_i\downarrow}) \quad (20)$$

Since this interaction term is formulated in real space, the Bogoliubov-de Gennes (BdG) formalism is again best adapted to solve this problem. Let us remind that for non-magnetic disorder there is a spin degeneracy of the eigenstates. So we introduced this BdG formalism using a 2×2 matrix formulation in equations (6,7,8,9) as a function of the spinor $(\Psi^\dagger(\mathbf{r}\uparrow) \Psi(\mathbf{r}\downarrow))$ which is the natural generalization of the BCS spinor $\Psi_k^\dagger = (c_{k\uparrow}^\dagger \ c_{-k\downarrow})$. Now this BdG formalism has to be generalized to include the four spin components of the Ψ operators since the spin degeneracy is lifted due to the term containing $JS/2$. This means that the BdG eigenstates have now to be searched in the more general form:

$$\Psi(\mathbf{r}\sigma) = \sum_n [u_n(\mathbf{r}, \sigma)\gamma_n + v_n^*(\mathbf{r}, \sigma)\gamma_n^\dagger] \quad (47)$$

where $u_n(\mathbf{r}, \sigma)$ and $v_n(\mathbf{r}, \sigma)$ can each have two components one for each spin value $\sigma = +1$ or $\sigma = -1$. As before the operators γ_n are the Bogoliubov operators diagonalizing the full system's Hamiltonian. We have seen in the introductory part of this HDR thesis that for a BCS superconductor the lowest energies of the quasi-particle excitations are gapped. These energies satisfy always $E \geq \Delta$. Yu, Shiba and Rusinov have shown that for a strong magnetic impurity characterized by a unitary parameter $0 < \mu \leq 1$ (see the relation (20) above) i.e. going beyond the Born approximation, there exists new quasi-particle excitation energy E_0 lying inside the spectral gap: i.e. verifying $0 \leq E_0 < \Delta$. The corresponding eigenstate is bound to the impurity. Its energy E_0 is conveniently expressed as a function of the parameters $\alpha = \pi v_0 JS/2$ and $\beta = \pi v_0 K$ depending on the exchange energy J and non-magnetic potential term K , v_0 being as before the DOS at E_F :

$$E_0 = \Delta \frac{1 - \alpha^2 + \beta^2}{\sqrt{4\alpha^2 + (1 - \alpha^2 + \beta^2)^2}} \quad (48)$$

E_0 can also be put in the more compact form:

$$E_0 = \Delta \cos(\delta^+ - \delta^-) \quad (49)$$

where δ^+ and δ^- are defined by:

$$\tan \delta^\pm = v_0(K \pm JS/2) = (\beta \pm \alpha)/\pi \quad (50)$$

To this energy E_0 correspond the eigenstates $\Psi_{E_0}(\mathbf{r}\sigma)$ with non-zero components only $u_{E_0}(\mathbf{r}, \uparrow)$ and $v_{E_0}(\mathbf{r}, \downarrow)$ for $J < 0$ (ferromagnetic coupling) and $u_{E_0}(\mathbf{r}, \downarrow)$ and $v_{E_0}(\mathbf{r}, \uparrow)$ for $J > 0$ (antiferromagnetic coupling). This simplification results from the fact that the 4×4 matrix decomposes into two 2×2 sub-systems differing by reversing the sign of J . Using the convention explained in the HDR introduction for electron-like and hole-like quasiparticle excitations energies (see the relation (4) and accompanying paragraph), we plot in figure 25 the energy dependence of E_0 on the parameters α and β for its components $u_{E_0}(\mathbf{r}, \uparrow)$ (electron-like excitation thus corresponding to $+E_0$ in red) and $v_{E_0}(\mathbf{r}, \downarrow)$ (hole-like excitation thus corresponding to $-E_0$ in green).

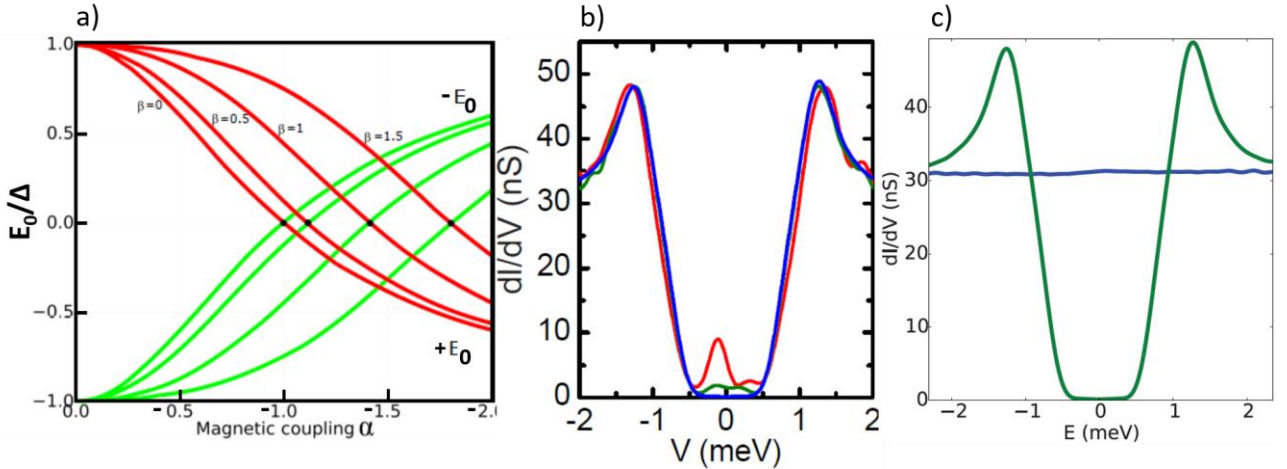


Figure 25. a) Energy dependence of the electron-like ($+E_0$, red curves) and hole-like energies ($-E_0$, green curves) of the quasi-particle excitations associated to a classical magnetic impurity embedded in a conventional BCS superconductor as a function of the parameters $\alpha = \pi v_0 JS/2$ and $\beta = \pi v_0 K$. b) Local $dI/dV(V)$ spectra measured at $T = 0.3$ K above a single magnetic atom embedded in the surface layer plane of $2H\text{-NbSe}_2$ superconductor. The red spectrum is measured at the impurity center, the green one 4 nm away and the blue one is the reference spectrum 20 nm away from any magnetic impurities. c) The blue $dI/dV(V)$ spectrum is measured at the impurity center at $T = 0.3$ K in a 5T perpendicular magnetic field, $2H\text{-NbSe}_2$ being in its normal state for this field. The green spectrum presents the reference spectrum in $B = 0$ T far away from any magnetic impurity.

One sees that these excitations are symmetric in energy and start as expected at $E_0 = \Delta$ for $\alpha = 0$. For $\alpha < 0$, which physically corresponds to $J < 0$, E_0 becomes lower than Δ and moves progressively toward 0 when α becomes more negative. When β increases, E_0 decreases less fast when α rises because non-magnetic potential is not pair-breaking and thus reduces the depairing effect produced by α . Let us note that these two excitations have a well-defined spin orientation: for $-1 \leq \alpha \leq 0$ the effective excitation of energy E_0 has the same S_z

spin component as the impurity spin $S_Z^{mag-imp}$, i.e. +1. Thus the excitation is 100% spin-polarized by the impurity. Nevertheless in practice the spin of a single impurity atom or molecule has very rarely a fixed orientation in space with respect to the lattice of the superconducting substrate: this requires a strong enough spin-orbit coupling leading to magnetic anisotropy. The spin of the impurity will thus usually fluctuate with a rotational disorder in space, together with the spin of the excitation E_0 .

When $\alpha \leq -1$ the electron-like and hole-like excitation energies cross zero and get a reversed sign. The value $|\alpha| = 1$ corresponds to the strong coupling limit where the ground state changes. For $|\alpha| < 1$ it remains a BCS-like ground state. For $|\alpha| \geq 1$ a pair is broken at the magnetic impurity site and this leaves an unpaired electron bound to the impurity with a spin parallel to the one of the impurity (for $J < 0$). In this case the excited state correspond to a spin polarization opposite to the one of the impurity spin, i.e. to a spin flip. Let us note also that there exists a local correction to the energy gap value associated to the magnetic impurity but this is a (very) small effect not observable for superconductors having a large number of single-electron states in the energy interval Δ .

The excited states are localized around the impurity on a length $\xi_{mag-imp}$ given by:

$$\xi_{mag-imp} = \frac{\hbar v_F}{\Delta |\sin(\delta^+ - \delta^-)|} = \xi_0 \left(1 - E_0^2/\Delta^2\right)^{-1/2} \quad (51)$$

where $\xi_0 = \hbar v_F/\Delta$. One sees from (51) that $\xi_{mag-imp}$ increases above the ‘‘bare’’ superconducting coherence length $\xi_0 = \hbar v_F/\Delta$ of the clean superconductor by a factor $(1 - E_0^2/\Delta^2)^{-1/2} \geq 1$ that is directly determined by the excitation energy E_0 .

Moreover, Rusinov has shown that in a 3D electron gas system the components $\Psi_{E_0}^+(\mathbf{r}) = u_{E_0}(\mathbf{r}, \uparrow)$ and $\Psi_{E_0}^-(\mathbf{r}) = v_{E_0}(\mathbf{r}, \downarrow)$ present spatial modulations at the Fermi wavelength [Rusinov1968]. Their asymptotic form (i.e. far from the impurity center) is given by:

$$\Psi_{E_0}^\pm(\mathbf{r}) = \frac{1}{\sqrt{A}} \frac{\sin(k_F r + \delta^\pm)}{k_F r} \exp\left(\frac{-r\Delta |\sin(\delta^+ - \delta^-)|}{\hbar v_F}\right) \quad (52)$$

where A is a normalization factor such that $1 = \int \frac{dr}{2\pi^3} (|\Psi_{E_0}^+(\mathbf{r})| + |\Psi_{E_0}^-(\mathbf{r})|)$. One sees that both components $\Psi_{E_0}^+(\mathbf{r})$ and $\Psi_{E_0}^-(\mathbf{r})$ are modulated by the Fermi wavelength $1/k_F = \lambda_F/2\pi$. One can also deduce the spatial decay length of these components. Their amplitude decay as $1/(2\pi r/\lambda_F)$ multiplied by an exponential decay over the length $\xi_{mag-imp}$. For a 3D electron gas system of Fermi energy $E_F \approx 10$ eV and standard free electron mass, $1/k_F = \lambda_F/2\pi \approx 0.6$ Å. Since $\xi_{mag-imp} > \xi_0 \gg 1/k_F$ one expects that the spatial decay of the $\Psi_{E_0}^\pm(\mathbf{r})$ components will be strongly dominated by the term $1/(2\pi r/\lambda_F)$ decaying much faster with r than the exponential term. As in STS experiments we don't probe the amplitude $\Psi_{E_0}^\pm(\mathbf{r})$ directly but $|\Psi_{E_0}^\pm(\mathbf{r})|^2$ this effect will be even stronger. Thus one expects that few Angströms away from the magnetic atom the tunneling conductance proportional to the LDOS $\propto |\Psi_{E_0}^\pm(\mathbf{r})|^2$ will already vanish. This situation corresponds precisely the one originally measured by A. Yazdani on single Mn atoms deposited on a niobium surface, shown in figure 26a). Panel 26b) shows that the excited states have a maximum amplitude right at the atom center, decaying to zero less than 1 nm away. These features were confirmed by another study also on Mn atoms performed at lower temperature with an increased energy resolution (using a superconducting tip) on ultrathin Pb films. The results are presented in panels 26c,d,e,f). They feature a double pair of excited states indexed by indices $l = 0$ and $l = 1$. The spatial extension of these excitations seen in panel 26f) is less than 1 nm in agreement with the relation (52) above. The fact that several pairs of Yu-Shiba-Rusinov excited states can be associated to a single magnetic atom suggests that the simplified magnetic and non-magnetic potential term used in the Hamiltonian (20) have to be generalized to $K(\mathbf{r})$ and $J(\mathbf{r})$ to include a spatial dependence. In this case Rusinov showed that each pair of Fourier components (K_l, J_l) of $K(\mathbf{r})$ and $J(\mathbf{r})$ lead to a pair of excited states at energy $E_0(l)$.

Nevertheless, two important predictions of (52) could not be measured:

- i) Most probably due this very rapid decay in 3D of the amplitude of $|\Psi_{E_0}^\pm(\mathbf{r})|$, the expected oscillations at $\lambda_F/2\pi$ were not observed.

- ii) There should exist a well-defined spatial phase-shift between the electron-like $u_{E_0}(\mathbf{r}, \uparrow)$ and hole-like $v_{E_0}(\mathbf{r}, \downarrow)$ wavefunctions equal to $\delta^+ - \delta^-$ which according to (49) is directly given by $\delta^+ - \delta^- = \arccos(E_0/\Delta)$.

As we show now, our work enabled to verify these two additional predictions in great details. In order to probe the full spatial dependence of the electron and hole components of the magnetic bound state, we studied a quasi-2D material superconductor. This has several advantages: it increases significantly the Fermi wavelength λ_F with respect to a 3D material, typically by almost one order of magnitude. Furthermore, for a 2D underlying electron gas the expression (52) changes and decays less fast:

$$\Psi_{E_0}^{\pm}(\mathbf{r}) = \frac{1}{\sqrt{A\pi}} \frac{\sin(k_F r + \delta^{\pm} - \pi/4)}{\sqrt{k_F r}} \exp\left(\frac{-r\Delta|\sin(\delta^+ - \delta^-)|}{\hbar v_F}\right) \quad (53)$$

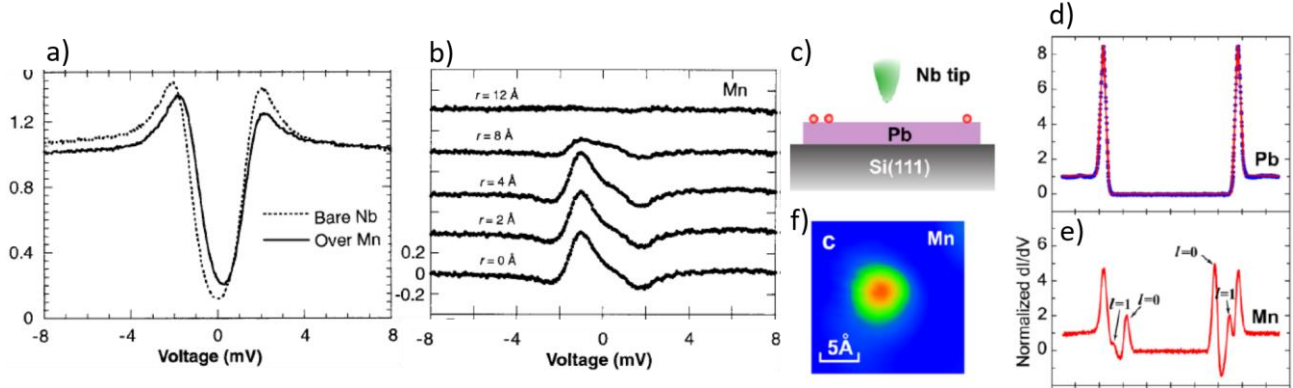


Figure 26. a) dI/dV spectra measured above a bare Nb substrate (continuous curve) and above a single Mn atom deposited on the Nb substrate (dotted curve). b) Difference between the dotted and continuous curves presented in panel a), plotted as a function of distance to the center of the Mn atom. c) Sketch of the second experiment. d) dI/dV spectra measured above the bare Pb/Si(111) ultrathin film with a Nb superconducting tip (blue curve). The red curve is a BCS fit. e) dI/dV spectrum measured above a single Mn atom with the Nb tip. f) 2D dI/dV map showing the spatial extension of the $l = 0$ excited state. Panels a-b) are from [Yazani1997] and c-f) from [Ji2008].

Indeed, one sees that instead of decaying as $1/(2\pi r/\lambda_F)$ the amplitudes now decay as $1/\sqrt{(2\pi r/\lambda_F)}$. By studying embedded magnetic impurities in the clean superconductor $2H\text{-NbSe}_2$, we could reveal all remaining features of the excited states. For this purpose, we cleaved in-situ in UHV this material and performed blind STS spectroscopy at $T = 0.3$ K until we found intra-gap spectroscopic signatures. Our results are presented in figure 27.

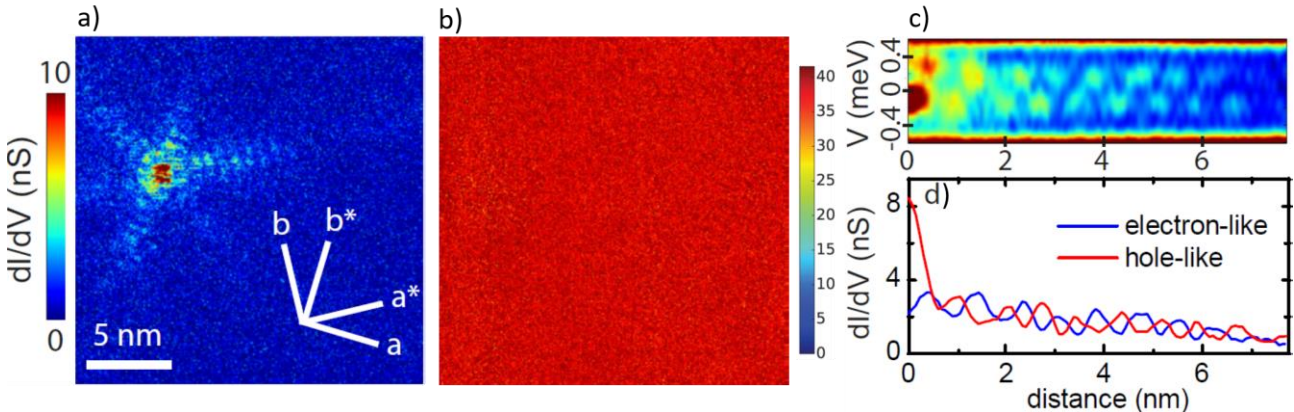


Figure 27. a) $dI/dV(x, y, V = -0.13$ meV) conductance map measured at 0.3 K and $B=0$ T in a 20×20 nm² region of $2H\text{-NbSe}_2$ including the single magnetic atom whose $dI/dV(V)$ spectra are presented in figure 25b) and 25c) above. The oscillating star-shaped pattern represents the square of the hole-like wavefunction of the excited magnetic bound state. b) Same quantity as in a) measured exactly at the same place but in $B = 5$ T perpendicular magnetic field. The homogeneous conductance map reflects that $2H\text{-NbSe}_2$ is in its normal state (the conductance scale bar expressed in nS for this map stands on its right). c) Top panel: $dI/dV(r, V)$ 2D plot of a 1D conductance linecut taken along an 8 nm line going from the center of the magnetic atom (located

at position $r = 0$ nm) toward a branch of the star seen in panel a). Thus horizontal axis is the distance in nm from the impurity center. Vertical axis is the excitation energy in meV around $\varepsilon_F = 0$. d) Bottom panel: $dI/dV(r, V = \pm 0.2$ meV) 1D plots of the conductance profiles showing the electron-like component $|u_{E_0}(\mathbf{r}, \uparrow)|^2$ (blue) and hole-like one $|v_{E_0}(\mathbf{r}, \downarrow)|^2$ oscillating with a well-defined phase-shift.

The panel 27a) presents the spatial oscillations of the hole-like component $|v_{E_0}(\mathbf{r}, \downarrow)|^2$ with the period $\lambda_F/2\pi$. This is measured above a single atom (presumably Fe) whose dI/dV spectra are presented in panels 25b) and 25c). Instead of being perfectly circular with respect to the impurity center (as expected from relations 52 or 53), these oscillations take the form of star whose directions are aligned with the ones of the reciprocal lattice vectors \mathbf{a}^* and \mathbf{b}^* . This panel 27a) is to be compared to the panel 26f), as it represents the same physical quantity: a 2D $dI/dV(x, y, V = -0.13$ meV) conductance map measured at the energy of the hole-like excitation: $E_0 = -0.13$ meV. The energy and spatial dependence of the components $|u_{E_0}(\mathbf{r}, \uparrow)|^2$ and $|v_{E_0}(\mathbf{r}, \downarrow)|^2$ are presented in panel 27c) and 27d). One sees that both components oscillate at $\lambda_F/2\pi \approx 0.8$ nm, the phase shift between them corresponding to $2(\delta^+ - \delta^-) \approx \pi$. This implies $\delta^+ - \delta^- \approx \pi/2$ which is in very good agreement with $E_0 = 0.13$ meV $\approx 0 \ll \Delta \approx 1$ meV so that the relation (49) is indeed verified. Above the critical perpendicular magnetic field of $2H$ -NbSe₂, the material is in its normal state. Then all spectroscopic features associated to the interaction between the iron atom and the superconductor vanish: one recovers a flat homogeneous LDOS as seen in panels 25c) and 27b). For completeness we also present in figure 28 the fit of the radial decay of the components $|u_{E_0}(\mathbf{r}, \uparrow)|^2$ and $|v_{E_0}(\mathbf{r}, \downarrow)|^2$ according to the asymptotic law $(1/\sqrt{(2\pi r/\lambda_F)})^2 = 1/(2\pi r/\lambda_F)$ expected from (53). One sees that both fits are quantitatively satisfactory.

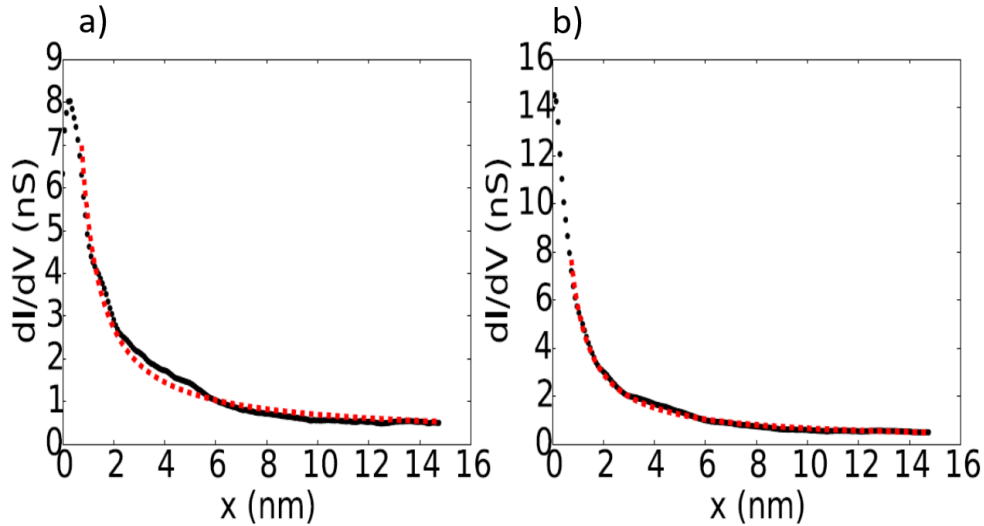


Figure 28. a) Radial decay the angularly integrated hole-like component $|v_{E_0}(\mathbf{r}, \downarrow)|^2$. b) Same quantity for the electron-like $|u_{E_0}(\mathbf{r}, \uparrow)|^2$ component. Black dots are experimental curves and dashed red curves are theoretical fits assuming the $1/(2\pi r/\lambda_F)$ asymptotic dependence predicted by equation (53).

In conclusion, I would like to emphasize that in our work we managed for the first time to measure the detailed spatial and energy dependence of the electron and hole components of Yu-Shiba-Rusinov excited states associated to a single magnetic impurity, using a quasi-2D electron gas based superconductor. We could reproduce this experiment and we observed several of such similar excited states located at various energies in the gap (see [Menard2015]). Depending on the energy we could verify that the dephasing between the electron and hole component of the wave function changes and goes to zero for energies close to the gap edge. Our work was published in [Coherent long-range magnetic bound states in a superconductor G. Ménard, et al. Nature Physics 11, 1013 \(2015\)](#). Our results are in very good agreement with theoretical predictions. There remain nevertheless unclear issues related to the peculiarities of the $2H$ -NbSe₂ bandstructure and its superconducting properties. I did not insist on this here, but this material is a multigap superconductor (which is seen on the spectrum of panel 25c) being a non-pure BCS one) with a complicated 3-band Fermi surface [Rahn2012]. If we try to relate the period of the observed oscillations seen in figure 27 to a simple quantity such as $1/k_F \approx 0.8$ nm, as suggested by the Rusinov expressions (53) above, this should provide us with some effective Fermi wavevectors for $2H$ -NbSe₂. In fact, looking at the detailed Fermi surface of this material

(see figure 6 in [Rahn2012]), there is no such agreement: the Fermi wavevector associated either to the Γ or K pocket is much larger. From our analysis, the only possible agreement is that the quantity $1/2\delta k_F^\Gamma \approx 0.8$ nm in fact corresponds to the $\delta k_F^\Gamma \approx 0.063 \text{ \AA}^{-1}$ wavevector difference existing between the two concentric Fermi pockets located around Γ . From [Rahn2012] this value is $\delta k_F^\Gamma \approx 0.07 \text{ \AA}^{-1}$. The reason why such a modulation would physically exist at all could be the following. We have shown in a special study dedicated to $2H\text{-NbSe}_2$ electronic properties that the DOS associated to these Γ pockets is associated to the small superconducting gap of $2H\text{-NbSe}_2$ (see [Noat2015], results not presented in this HDR thesis), which is also the gap component that dominates the tunneling along \mathbf{c}^* due tunneling selectivity effects. This wavevector modulation at δk_F^Γ would then reflect the strong scattering of the electrons by the impurity between these two Fermi sheets located around Γ . These considerations underline the fact that the peculiarities of the $2H\text{-NbSe}_2$ bandstructure play an important role on some fine features seen in the $dI/dV(x, y, V)$ conductance maps. These aspects are related to quasi-particle interferences that we will address in **Topic5** later.

A last important issue concerns the fact of knowing whether our single impurity is in the weak coupling regime ($|\alpha| < 1$) or strong coupling one ($|\alpha| > 1$). This is in fact not straightforward since this requires knowing precisely the value of J , its sign, and also the value of K in order to properly interpret the excitations shown in panel 25a). We think that there is quite some confusion in the literature about this issue. From the calculations by Shiba we can infer that at the impurity center the following relation is satisfied for the ratio of the amplitudes of the electron and hole components:

$$\frac{\Psi_{E_0}^+(\mathbf{r} = \mathbf{0})}{\Psi_{E_0}^-(\mathbf{r} = \mathbf{0})} = \frac{\cos(\delta^+)}{\cos(\delta^-)} \quad (54)$$

This shows that in conjunction with the relation (50) above, as soon as there is a non-magnetic scattering term $\cos(\delta^+) \neq \cos(\delta^-)$ which leads to an asymmetry in the amplitudes of the electron and hole components. This fact is often observed experimentally both in our case (see figure 25b) and others' (see figure 26b and 26e). Nevertheless one cannot simply conclude from the observation by STS of an asymmetry of the amplitudes at the impurity center, in which regime weak or strong, is the impurity. All possibilities are represented in the diagram in figure 29a) below. For instance a much larger hole-component at the impurity center, as we observe in our case (see figure 25b), implies $\Psi_{E_0}^+(\mathbf{r} = \mathbf{0})/\Psi_{E_0}^-(\mathbf{r} = \mathbf{0}) < 1$ which could correspond either to $[\alpha > 0$ and $\beta > 0]$ or $[\alpha < 0$ and $\beta < 0]$. Then depending on whether $|\alpha| < 1$ or $|\alpha| > 1$ this hole component will be situated respectively at negative energies or at positive ones. Thus without knowing precisely the values of α and β and their signs it seems not possible to conclude anything only from the STS measurements of an asymmetry existing between the amplitudes of $\Psi_{E_0}^+(\mathbf{r} = \mathbf{0})$ and $\Psi_{E_0}^-(\mathbf{r} = \mathbf{0})$. We will discuss this aspect further in the next part **Topic2 I** below.

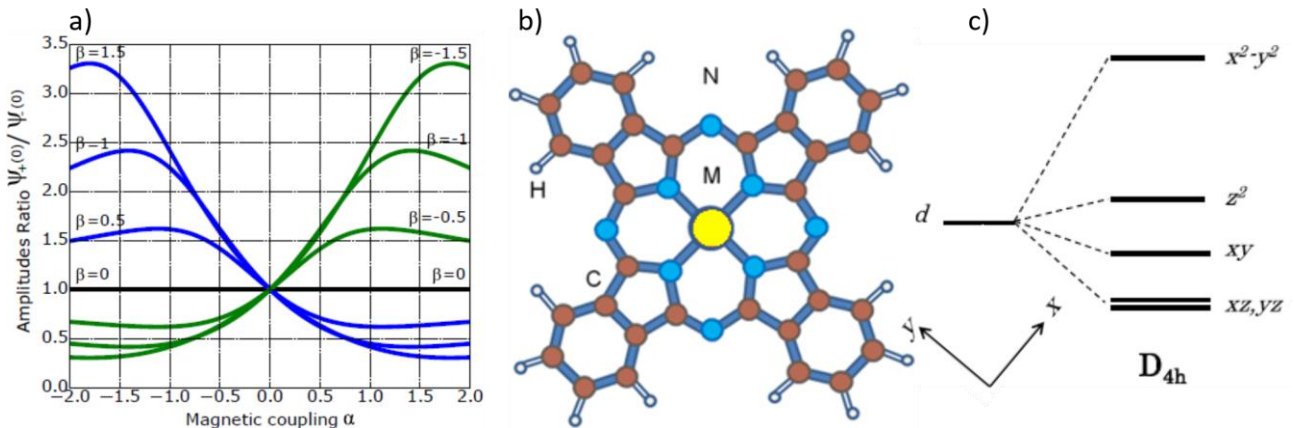


Figure 29. a) Ratio of the amplitudes of the electron component to the one of the hole component at the impurity center, as a function of the parameters α and β characterizing respectively the magnetic and non-magnetic coupling. b) Schematics of a manganese phthalocyanine molecule. The central yellow M atom is a Mn one. Blue atoms are nitrogen ones, brown atoms are carbon ones and white atoms represent hydrogen ones. c) Energy level splitting for Mn^{2+} including the D_{4h} site symmetry in MnPc, from [Kitaoka2013].

I) Coupling between magnetic molecules and ultrathin superconducting films: MnPc/Pb/Si(111)

One disadvantage of the work that we presented in the previous part **Topic2H** lies in the fact that the identity of the measured magnetic atoms is unknown. From the chemical analysis of the purity of the niobium and selenium sources used by our colleagues from the Institut des Matériaux Jean Rouxel in Nantes, we ended up to the conclusion that the magnetic atoms should most probably be iron atoms substituted to niobium ones. Nevertheless, we wanted to use well-defined magnetic atoms or molecules to extend our studies in a better controlled way, in particular to render them accessible to Density-Functional-Theory (DFT) *ab initio* calculations. To this end we have tried to deposit cobalt atoms on both 2H-NbSe₂ and Pb/Si(111) ultrathin films. These experiments did not succeed very well because on both substrates the atoms diffuse a lot and clusterize. As we could not deposit the magnetic atoms on a sample maintained at very low temperature (≤ 10 K) we turned to another option using magnetic molecules. Our idea was also that we could exploit the natural self-organization of the molecules to form interesting arrays of magnetic molecules. We set-up a collaboration with Nadine Witkowski, researcher in our lab, who had already some experience with magnetic phtalocyanines molecules. During the PhD thesis of Danilo Longo, we first developed a homemade compact modular chamber to evaporate these molecules under clean UHV conditions in a separate dedicated chamber. The main reason is that these molecules sublime at rather low temperature and can easily contaminate the main preparation chamber. This modular chamber is versatile and designed to be mounted on a CF-40 flange of any apparatus accepting Omicron sample holders. This modular chamber was presented in figures 2 and 3 in the beginning of the HDR thesis. As interesting molecules, we have selected manganese phtalocyanines (abbreviated MnPc in the following).

The schematic of a single MnPc molecule is shown if figure 29b), where the central metal atom M stands for a Mn atom. All nearest-neighbor atoms of the central atom are nitrogen atoms. Due to the magnetic properties of the central Mn atom, single MnPc molecules also possess magnetic properties. We first characterized the purity of our commercial MnPc source by performing magnetization measurements versus temperature of a powder sample and extracted from it the magnetic susceptibility measurements. The results are shown in figure 30 below. They are typical of a paramagnetic material revealing a magnetic susceptibility $\chi = M/B \approx C/T$ in good agreement with the Curie-Weiss law. A small offset with a negative temperature exists pointing to some kind of magnetic interactions existing inside or between molecules in the powder. Our results lead to an effective number of Bohr magneton of about $4.2 \mu_B$ per molecule at room temperature, in good agreement with previous reports suggesting a magnetic moment close to the theoretical value $\mu = g\sqrt{J(J+1)} \mu_B \approx 3.88 \mu_B$ corresponding to a pure spin moment $S = 3/2$ with no orbital momentum $L = 0$ and $g = 2$ [Barraclough1970].

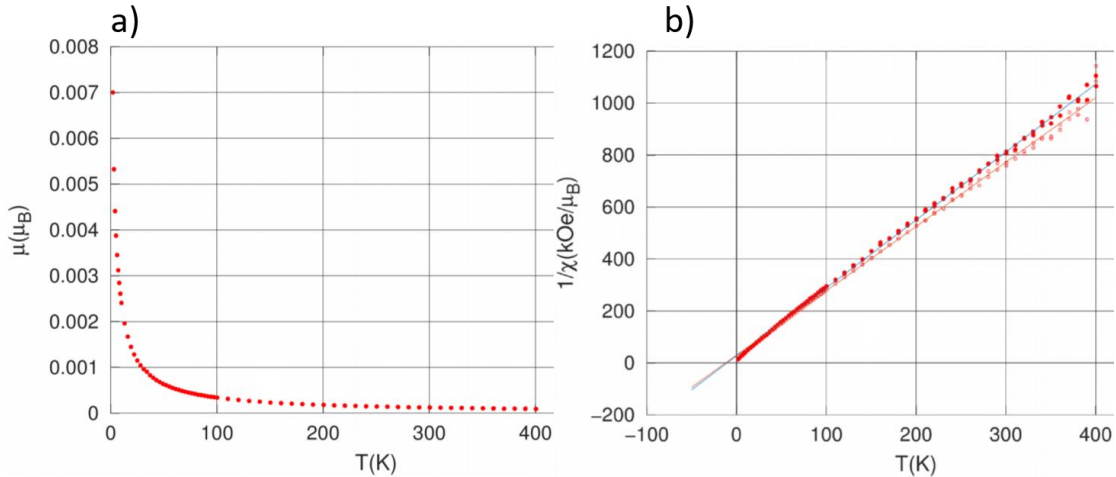


Figure 30. a) Magnetization versus temperature of a powder of MnPc molecules (expressed in units of Bohr magneton). b) Inverse susceptibility $1/\chi = 1/(M/B)$ as a function of temperature extracted from panel a). It is in good agreement with a simple Curie-Weiss law. These measurements were carried out and analyzed under the guidance of David Hrabovsky from the low-temperature measurements characterization platform of Sorbonne Université.

In fact it appears to be not so simple to link these spin values to the description of the groundstate of the free MnPc. As seen from the schematic representing the energy of the *d*-levels of the Mn ion in the MnPc molecule, the ligand-field has a D_{4h} symmetry which splits the Mn *d*-orbitals into three singlets (d_{xy} ; d_{z^2} ; $d_{x^2-y^2}$) and one doubly degenerate level (d_{xz}/d_{yz}). In the description of the occupied energy levels of the free MnPc

molecule the high-lying $d_{x^2-y^2}$ levels can be forgotten. The difficulty in finding the proper theoretical description of the ground state of the free molecule lies in the fact that there exists a strong hybridization of the d_{xz}/d_{yz} orbitals with the ligands π orbitals both belonging to the E_g irreducible representation in the D_{4h} symmetry. A partial agreement exists to describe the groundstate as [Minamitani2015]:

$$d_{xy} \uparrow; d_{z^2} \uparrow; d_{xz}/d_{yz} (E_g I) \uparrow\uparrow; d_{xz}/d_{yz} (E_g III) \downarrow \quad (55)$$

This indeed corresponds to a $S = 3/2$ and $L = 0$ groundstate but with additional subtleties. A ferromagnetic coupling is believed to exist between the $d_{xy}; d_{z^2}; d_{xz}/d_{yz} (E_g I)$ orbitals while an antiferromagnetic coupling exist between $E_g I$ and $E_g III$ through the $\pi - d$ interaction.

Our first idea was to study the interaction of MnPc molecules with the superconducting Pb/Si(111) monolayer phases that we have studied in the parts **Topic2E-F-G** above, namely the $\sqrt{7} \times \sqrt{3}$ -Pb and SIC-Pb. In the same spirit that the 2D electronic properties of $2H$ -NbSe₂ were an advantage to study the spatial resolution of Yu-Shiba-Rusinov excited states, we expected that the two-dimensionality of these Pb monolayers grown on silicon would also be an advantage to study the interaction of single MnPc molecules with the superconducting monolayers. To this end, we deposited a small coverage of MnPc molecules (much below one monolayer) on the $\sqrt{7} \times \sqrt{3}$ -Pb and SIC-Pb phases kept at room temperature. We have found a completely unexpected result: when deposited on the clean $\sqrt{7} \times \sqrt{3}$ -Pb monolayer, MnPc molecules reconstruct the surface and transforms it into a defected SIC-Pb like phase. On the other hand, when deposited on the clean SIC-Pb phase, MnPc molecules leave the structure of the surface unchanged. These results are presented in figure 31 below, showing both STM images and corresponding electron-diffraction patterns of the various studied phases. Another surprising result was the type of self-organization that is obtained. MnPc molecules usually self-assemble in square arrays, as reported on bulk Pb(111) [Franke2011] and as we could also observe on Pb/Si(111) thin films (see figure 32c). In contrast, MnPc molecules prefer self-organizing in trimers on Pb/Si(111) monolayers (see figure 32a-b). This points out to a very different nature of the MnPc/substrate and MnPc-MnPc interactions between Pb/Si(111) monolayers and thicker Pb films.

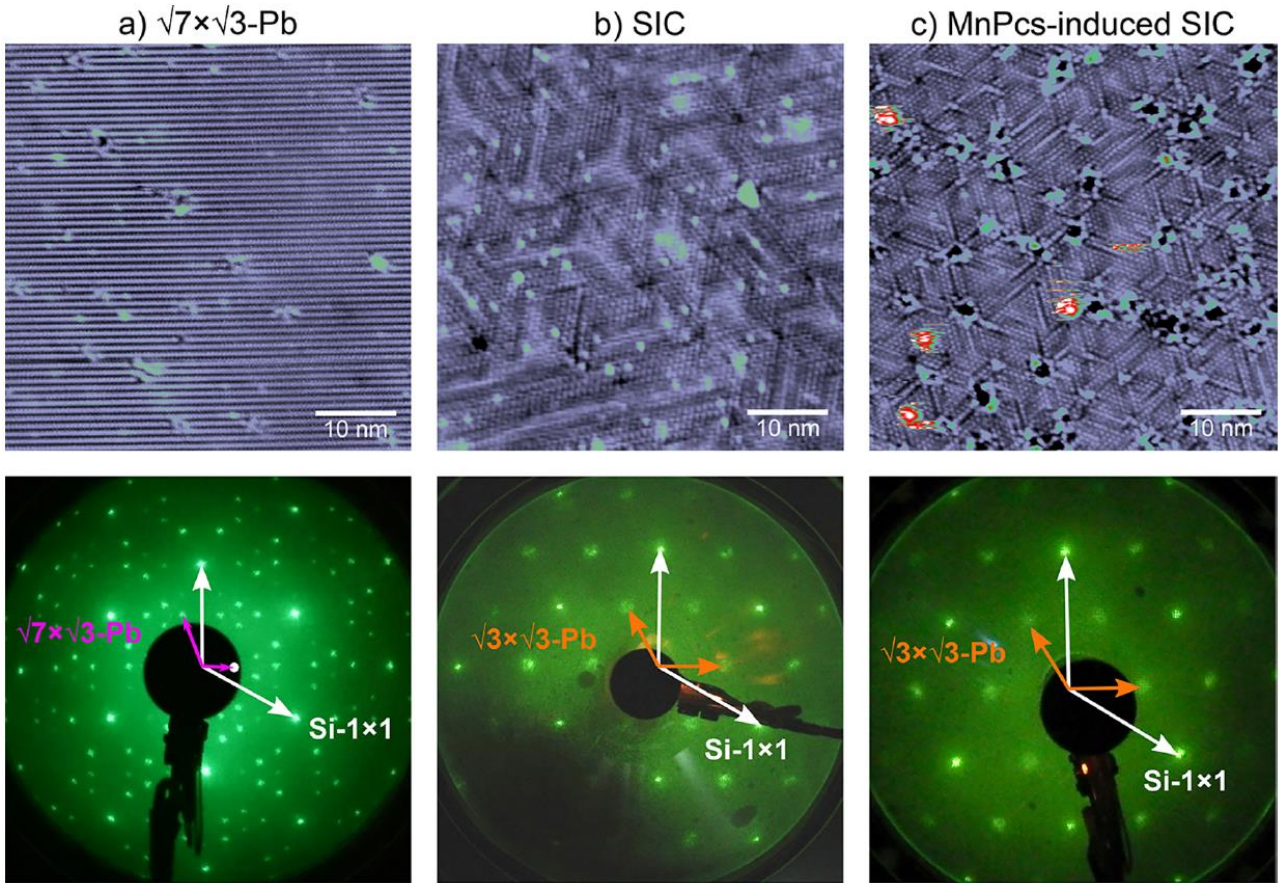


Figure 31. STM images (top row) and corresponding low-energy-electron diffraction (LEED) patterns (bottom row) of the various Pb/Si(111) monolayer phases. a) Clean $\sqrt{7} \times \sqrt{3}$ -Pb phase. b) Clean SIC-Pb phase. c)

low-density of MnPc molecules (0.2 molecules/100 nm²) deposited on the clean $\sqrt{7} \times \sqrt{3}$ -Pb phase: a disordered SIC-Pb like phase is induced. Figure reproduced from [Longo2020].

In order to rationalize these experimental results we set-up a collaboration with Marie-Laure Bocquet from the Chemistry Institute of ENS-Paris and Nicolas Lorente from Donostia International Physics Center in San Sebastian-Spain. They are specialists of the theoretical description by *ab initio* DFT calculations of the adsorption of molecules on surfaces. Nicolas is also a specialist of modelling the interaction between magnetic atoms or molecules and metallic or superconducting substrates. The DFT calculations enable to determine with high precision the total energy of the system under consideration. Nevertheless such numerical technique is limited by the number of atoms it can consider. In our case it was possible to simulate a real system consisting of a single MnPc molecule adsorbed on the $\sqrt{7} \times \sqrt{3}$ -Pb/Si(111) or on the $\sqrt{3} \times \sqrt{3}$ -Pb/Si(111) monolayer (since the SIC-Pb monolayer is an incommensurate phase, its structural and electronic properties are best approximated by the commensurate $\sqrt{3} \times \sqrt{3}$ -Pb/Si(111) phase [Ren2016]). The Si substrate can be efficiently modelled by three Si(111) double-layers passivated by hydrogen atoms on the rear side. The outcomes of these DFT calculations are the following. The adsorption energy of a single MnPc molecule is much larger on the Pb monolayers (-2.86 eV on $\sqrt{3} \times \sqrt{3}$ -Pb and -2.74 eV on $\sqrt{7} \times \sqrt{3}$ -Pb) than on bulk Pb substrate (-1.52 eV).

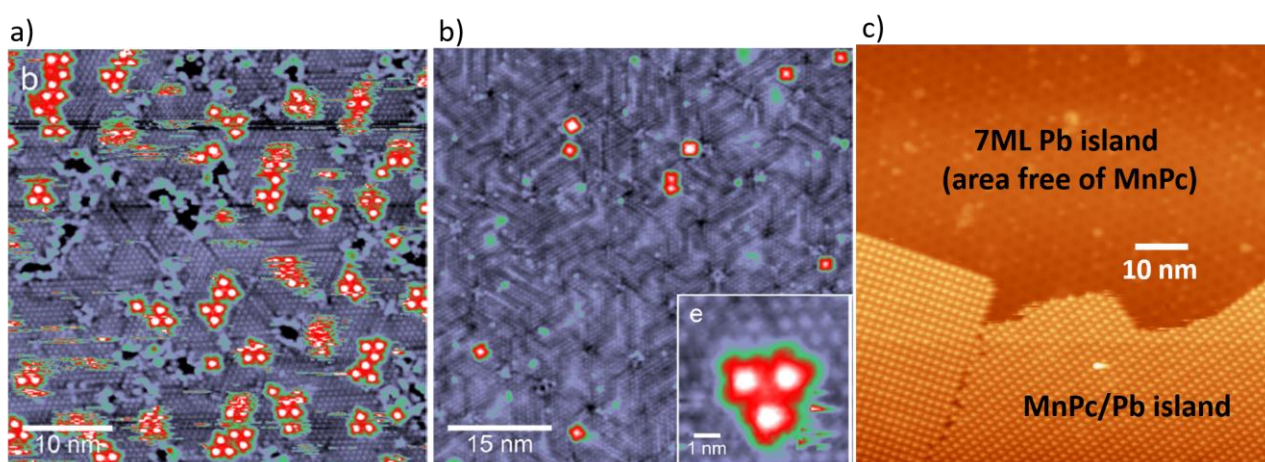


Figure 32. STM topographic images of MnPc molecules deposited on various ultrathin Pb/Si(111) films. a) MnPc molecules deposited on the clean $\sqrt{7} \times \sqrt{3}$ -Pb phase (4.6 molecules/100 nm²) which reconstructs the whole surface in a SIC-Pb like disordered phase. b) MnPc molecules deposited on the clean SIC-Pb phase (1.3 molecules/100 nm²). c) MnPc molecules deposited on a thicker Pb/Si(111) sample containing 7ML high Pb islands (2 molecules/100 nm²). All MnPc clusterize on such islands in square molecular arrays. Figure reproduced from [Longo2020].

This large difference in adsorption energy between the Pb monolayers and bulk Pb is accompanied with a much shorter vertical Mn-Pb atomic distance on the monolayers (2.7 Å and 2.9 Å respectively) than on bulk Pb (3.3 Å) which indicates a stronger local bonding. An important difference lies also in the electronic charge transfer in these various situations, and in the spatial distribution of the charge and spin density. For instance on bulk Pb the charge and spin density are localized on the molecule and do not extend on Pb atoms. In contrast on the Pb monolayers, both densities extend largely on Pb atoms and even below on the first Si double layer for the spin density. Regarding the charge transfer, about 2.3 electrons are transferred from the bulk Pb substrate to the molecule. They are essentially localized on the organic ligands and a small contribution of 0.1 electron sits on the Mn atom. On the Pb monolayers, the charge transfer is in the same direction than on bulk Pb but is smaller: 1.2 electron on $\sqrt{3} \times \sqrt{3}$ -Pb and 0.8 on $\sqrt{7} \times \sqrt{3}$ -Pb.

Our calculations cannot explain quantitatively the origin of the reconstruction because it is beyond what can be achieved by DFT calculations. Nevertheless, our analysis reveals that the reconstruction of the $\sqrt{7} \times \sqrt{3}$ -Pb phase upon MnPc adsorption is a complex process due to several factors:

- i) Larger energy gain on the $\sqrt{3} \times \sqrt{3}$ -Pb.
- ii) Strain effect already present in the clean $\sqrt{7} \times \sqrt{3}$ -Pb phase modified upon molecular adsorption.
- iii) High atomic mobility of the Pb atoms on the Si(111) surface.

Another interesting aspect that our work predicts is that the electronic filling of the d levels should be different between the two Pb monolayers due to the different charge transfer. This should lead to a different magnetic behavior of the single MnPc molecule on both substrates. It is presented in figure 33. On the $\sqrt{7} \times \sqrt{3}$ -Pb/Si(111) surface the predicted simplified spin state seen in panel 33a) is $S = 1$ carried by the singly occupied d_{xy} and d_{z^2} levels. This spin state value is qualitatively similar to the one observed on thicker Pb/Si(111) films or on Pb(111) [Minamitani2015]. In contrast the larger charge transfer from the $\sqrt{3} \times \sqrt{3}$ -Pb/Si(111) surface to the MnPc molecule further reduces the total spin state as seen in panel 33b). The d_{z^2} level becomes doubly occupied. A $S = 1/2$ spin state is then predicted associated to the only d_{xy} singly occupied level. We thus expect an important difference between the magnetic behavior of the MnPc molecule on both Pb/Si(111) monolayers. Since a very small density of molecules is enough to reconstruct the $\sqrt{7} \times \sqrt{3}$ -Pb surface we could measure and test this prediction only on the SIC-Pb ($\sqrt{3} \times \sqrt{3}$ -Pb) phase. It is in principle also possible to do it on the $\sqrt{7} \times \sqrt{3}$ -Pb for very low molecular coverage (1 molecule per 10^4 nm^2) but it becomes hard to find isolated MnPc molecules inside terraces.

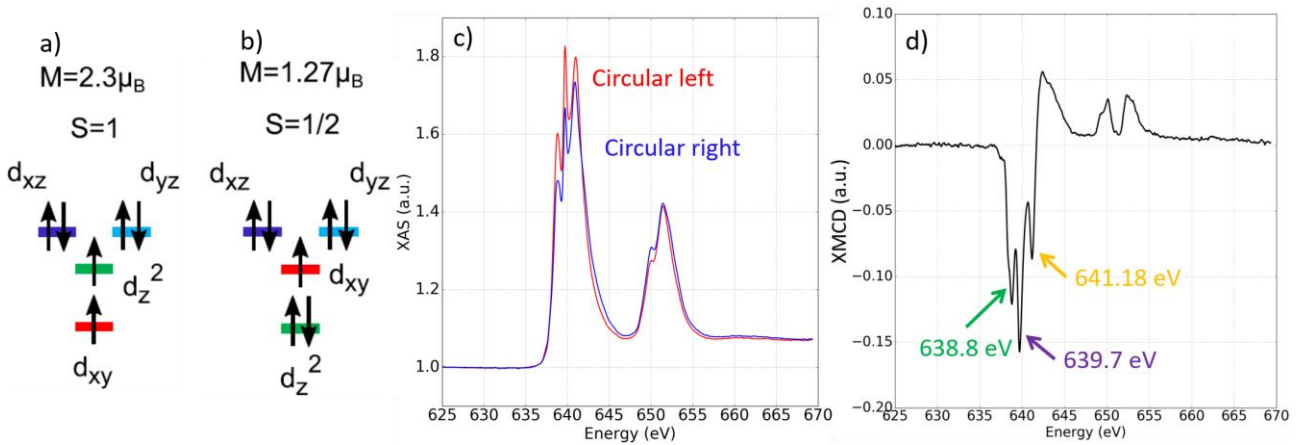


Figure 33. Filling of the effective d -levels of the Mn atom of single MnPc molecules adsorbed on a) $\sqrt{7} \times \sqrt{3}$ -Pb/Si(111) and b) $\sqrt{3} \times \sqrt{3}$ -Pb/Si(111) calculated from *ab initio* DFT calculations. Figure reproduced from [Longo2020]. c) X-ray absorption (XAS) spectra of a MnPc powder deposited on a carbon tape measured at 2K and 6T magnetic field in grazing incidence. d) XMCD spectra corresponding to the difference of the X-ray absorption spectra (XAS) spectra for the circular left and right polarization presented in panel c).

With respect to the situation of a classical large spin value discussed in the previous section **Topic2H** we see that in the case of single MnPc molecules on Pb thin films or monolayers, we are dealing with small spin values $S = 1$ or $S = 1/2$. Thus the quantum treatment of this situation is necessary because the electrons spin of the superconductor can interact and flip the spin of the impurity. The theoretical description of this situation is much more complicated than what we previously discussed as it involves the interplay between (partial) Kondo screening of a localized spin and superconductivity. As the theoretical description of the energy levels of the MnPc molecule itself is not that straightforward, one sees that this is a complicated subject. Nevertheless conclusive theoretical results exist in some model cases [Matsuura1977] but not in the general case. Furthermore, on the experimental side, contradictory results exist about the STS measurements of single MnPc molecules:

- i) Two site-dependent Kondo resonances were initially reported on Pb(111) in [Franke2011,Bauer2013]. Measurements at lower temperature on Pb/Si(111) thin films reported only one Kondo resonance spatially delocalized on the central Mn atom and neighboring pyrrole groups containing N atoms [Minamitani2015]. This main Kondo resonance implies the d_{z^2} orbital, overlapping largely with the Pb substrate. Furthermore the results and modelling suggest that the d_{z^2} orbital is coupled antiferromagnetically to the minority spin E_g III orbital of the ligands on which the Kondo resonance is also measured.
- ii) Several numbers of Yu-Shiba-Rusinov excited states were reported in the superconducting phase [Franke2011,Bauer2013,Hatter2015]. Measurements with the highest resolution and lowest temperature seem to report a multiplet of three pairs of excited states, whose electron-hole amplitude asymmetry strongly depends on the MnPc adsorption site. It is argued that from the analysis of the evolution of this asymmetry in the electron-hole amplitudes with the energies of the multiplet a

quantum transition between two different groundstates can be detected. A Kondo-screened state on one hand ($S = 1/2$ in the groundstate) and an unscreened free-spin state ($S = 1$ in the groundstate) are proposed. From our point-of-view all these measurements suffer from the criticism that we presented above in the last paragraph of **Topic2H**: the precise signs and ratio of the J and K parameters are unknown, preventing the unambiguous determination of the weak or strong coupling regime.

Our preliminary STS measurements on single MnPc molecules deposited at low coverage on the SIC-Pb phase seem to be in agreement with the predictions shown in figure 33b). The large Kondo resonance observed for single MnPc deposited on thicker Pb/Si(111) films [Minamitani2015] and Pb(111) [Franke2011] is not observed in our case, suggesting that indeed the d_{z^2} orbital became doubly occupied. We observe other interesting spectral features in the energy scale associated to the superconducting gap. They need to be confirmed and this will be done soon in spring 2021 (for this reason I preferred not to show these features here!). Our results seem to suggest a weak magnetic exchange interaction between the d_{xy} level and the SIC-Pb monolayer, which seems not to exist or to be very weak on thicker Pb/Si(111) films or bulk Pb(111).

With our former PhD student Danilo Longo, who is now post-doc on the [DEIMOS](#) beamline at the synchrotron Soleil in Saclay since July 2019, I have launched a common research project aiming at determining the atomic magnetic properties of single MnPc molecules adsorbed on various metallic and superconducting substrate, using X-ray magnetic circular dichroism (XMCD) absorption spectroscopy. My main motivation is that this will enable understanding better the STM/STS results by knowing the quantitative internal magnetic degrees of freedom, their possible mutual coupling, possible magnetic crystalline anisotropy etc. I am not at all a specialist yet of this technique that is new to me. To this end, we brought our modular UHV chamber dedicated to the deposition of MnPc molecules and installed it on the DEIMOS endstation (see figure 3 in the beginning of the HDR thesis).

XMCD is a very powerful technique compatible with ultrahigh vacuum environment which enables probing the magnetization associated to a low coverage of magnetic molecules deposited on a conducting substrate. This technique probes a signal proportional to the X-ray absorption by the sample in the energy range [300-1500] eV well-suited to magnetic d -level atoms. An example is shown in figure 33 presenting in panel c) the X-ray absorption spectra (XAS) at the Mn L_3 and L_2 edge for a test sample consisting of a powder of MnPc molecules deposited on a carbon tape. The two families of peaks seen around 640 eV (L_3) and 652 eV (L_2) correspond to electronic transitions between $2p_{3/2}$ and $2p_{1/2}$ occupied core levels of the Mn atoms and unoccupied d -levels close to the Fermi level, induced by X-ray absorption. Sharp peaks are observed due the high unoccupied DOS of the d -levels. It is seen that a strong difference exists between the XAS spectra obtained for circularly polarized left and right light when the electronic orbitals are polarized under a 6T magnetic field aligned with the direction of incidence of the light (here in grazing incidence). When such a difference exists, it is due to the existence of magnetic states among the d -levels. The corresponding magnetic signal, called X-ray magnetic circular dichroism (XMCD) is obtained by taking the difference of the XAS signals for the two opposite circular polarizations. The result is plotted in panel 33d). Three sharp negative peaks are seen in the L_3 group whose energies are indicated between 638 eV and 642 eV. The assignment of a given peak in the XMCD signal to particular transitions between the d -levels is not straightforward and most often several levels can contribute simultaneously. This needs to be calculated precisely from DFT ab initio calculations.

An important physical quantity that can be measured using the XMCD signal is the magnetization associated to the different peaks such as the ones observed at 638.8 eV; 639.7 and 641.2 eV in panel 33d). An example is shown in figure 34, for the MnPc powder sample. An hysteresis cycle of the XMCD signal at the energy of each peak was measured at 2 K and at 20 K. Only one cycle for the lowest energy peak is shown here, the other two behaving similarly. A linear dependence with magnetic field is observed, showing a paramagnetic behavior of the magnetization associated to these 3 peaks. This is in agreement with what is expected for a powder sample where the molecules are disordered in all directions in space. It also agrees with the initial magnetic characterization presented in figure 30 above. Between 20 K and 2 K, the same general dependence is observed but small features appear at 2 K forming reproducible kinds of oscillations. These are probably due to intermolecular interactions existing in the powder. Finally, as the powder presents all spatial orientations of the MnPc molecules we observed similar results in grazing and normal incidence.

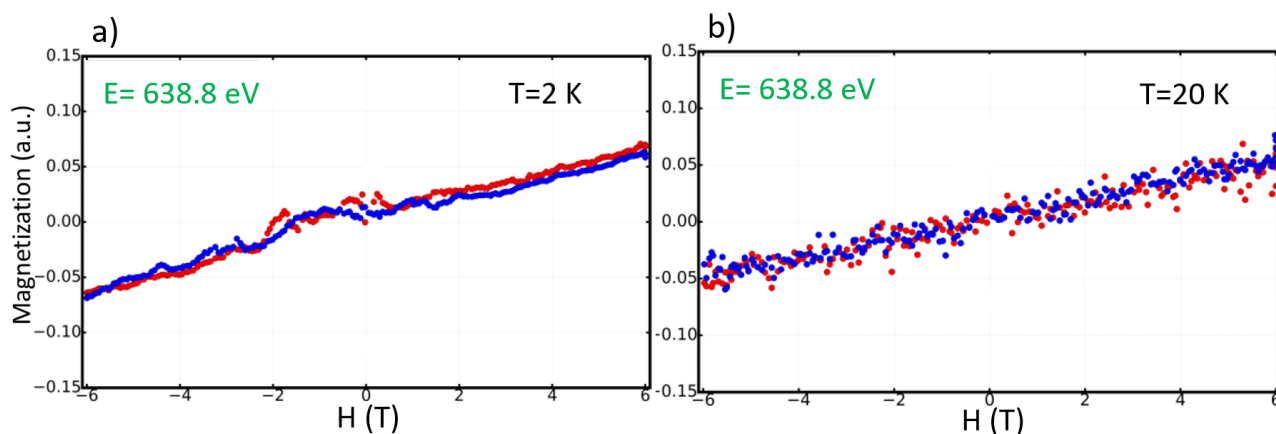


Figure 34. Grazing incidence magnetization curves of a MnPc powder deposited on a carbon tape sample. a) Hysteresis cycle between -6 T and 6 T of the XMCD signal measured at 2 K for the peak located at $E = 638.8$ eV (see panel 33d). Rising field corresponds to red dots and decreasing field to blue dots. b) Same quantity as in a) but measured at 20 K.

In order to study the interaction of MnPc molecules with superconducting and metallic substrates we have performed similar XMCD experiments on Pb(111), $2H$ -NbSe₂ and HOPG. We first prepared in-situ in UHV these substrates to obtain a clean surface, either by cleavage, heating or sputtering/annealing cycles. Then we were able to deposit much less than 1 monolayer of MnPc molecules on these various substrates. We are still in the process of analyzing in details all the results but I would like to present here some of the main outcomes of our measurements. The first important difference with respect to the powder sample is that since MnPc molecules lie flat on all the studied surfaces (in the submonolayer coverage range), different XAS and XMCD signal are observed between grazing and normal incidence. We present an example of such XMCD spectra on $2H$ -NbSe₂ sample in figure 35. By comparing them with the powder spectrum presented in panel 34d), one notices clear differences.

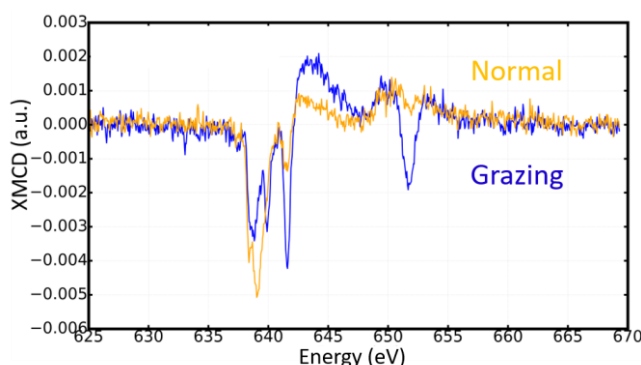


Figure 35. XMCD spectra for ~ 0.4 monolayer of MnPc molecules deposited at room temperature on in-situ cleaved $2H$ -NbSe₂. The spectra are measured at $H=6$ T and $T=2$ K under normal and grazing X-ray incidence.

The fact that the XMCD signal varies strongly with the light angle of incidence on the surface is due to the fact that MnPc molecules are lying flat on the surface. Thus, changing the angle of incidence enables being sensitive to different absorption transitions allowed by the orbital symmetry and its coupling to the electric field by a dipolar term. Since we know that the Mn d -levels consist in d_{xy} ; d_{z2} ; d_{xz}/d_{yz} orbitals hybridized with the in-plane ligands $E_g I$ and $E_g III$ orbitals, one sees that in normal incidence one will probe more the transitions associated to the orbitals having a large in-plane component, i.e. d_{xy} , d_{xz}/d_{yz} $E_g I$ and $E_g III$. In contrast, grazing incidence should be more sensitive to transitions associated with the orbitals possessing an out-of-plane component, i.e. d_{z2} and d_{xz}/d_{yz} . Furthermore, measuring the hysteresis cycles of the XMCD signal for the set of peaks appearing as previously around 640 eV, revealed a striking difference between normal and grazing incidence. This is illustrated in figure 36 below.

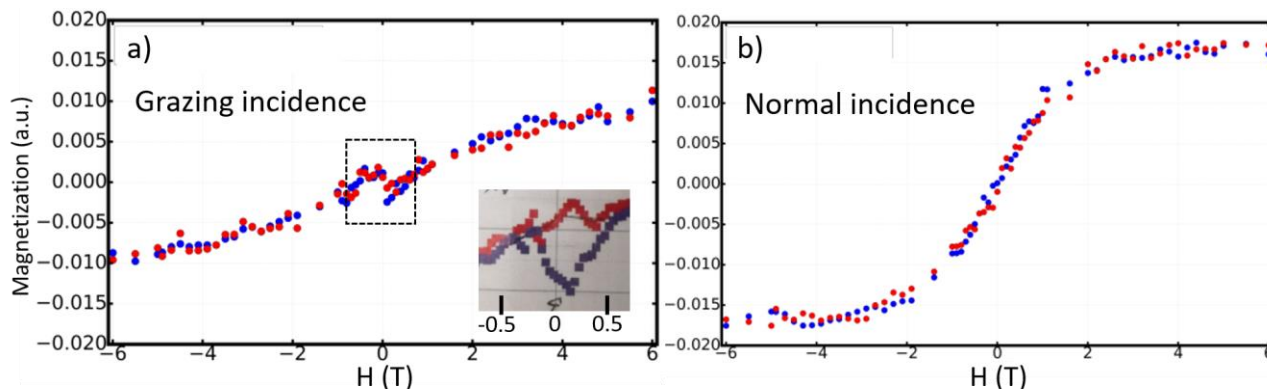


Figure 36. Magnetization curves for ~ 0.4 monolayer of MnPc molecules deposited at room temperature on *in-situ* cleaved $2H\text{-NbSe}_2$. a) Hysteresis cycle between -6 T and 6 T of the XMCD signal measured at 2 K for the peak located at $E = 641.5$ eV (see panel 35) under grazing incidence. Rising field corresponds to red dots and decreasing field to blue dots. b) Same quantity as in a) but measured under normal incidence.

One sees that under normal incidence, the magnetization presents a dependence very different from the linear one seen for the powder in panels 34a-b). In contrast the magnetization saturates for a magnetic field around 3 T. Under grazing incidence, the magnetization does not saturate at the maximum field (6 T) and continues to rise slowly, with a kind of linear dependence, as observed in the powder case. One deduces from this that the easy magnetization axis is the out-of-plane direction, revealing a strong magnetic anisotropy. Another striking difference observed in grazing incidence with respect to the normal incidence behavior is the opening of the curves around 0 T in the interval $[-0.5$ T; $+0.5$ T] indicated by the dashed rectangle. The magnetization becomes negative for positive field below about 0.5 T and vice-versa for negative field. A refined measurement at lower fields with higher resolution enables to see better what happens and is presented in the inset of panel 36a). It suggests that an hysteresis cycle exists around 0 T. We could measure the temperature evolution of this curve and confirm this phenomenon. We are currently trying to understand these signatures. I believe that they are linked to the intramolecular spin-splitting existing between the orbitals of the majority spins d_{z^2} d_{xy} $E_g I$ being all fully occupied (and thus polarized by the in-plane magnetic field applied in panel 36a) and their minority spin counterpart that together with the one of the $E_g III$ orbital are being all empty. Furthermore, the existence of an internal ferromagnetic coupling between the $E_g I$ orbital and the d_{z^2} d_{xy} orbitals accompanied by an antiferromagnetic interaction between $E_g I$ and $E_g III$ orbitals [Minamitani2015], contribute to stabilize in the single molecule adsorbed on a surface a minority spin component anti-ferromagnetically coupled to the applied magnetic field, presumably associated to the large DOS of the unoccupied $E_g III$ orbital.

This work is still in progress regarding the analysis and further modelling by advanced DFT calculations. In addition to the PhD thesis of Danilo Longo, a first article was published last year about these results: D. Longo et al. [J. Phys. Chem. C 124, 36, 19829 \(2020\)](#). We also plan to investigate by XMCD measurements the very interesting case of MnPc deposited on the SIC-Pb/Si(111) monolayer that we studied by STM/STS and for which DFT predictions already exist for the electronic structure. This whole study will enable shedding new light and understanding in more details the magnetic interaction between single MnPc molecules and metallic or superconducting substrates. This should enable us *in fine* to be able to make more definite statements regarding the possible competition between Kondo physics and superconductivity in the case of MnPc molecules adsorbed on Pb substrates, and to determine the proper interpretation of the Yu-Shiba-Rusinov excited states appearing in the superconducting state.

During the PhD thesis of Danilo Longo we also studied by STM/STS the coupling of single/arrays of MnPc molecules with Pb/Si(111) thin films of having a height of three atomic monolayers. This kind of ultrathin film appear somehow in between the case of thicker Pb/Si(111) films studied previously [Fu2007,Minamitani2015] and our own study on the Pb/Si(111) monolayer. I prefer not to present these results in details here but I will flash them in the next section **Topic3** related to topological superconductivity.

Topic 3: Topological superconductivity

The development of this topic of topological superconductivity was put forward by my colleague Tristan Cren

during the PhD thesis of Gerbold M  nard. I strongly collaborated with Tristan on this matter, since we quickly realized in 2013 that the Pb/Si(111) superconducting monolayers, that I started to investigate in 2012 (see the results in **Topic2E-F-G**), possessed all ingredients sufficient to induce 2D topological superconductivity. In our case these ingredients are three, as we will see in details below: 2D superconductivity with a conventional electron-phonon pairing mechanism, strong Rashba spin-orbit coupling induced by the presence of a Pb-vacuum interface, and local magnetism introduced by ferromagnetic CoSi subsurface clusters. At the international level this research activity is very recent and started experimentally in 2012 from transport experiments in superconducting nanowires contacted to superconducting electrodes. One of the goal of this field aims at proving experimentally that the concepts put forward for topological insulators about 10 years before also apply to superconductors. This is possible since superconductors as insulators possess a one-particle gap in their excitation spectrum. There are nevertheless several important new developments that are specific to topological superconductivity, as we will see. Here are our main achievements that I will develop below in a dedicated part:

- i) Evidence for 2D topological superconductivity
- ii) Evidence for Pairs of spatially separated Majorana excitations in 2D topological superconductors

I also strongly contributed to another approach to investigate topological superconductivity using the magnetic molecules (MnPc) presented in **Topic2I** previously. This very promising approach led to very interesting results that we need to confirm. For this reason and also in order to keep this HDR short I will not present these results here. They are nevertheless detailed in the PhD thesis of Danilo Longo.

During this work I co-supervised the **PhD work of Gerbold M  nard** (during 3 years), the **master 2 of Mathieu Leclerc** (during 4 months), of **Rapha  l Leriche** (during 4 months) and the **PhD work of Danilo Longo** (during 4 years). My supervision here consisted mostly in taking care of almost all the experimental lab work. I learned Python programming together with Gerbold M  nard, we analyzed the STS spectroscopic conductance maps and introduced Rapha  l Leriche and Danilo Longo to it. This research activity is still ongoing and has some overlap with the **Topic2** above with respect to the interaction and coupling of magnetic atoms or molecules with superconductors. This work was supported by the finished ANR Mistral (2014-2018, ANR-14-CE32-0021), coordinated by Pascal Simon from LPS-Orsay, and to which Tristan and myself were partner. It gave rise to the following publications where the people I co-supervised are in bold:

- a) *Two-dimensional topological superconductivity in Pb/Co/Si(111)*
G.C. M  nard, S. Guissart, **C. Brun**, M. Trif, F. Debontridder, **R. Leriche**, D. Demaille, D. Roditchev, P. Simon, T. Cren, Nature Communications 8, 2040 (2017)
- b) *Isolated pairs of Majorana zero modes in a disordered superconducting lead monolayer*
G. M  nard, A. Mesaros, **C. Brun**, F. Debontridder, D. Roditchev, P. Simon, T. Cren Nature Communications 10, 2587 (2019)
- c) The PhD thesis of Gerbold M  nard entitled “*2D superconductors perturbed by local magnetism: from Yu-Shiba-Rusinov bound states to Majorana quasiparticles*” was defended in public the 16th of September 2016. This work gave rise to 5 publications until now. Gerbold M  nard is now post-doc at CEA Saclay in the quantronics group. The official PhD advisor was Dimitri Roditchev. The other co-supervisor was Tristan Cren. The two main co-supervisors were Tristan and myself, and it was about half-half concerning the allocation of supervision time.
- d) The PhD thesis of Danilo Longo entitled “*Engineering topological states in arrays of magnetic molecules in interaction with a 2D superconductor*” was defended in public the 13th of May 2019. Danilo Longo is now post-doc on the DEIMOS beamline at the synchrotron Soleil. The official PhD advisors were Tristan Cren and Nadine Witkowski. In terms of the allocation of supervision time, I was the main co-supervisor of the PhD work of Danilo Longo.

A) General background

Brief account about topology in band theory in solid-state physics

I will give here very basic elements to introduce topology in band theory of solids. This topic has in principle a complicated mathematical formulation linked to the way the Bloch wavefunctions of electrons in solids should be properly described (through vector bundles etc). Since I do not master these mathematical tools, I will explain in a simpler way what I understood about topology in band theory of solids. The following notes are based on a course by Jean-Noël Fuchs on topological insulators given in 2017 at our physics department. I will discuss here only the case of non-interacting electrons with negligible disorder. I give here only a general introduction and further theoretical considerations applicable to our investigated systems will be given in subsequent sections.

The Bloch states are indexed by an integer n and a crystal momentum \mathbf{k} and are written $|\psi_{n\mathbf{k}}\rangle = e^{i\mathbf{k}\cdot\mathbf{r}} |u_n(\mathbf{k})\rangle$. They are eigenstates of the Hamiltonian H of the solid with eigenvalues $E_n(\mathbf{k})$. The wavefunction associated to $|u_n(\mathbf{k})\rangle$ is periodic on the Bravais lattice of the solid and the $|u_n(\mathbf{k})\rangle$ can be taken such as $\| |u_n(\mathbf{k})\rangle \| = 1$. From the Hamiltonian H of a solid one defines the Bloch Hamiltonian $H(\mathbf{k})$ by $H(\mathbf{k}) = e^{-i\mathbf{k}\cdot\mathbf{r}} H e^{i\mathbf{k}\cdot\mathbf{r}}$. This leads to $H(\mathbf{k})|u_n(\mathbf{k})\rangle = E_n(\mathbf{k})|u_n(\mathbf{k})\rangle$. Then a central concept is to look how a given eigenstate $|u_n(\mathbf{k})\rangle$ will evolve under a continuous displacement of \mathbf{k} through a path. This enables introducing a central concept in this field, the geometrical Berry phase. A simple way to see it is to assume an adiabatic evolution $\mathbf{k}(t)$ of the crystal momentum \mathbf{k} with time t , assuming that the system is in a state $|\psi(t)\rangle \propto |u_n(\mathbf{k}(t))\rangle$ of the band n that does not cross with other bands of index $n' \neq n$. Then we can write $|\psi(t)\rangle = e^{i\gamma(t)} |u_n(\mathbf{k}(t))\rangle$. By writing the time evolution of the state $|\psi(t)\rangle$ with the Schrödinger equation and integrating it with respect to time one can find the following expression for $\gamma(t)$:

$$\gamma(t) = - \int_0^t E_n(\mathbf{k}(t)) dt + \int_0^t \frac{d\mathbf{k}}{dt} \cdot \langle u_n(\mathbf{k}) | i\hbar \vec{\nabla}_{\mathbf{k}} u_n(\mathbf{k}) \rangle \quad (55 - 2)$$

The first term of (55 - 2) is the standard dynamical phase. The second term is a geometrical term, called geometrical phase. It can be also written as:

$$\int_0^t \frac{d\mathbf{k}}{dt} \cdot \langle u_n(\mathbf{k}) | i\hbar \vec{\nabla}_{\mathbf{k}} u_n(\mathbf{k}) \rangle = \int_{\mathcal{C}} d\mathbf{k} \cdot \langle u_n(\mathbf{k}) | i\hbar \vec{\nabla}_{\mathbf{k}} u_n(\mathbf{k}) \rangle = \int_{\mathcal{C}} d\mathbf{k} \cdot \vec{\mathcal{A}}_n(\mathbf{k}) \quad (55 - 3)$$

The term $\vec{\mathcal{A}}_n(\mathbf{k}) = \langle u_n(\mathbf{k}) | i\hbar \vec{\nabla}_{\mathbf{k}} u_n(\mathbf{k}) \rangle$ is called the Berry connection and is analogous to the potential vector $\vec{\mathcal{A}}$ associated to a magnetic field $\vec{\mathbf{B}} = \vec{\nabla} \times \vec{\mathcal{A}}$. Indeed we have seen in the **Topic1E** that in presence of a magnetic field the potential vector $\vec{\mathcal{A}}$ couples geometrically to the phase of the electrons or quasiparticles wavefunctions leading to interference effects such as in the well-known Aharonov-Bohm effect. Here, the expression (55 - 3) shows that a geometrical phase is acquired by the electron wavefunction when the electron evolves in time with $\mathbf{k}(t)$. It acts as if an effective potential vector was present which is given by the Berry connection $\vec{\mathcal{A}}_n(\mathbf{k}) = \langle u_n(\mathbf{k}) | i\hbar \vec{\nabla}_{\mathbf{k}} u_n(\mathbf{k}) \rangle$. The corresponding effective magnetic field is called the Berry curvature and is naturally given by $\vec{\Omega}_n(\mathbf{k}) = \vec{\nabla}_{\mathbf{k}} \times \vec{\mathcal{A}}_n(\mathbf{k})$. Importantly when a change of gauge occurs for $|u_n(\mathbf{k})\rangle$ it corresponds to a multiplication by a complex phase belonging to $\mathbb{U}(1)$: it takes the form $|\tilde{u}_n(\mathbf{k})\rangle = e^{i\Phi(\mathbf{k})} |u_n(\mathbf{k})\rangle$. Then $\vec{\mathcal{A}}_n(\mathbf{k}) = \vec{\mathcal{A}}_n(\mathbf{k}) - \vec{\nabla}_{\mathbf{k}}\Phi$ which implies that $\vec{\Omega}_n(\mathbf{k}) = \vec{\Omega}_n(\mathbf{k})$ showing that the Berry curvature, as the magnetic field, is a gauge invariant quantity. Recently this geometrical phase or Berry phase could be measured directly in graphene in an STM experiment probing electronic standing waves scattered by point defects due to single hydrogen atoms bound to carbon ones [Dutreix2019]. In this case the electron scattered by a point-defect takes phase-coherent paths in real-space, making the electron interfere with itself, as in the Aharonov-Bohm experiment, and making it feel the Berry phase.

From the relation (55 - 3) an important gauge invariant quantity can be defined that is quantized and characterizes whether or not particular bands possess a non-trivial topology: the Chern number. It corresponds to the following expression for the band n :

$$C_1^{(n)} = \frac{1}{2\pi} \iint_{\text{First Brillouin Zone}} d^2\vec{k} \cdot \vec{\Omega}_n(\mathbf{k}) \quad (56 - 4)$$

In the expression (56 – 4) the flux of the Berry curvature is taken over the whole first Brillouin zone which includes all physically different \mathbf{k} states. The Chern number is quantized as an integer and $C_1^{(n)} \in \mathbb{Z}$. Thus when $C_1^{(n)} = 0$ the band n has a trivial topology and when $C_1^{(n)} \neq 0$ it has a non-trivial topology. Then the whole bandstructure of the material can be characterized by a single Chern number, called the first Chern number C_1 . It is given by the sum of all Chern numbers for each band n for all occupied bands:

$$C_1 = \sum_{n < n_F} C_1^{(n)} \quad (56 - 5)$$

C_1 is called a topological invariant characterizing the occupied bands of the material. The general classification of topological insulators shows that various topological invariants are obtained depending on the dimension of the system and on which symmetry is preserved or broken [Qi2011]. For instance for 2D and 3D materials when time-reversal symmetry is preserved the topological invariant C_{FK} named after Fu and Kane's work is such that $C_{FK} \in \mathbb{Z}_2$ meaning that is equal to 0 or 1. This situation corresponds to the one of topological insulators. In this case there appear symmetry-protected helical edge states dispersing in the bulk gap that counter propagate with opposite spin polarization. This is a bulk-edge correspondence: if $C_{FK} = 1$ then there is one protected pair of helical modes. When time-reversal symmetry is broken $C_1 \in \mathbb{Z}$ but a strong topological invariant exists only in 2D. Interestingly a bulk-edge correspondence exists for the non-trivial topological states verifying $C_1 \neq 0$: in this case the number of chiral edge states is exactly given by C_1 as in the case of the integer quantum Hall effect.

This theory developed for Hamiltonians describing solids can be expanded to superconductors using their Bogoliubov-de Gennes Hamiltonian, since superconductors naturally possess a gapped quasiparticle spectrum. An important difference is then that the space in which the analysis is performed is not anymore the one of the Bloch states as exposed above. For a superconductor, the general natural basis becomes what is called a Nambu spinor, that can be written $\psi_k^\dagger = (c_{k\uparrow}^\dagger, c_{k\downarrow}^\dagger, c_{-k\downarrow}, c_{-k\uparrow})$. It can be written differently depending on the convention that is used but the important thing is that it treats simultaneously electron and hole excitations of up and down spins. A very important difference with the situation of topological insulators is that superconductors naturally possess a "built-in" particle-hole symmetry which can take different forms depending on the type of pairing. The classification of superconductors according to their possible symmetries and dimensions lead to multiple classes of BdG Hamiltonians characterized by a topological invariant, as it was done for topological insulators. In particular in 1, 2 and 3 dimensions a \mathbb{Z}_2 topological invariant also exists for time-reversal symmetric superconductors. In this case a topological regime also exists and it is associated with helical edge states located at the boundary of the superconductor. When time-reversal symmetry is broken, topological regimes with a \mathbb{Z} invariant exist exhibiting chiral edge states located at the sample edge. A bulk-edge correspondence therefore also exists for topological superconductors as for topological insulators.

Due to the natural particle-hole mixing of the superconductor elementary excitations (see the relations (3) and (3bis) in the introductory part), these states can present under certain conditions the property of being their own antiparticles. When such a fermion excitation verifies this condition, i.e. $\gamma_i^\dagger = \gamma_i$, it is named Majorana excitation. This can occur for instance exactly at zero energy in a 1D topological superconductor where a pair of Majorana fermions is localized at the edge of the material as in the Kitaev chain (see for instance [Bernevig2013]). It can be generally shown that a spin 1/2 fermion, such as an electron associated to the creation operator c_j^\dagger , can be decomposed in a Majorana pair consisting of two distinct Majorana fermions labelled A and B through the relations:

$$\begin{aligned} \gamma_j^A &= c_j + c_j^\dagger \\ \gamma_j^B &= i(c_j - c_j^\dagger) \end{aligned}$$

In 2D such excitations are expected to present an exchange statistics different from the one of usual fermions (for usual fermions one gets a minus sign in the total wavefunction upon the exchange of two particles), which could lead to interesting new quantum effects due to the topological protection of such Majorana fermions. The necessary step but difficult to achieve, to reveal these Majorana fermions, is to spatially separate the A and B partner. A well-known example when this happens is the Kitaev chain where the A and B partner sit at the two end of the chain whatever its length. The possible existence of such excitations was predicted about one hundred years ago in theoretical physics. Until now their observation is still debated and it has also not been clearly established in other fields of physics like particle physics where it is also discussed in the context

of neutrinos. Thus condensed matter physics appears as an interesting playground to study this type of fundamental physics, in the context of topological superconductivity.

Searching for topological superconductivity in experimental systems became a hot topic in the past ten years. Furnishing clear-cut experimental results appeared more difficult than for topological insulators. This is partly due to the fact that superconductivity is a low-temperature phenomenon, not easily accessible to ARPES experiment for materials using conventional superconductors, as it was the case for 3D topological insulators possessing a quasi-2D crystal structure. Nevertheless, progress was made in this field using various approaches, techniques and experimental systems. I don't aim here at furnishing a state-of-the-art status of the results presenting all possible manifestations of topological superconductivity. I would like however to say a few words about 1D and 2D experiments. From our brief account here, it is clear that fingerprints of topological superconductors are edge states living in the superconducting gap of these materials. Several groups tried to provide evidence for topological superconductivity in 1D materials using semiconducting nanowires connected to superconducting electrodes using transport experiments [Mourik2012]. Another approach was to use magnetic chains of atoms on a superconducting surface [Nadj-Perge2014]. I don't refer here to all subsequent reports following these approaches and trying to improve on them. However these attempts all suffer from a strong common weakness: in 1D systems the edges are 0D, i.e. zero-dimensional, so that evidencing topological superconductivity only from the spectroscopy of edge states furnish only a weak signature: the one of zero-energy states. As is well-known zero-energy states, or close to zero energy states, can have many different origins. A common origin for zero-energy states is the usual Yu-Shiba-Rusinov states induced by magnetic atoms in superconductors (see **Topic2H**) or usual Andreev states in clean-limit superconducting proximity effect structures, or even the Kondo effect in a quantum dot context. Until now none experimental report could unambiguously demonstrate that the probed zero-energy signatures are indeed related to topological properties. For instance, in the case of most advanced experiments using semiconducting nanowires covered by epitaxial superconducting electrodes, theoretical modelling supports trivial induced superconductivity [Reeg2018]. In the case of atomically controlled Fe chains forming a spiral magnetic chain on a Re(0001) substrate [Kim2018] or Fe self-organized atoms on Pb(110) [Nadj-Perge2014], both experiments do not present the expected robustness of the zero-energy states upon disordering the end of the atomic chain: in contrast the edge states disappear upon disordering the end of the chain. With my colleague Tristan Cren, we early realized this "intrinsic" weakness of 1D systems and decided to go for 2D systems. In this case, the situation is much more favorable because edge states become 1D instead of 0D: they are thus spatially extended around the 2D domain and disperse in energy inside the whole superconducting gap instead of showing only zero-energy signatures. This actually furnishes much stronger signatures to my opinion than in the 1D geometry.

Rashba spin-orbit coupling in a 2D electron gas

In topological insulators and superconductors a crucial role is played by the spin-orbit coupling. This is a relativistic effect that was theoretically introduced by Dirac when trying to generalize the Schrödinger equation for a free electron in order to conform to special relativity. From this more general formulation, a spin-orbit coupling Hamiltonian term naturally appears when developing the Dirac equation to the first-order in $(E - V)/mc^2$ where $V(\vec{r})$ is an external potential term felt by the electron. This leads to a term H_{SOC} :

$$H_{SOC} = \frac{\hbar}{(2mc)^2} \vec{\sigma} \cdot (\vec{\nabla}V \times \vec{p}) \quad (56)$$

Where $\vec{\sigma} = (\sigma_x, \sigma_y, \sigma_z)$ are Pauli matrices. The primary effect of such a term is to couple the orbital motion of the electron to its spin. A classical vision of this effect is that the movement of the electron in the electric field corresponding to $-\vec{\nabla}V$ generates an effective magnetic field that couples to the electron's spin. In isolated atoms the term $\vec{\nabla}V$ is produced by the nucleus and gives rise to a term directed radially from the nucleus. In solids, various situations can occur taking into account the various symmetries which characterize the solid and its interfaces.

In the situation we are interested in, using Pb/Si(111) superconducting monolayers, the spin-orbit coupling term is called Rashba spin-orbit coupling. This case has been worked out by Bychkov and Rashba [Bychkov1984]. This situation is generic to surfaces of solids (and also sometimes to material interfaces) and corresponds to the fact that the inversion symmetry is broken between the bulk of the solid and the vacuum. Let us denote z the direction along which this symmetry is broken, z being thus oriented perpendicular to the

solid's surface along \vec{u}_z . In this case, the electric field will be strongest along this direction at the atomic vicinity of the surface. If we assume that our solid is two-dimensional and hosts a two-dimensional free electron gas, the term H_{SOC} can be recast under the following expression:

$$H_{SOC}^{Rashba} = \alpha(\vec{k} \times \vec{\sigma}) \cdot \vec{u}_z = \alpha(k_x \sigma_y - k_y \sigma_x) = \vec{\gamma}(\vec{k}) \cdot \vec{\sigma} \quad (56bis)$$

This term does not commute with S_x, S_y or S_z the spin components of the electron, which are thus not conserved anymore. One sees that the term (56bis) will energetically favors an in-plane spin orientation perpendicular to $\vec{k} = (k_x, k_y)$. A consequence is that in presence of strong spin-orbit coupling the spin is not free to rotate anymore, but is locked to the electron's momentum \vec{k} . The eigenenergies of the 2D free electron Hamiltonian including a Rashba spin-orbit coupling term are then:

$$E_\lambda(\vec{k}) = \frac{\hbar^2 k^2}{2m} + \lambda \alpha k \quad (57)$$

Here $\lambda = \pm 1$ is a quantum number corresponding to a chirality index characterizing the eigenstates and $k = |\vec{k}|$. The 2D parabolic dispersion is modified in a way presented in figure 37. $E_+(\vec{k})$ is shown in red while $E_-(\vec{k})$ is in blue in panel 37a. A cut of $E_\lambda(\vec{k})$ by a vertical plane passing through $\vec{k} = (0,0)$ is shown in panel 37b along an arbitrary direction $\vec{k} = k_\theta(\cos\theta, \sin\theta)$. It is seen in panel 37c that the constant energy surfaces are circular and the conserved spin projection locally orthogonal to \vec{k} is represented by arrows.

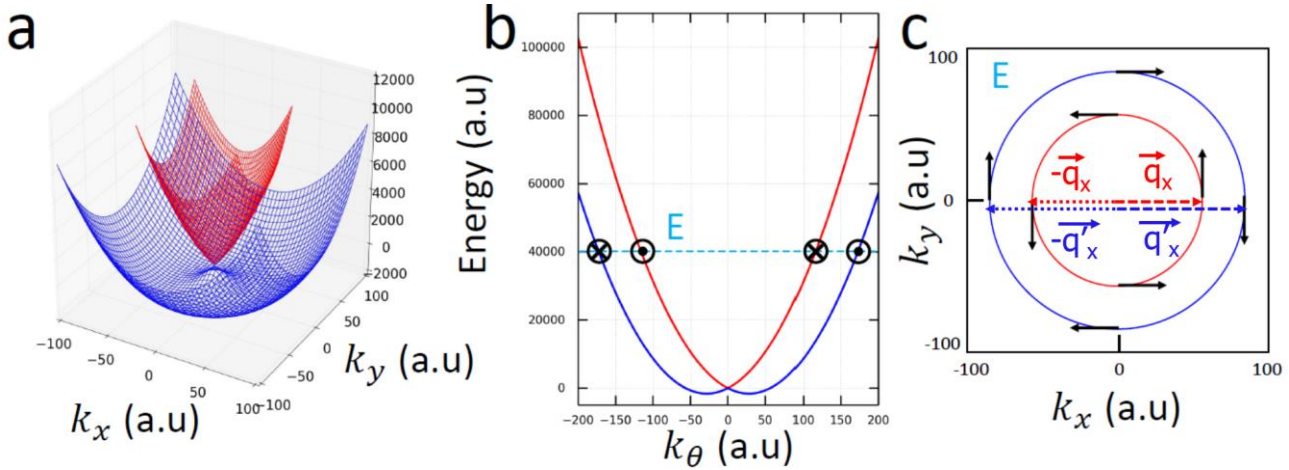


Figure 37. Effect of the Rashba spin-orbit coupling Hamiltonian on a 2D free electron gas with parabolic dispersion. **a**) $E_\lambda(\vec{k})$ eigenenergies with $\lambda = +1$ in red and in $\lambda = -1$ blue. **b**) Cut of $E_\lambda(\vec{k})$ along an arbitrary direction $\vec{k} = k_\theta(\cos\theta, \sin\theta)$. The conserved spin projection locally orthogonal to \vec{k} is indicated in black. **c**) Circular constant energy surfaces where the conserved spin projection locally orthogonal to \vec{k} is represented by black arrows. Red, blue dashed arrows with $\pm q_x$ and $\pm q'_x$ vectors indicate Cooper pairing satisfying zero total momentum for each $\lambda = +1$ and $\lambda = -1$ band. Figure modified from the PhD thesis of Raphaël Leriche.

The new eigenstates can be expressed as a function of the degenerate free electron eigenstates with spin up and down projection forming a basis:

$$|\vec{k}\lambda\rangle = \frac{|\vec{k}\uparrow\rangle + i\lambda e^{i\theta_{\vec{k}}}\vec{k}\downarrow\rangle}{\sqrt{2}} \quad (58)$$

where $\theta_{\vec{k}}$ is the polar angle defined by the vector \vec{k} between its k_x and k_y components. From (57) and (58) one sees that associated to the fact that the inversion symmetry is broken at the surface of solids, the Parity symmetry is broken: $E(\mathcal{P}|\vec{k}\uparrow\rangle) = E(|-\vec{k}\uparrow\rangle) \neq E(|\vec{k}\uparrow\rangle)$. Nevertheless, the time-reversal symmetry is still preserved since $E(\mathcal{T}|\vec{k}\uparrow\rangle) = E(|-\vec{k}\downarrow\rangle) = E(|\vec{k}\uparrow\rangle)$. These theoretical predictions have been thoroughly evidenced by experimental measurements in various systems at surfaces or interfaces of solids. We present in figure 38a such an example for the surface state of Au(111). This case is a canonical example corresponding

exactly to the theoretical modelling developed by Bychkov and Rashba, whose predictions were presented in figure 37. In this case the measured value of α is $\alpha \approx 0.5 \text{ eV\AA}$.

We also present in figure 38b the theoretical bandstructure predicted using ab initio DFT calculations for our Pb/Si(111) monolayer in the $\sqrt{3} \times \sqrt{3}$ phase [Ren2016] (which is an excellent approximation of the experimentally realized SIC phase as we have seen previously in **Topic2E-F-G**). One sees that a single electronic band disperses downwards from about 0.5 eV above E_F with its origin at the K point (in the region with a dashed rectangle in panel 38b). One recognizes for this band the characteristic pattern of the spin splitting bandstructure induced by Rashba spin-orbit coupling. The measured value of α is $\alpha \approx 2.8 \text{ eV\AA}$ along $[\Gamma\text{K}]$ and $\alpha \approx 0.5 \text{ eV\AA}$ along $[\Gamma\text{M}]$. These values are comparable with the one measured in Au(111). This seems reasonable since Au and Pb are neighboring heavy elements in the periodic table. The K and M points are time-reversal invariant momenta for this system, so that a band degeneracy exists at these points.

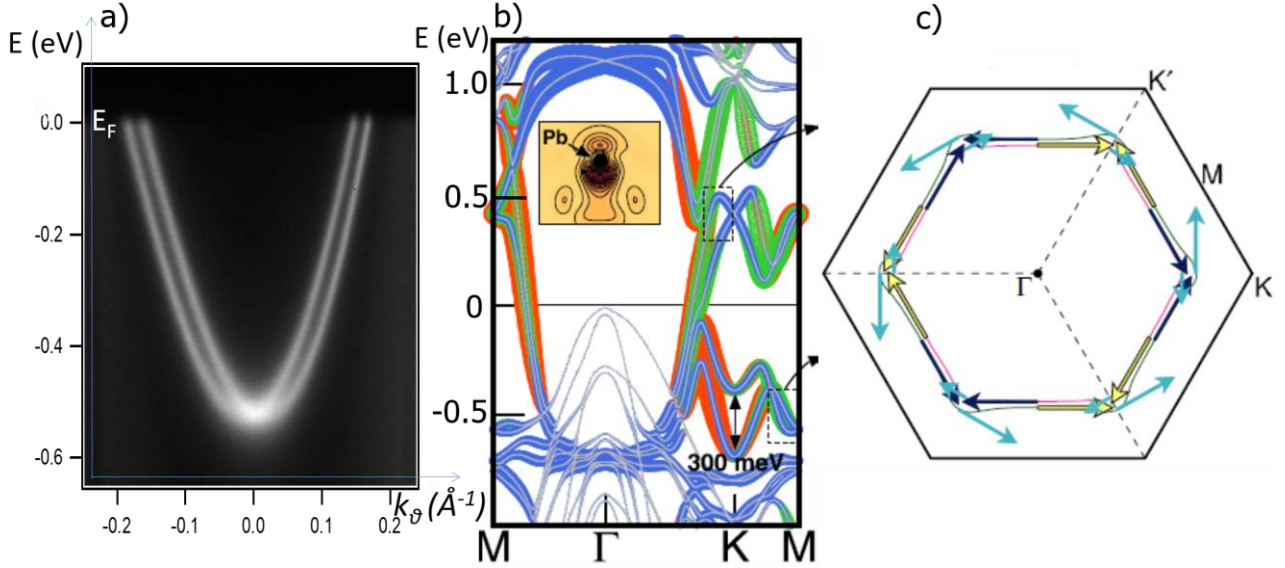


Figure 38. Experimental signatures of the effect of Rashba spin-orbit coupling on the energy dispersion of 2D electron gas systems. a) 2D surface states of Au(111) measured by ARPES (from Lashell et al. PRL77, 3419, 1996). b) Ab initio DFT calculations of the electronic bandstructure of the Pb/Si(111) monolayer in the $\sqrt{3} \times \sqrt{3}$ phase. c) Fermi surface of the Pb/Si(111) monolayer in the $\sqrt{3} \times \sqrt{3}$ phase, the arrows indicating the spin components. In panels a) and b) the Fermi energy E_F corresponds to 0 eV. Panels b), c) are from [Ren2016].

Superconducting pairing on a Rashba split band-structure

From the modified bandstructure induced by Rashba spin-orbit coupling, one can analyze the formation of Cooper pairs mediated by a conventional electron-phonon mechanism as in the BCS theory [Gorkov2001, Smidman2017, Sigrist1991]. Let us first remind what happens in the BCS situation. We have seen that the main requirement of Cooper and BCS pairing was to pair two single electron states so that they have zero total momentum and form a time-reversal invariant pair: $|\vec{k} \uparrow\rangle$ is paired with $|\vec{-k} \downarrow\rangle$. In the case of BCS pairing for a 2D free electron gas without spin-orbit coupling, the parity symmetry is not broken: this leads to a single gap opening on the Fermi surface with a gap function that is even in \vec{k} , $\Delta(-\vec{k}) = \Delta(\vec{k})$. Thus to satisfy the Fermions' anticommutation rules, the associated BCS wave function (in the groundstate) has to be antisymmetric in the spin components. This implies that the BCS groundstate is a spin-singlet state. This corresponds to a Cooper pair wave function $|\psi_{Cooper}\rangle$ that can be expressed as:

$$|\psi_{Cooper}\rangle = \frac{|\vec{k} \uparrow\rangle|\vec{-k} \downarrow\rangle - |\vec{-k} \uparrow\rangle|\vec{k} \downarrow\rangle}{\sqrt{2}} \quad (59)$$

Thus in the BCS case, the spin part of the wave function is identical for all pairs since S_z is a good quantum number.

In contrast, Rashba spin-orbit coupling splits the bandstructure of the 2D electron gas as presented in figure 37. The parity symmetry is broken but the time-reversal symmetry is preserved. Let us consider the case where the spin-orbit coupling is strong enough so that:

- i) its characteristic energy $2|\alpha|k_F$ is much larger than the superconducting energy gap
- ii) pairing between fermions from different helical band can be ignored (another way of formulating the same statement is that two fermions pair only on the same helicity band: either on the $\lambda = +1$ one or on the $\lambda = -1$)

In this case, looking at panel 37c) and at the vectors $\pm q_x$ and $\pm q'_x$, one sees that it is possible to pair electron states $|\vec{q} + \rangle$ with $|\overline{-\vec{q}} + \rangle$ in the band of chirality $\lambda = +1$ and electron states $|\vec{q}' - \rangle$ with $|\overline{-\vec{q}'} - \rangle$ in the band of chirality $\lambda = -1$. Thus it appears that while in the situation of a 2D spin-degenerate electron gas the BCS pairing was a single band problem, it is now a 2 band problem in presence of Rashba spin-orbit coupling (SOC). Depending on the microscopic nature of the pairing and on the amplitude of the SOC two cases can occur:

- i) The same gap magnitude opens on the two helicity bands. In this case the system is very similar to the BCS situation: it behaves as essentially as a single gap system. The Cooper wavefunction (59) can be re-written in the new chiral eigenstates basis:

$$|\psi_{Cooper}\rangle = \frac{i[e^{i\theta_{\vec{k}}|\vec{k}-\rangle}|\overline{-\vec{k}}-\rangle - e^{-i\theta_{\vec{k}}|\vec{k}+\rangle}|\overline{-\vec{k}}+\rangle]}{2\sqrt{2}} \quad (60)$$

The expression (60) shows that the system is a spin-singlet superconductor in the helical basis.

- ii) The gap magnitude is different on the two bands. This implies a mixing of spin-singlet and spin-triplet pairing which is enabled since parity symmetry is broken. In this case the gap function possess a spin-triplet component.

For the Rashba spin-splitting that we have considered the most general pairing Hamiltonian can be written under the form:

$$H_{Supra-Rashba} = \frac{1}{2} \sum_{\lambda, \mathbf{k}} \Delta_{\lambda}(\mathbf{k}) c_{\mathbf{k}\lambda}^{\dagger} c_{-\mathbf{k}\lambda}^{\dagger} + \Delta_{\lambda}^*(\mathbf{k}) c_{-\mathbf{k}\lambda} c_{\mathbf{k}\lambda} \quad (61)$$

The expression (61) shows that two gaps $\Delta_{+}(\mathbf{k})$ and $\Delta_{-}(\mathbf{k})$ open on each helicity band indexed by λ . The anticommutation relation of the fermions implies $\Delta_{\lambda}(\mathbf{k}) = -\Delta_{\lambda}(-\mathbf{k})$. $\Delta_{\lambda}(\mathbf{k})$ can be further written as:

$$\Delta_{\lambda}(\mathbf{k}) = t_{\lambda}(\mathbf{k}) \tilde{\Delta}_{\lambda}(\mathbf{k}) \text{ with } t_{\lambda}(\mathbf{k}) = i e^{i\lambda\theta_{\vec{k}}} \text{ which implies } \tilde{\Delta}_{\lambda}(\mathbf{k}) = \tilde{\Delta}_{\lambda}(-\mathbf{k}).$$

Generally it can be shown that the gap function can be written in the original spin basis ($|\uparrow\rangle, |\downarrow\rangle$) of the degenerate 2D electron gas under the form:

$$\bar{\Delta}_{\alpha\beta} = i\sigma_y [\psi(\mathbf{k}) + \mathbf{d}(\mathbf{k}) \cdot \boldsymbol{\sigma}] = \begin{pmatrix} -d_x(\mathbf{k}) + id_y(\mathbf{k}) & \psi(\mathbf{k}) + d_z(\mathbf{k}) \\ -\psi(\mathbf{k}) + d_z(\mathbf{k}) & d_x(\mathbf{k}) + id_y(\mathbf{k}) \end{pmatrix} \quad (62)$$

From the general expression (62) one sees that the $\psi(\mathbf{k})$ component corresponds to the only spin-singlet term so that $\psi(\mathbf{k})$ has to be even in \mathbf{k} . Furthermore, there are three spin-triplet components. Two spin-triplet components are along the diagonal meaning that they couple ($|\uparrow\uparrow\rangle$) or ($|\downarrow\downarrow\rangle$). The third spin-triplet component is $d_z(\mathbf{k})$ along the anti-diagonal and corresponds to spin vectors ($|\uparrow\downarrow\rangle + |\downarrow\uparrow\rangle$). In the case of our 2D Rashba system one can express all components of the gap function $\bar{\Delta}_{\alpha\beta}$:

$$\psi(\mathbf{k}) = (\tilde{\Delta}_{+}(\mathbf{k}) + \tilde{\Delta}_{-}(\mathbf{k}))/2 \text{ and } \mathbf{d}(\mathbf{k}) = \frac{\vec{\gamma}(\vec{k})}{|\vec{\gamma}(\vec{k})|} (\tilde{\Delta}_{+}(\mathbf{k}) - \tilde{\Delta}_{-}(\mathbf{k}))/2 \quad (63)$$

Since $\vec{\gamma}(\vec{k})$ is defined from the expression (56bis) of the Hamiltonian, $\vec{\gamma}(\vec{k}) = \alpha(-k_y, k_x, 0)$ it follows that the components of the vector $\mathbf{d}(\mathbf{k})$ can be expressed as:

$$\begin{aligned} d_x(\mathbf{k}) &= -\sin\theta_{\vec{k}} (\tilde{\Delta}_{+}(\mathbf{k}) - \tilde{\Delta}_{-}(\mathbf{k}))/2 \\ d_y(\mathbf{k}) &= \cos\theta_{\vec{k}} (\tilde{\Delta}_{+}(\mathbf{k}) - \tilde{\Delta}_{-}(\mathbf{k}))/2 \\ d_z(\mathbf{k}) &= 0 \end{aligned}$$

One finally can relate the two gaps $\tilde{\Delta}_+(\mathbf{k})$ and $\tilde{\Delta}_-(\mathbf{k})$ opening on each helicity band indexed by λ (expressed in relation (61)) to the spin-singlet and spin-triplet components of $\bar{\Delta}_{\alpha\beta}$:

$$\tilde{\Delta}_\lambda(\mathbf{k}) = \psi(\mathbf{k}) + \lambda \frac{\vec{\gamma}(\vec{\mathbf{k}})}{|\vec{\gamma}(\vec{\mathbf{k}})|} \cdot \mathbf{d}(\mathbf{k}) \quad (64)$$

Which leads to:

$$\tilde{\Delta}_\lambda(\mathbf{k}) = \Delta_S(\mathbf{k}) + \lambda \Delta_T(\mathbf{k}) \quad (65)$$

Where the gap $\tilde{\Delta}_\lambda(\mathbf{k})$ on each helicity band is decomposed into its spin-singlet component $\Delta_S(\mathbf{k}) = \psi(\mathbf{k})$ and triplet component $\Delta_T(\mathbf{k}) = (\vec{\gamma}(\vec{\mathbf{k}})/|\vec{\gamma}(\vec{\mathbf{k}})|) \cdot \mathbf{d}(\mathbf{k})$.

We conclude from this part that in a superconductor hosting a 2D electron gas whose bandstructure is split by a Rashba SOC one gap opens on each helicity band. Depending on the electron-phonon coupling, bandstructure and spin-orbit coupling, a spin-singlet and spin-triplet component can coexist as parity symmetry is broken. When this is the case, then the two gaps on each helicity band differ. According to (63), the spin-singlet component $\Delta_S(\mathbf{k})$ is given by the average of the two gaps, while the spin-triplet component $\Delta_T(\mathbf{k})$ is given by their difference. Furthermore, it can be shown that when $|\Delta_S(\mathbf{k})| > |\Delta_T(\mathbf{k})|$ the superconductor has a trivial topology. In contrast, when $|\Delta_T(\mathbf{k})| > |\Delta_S(\mathbf{k})|$ the superconductor becomes topological and exhibits two counter-propagating edges states corresponding to a helical state. For our 2D time-reversal invariant superconductors a \mathbb{Z}_2 topological index characterizes the topological superconductivity.

Signatures of Rashba SOC in the superconducting Pb/Si(111) monolayers

We discuss here shortly the STM/STS results that we have obtained in the superconducting phase of Pb/Si(111) monolayers. I rely on the results presented in more details in parts **Topic2E-F-G**. We have studied two different structural phases: the Striped Incommensurate (SIC) that is close to the ideal commensurate $\text{Pb}-\sqrt{3} \times \sqrt{3}$ phase, and the anisotropic $\text{Pb}-\sqrt{7} \times \sqrt{3}$ phase. Both Pb monolayers show spectroscopic signatures supporting the existence of a strong spin-orbit coupling modifying the superconducting order parameter and leading to the appearance of a (very) small spin-triplet component accompanying a (much) larger spin-singlet component.

We have seen that the SIC electronic bandstructure measured by ARPES is compatible with a 2D parabolic band split by Rashba SOC. On this phase our $dI/dV(V)$ spectra, obtained with a normal platinum tip or with a superconducting Pb tip shown previously in part **Topic2F** in figure 22, reveal a fully developed superconducting gap. In our studies about proximity effects we have investigated in part **Topic1D** the situation of single Pb islands, which are trivial superconductors, in very good electrical contact with the SIC monolayer. The results presented in this HDR thesis in this proximity effect study clearly show that topological edge states were not observed at the interface between the Pb islands and the SIC monolayer. We conclude from these set of results that the SIC Pb/Si(111) monolayer is a trivial superconductor. According to the theoretical part developed above in the previous section one deduces that the SIC phase should be in the regime $|\Delta_S(\mathbf{k})| \gg |\Delta_T(\mathbf{k})|$. This implies that the triplet component is much smaller than the spin-singlet part. This could explain why a tiny non-zero residual LDOS is measured in the gap of the SIC by STS (see panel c in figure 22). Indeed if a pure spin-singlet $\Delta_S(\mathbf{k})$ component with $\Delta_T(\mathbf{k}) = 0$ would exist in the SIC, this would imply a strictly zero LDOS inside the superconducting gap because non-magnetic disorder is not pair-breaking for $\Delta_S(\mathbf{k})$ while it is pair-breaking for $\Delta_T(\mathbf{k})$.

On the $\text{Pb}-\sqrt{7} \times \sqrt{3}$ phase, our results are more complicated. I have not presented them in details in the parts **Topic2E-F-G** before. I will just mention here without showing it that the $dI/dV(V)$ spectra on this phase show larger gap filling than on the SIC phase (see figure 1 in [Brun2014] or figure 19 in [Brun2017]), for non-magnetic scattering. Since this phase has an anisotropic structure and shows a strongly anisotropic Fermi surface with quasi-1D lines and small electron/hole pockets [Kim2010], the hypothesis of an electron gas giving two Rashba split parabolic bands is not satisfied here. Thus the full theoretical treatment of this case is more complicated than the simple one proposed above. Nevertheless the observation of gap filling in some local region of the sample associated to non-magnetic scattering strongly suggests the existence of a spin-

triplet component of the order parameter, presumably larger than in the SIC phase. We continue to study this issue to have a better understanding of the order parameter of this phase.

B) Evidence for 2D topological superconductivity

From the arguments developed above to understand the type of superconductivity existing in the Pb/Si(111) monolayers in the SIC or $\sqrt{7} \times \sqrt{3}$ phase, we could show that a small spin-triplet component is present in both phases.

One way to render the SIC phase topological is to keep the same bandstructure but increasing the coupling in order to render the $|\Delta_T(\mathbf{k})|$ component larger than $|\Delta_S(\mathbf{k})|$, so that we reach $|\Delta_T(\mathbf{k})| > |\Delta_S(\mathbf{k})|$. Nevertheless we do not have such a knob for this operation since until now we do not know why $|\Delta_T(\mathbf{k})| \ll |\Delta_S(\mathbf{k})|$ in the SIC phase. An easier way to induce topological superconductivity is to use a strong perpendicular magnetic field to gap one of the two helicity subbands. Indeed the following phase diagram shown on figure 39 can be derived using a perpendicular magnetic field integrated in the following effective Hamiltonian given by the formula:

$$H_{Rashba-Zeeman} = \left[\left(\frac{\hbar^2 k^2}{2m} - \mu \right) + \alpha (\vec{k} \times \vec{\sigma})_z \right] \tau_z + V_z(\mathbf{r}) \sigma_z + \left[\Delta_S + \frac{\Delta_T}{k_F} (\vec{k} \times \vec{\sigma})_z \right] \tau_x \quad (66)$$

In the expression (66) one recognizes the 2D Rashba Hamiltonian, a mixed singlet-triplet superconducting order parameter with the triplet component oriented along the Rashba effective magnetic field and an external magnetic field oriented along the z direction. As before $\vec{\sigma} = (\sigma_x, \sigma_y, \sigma_z)$ are Pauli matrices acting in spin space. $\vec{\tau} = (\tau_x, \tau_y, \tau_z)$ are Pauli matrices acting in the particle-hole space. Thus the basis spinor, called Nambu spinor, is given here by $\psi_k^\dagger = (c_{k\uparrow}^\dagger, c_{k\downarrow}^\dagger, c_{-k\downarrow}, -c_{-k\uparrow})$. The phase diagram corresponding to this Hamiltonian is represented in figure 39.

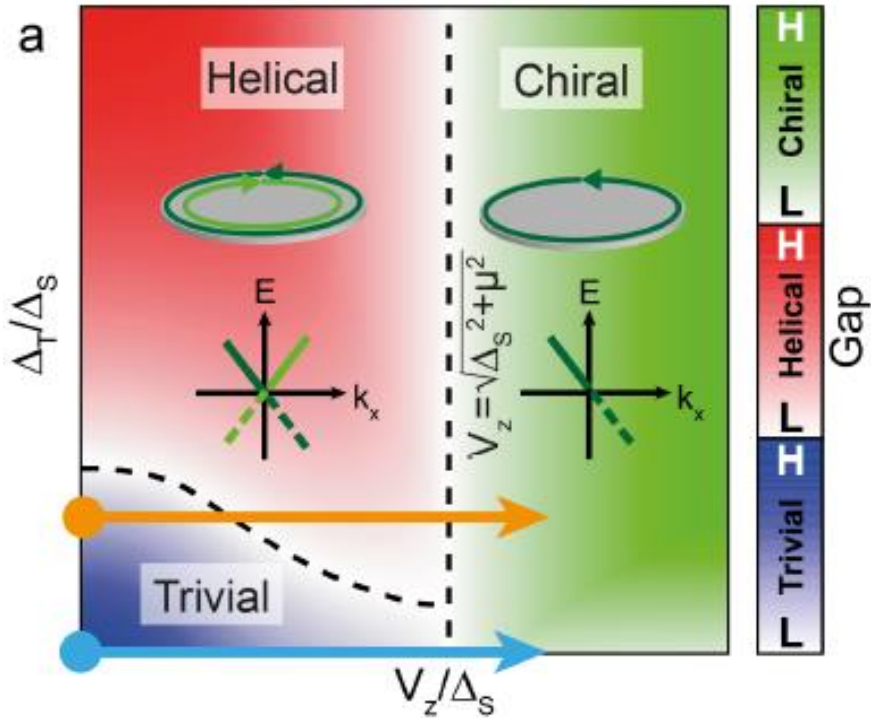


Figure 39. Theoretical phase diagram corresponding to a 2D Hamiltonian given by the expression (66) integrating a parabolic band split by a Rashba term, a mixed singlet-triplet superconducting order parameter and a Zeeman term due to a magnetic field perpendicular to the 2D direction. Three phases with different topological orders are obtained.

One sees that three different phases are obtained. A trivial phase with no edge states exists for $\Delta_T \ll \Delta_S$ and $V_z \ll \sqrt{\Delta_S^2 + \mu^2}$. It has a $C = 0$ Chern number. A topological helical phase exists with two counter-

propagating edge states for $\Delta_T > \Delta_S$ and $V_z < \sqrt{\Delta_S^2 + \mu^2}$. This phase has a total $C = C_+ + C_- = 0$ Chern number that decomposes into $C_+ = 1$ and $C_- = -1$ for each helical subband. A topological chiral phase exists with one propagating edge state for $V_z > \sqrt{\Delta_S^2 + \mu^2}$. This phase has a $C = 1$ Chern number.

We could experimentally realize a situation corresponding to this general framework. We implemented the perpendicular Zeeman field using magnetic CoSi clusters embedded in the silicon substrate at its surface, below the Pb monolayer. This was made possible since cobalt atoms are well-known to alloy with silicon. Co atoms integrate themselves into a Co-rich CoSi₂ crystal structure when the sample is heated below 500°C [Tung1992]. Furthermore CoSi clusters were shown by DFT calculations to be all magnetic with a large magnetic moment [Jo2006], while magneto-optical Kerr effect measurements performed at room temperature showed that CoSi ultrathin films below 2 ML thickness are paramagnetic [Chang2007]. This strongly suggests that at very low temperature the crystalline magnetic anisotropy will tend to align the magnetization of the CoSi clusters perpendicular to the surface, as often observed: see for instance the case of Co clusters on Cu(111) [Pietzsch2004].

We could image the subsurface CoSi clusters by two ways. i) We used transmission electron microscopy (TEM). ii) We desorbed partially the Pb monolayer and could scan directly the clusters using STM. This is presented in figure 40 which shows in panel a) the schematics of the sample, and in panels b) and c) the CoSi clusters imaged by STM of sizes ranging between 5 and 10 nm.

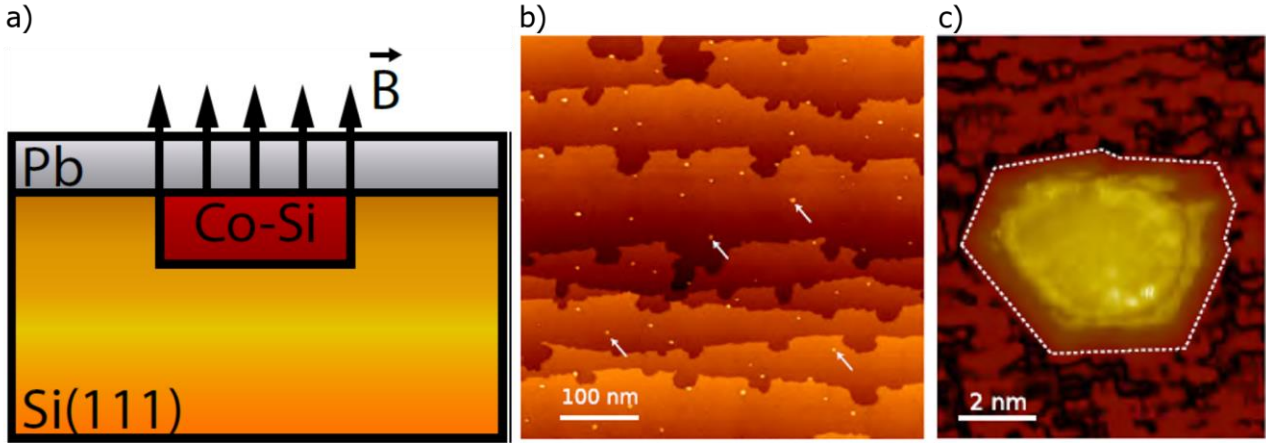


Figure 40. a) Principle of the experiment to reach topological phases using CoSi magnetic clusters buried below the Pb superconducting monolayer. b) STM topography of a Pb/Co/Si(111) monolayer sample that was heated at 400°C during 30 minutes in order to remove most surface Pb atoms and to reveal buried CoSi clusters. The CoSi clusters correspond to the little dots and some of them are indicated by white arrows. c) STM topography of an individual CoSi cluster. Their typical size is between 5 and 10 nm.

The main difficulty in this work was to find the subsurface CoSi clusters, since no signatures appeared in the STM topography at low bias voltages, except for the spectroscopic signatures occurring in the superconducting energy gap region! In a sense, this situation was identical to the one we experienced with 2H-NbSe₂ when we imaged the Yu-Shiba-Rusinov wave functions associated to the excited states of single paramagnetic impurities. Fortunately for us, some of these CoSi clusters but not all, revealed indeed the expected topological properties that we could infer by evidencing closed edge states at the boundary of the buried cluster. Our best measurement is presented below in figure 41.

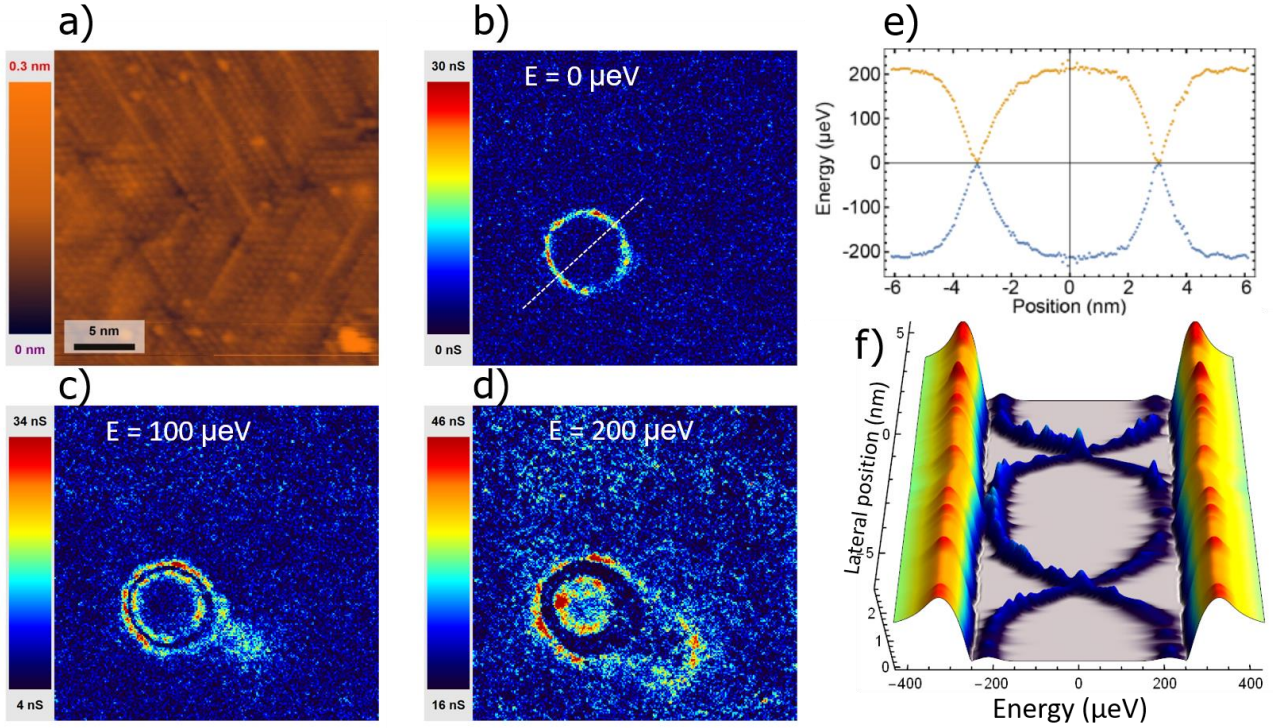


Figure 41. a) STM topography of the region of interest of the Pb/Co/Si(111) monolayer in the SIC phase containing buried CoSi clusters. The scale bar is indicated in nanometer. b)-d) $dI/dV(x, y, E)$ conductance maps of the region corresponding to panel a) measured at $T = 300$ mK at various energies $E = 0$ μeV (panel b), $E = 100$ μeV (panel c), $E = 200$ μeV (panel d). e) This graph enables following the energy E of the in-gap states as a function of position along the radial profile drawn across the topological region following the dashed line seen in panel b). f) Same quantity as in panel e) but showing the amplitude of the local conductance $dI/dV(r, E)$ for each energy E and position r .

Since the superconducting energy gap of the SIC Pb/Si(111) monolayer is only of the order of 0.3 meV, we used a superconducting Pb-coated tip in order to ensure the best spectroscopic resolution. Otherwise with a normal tip at $T = 300$ mK the spectral resolution is $3.5 k_B T \approx 80$ μeV . Since we are in a S-I-S tunneling junction all raw $dI/dV(V)$ spectroscopic results are offset by the energy gap of the tip. We thus deconvoluted all our $dI/dV(V)$ spectra from the tip superconducting LDOS. In order to have more control on the exact value of the tip energy gap, we followed the temperature dependence of the S-I-S spectra up to above the critical temperature of the Pb monolayer and extracted the tip energy gap value from the spectra measured in the normal state of the Pb monolayer. A very small pair breaking Usadel parameter $\Gamma \approx 1$ μeV was assumed for the tip LDOS, leading to $\Delta_{tip} \approx 1.41 \pm 0.02$ meV, in good agreement with the one expected for Pb. At $T = 300$ mK the S-I-S spectra could be deconvoluted assuming the previous tip gap and a Lorentzian broadening of ≈ 30 μeV . The extracted energy gap of the Pb SIC monolayer was found to be $\Delta_{SIC} \approx 0.29 \pm 0.02$ meV, in good agreement with our previous measurements [Brun2014] and the ones reported earlier [Zhang2010]. For the description of the LDOS of the in-gap states we assumed Lorentzian peaks (of width ≈ 30 μeV) and took as parameters their energy and amplitude.

The panels 41a) to d) present the STM topography of the region of interest of the SIC Pb/Co/Si(111) monolayer. This region contains a single buried CoSi cluster. For low bias voltages such as ± 50 meV, no signatures of the buried cluster appear in the topography. However, the $dI/dV(E)$ conductance maps measured on the same region at $T = 300$ mK reveal closed edge states spatially dispersing in the superconducting energy gap. For the sake of simplicity, the energy E plotted for each $dI/dV(E)$ map is the deconvoluted energy, i.e. it represents the excitation energy of the injected quasiparticles with respect to the Fermi energy ϵ_F , taken here to be at 0 eV. A single ring of size larger than 5 nm and of width about 0.7 nm is observed around ϵ_F . Note that in the Pb-SIC monolayer the Fermi wavelength measured by ARPES is about 5 \AA , very close to the thickness of the observed ring at $E = 0$ eV. At larger energies $0 < E < \Delta_{SIC}$ this ring splits in 2 concentric features, one moving inward the other moving outward, as shown in the panels c) for $E = 100$ μeV and d) for $E = 200$ μeV . The panels e) and f) enable visualizing the energy and position dependence of these in-gap

states along a line crossing the center of the domain. It can be seen that, up to the experimental resolution and uncertainty of our spectroscopy measurements, this pair of states arise in the close vicinity of the domain near the gap edges and disperse spatially toward 0 and cross the Fermi level. We could reproduce this experiment and we observed several of such similar features (see [Menard2017]).

From our experimental results we could discard any serious alternative scenario other than the ones including a local topological transition giving rise to edge states. Interpreting in more details and modelling quantitatively our results was nevertheless difficult for several reasons. First, our on-site Bogoliubov-de Gennes calculations could not be performed in the limit of parameters encountered in the experiment due to strong numerical constraints, which would have required: $\lambda_F \ll D_C \ll \xi$ and $\Delta \ll E_{Rashba} < E_F$ where D_C is the size of the cluster. Second, the actual bandstructure of the Pb-SiC monolayer differs from the ideal single parabolic band centered at Γ and split under the Rashba field. Since we observe two edge states and not only one, our phase diagram suggests that our system would be in a helical phase (see figure 39). But in fact it could also be that the topological regime could correspond to a chiral phase with a $C = 2$ Chern number, leading automatically to two edge states. Thus more experiments are needed on our side to investigate these issues and clarify the topological regime with respect to the actual bandstructure. Along with this issue, it would be also great to characterize in situ at low-temperature the magnetism of the buried CoSi clusters. We could use for instance x-ray magnetic circular dichroism (XMCD) measurements, such as the ones presented in part **Topic2I** previously.

This work was published in *Two-dimensional topological superconductivity in Pb/Co/Si(111)*
G.C. Ménard, S. Guissart, C. Brun, M. Trif, F. Debontridder, R. Leriche, D. Demaille, D. Roditchev, P. Simon, T. Cren, Nature Communications 8, 2040 (2017).

C) Evidence for Pairs of spatially separated Majorana excitations in 2D topological superconductors

As I briefly presented in part **Topic3A**, another important theoretical prediction associated to topological superconductivity, is the possibility to create pairs of spatially separated localized zero-energy Majorana excitations. This has theoretically been predicted for instance in vortices of p -wave superconductors [Volovik1999, Ivanov2001] and was predicted even before in superfluid ^3He . In this case one zero-energy Majorana mode exists at the core of each vortex, which implies a total number of even vortices since a usual fermion can give rise to two spatially separated Majorana fermions. It seems that a rather convincing realization of this situation was presented recently in the Fe(Se,Te) quasi-2D material [Machida2019]. In such cases the very difficult task, in order to truly identify Majorana zero-mode by STS, is to be able to separate them from Caroli-de Gennes-Matricon discrete states that naturally appear in the vortex core at finite energies [Caroli1964]. This requires typically a very small Fermi energy ε_F in order to ensure that the energy spacing $\delta = \Delta^2/\varepsilon_F$ between the consecutive Caroli-de Gennes-Matricon discrete states is larger than the spectroscopic energy resolution of the STS measurement. Only in these conditions one can spectroscopically separate without ambiguity the Majorana zero-mode from the first finite-energy Caroli-de Gennes-Matricon excited state.

Our superconducting Pb/Co/Si(111) monolayer appears as an interesting system to search for spatially separated localized Majorana excitations in the topological phase that I have presented before in the part **Topic3B**. To go in this direction we tried to increase the size of our CoSi buried clusters. With respect to the experiments summarized in the previous section we deposited two times more Co atoms. While the cluster size was 5 – 10 nm in the previous part **Topic3B** it is here about 15 – 20 nm. This experimental situation led to completely unexpected new results in zero external magnetic field inside some of the topological domains. Our results are consistent with the observation of pairs of spatially separated Majorana zero-mode in topological domains. One zero mode is located at the center of the topological region while the second partner is located at the boundary of the topological region. Since we did not use an external magnetic field to create a vortex structure inside the topological domain, our interpretation of the results is that a vortex structure naturally exists in our system. This vortex could be either intrinsic to the magnetic texture of some CoSi domains or developed in the spin-orbit field.

Our central result is presented in figure 42. It was carried out with a normal platinum tip. The panel 42a) presents the STM topography of the region of interest where a large buried CoSi cluster is present on the upper

terrace (brighter area). On this area we performed a grid spectroscopy measurement where an $I(x, y, V)$ spectrum is measured every 0.5 \AA . From this set of measurements we could extract the conductance map at every energy around the Fermi energy ε_F , which is proportional to the LDOS map. The conductance map at zero energy, i.e. $dI/dV(x, y, E = 0)$, is presented in panel 42b). It is seen that a large zero-bias peak exists localized on a spot (x_0, y_0) of size $\sim 1 \text{ nm}$. The corresponding $dI/dV(x_0, y_0, V)$ spectrum measured at this location is shown in panel 42d). It is seen that the height of this peak at its maximum is about 4 times the one of the superconducting coherence peaks. The width of this peak, indicated by the black dashed line, corresponds to $3.5 kT_{eff}$ with an effective electronic temperature slightly larger than our bath temperature. This large zero-bias peak is surrounded about 10 nm away by a circularly concentric corona (light blue conductance in panel 42b) having also a zero-bias contribution that is of much less amplitude than the central peak. The $dI/dV(x_1, y_1, V)$ spectrum measured at the purple dot, located at the corona maximum amplitude, enables comparing the two zero-bias peak spectra (see the light blue curve in panel 42e). This second zero-bias peak of much lower amplitude has about the same width as the central peak. The amplitude of this zero-bias corona decays very rapidly in less than few nm toward the interior of the CoSi domain, i.e. toward the direction of the central peak. In contrast, in the opposite direction, i.e. toward the exterior of the CoSi domain, the decay length of the amplitude of the corona is much longer and occurs on several tens of nm compatible with the superconducting coherence length of the trivial SIC monolayer ($\xi \sim 50 \text{ nm}$). In-between the central zero-bias peak and the beginning of the zero-bias corona, a gapped region exists (dark blue conductance in panel 42b), a spectrum of which is measured at the green dot and presented in panel 42e) with the dark blue curve. One sees that this gap is a “hard” gap in the sense that it is equal to the one of the trivial SIC monolayer and does not contain any new in-gap states (for instance compare with the spectra presented in figure 22c in **Topic2F**).

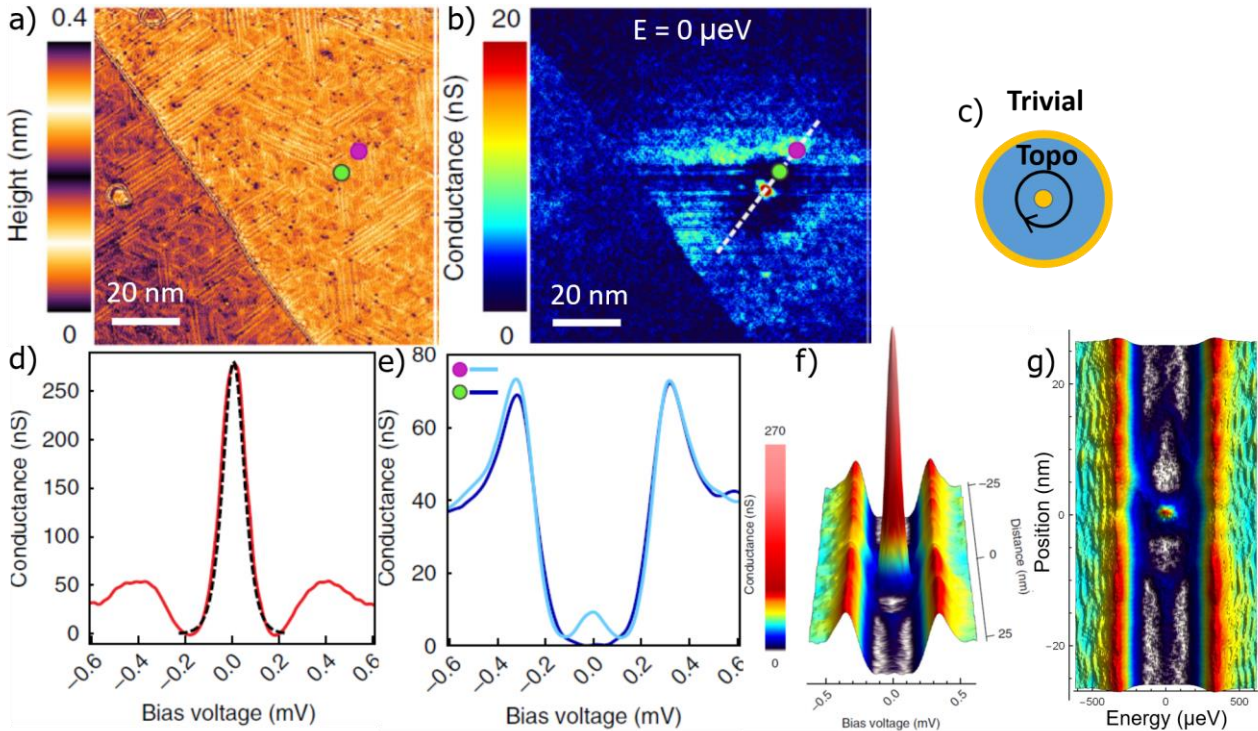


Figure 42. a) STM topography of the region of interest of the Pb/Co/Si(111) monolayer in the SIC phase containing one buried CoSi cluster. A monoatomic step edge exists and crosses this region from the top left corner. The brighter region (right) is the upper terrace while the darker one is the lower terrace. The scale bar is indicated in nanometer. b) $dI/dV(x, y, E)$ conductance map measured on the same region at $T = 300 \text{ mK}$ at the energy $E = 0 \text{ } \mu\text{eV}$. Along the dashed line a strong zero-energy peak exists in the center (location of the red dot), surrounded by a circular gapped region (dark blue conductance where there is the green dot) and itself surrounded by a circular zero-energy corona (bright blue conductance where there is a purple dot). c) Sketch of a single vortex sitting at the center of the topological domain comprising a Majorana zero mode paired with a second one located at the domain boundary. Outside this region is the trivial superconductor. d) $dI/dV(V)$ spectrum measured at the vortex center (red dot in panel b). The black dashed line is a fit to a state centered at $6 \text{ } \mu\text{eV}$ and width corresponding to an electronic temperature of 350 mK . e) $dI/dV(V)$ spectra measured in the gapped region (blue curve, location: green dot in panel b) and on the

corona (light blue curve, location: purple dot in panel b). f) 3D colored view showing the spatial dependence of the $dI/dV(V)$ spectra measured along the white dashed line in panel b. g) Same quantity as in panel f) but in a 2D colored map.

We thus interpret our experimental results as showing a pair of spatially separated Majorana fermions existing in a topological superconducting domain, as schematically drawn in panel 42c). We could reproduce this experiment and we observed several of such similar features (see [Menard2019]). As our theoretical modelling suggests, the radius of the buried magnetic CoSi domain corresponds to the distance between the central zero-bias peak (located at the red dot in panel 42b) and the zero-bias corona at its maximum amplitude (i.e. at the pink dot in panel 42b). We would like to mention that the precise analysis of the energy value of the central zero-bias peak seen in panel 42d) shows that it is centered at 6 μeV (position in energy of the black dashed line). This suggests that this peak might actually be a doublet of peaks very-close to zero-energy resulting from an interaction between the two Majorana modes. With such an assumption the zero-bias peak is almost perfectly fitted (not shown here, see figure 1 of the supplementary material of [Menard2019]).

The theoretical modelling was carried out by Andrej Mesaros and Pascal Simon from LPS Orsay. The simplest hypothesis explaining our results is the existence of a vortex formed either in the magnetic texture of the CoSi cluster or in the spin-orbit field of a topological chiral phase. In line with what I presented previously in part **Topic3B**, this topological chiral phase originates from a Rashba spin-split band with a large Zeeman term such

that $V_z > \sqrt{\Delta_S^2 + \mu^2}$ in the direction perpendicular to the 2D plane. Thus the topological phase corresponds precisely to the one described in the previous section. The microscopic origin of the vortex is not elucidated up to now. Nevertheless we believe that there exists a major structural difference between our previous experiments for smaller CoSi clusters presented in part **Topic3B** and these ones for larger clusters. The main difference is the fact that the Pb monolayer was more homogeneous and closer to the ideal commensurate $\sqrt{3} \times \sqrt{3}$ phase in the former experiments. In contrast, in the present experiments showing the Majorana pairs, the Pb monolayer exhibits a mixing of different phases combining many irregular $\sqrt{7} \times \sqrt{3}$ local patches and small SIC $\sqrt{3} \times \sqrt{3}$ areas. This large mixing of two different phases in the present case is clearly seen in the STM topography of panel 42a) when compared to the STM topography of panel 41a). Indeed the topography presented in panel 41a) is much closer to the ideal SIC phase that was presented previously in figure 22a) or 22e) of **Topic2E-F-G**. Thus, we believe that structural changes occurring at the atomic scale have enabled the mixing of spin-orbit terms such as $k_x \sigma_x + k_y \sigma_y = \vec{k} \cdot \vec{\sigma}$ with the Rashba term $(\vec{k} \times \vec{\sigma}) \cdot \vec{u}_z$ because of reduced spatial symmetries. If this mixing is allowed for our system, the spin-orbit coupling Hamiltonian can be written:

$$H_{SOC}^{Mix} = \alpha [\cos(\chi) (\vec{\sigma} \times \vec{k}) \cdot \vec{u}_z - \sin(\chi) \vec{\sigma} \cdot \vec{k}] \quad (67)$$

$$H_{SOC}^{Mix} = \alpha e^{i\chi} (k_y + ik_x) c_{k\uparrow}^\dagger c_{k\downarrow} + H.C. \quad (68)$$

One sees from (67) that χ represents the constant mixing angle between the linear and Rashba term. From (68) one sees that χ plays the role of an effective phase of the spin-orbit coupling constant. The spin-orbit vortex is easily integrated in the Hamiltonian (68) assuming that χ now possesses a spatial dependence and winds around a singular point as $\chi(x, y)$. As this spin-orbit vortex is fully integrated in the kinetic energy term, it is not expected to inhibit the s -wave singlet pairing. The full Hamiltonian of our system can be written adding the spin-orbit vortex to the term (68) and taking into account the other components: kinetic energy, Zeeman term and s -wave pairing:

$$H_{Rashba-Zeeman}^{vortex} = \int \Psi_r^\dagger \left[\left(-\frac{\hbar^2}{2m} \nabla^2 - \mu \right) \tau_z + V_z(\mathbf{r}) \sigma_z + \Delta_S \tau_x \right] \Psi_r + H_{SOC}^{Mix-vortex} \quad (69)$$

The numerical simulations of the 2D Hamiltonian given by (69) assuming a constant Zeeman term V_z inside a circular disk and zero outside furnishes results in good agreement with our observations, for a reasonable set of parameters with respect to the experimental ones. In particular, when the chiral phase is reached i.e. for $V_z^2 > \Delta_S^2 + \mu^2$, the LDOS calculations predict the appearance of two spatially separated Majorana wavefunctions: one at the disk center, the second one at its periphery. These zero-mode wavefunctions decay very fast in the interior of the topological region as $l_V \approx \hbar v_F / V_z$ as observed in the experiment. Outside the topological domain the external zero-mode decays on the much longer lengthscale ξ . A hard gap indeed is preserved in the topological region when V_z is large enough with respect to Δ_S . Furthermore, by rotating the

spin axis of the electrons, Andrej Mesaros and Pascal Simon could show that this model can be rewritten in a similar form as (69) but with an homogeneous spin-orbit coupling term and a magnetic texture appearing in $V_z(\mathbf{r})$. For the magnetic texture they assumed a skyrmion and found that it leads to similar theoretical results such as the ones presented in this paragraph. One can draw the following conclusion from these theoretical models. They support by various means the statement that instead of having a vortex in the superconducting phase of the order parameter to induce Majorana zero-modes, a vortex can exist in the spin-orbit coupling field or in the magnetic texture and induce spatially separated Majorana zero-modes.

In conclusion of this work, we could evidence experimentally in zero magnetic field a pair of spatially separated zero-energy excitations bearing all characteristics of Majorana wavefunctions in a 2D topological chiral region. Our theoretical work supports these findings and indicates that a reasonable hypothesis is that a vortex exists either in the spin-orbit coupling field of the Pb monolayer or in the magnetic texture of the buried CoSi clusters. Further work is needed to elucidate which hypothesis is the good one. This work was published in *Isolated pairs of Majorana zero modes in a disordered superconducting lead monolayer*, Gerbold C. Ménard, Andrej Mesaros, Christophe Brun, François Debontridder, Dimitri Roditchev, Pascal Simon, Tristan Cren, Nature Communications 10, 2587 (2019).

Topic 4 and Research Project: electronic correlations and unconventional superconductivity

This topic deals with the study of low-dimensional materials where electronic correlations play an important role and determine the groundstate of the system. I started the development of this topic during the master 2 internships of Gerbold Ménard and Rémi Federicci in 2013. I have been interested in two different types of systems:

- i) Correlated electronic systems in a single atomic plane
- ii) Unconventional superconductivity in the quasi-1D organic solid $(\text{TMTSF})_2\text{ClO}_4$

I start here by briefly introducing the main interest of the study i). A complementary part of the **Topic2E-F-G** and **Topic3** presented above is that it is possible to grow atomic monolayers of tetravalent metal atoms (Pb or Sn) on tetravalent Si(111), Ge(111) or SiC substrates with a coverage that is less than the dense superconducting monolayers studied previously. This less dense coverage is precisely 1/3 ML. In this situation it has been shown that the metal atoms are far enough from each other so that correlated electron physics takes place because the on-site Coulomb repulsion becomes larger than the electron bandwidth. Thus this class of systems offers a very well-controlled way to study Mott physics in 2D at the surface with STM/STS techniques. As very little has been made performing high-resolution spectroscopy with STM on these systems, I launched a new research activity on this topic. The very nice thing with this class of systems is that they ideally realize the paradigmatic model of correlated electron systems on a triangular lattice: the single-band half-filled Hubbard model. Additionally there is the interesting new features that the correlated electron physics in 2D includes a strong spin-orbit coupling in the problem because of the heavy mass of the Pb atoms. I initiated this activity in 2013 during the **master 2 internships of Gerbold Ménard** (during 4 months) and **Rémi Federicci** (during 6 months) that I supervised together with our **post-doc Vladimir Cherkez** (during 2 years). Here my supervision consisted mainly in lab work, sample/tip preparation, conduction of proper experiment and analysis of the results. I pursued this activity in 2017 supervising the **master 2 of Tobias Bilgeri** (during 6 months). Here my supervision consisted both in new runs of experimental work and heavy data analysis by summarizing and comparing all data acquired on this system. It gave rise to the following publication where the people I supervised are in bold:

- a) *Chiral spin texture in the charge-density wave phase of the correlated metallic Pb/Si(111) monolayer*
C. Tresca, **C. Brun**, **T. Bilgeri**, **G. Menard**, **V. Cherkez**, **R. Federicci**, **D. Longo**, F. Debontridder, M. D'angelo, D. Roditchev, G. Profeta, M. Calandra, and T. Cren. Phys. Rev. Lett. 120, 196402 (2018)

I continued this research activity in 2019 and 2020 in close collaboration with my colleague Tristan Cren on the experimental side. On the theoretical side, I strongly collaborated with Matteo Calandra specialist of advanced DFT calculations. I co-supervise with Tristan the PhD thesis of **Mehdi Torkzadeh** (2019-now) on

this subject, and co-supervised with Matteo Calandra in 2020 the master 2 internship of **Amitayush Thakur** (7 months) from the Indian Institute of Science Education and Research in Pune. I have written an ERC consolidator project on this particular topic that was unfortunately not granted, but that I will present below and will constitute the main project part of my HDR thesis.

Another aspect of this topic is the study ii) of the electronic properties of quasi-1D organic materials exhibiting a competition of phases between a spin-density wave groundstate and an unconventional superconductor. Denis Jérôme, a CNRS researcher from LPS Orsay who is a specialist of the physics of this family of materials and who co-discovered superconductivity in organic materials [Jerome1980], contacted us because he was interested in STM/STS measurements on $(\text{TMTSF})_2\text{ClO}_4$ materials. This is how I started to study these compounds in 2019-2020 during the master 2 internship of **Mehdi Torkzadeh**. We are now pursuing this work during his PhD thesis.

A) Electronic correlations and Mott physics in a single atomic plane

Introduction

The idea of using the dangling bonds of semiconducting surfaces to build 2D correlated systems [Tosatti1974] has found an ideal realization in the so-called α -phase systems, consisting in $1/3$ monolayer (ML) Pb or Sn grown on Si(111), Ge(111) or 4H-SiC(0001) [Santoro1999]. Generally in 2D systems one expects an increase of correlation effects due to a simultaneous reduction of the number of nearest-neighbours and of electronic screening [Perfetti2003]. In the α -phase systems, one tetravalent metal atom sits at each triangular T4 site, spaced by $\sim 7 \text{ \AA}$ from the neighbouring one: as seen in Figure 43a the X atom (X can be Sn or Pb) is located exactly above one Si or Ge atom situated in the second (111) atomic plane, enabling it to form covalent bonds with three semiconductor atoms from the top (111) surface plane (represented by small bright red dots). A single electron per site is then left giving rise to a narrow half-filled band of width W well isolated from the bulk bands (see Fig.43c). The strong on-site electron-electron repulsion is denoted U . The triangular unit cell is commensurate, comprises one single X atom and is written $\sqrt{3} \times \sqrt{3}$ with respect to the semiconductor lattice parameter in the (111) plane (the unit cell is the grey area delimited by dashed lines in Fig.43a).

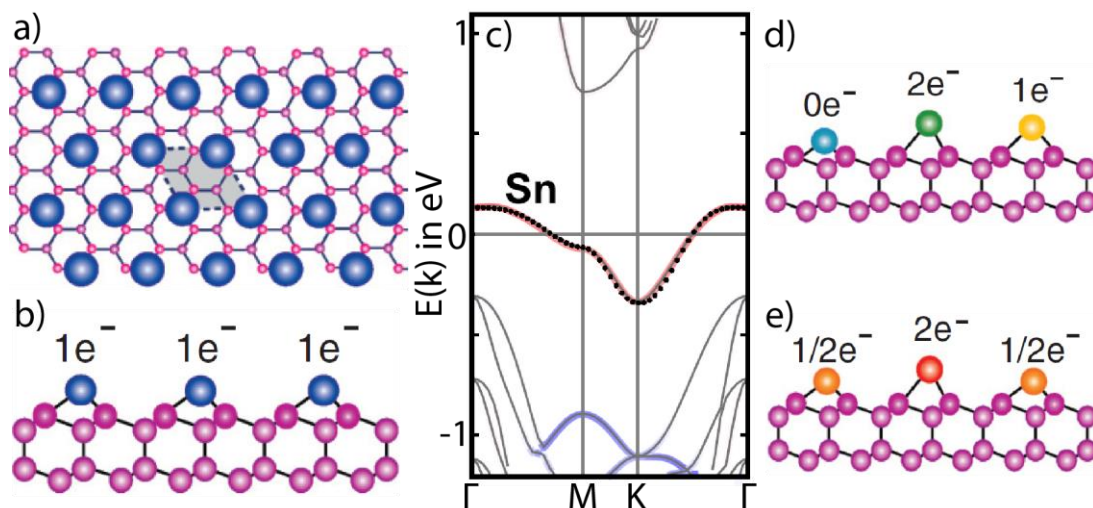


Figure 43: a) Structure of the α -phase $1/3$ monolayer $X/\text{Si,Ge}(111)$. In the top-view X blue balls represent Sn or Pb atoms. Smaller balls are Si or Ge atoms in the top (111) plane (brighter red) or in the second (111) plane (darker red). The triangular lattice has a $\sqrt{3} \times \sqrt{3}$ unit cell (grey area) depicted by black dashed lines. b) The side-view of the material shows 4 Si or Ge (111) atomic planes. Reproduced after [Cortes2013]. c) Bandstructure calculation of Sn/Si(111) in the DFT-LDA approximation. Reproduced after [Hansmann2013]. d) Charge-order phase having 3 inequivalent atoms in a 3×3 unit cell. e) Metallic phase having 2 inequivalent atoms (1 up, 2 down) in a 3×3 unit cell. Reproduced after [Cortes2013].

I now briefly remind the generic physics of 2D and 3D Mott insulators, assuming a half-filled single band system with on-site repulsion U [Georges1996]. This long-standing problem could be solved by modern approaches such as dynamical mean-field theory (DMFT). The results are displayed in Fig.44a as a function of U/W and $k_B T/W$, T being the temperature [Janod2015]. For $U=0$ the material is a half-filled band uncorrelated metal well-described by Fermi liquid theory and showing a standard density-of-states (DOS, shown in the right inset). When U/W increases there is a first-order phase transition between a paramagnetic correlated metal showing a quasi-particle peak in the DOS, and a paramagnetic Mott insulator state having a gapped DOS characterized by the opening of a gap $E_G \sim U - W$ between a lower filled (denoted LHB) and upper empty (UHB) Hubbard band. This phase transition is indicated by the thick continuous Mott line around $U/W \sim 1,15$. Importantly, the transition occurs without symmetry breaking between the two phases and ends up at a critical point (large dot) for $k_B T/W = 0,025$. This coloured part of the phase diagram is universal and common to all Mott insulators. At lower temperature (below the dashed line), various phase transitions can occur that are material dependent and accompanied by symmetry breaking. In this latter region, there can be for example spin and/or charge ordering, and also lattice re-ordering.

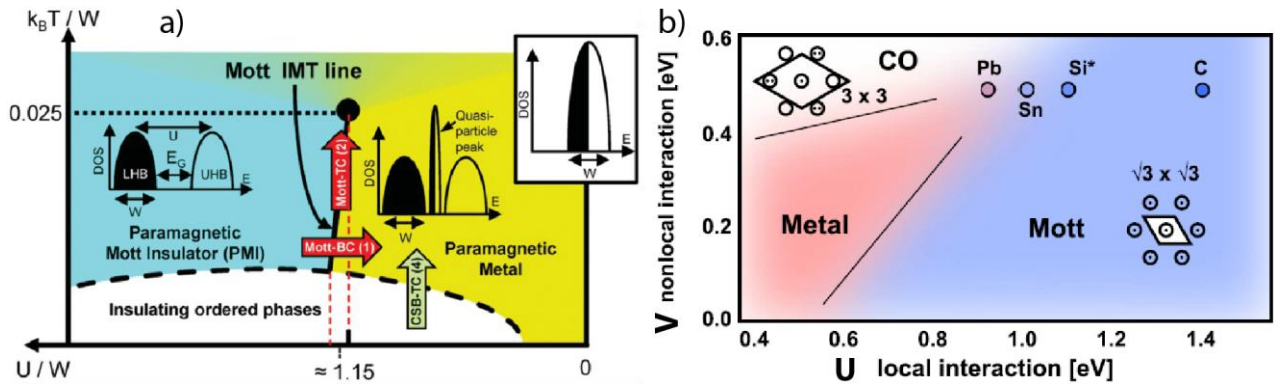


Figure 44: a) Phase diagram of the universal Mott transition. Red and green large arrows stand for Mott Bandwidth-Controlled (Mott-BC 1), Mott Temperature-Controlled (Mott-TC 2) and Crystallographic-Symmetry-Breaking Temperature-Controlled (CSB-TC 4). Reproduced after [Janod2015]. b) Predicted phase diagram for $X/\text{Si}(111)$ with $X=\text{C}, \text{Si}, \text{Sn}$ and Pb as a function of on-site repulsion U (horizontal axis) and nearest-neighbour repulsion V (vertical axis). For all X compounds the bandwidth W is about 0.5 eV. CO represents the charge order state such as the one shown in Figure 43d. Reproduced after [Hansmann2013].

For the α -phase systems, the typical bandwidth W calculated from one-electron energies using density-functional theory (DFT) in the local density approximation (LDA) is $W \sim 0.5$ eV, as illustrated in Fig.43c. Although this value is small, it may seem rather large for nearest-neighbour X atoms placed 7 Å apart. This is because the actual X - X hybridization is indirect and occurs through successive hopping onto three nearest-neighbour semiconducting atoms (2 semiconductor atoms are located in the top atomic plane and 1 is in the second atomic plane as seen from Fig.43b). An important consequence is that the Wannier wavefunction associated to the LDA surface band is not simply localized at the X atom but extends up to 4 atomic layers below the X atom in the semiconductor. This implies that the electronic charge is strongly delocalized over many atoms around the X one, which has to be considered in realistic theoretical descriptions of these systems. Precise calculations by the group of Silke Biermann of the screened on-site energy U by self-consistent GW+DMFT for the $X/\text{Si}(111)$ samples give values in the range 1 – 1.5 eV [Hansmann2013]. This value is consistent with the one calculated by Cesare Tresca and Matteo Calandra, $U = 1.75$ eV, for the $\text{Pb}/\text{Si}(111)$ system from our own work [Tresca2018]. **As a consequence we see that the α -phase materials seem to represent an ideal case for the application of the 2D single-band Hubbard model on a triangular lattice with spin $\frac{1}{2}$ electrons** [Santoro1999, Flores2001, Profeta2007, Hansmann2013]. This is a very important point for my HDR project since the single-band Hubbard model on a square lattice is at the core of many-body approaches trying to describe unconventional superconductivity in cuprates materials starting from a doped Mott insulator [Lee2006]. Let us also note that on a triangular lattice, there exist quasi-2D organic materials showing Mott physics and d -wave superconductivity upon doping, described by an anisotropic single-band Hubbard model [Kanoda2006]. In practice the theoretical models that have proved to be most appropriate to describe the α -phase systems are as follows: DFT+ U for effective single-particle approaches [Profeta2007] and implementations of the single-band Hubbard model for many-body approaches (such as DMFT for example in [Hansmann2013]).

Several experimental studies and theoretical works on the α -phase systems enable us to draw the following conclusions. For all X/Si(111), X/Ge(111), X/SiC compounds the strong on-site electron-electron repulsion U is the main driving force of the various low-temperature instabilities. From the $U \approx 1 - 1.75$ eV and $W \approx 0.5$ eV values quoted above, we see that U/W is larger than 2. From the phase diagram shown in Fig.44a) all compounds should be on the Mott side with a Mott transition developing below $T \approx 150$ K. Experimentally this situation may occur for some compounds but not for all. This discrepancy is due to the fact that other parameters may play an important role. On one hand, advanced DFT+U calculations indicate that the electron-lattice coupling should be taken into account and contributes to lattice distortion and charge re-ordering. On the other hand, various authors argued that nearest-neighbour electron-electron repulsion V should also be taken into account in addition to on-site electronic repulsion U to give a fully consistent picture (see for instance [Hansmann2013] and other references therein). Moreover our recent work on the 1/3 ML Pb/Si(111) phase showed that spin-orbit coupling also matters for heavy atoms such as Pb [Tresca2018]. Regarding the charge degrees of freedom, a general picture emerging in the α -phase systems is the existence of a competition between three different ground states [Profeta2007,Hansmann2013,Cortes2013], as illustrated in Fig.43b-d-e for X/Si(111):

- i) A Mott insulating state with a $\sqrt{3} \times \sqrt{3}$ unit cell having one electron per site. All X atoms are equivalent (this corresponds to the situation depicted in Fig.43b).
- ii) An insulating charge-order state with a 3×3 unit cell containing three inequivalent X atoms having nominally 0, 1 and 2 electrons per X atom (situation depicted in Fig.43d).
- iii) A metallic state having a 3×3 unit cell containing three X atoms among which two are inequivalent. One X atom is distorted up and carries nominally 2 electrons. The remaining two atoms are distorted down and share each $\frac{1}{2}$ electron (situation depicted in Fig.43e).

Looking at the phase diagram presented in figure 44b) calculated by Hansmann et al. using self-consistent GW+DMFT is instructive. It reports well the three types of ground states observed experimentally at various temperatures. It also places the Pb and Sn systems in the correct regions (experimentally the X=C or Si could not be synthesized until now). When $V = 0$ eV one recovers the standard first-order metal/Mott transition with increasing ratio U/W , the critical value being slightly above 1. When V becomes finite and smaller than U , it extends the domain of the metallic phase since it acts against U . When V increases above 0.4 eV and U is below 1 eV, an insulating charge order state is favoured where the electrons localize as in Fig.43d. As I mentioned above a drawback of these GW+DMFT calculations with respect to advanced DFT+U approaches is that they do not calculate the total energy of the system which can lead to erroneous conclusions when a coupling that is not taken into account plays an important role, as for instance the electron-lattice coupling. Thus my position with respect to this issue is the following. It is more careful to try to model first the whole system's electronic/lattice properties using most advanced DFT+U approaches and then compare to experimental results. In case of discrepancies between experimental and theoretical results, then many-body techniques might help rationalizing these differences and going one step further when all important parameters are well understood and under control.

Experimental studies using angular-resolved photoemission (ARPES), core level photoemission, surface x-ray diffraction, LEED, STM and in-situ transport [Cortes2006,Modesti2007,Cortes2013,Li2013,Odobescu-2017,Ming2017,Jäger2018] strongly suggest that a Mott insulating state is realized at helium temperature in Sn/Si(111) and Sn/Ge(111). Generally, the bandwidth W of Pb and Sn is comparable for Si and Ge substrate but is smaller on SiC. Larger values of the U/W are thus expected on SiC substrate, which should put these systems on the Mott side. This was indeed observed for Sn [Glass2015] but not yet for Pb. In Pb/Ge(111) the ground state at lowest temperature is unknown but a 3×3 distortion is reported between 250K and 50K. In Pb/Si(111), the low-temperature groundstate was also unknown before our work. I led the experimental part of a combined experimental and theoretical study [Tresca2018]. Using STM/STS at $T = 300$ mK we showed that the ground state is a correlated metallic state with a 3×3 unit cell having a “one up”- “two down” atomic configuration, in agreement with iii) above. Using DFT+U we could disentangle with great details the rich spectroscopic signatures appearing in the dI/dV spectra and showed that the 3×3 structure is stabilized both by an electron-phonon coupling and an electron-electron repulsion effect. We also showed that including spin-orbit coupling in the DFT+U calculations is crucial to give a consistent agreement with the experimentally measured site-dependent density of states. Through measurements of quasiparticle interference spectra (to be

explained below) [Crommie1993,Kohsaka2017], we went one step further and showed quantitatively that this strongly correlated 2D metal exhibits a well-defined Fermi surface split by Rashba spin-orbit coupling which leads to two concentric hexagons with opposite spin helicity. This is what I will present in the next section.

Correlated metallic groundstate of the 1/3 monolayer Pb/Si(111) with strong spin-orbit coupling

A peculiarity of the 1/3 monolayer Pb/Si(111) system is that this phase cannot be grown homogeneously over the whole silicon surface [Brihuega2005]. Indeed when trying to grow large domain sizes the 1/3 monolayer regions get more and more disordered, transforming significantly their electronic properties. Thus, an optimal size of the domains has to be chosen. We managed to grow rather nice patches of lateral size going from several tens of nanometers to less than 100 nm. In order to ensure a good electrical connection of the domains to the molybdenum contact electrodes placed on the sample surface, the 1/3 ML Pb/Si(111) patches are connected to the denser Pb/Si(111) monolayer having the $\sqrt{7} \times \sqrt{3}$ reconstruction. This is due to the fact the 1/3 ML Pb/Si(111) patches grow out of the denser Pb/Si(111) monolayer by sublimating Pb atoms. The sample surface is shown in figure 45a where the patches of interest grow first close to step edges or more rarely in the interior of terraces. Some of these patches are surrounded by a white circle in the image. Let us note that most of the sample is covered by the denser $\sqrt{7} \times \sqrt{3}$ - Pb/Si(111) monolayer (homogeneous yellow color), which is the same phase as the one studied previously in **Topic2E-G** (i.e. being superconducting below about 1.5 K). A close-up STM topography of a domain of interest is seen in panel 45b. As this is a high-resolution STM image, zooming on it with the mouse enables to see small dots organized in a Pb “one up”- “two down” atomic configuration, in agreement with iii) above and with panel e) in figure 43. According to the reference [Brihuega2005], the structural transition from the $\sqrt{3} \times \sqrt{3}$ homogeneous phase (corresponding to panel 43b) to the 3×3 low-temperature distorted phase having one Pb “up”- “two down” occurs around $T \approx 90$ K.

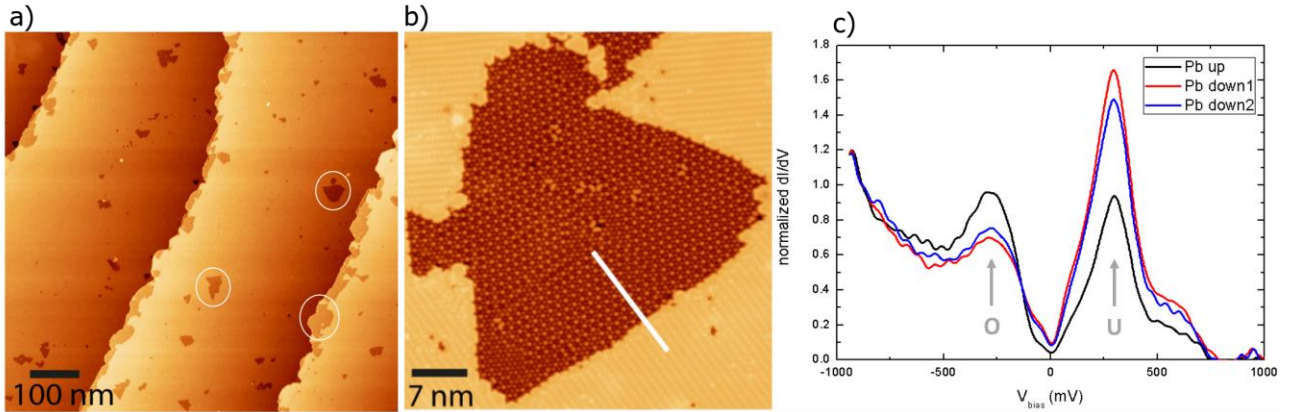


Figure 45: a) Large scale STM topography of the Pb/Si(111) sample. The domains of interest having the 1/3 monolayer 3×3 Pb/Si(111) reconstruction are the small dark areas of lateral size less than 100 nm. b) Small scale STM topography of such a 3×3 Pb/Si(111) domain. Each little dot is a Pb atom in a one up-two down configuration as depicted in figure 43e). c) Local dI/dV spectra measured by STS on the three different Pb atoms inside the unit cell. All presented measurements are performed at $T = 300$ mK. Set-point for topography and spectroscopy $V = -1.0$ V, $I = 200$ pA.

The local conductance spectra $dI/dV(V)$ measured on the three different Pb sites are presented in the panel 45c in the energy interval $[-1; 1]$ eV. They show that the single-particle LDOS is strongly reduced around the Fermi level ϵ_F (located here at zero-energy). Nevertheless the LDOS is not gapped at ϵ_F showing that this phase remains metallic. Furthermore, the LDOS consists in two large peaks labelled O and U, one located in the occupied states around -0.25 eV (O) and one in the unoccupied states around $+0.30$ eV (U). As our analysis shows below, this shape is the result of both the strong on-site repulsion U and large spin-orbit coupling. When comparing the $dI/dV(V)$ spectra, one also notices that they present the following characteristics: the spectrum measured on the Pb-up atom possesses a larger LDOS at the occupied peak O than the spectra measured at Pb-down atoms. Conversely, at the unoccupied peak U a much smaller LDOS is measured on the Pb-up atom than on the two Pb-down ones. These observations are consistent with the charge ordering associated to the “one Pb up-two Pb down” calculated by DFT+U in the Generalized Gradient Approximation, as shown in figure 46d) with the blue (Pb-up) and red (Pb-down) curves.

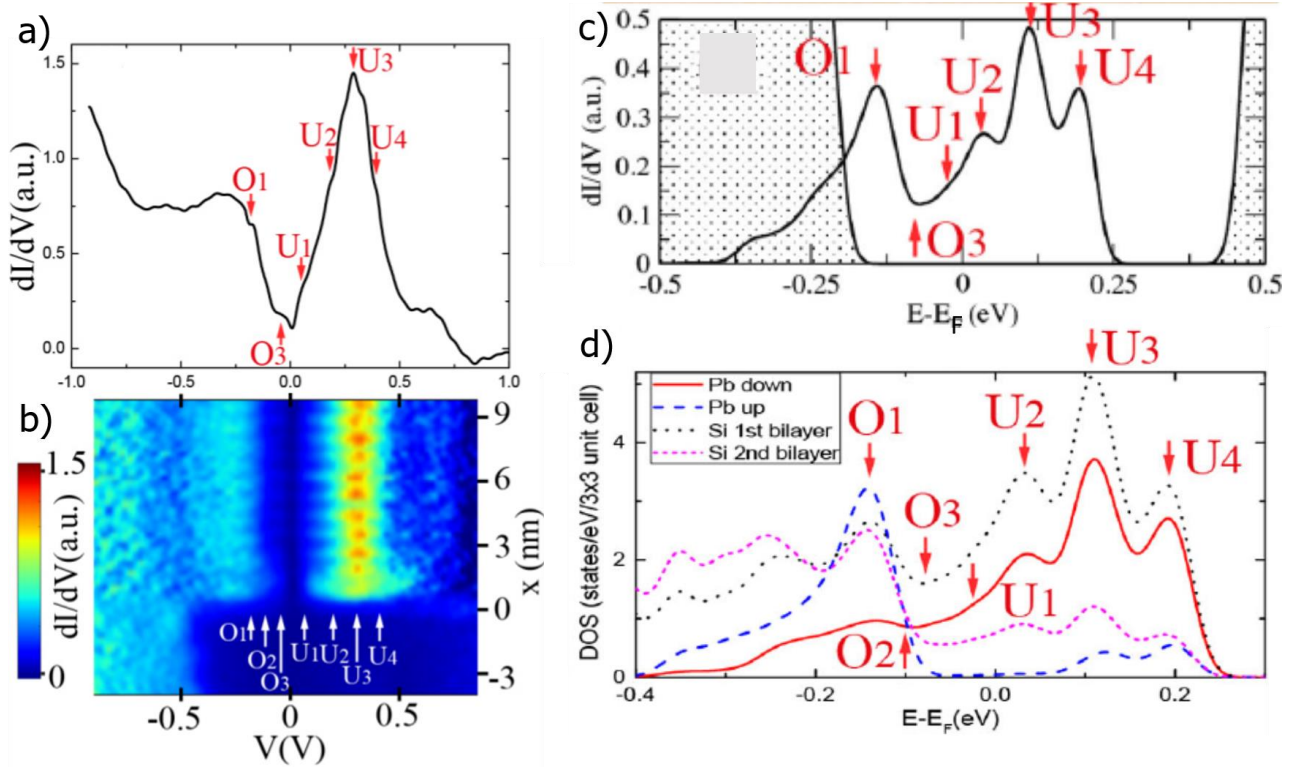


Figure 46: a) Average of the normalized dI/dV spectra of the $1/3$ monolayer $3 \times 3 - \text{Pb}/\text{Si}(111)$ phase. b) One-dimensional colour-plot of the dI/dV conductance measured along the white segment seen in figure 45b. The x-axis represents the bias voltage. The voltage scale is the same as the one of the panel a) enabling a direct comparison. The y-axis is the distance in nanometers, the origin 0 being taken at the interface between the 3×3 domain and the $\sqrt{7} \times \sqrt{3} - \text{Pb}/\text{Si}(111)$ dense monolayer. The differential conductance is plotted in colour, its scale being indicated on the left bar in arbitrary units. c) Total LDOS calculated using DFT+U approximation including spin-orbit coupling. The grey regions correspond to Si bulk states. d) Projection of the calculated LDOS onto the various atomic sites relevant for the $3 \times 3 - \text{Pb}/\text{Si}(111)$ phase (see figure 43b and 43e).

We make here a more detailed comparison between experimental measurements presented in figs 45c) and 46a) and the theoretical predictions for the total DOS or projected LDOS seen in figs 46c) and 46d). A qualitative agreement exists regarding the energy location of the main (indicated by the label O and U) and secondary peak structures (indicated by the labels O_i and U_i). Nevertheless, the spectral features appear less sharp in the experiment than in the calculations suggesting possible additional smearing of the excitations. Moreover, the spectral features observed in the experimental LDOS appear systematically at larger binding energies than in the calculations, especially for unoccupied states. Considering a functional that better treats the exchange and correlation term reduces this discrepancy and predicts a bandwidth $W_{th} \approx [-0.4; +0.4]$ eV closer to the experimentally observed $W_{exp} \approx [-0.5; +0.5]$ eV. Another important remark is that the experimental spectra show a larger suppression of the LDOS around the Fermi level than in the calculation. Interestingly, the panel 46b) enables measuring and visualizing the distance over which the bandstructure of the 3×3 domain establishes away from the dense $\sqrt{7} \times \sqrt{3}$ Pb/Si(111) monolayer. It shows that it is established over less than few nanometers, as expected for a sharp structural transition between a good metal and a bad metal. Moreover, as the panel 46b) shares the x-axis (voltage) with the panel 46a), a direct vertical inspection enables visualizing the O and U peaks with their oscillating height along the y-axis (distance x in nanometers along the white segment drawn in 45b) due to the “one Pb up-two Pb down” charge ordering in the 3×3 unit cell.

I address now an important issue related to the possibility of measuring with STM/STS technique the LDOS of a correlated system. I did not insist at all on this issue up to now, but here it appears to be crucial. The STS spectra presented in Figs 45c) and 46 a) are all normalized by their conductance values around -1 V.

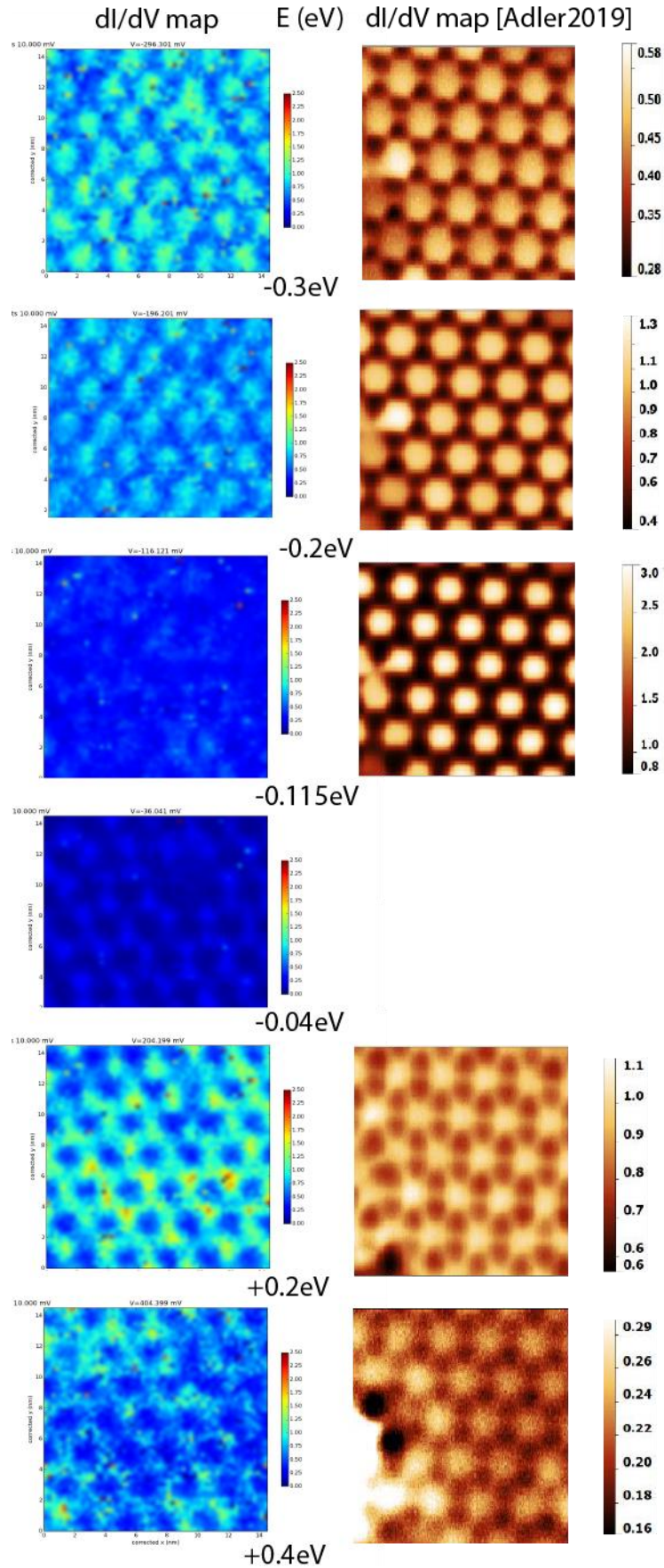


Figure 47: Comparison between our $dI/dV(E = eV, x, y)$ conductance map measurements (shown in the left column) and the ones from reference [Adler2019] (shown in the right column, extracted from figure S3). The area of the 3×3 region of interest is $14 \times 14 \text{ nm}^2$ for the left column and $12 \times 12 \text{ nm}^2$ for the right one. The energy E at which the $dI/dV(E, x, y)$ maps are measured is indicated below each pair of images. The energy value E equals successively -0.3 eV , -0.2 eV , -0.115 eV , -0.04 eV , 0.2 eV , 0.4 eV . The conductance

scale bar for the left column is constant for all images and is between 0 and 2,5. For the right column the conductance scale varies for each image and is indicated on the right next to each conductance map. N.B.: The right column image corresponding to -0.115 eV was in fact measured for -0.100 eV which makes very little difference.

This normalization procedure assumes that the LDOS is homogeneous over all different sites of the surface around this energy value. I chose this bias voltage or energy value because as seen from panel 46c) it is located already far from the 3×3 bandstructure that has an experimental bandwidth $W_{exp} \approx [-0.5; +0.5]$ eV. This energy of -1 eV below ϵ_F is actually located in the silicon valence band rather deep with respect to its onset (situated at -0.1 eV according to DFT+U calculations seen in panel 46c). One thus expects that for such excitation energies around -1 eV no strong spatial dependence of the LDOS should exist over the sample surface. Making this reasonable assumption enabled us to find a sound physical criterion to compare the local dI/dV spectra in the region of interest $E \in [-0.5; +0.5]$ eV. We found a qualitative agreement between our experimental results and the theoretical modelling, this agreement becoming even quantitative close to the Fermi level as we will show later. Nevertheless, if care is not taken during the STS measurements with respect to this normalization procedure, it can lead to erroneous conclusions and even contradictory results as we show now.

Figure 47 shows a comparison between two different types of measurements aiming at presenting the atomic scale evolution of the LDOS as a function of the energy $E \in [-0.5; +0.5]$ eV. The left column presents our measurements. Our various $dI/dV(E, x, y)$ conductance maps were all numerically differentiated and normalized according to the procedure described above from an $I(V, x, y)$ grid spectroscopy measured every Angstrom in x and y direction in the $14 \times 14 \text{ nm}^2$ area of interest at $T = 300$ mK. The set-point for single $I(V, x, y)$ spectroscopy measurement was $V = -1.0$ V, $I = 200$ pA. One sees that the energy evolution of this left column follows closely what was shown in the local $dI/dV(V)$ spectra in figure 45c): for energies $E \in [-0.5; -0.1]$ eV the LDOS is larger on the Pb-up atoms than on the down ones. Thus the conductance maps feature a brighter triangular lattice of dots associated to the Pb up atoms. This behavior also agrees with the theoretical predictions shown in panel 46d). For $E = -0.115$ eV there is experimentally an equal weight of the LDOS on Pb up and down atoms: thus for this particular energy $E \approx -0.1$ eV, the conductance map is homogeneous on all three Pb sites. This observation agrees very well with the prediction by the theory (see the red arrow O_2 in panel 46d) where the red and blue curves giving the projected LDOS on the Pb up and down atoms curves intersect). For energies $E \in] -0.1; +0.4]$ eV the weight reverses and the LDOS becomes larger on the two down Pb atoms than on the Pb up ones. Thus in this energy range, the conductance maps feature a brighter honeycomb lattice associated to the two down Pb atoms, while the LDOS associated to the Pb up atoms forms a triangular lattice of dark dots. This behavior agrees very well with the DFT+U theoretical predictions showing that for $E \in] -0.1; +0.4]$ eV the LDOS projected onto the Pb down atoms indeed dominates over the one of the Pb up.

In strong contrast with our measurements, the right column does not show such an energy dependence and presents always a triangular lattice of bright dots associated to the LDOS of Pb up atoms. These measurements from the STM/STS study of [Adler2019] were carried out in a different manner than ours. In their case, the $dI/dV(E, x, y)$ map is registered with a lock-in technique during the measurement of the STM topography performed in closed feedback loop, a small AC voltage being added to the DC bias voltage V . One sees that this procedure introduces here strong artefacts. This is due to the strong spatial dependence of the LDOS of the correlated $3 \times 3 - \text{Pb}/\text{Si}(111)$ material. With their method Adler et al. artificially modify the set-point of the spectroscopy measurements performed at different atomic sites which strongly changes the tip-sample distance between atomic sites presenting a different LDOS. Indeed in their case this set-point is determined by the bias voltage V used in the topography which furthermore changes for each different V value. The consequence is that this results in unphysical measurements. These considerations are very general and apply to any kind of correlated materials presenting a strongly site-dependent LDOS measured by STM/STS technique.

It is instructive to look in more details at the bandstructure calculated by DFT calculations by our colleagues Cesare Tresca and Matteo Calandra. The various steps are presented in figure 48. The material being modelled comprises the single layer of Pb atoms, and three silicon double layers underneath. The bottom Si bilayer is saturated with hydrogen atoms in order to avoid unphysical surface states appearing on the bottom side of the

sample, which should in fact correspond to a semi-infinite Si substrate. The atomic positions of the Si atoms of this bottom bilayer are taken equal to the reference positions of bulk Si atoms.

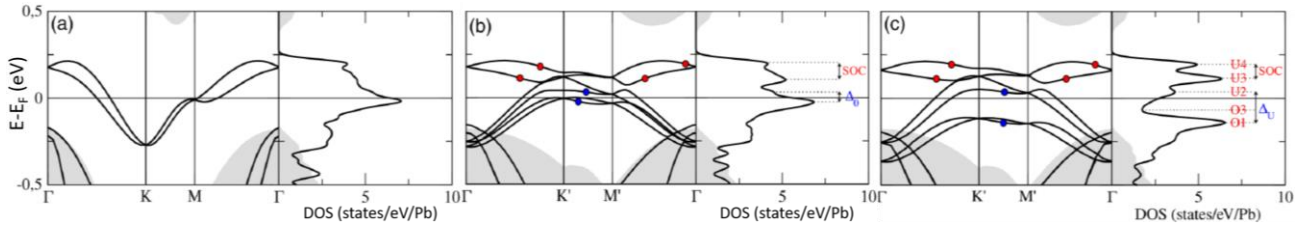


Figure 48: Bandstructure calculations using DFT in the Generalized Gradient Approximation taking into account spin-orbit coupling. a) Assuming a $\sqrt{3} \times \sqrt{3}$ unit cell, i.e. that all Pb atoms are equivalent as in panel 43b). b) Assuming a 3×3 unit cell with one Pb up, two Pb down configuration as in panel 43e). c) Assuming a 3×3 unit cell as in b) plus an on-site repulsion term $U = 1.75$ eV determined self-consistently.

A unit cell contains 3 Pb atoms and many more Si atoms. Periodic boundary conditions are assumed in all directions, with 16 \AA vacuum in the direction perpendicular to the surface. For Pb atoms 5d, 6s and 6p pseudo-potentials are considered to model these orbitals, while 3s and 3p ones are used for silicon. The lower energy cutoff is set to $45 \text{ Ry} \approx 610 \text{ eV}$.

The first simulated configuration shown in panel 48a) presents DFT calculations in the spin polarized Generalized Gradient Approximation (GGA) including spin-orbit coupling and assuming a $\sqrt{3} \times \sqrt{3}$ unit cell, i.e. that all Pb atoms are equivalent. When comparing the panel 48a) with the panel 43c), one sees that spin-orbit coupling provokes a large band splitting around the K point, in fact of Rashba-type, due the Pb heavy atoms. This type of bandstructure calculation is a starting point but should not correspond to the experimentally measured one since a 3×3 unit cell with one Pb up, two Pb down configuration is actually observed. Searching for a possible 3×3 structural distortion indeed leads to a larger energy gain (5 meV per Pb atom) with respect to the undistorted case. This distortion is here favoured by a coupling to phonons. The calculated height difference between the up and down Pb atoms is $\Delta h \approx 0.24 \text{ \AA}$, in good agreement with the experimental results giving a typical corrugation of 0.3 \AA for $V = +1 \text{ V}, I = 200 \text{ pA}$ scanning parameters. The optimized bandstructure with a 3×3 unit cell having one Pb up, two Pb down configuration is presented in panel 48b). The result is a folding of the Rashba-split bandstructure into a new smaller Brillouin zone leading to 6 bands instead of 2. The corresponding total DOS is presented on the right graph of the panel 48b). This clearly does not match with the experimental results featuring a large depletion of the DOS around the Fermi level. In this structural configuration, searching for a magnetic state does not lower the total energy of the system, suggesting that the metallic state would be paramagnetic. The third attempt was to include an on-site energy repulsion parameter U , associated to Mott physics as explained in the introductory section. The parameter U was evaluated self-consistently and found to be $U \approx 1.75 \text{ eV}$. The structure was again optimized and the 3×3 unit cell having one Pb up, two Pb down configuration was found to be the most favourable energetically, with an energy gain of 8 meV per Pb atom, thus larger than for $U = 0 \text{ eV}$. Interestingly, the local Coulomb repulsion is found to increase to the 3×3 distortion since $\Delta h \approx 0.32 \text{ \AA}$ which larger than $\Delta h \approx 0.24 \text{ \AA}$ found for $U = 0 \text{ eV}$. Again, the paramagnetic state was found to be the lowest energy state. The corresponding bandstructure is shown in panel 48c), which is identical to the ones presented in figure 46c) and 46d). We have seen in the previous paragraphs that these predictions present a good qualitative agreement with the experimental spectroscopic features. The agreement on the unoccupied states can be even improved using a functional (called HSE06) that treats the exchange term exactly. Furthermore, at small excitation energy E the agreement is very good as we will show now, by introducing another type of measurement called quasi-particle interference.

The Fermi surface calculated by DFT+U, associated to the optimized crystal structure presented above in panel 48c), is shown in figure 49a). It features two concentric hexagons centered on the Γ point, associated to a Rashba spin-split band. The spin components are mostly in-plane and orthogonal to the local \mathbf{k} vector, as we have seen previously in **Topic 3A** in figure 37c), and they run in opposite directions for the two sheets. Experimentally, since we have found that the groundstate of the $3 \times 3 - \text{Pb}/\text{Si}(111)$ phase is a correlated 2D metal, one can wonder whether it exhibits or not a well-defined Fermi-surface, such as the one predicted by DFT+U calculations. Our measurement presented in figure 49b) gives a positive answer to this question. The idea behind this measurement is that phase-coherent quasi-particle scattering occurring at low-temperature will

manifest itself by contributing to the $dI/dV(E, x, y)$ conductance map. This technique is called quasi-particle interference and has been pioneered by Don Eigler's group at IBM [Crommie1993]. One can refer to the reference [Simon2011] for a basic review paper. In presence of scattering centers in the probed material, the quasi-particle excitations injected at energy E will be scattered off from defects. Thus, quasi-particles will interfere with themselves which will lead to an additional spatial dependent signal in the LDOS and thus in the measured excitation spectra through the $dI/dV(E, x, y)$ conductance map. The scattering potential of the defects is usually unknown, but since our STM experiments are performed on a 2D Pb layer strongly bound to a Si substrate, we can image the surface defects directly. Looking at an image like the one seen in figure 45b) one sees that most of the defects are point-defects (i.e. vacancies or substitutional/interstitial atoms). There are also few extended defects such as domain boundaries. Thus the simplest practical assumption is to look first at the effect of point-defect assuming that it behaves as a scalar potential, i.e. that it corresponds to a non-magnetic impurity. This is highly reasonable since we use only silicon and lead atoms. In this case, the corresponding Hamiltonian of the point-scatterer centered in $\mathbf{r} = 0$ is $H_{defect} = V\delta(\mathbf{r})$ where V is the scattering potential.

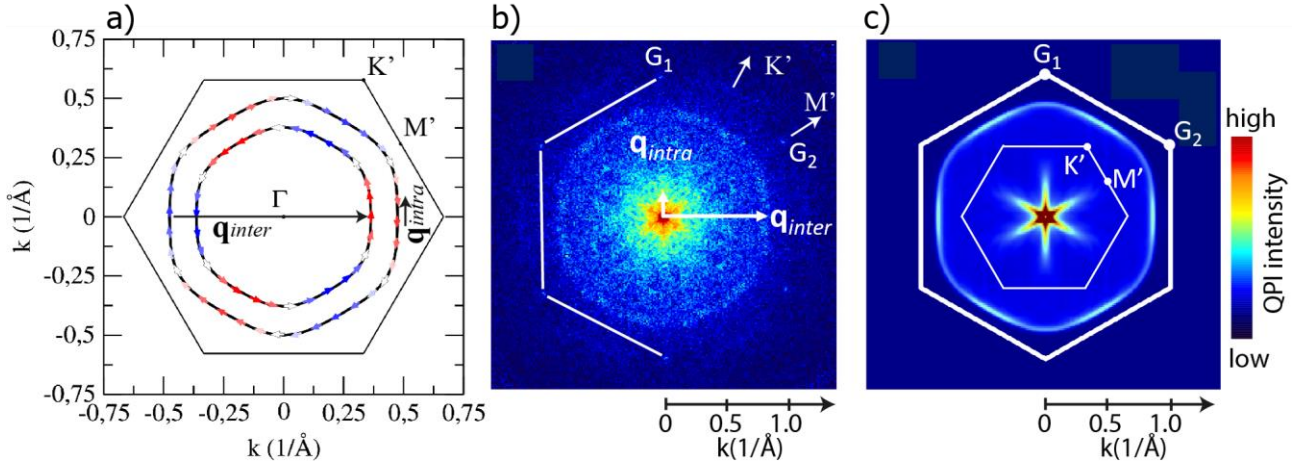


Figure 49: a) Fermi surface calculated from DFT+U for the optimized $3 \times 3 - \text{Pb}/\text{Si}(111)$ structure having one Pb-up two Pb-down atoms, corresponding to the bandstructure presented in panels 48c), 46c) and 46d). The thin continuous hexagon is the 3×3 first Brillouin zone. The coloured little arrows show the spin component which is mostly in-plane and of Rashba-type, the out-of-plane spin component being at most 1% of the in-plane component. Black arrows \mathbf{q}_{inter} and \mathbf{q}_{intra} indicate spin-conserving scattering vectors associated to scalar impurities. b) Fourier transform of a $60 \times 60 \text{ nm}^2$ $dI/dV(E = 0 \text{ eV}, x, y)$ conductance map measured at $T = 300 \text{ mK}$ and $B = 0.5 \text{ T}$, revealing quasi-particle interferences occurring at the Fermi level associated to scalar impurity scattering. c) Calculated quasi-particle interference map at $E = 0$ assuming pure scalar impurity scattering.

There are several theoretical methods to solve the effect produced by such point scatterers on the material's electronic properties. The most accurate one is called the T-matrix formalism [Mahan2000, Simon2011]. It can be solved in real-space and provides the space dependence of the LDOS we are interested in. Then a Fourier transform of the calculated LDOS can be directly compared with the Fourier transform of the experimental $dI/dV(E, x, y)$ map. This T-matrix formalism is equivalent to the summation to all orders of perturbation theory treating $H_{defect} = V\delta(\mathbf{r})$ as a perturbation. It is mandatory to use this T-matrix approach for materials presenting eigenstates that are not simply Bloch states. This is for instance the case of graphene, where the eigenstates have a spinor structure due to the existence of a sublattice spin $\frac{1}{2}$. This is also the case of superconductors since we have seen that the excitations are Bogoliubov quasi-particles with an electron and hole component. In the case we are interested in here, the bandstructure close to the Fermi level shown in panel 48c) and 49a) reveals 2 bands but the eigenstates can be simply described as Bloch states for each band, and are in fact close to the pure 2D Rashba case presented in the introductory part of **Topic3** (see the relation 58 where for each helicity band characterized by an index λ the eigenstates can be indexed as $|\vec{k}\lambda\rangle$). In this case, there is a simpler way to estimate theoretically the main elastic scattering channels than using the T-matrix formalism. This is called the Joint DOS approximation (see [Simon2011] for details). This is what our colleagues Cesare Tresca and Matteo Calandra did in our study. We present this approach and results now.

The joint DOS approximation relies on the Lindhard theory of screening of a localized impurity by an electron gas. A central physical quantity in this theory is the electronic susceptibility $\chi(\mathbf{q})$ given by:

$$\chi(\mathbf{q}) = \sum_{\mathbf{k}} \frac{f(E_{\mathbf{k}}) - f(E_{\mathbf{k}+\mathbf{q}})}{E_{\mathbf{k}} - E_{\mathbf{k}+\mathbf{q}}} \quad (70)$$

$\chi(\mathbf{q})$ relates the Fourier component of the induced charge $\rho_{ind}(\mathbf{q}) = \chi(\mathbf{q})\phi(\mathbf{q})$ to the screened potential $\phi(\mathbf{q})$. In the expression (70) $f(E)$ is the Fermi-Dirac function. This expression shows that the main contribution to the charge-density variation induced by the localized impurity will come from states verifying $E_{\mathbf{k}} = E_{\mathbf{k}+\mathbf{q}}$. These states are thus degenerate in energy and belong to a constant energy contour. A related quantity of interest for us is the Fourier component of the LDOS $\rho(E, \mathbf{q})$ at energy E and at wavevector $\mathbf{q} = \mathbf{k}' - \mathbf{k}$, where a Bloch state \mathbf{k} is scattered into a Bloch state \mathbf{k}' . In this approximation the localized scattering potential is considered to be weak and treated in first order perturbation theory. In our case we are interested in the Fourier components of the LDOS at the Fermi level, i.e. $\rho(E = 0, \mathbf{q})$ which is given by:

$$\rho(E = 0, \mathbf{q}) = \frac{1}{N} \sum_{\mathbf{k}, n, \mathbf{k}', m} |M_{\mathbf{k}n, \mathbf{k}'m}|^2 \delta(\epsilon_{\mathbf{k}n} - \epsilon_F) \delta(\epsilon_{\mathbf{k}'m} - \epsilon_F) \quad (71)$$

$M_{\mathbf{k}n, \mathbf{k}'m} = \langle \mathbf{k}n | \sigma_0 \exp\{i(\mathbf{k}' - \mathbf{k}) \cdot \mathbf{r}\} | \mathbf{k}'m \rangle$ is the matrix element between electronic states of the type $|\mathbf{k}n\rangle$ of energy $\epsilon_{\mathbf{k}n}$ calculated by DFT+U calculations and corresponding to the bandstructure presented in panels 48c) and 49a). N is a normalization factor linked to the finite number of $|\mathbf{k}n\rangle$ states used in the calculation. σ_0 is the identity matrix in spin states. The calculated quantity $\rho(E = 0, \mathbf{q})$ is presented in panel 49c). The vertices of the external white thick continuous hexagon are the Bragg reciprocal lattice vectors $\mathbf{G}_1, \mathbf{G}_2$ and their integer combinations. The thin continuous white hexagon is the first Brillouin zone where the \mathbf{K}' and \mathbf{M}' points are indicated, as in panel 49a). The center of the whole square is thus the Γ point. It is seen that the locus of $\rho(E = 0, \mathbf{q})$ presents two components:

- i) A six-branch star close to the Γ point whose directions are aligned with the Bragg vectors (i.e. with $\mathbf{G}_1, \mathbf{G}_2$ and their integer combinations).
- ii) An hexagonal-like contour whose most intense signal is along the \mathbf{K}' direction and along the other directions equivalent by 6-fold symmetry. A less intense signal exists along the \mathbf{M}' direction and the ones equivalent by 6-fold symmetry. This locus of \mathbf{q} -vectors is located in between the first Brillouin zone and the external hexagon joining the reciprocal lattice vectors.

The Fermi surface presented in panel 49a) enables interpreting easily these two components. The six-branch star is due to close to $\mathbf{q} = 0$ intra-band scattering processes, such as the one indicated by the black arrow \mathbf{q}_{intra} . Indeed such processes correspond to wavevectors aligned with the reciprocal lattice vector \mathbf{G}_1 . Similar processes taking place on other straight segments of the Fermi surface will give rise to the other directions aligned with the reciprocal lattice vectors. The hexagonal-like contour corresponds to inter-band processes, such as the one indicated by the black arrow \mathbf{q}_{inter} . In this case, the scattering process couples the two helicity bands by quasi-particles states having a quasi-parallel spin component. Such scattering processes are indeed mostly efficient along the \mathbf{K}' directions (and the ones equivalent by 6-fold symmetry) since there are large straight segments of the Fermi surface perpendicular to these directions. In contrast, such inter-band processes are weaker along the \mathbf{M}' direction where there are less electronic states. In addition, **the Fermi surface seen in panel 49a) also implies that intra-band backscattering is forbidden since it couples opposite spin components.** Let us note that such condition also exists in topological insulators or in graphene for instance, but does not hold in simple metals like Cu(111). This condition actually puts strong constraints on the processes that are allowed as far as non-magnetic point-scattering is concerned.

The Fourier transform of the experimental $dI/dV(E = 0 \text{ eV}, x, y)$ conductance map integrated over 0.5 meV is presented in panel 49b). In order to benefit from the largest phase coherence length the measurements were carried out at $T = 300 \text{ mK}$. A disadvantage of this operating condition is that we had to use a $B = 0.5 \text{ T}$ perpendicular magnetic field in order to prevent superconducting correlations, coming from the neighbouring $\sqrt{7} \times \sqrt{3} - \text{Pb/Si}(111)$ superconducting monolayer, from influencing the low-energy DOS of our $3 \times 3 - \text{Pb/Si}(111)$ area of interest. Nevertheless, the two main locus predicted by the simple joint DOS model for a scalar scattering potential are indeed observed experimentally. We also verified that a similar result was obtained at 4 K in zero magnetic field. This strongly supports the Rashba-like spin components predicted by DFT+U. Moreover, the six-branch star centered on Γ as well as the hexagonal-like contour corresponding to

q_{inter} processes almost quantitatively agree with the calculated ones. An additional signal is also seen for larger $|q|$ vectors than the ones of the six-branch star which is not present in the calculated $\rho(E = 0, q)$. The origin of this additional signal is not clear at present. Extended defects or correlation effects could contribute to it, as well as spin-orbit scattering induced by misplaced Pb atoms.

In conclusion of this study, there is a general agreement between experiment and theory regarding large-energy scale features (Figure 46), spatial and energy dependence of the LDOS (Figure 47) and last but not least fine spectroscopic features linked to low-energy scattering processes (Figure 49). This strongly suggests that our analysis and modeling by DFT+U of the structural and electronic properties of the $3 \times 3 - Pb/Si(111)$ phase is mostly adequate. This is an important result since this was not guaranteed in advance. It also shows that advanced DFT approaches can deal with correlated electronic materials with a high efficiency. Since these approaches can handle the lattice degrees of freedom together with the charge and spin degrees of freedom, this confers them a high degree of confidence to my opinion. The present results were published as: *Chiral spin texture in the charge-density wave phase of the correlated metallic Pb/Si(111) monolayer*, C. Tresca, C. Brun, T. Bilgeri, G. Menard, V. Cherkez, R. Federicci, D. Longo, F. Debontridder, M. D'angelo, D. Roditchev, G. Profeta, M. Calandra, and T. Cren. Phys. Rev. Lett. 120, 196402 (2018). Based upon this study, I built a research project aiming at studying the whole family of $1/3$ monolayer systems consisting of X/Si(111), X/Ge(111) or X/SiC(0001) where X stands for a Pb or Sn atom. Among these 2D materials some of them should be Mott insulators and present a magnetic groundstate. For these latter materials it should be possible to induce unconventional superconductivity out of their magnetic Mott state. Since on one hand the lattice, charge and spin degrees of freedom can be efficiently measured in such materials by STM/STS and other surface sensitive techniques, and on the other hand modelled by advanced DFT+U and related approaches, it should enable further precise modelling of the nature of the unconventional superconductivity. This is the essence of the research project that I present below.

Research Project: From Mott to superconductivity in a single atomic plane

Project introduction

I present in this section my research project for the next years. Among the various research topics I presented in this HDR thesis, during which I co-supervised many master students, PhD students and post-docs, I plan pursuing most of them. The reason for this is that these topics are deep and broad enough so that there remains numerous open questions I am willing to tackle. Nevertheless I will not present here in details for each topic addressed above what I plan to do in the near future. In contrast I chose to retain only one topic among the numerous ones, because of its innovative character and also because I wrote an ERC consolidator project about it which was unfortunately rejected. I used here large parts of this text as it was written but in a more compact version. This project deals with the **Topic4** addressed above. Thus I strongly suggest the reader to read this section after having read the previous 2 sections of the present **Topic4A**) entitled “*Electronic correlations and Mott physics in a single atomic plane*”, since there is a continuity.

- There is one PhD student working on this project. His name is **Mohammadmehdi Torkzadeh**. He started in November 2019. Currently his official PhD advisor is my colleague Tristan Cren. Having this HDR habilitation I will become official co-advisor.

The understanding of complex phenomena in condensed matter physics greatly benefited from the simplification in the chemistry of experimentally available materials. Let us think for instance about conventional superconductivity in Al or Pb. The very fact that these cubic metals have a single atom per unit cell and behave as good Fermi liquids enabled a full understanding in every details of the Bardeen-Cooper-Schrieffer theory. Recent progresses in the modelling of the electronic and structural properties of such simple materials even enabled calculating ab initio their complex superconducting properties. Another illuminating example is the recent discovery of topological properties in the electronic bandstructure of solids. This great achievement was initiated through model systems incorporating only the necessary ingredients enabling the demonstration of topological properties. It was first implemented in graphene, one of the simplest two-dimensional (2D) material having only one single type of atom per unit cell. This great simplification in the

system's chemistry enabled setting solid theoretical grounds. This gave rise later to a burst of studies of topological properties of materials beautifully ending with a systematics proposed for complete electronic band theory describing all possible weakly correlated materials [Bradlyn2017]. If one now considers the emblematic case of high-temperature superconductors, one faces a situation where the great chemical complexity of the cuprates materials give rise to several coexisting orders: d -wave superconductivity, charge-density waves, charge stripes, spin-density waves, etc [Norman2003]. These orders have an unclear relationship with respect to the mechanism responsible for unconventional superconductivity and add many extra complications. A reasonable consensus is that the parent undoped compound is a Mott antiferromagnetic insulator, from which unconventional superconductivity is induced upon hole or electron doping [Lee2006]. It would then be highly desirable to find much simpler materials that would present only these basic ingredients in order to test available theoretical models with much stronger constraints on the possible microscopic parameters actually realized in real materials. This is precisely the aim of the present HDR project: furnishing a canonical class of simple systems presenting two-dimensional Mott physics from which unconventional superconductivity can be induced and studied in its full complexity.

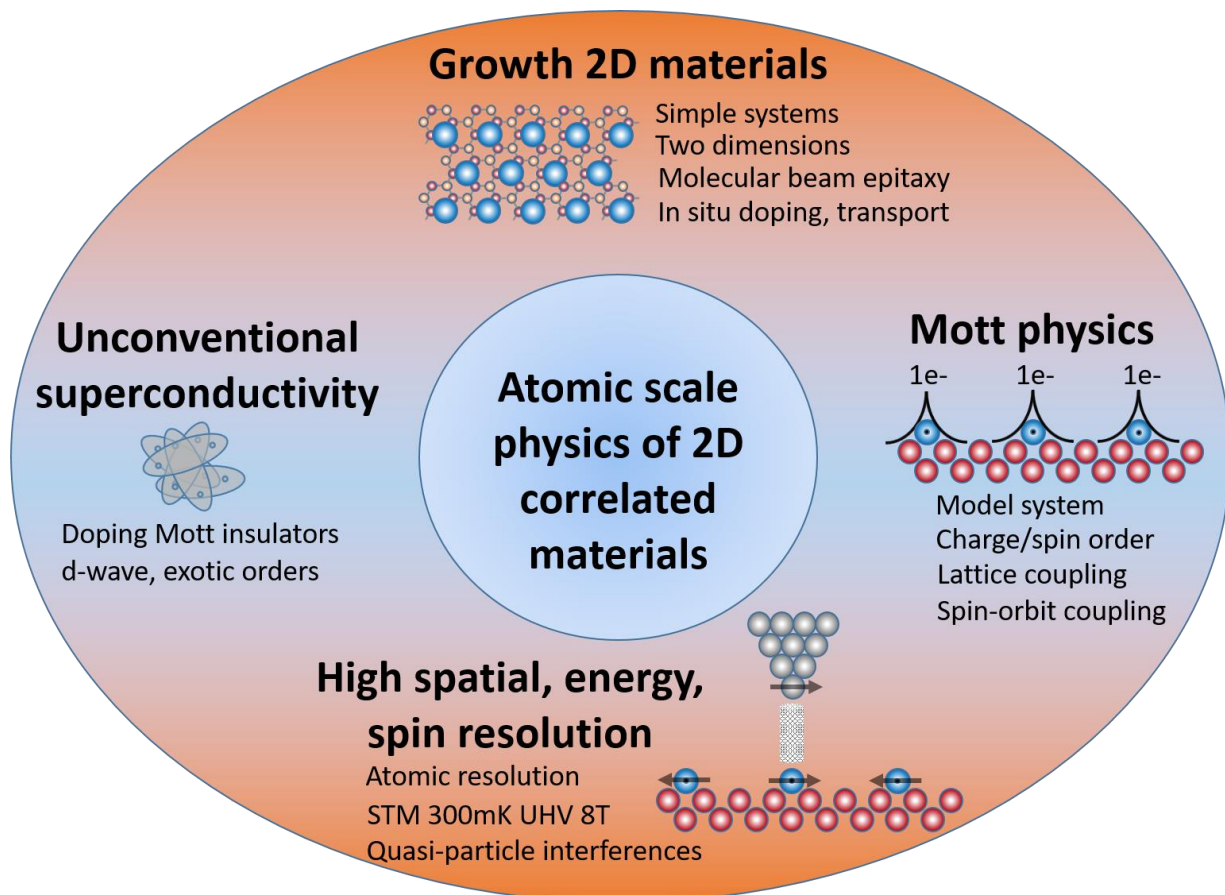


Figure 50: Graphical project's summary.

The prototypical class of systems I propose to investigate consists in a monolayer of group IV metal atoms (Sn or Pb) grown at the surface of group IV semiconducting substrates (silicon, germanium or SiC) [Santoro1999]. They are called α -phase materials in the surface physics community. I have shown above that these systems can be prepared in a crystalline phase having a 2D triangular lattice where each tetravalent metal atom (Sn or Pb) sits about 7 \AA from its next-nearest neighbor (see Figure 43a). Each tetravalent metal atom forms covalent bonding with three underlying Si or Ge atoms, leaving one free electron per site. This system ideally realizes a 2D crystal having a single half-filled electronic band, isolated in the bandgap of the semiconductor [Santoro1999]. These surface systems also provide a great simplification for modelling their electronic and structural properties since they possess only two different atoms with $s-p$ hybridized orbitals, organized in a well-defined crystalline order with a small unit cell. Sn/Ge(111) and Sn/Si(111) were suggested to have a Mott insulating ground state, although there remain many open issues about their charge order at low temperature. Their magnetic order is also completely unknown at present [Cortes2006, Modesti2007]. The ground state of Pb/Ge(111) is unknown. Our colleagues Cesare Tresca and Matteo Calandra performed DFT+U calculations for Pb/Ge(111) (similar to the ones presented above for Pb/Si(111)) and predicted a

correlated 3×3 metallic groundstate. Pb/Si(111) was studied by our own group and we have shown that it is a strongly correlated metal close to a Mott transition but strongly affected by spin-orbit coupling [Tresca2018]. Under the guidance of Matteo Calandra and myself, Amitayush Thakur performed DFT+U calculations of the Sn/Si(111) phase during his master 2 internship in 2019-2020. He found that the groundstate should be a small gap insulator ($E_g \approx 70$ meV) having a magnetic groundstate most probably being an antiferromagnetic so-called row-wise order. Our preliminary STM/STS measurements in 2021 during the PhD thesis of Mehdi Torkzadeh seem to confirm these predictions, although the existence and nature of the magnetic state is not yet elucidated at present.

Taking advantage of the great simplification in the chemistry of the materials, this project aims first at determining the microscopic parameters, i.e. charge, spin and lattice orders, characterizing these 2D strongly correlated materials from high-resolution spectroscopy. Spectroscopy measurements will be carried out by us using a state-of-the-art scanning tunneling microscope (STM) operating at very-low temperature (300mK) and in high magnetic field (10T). Non spin-polarized STS measurements will be carried out as usual with a Pt tip. Spin-polarized measurements will be carried out with Marie Hervé a young CNRS researcher hired 2 years ago in our group, who is specialist of spin-polarized STS on magnetic materials. Through various collaborations to be presented hereafter, other spectroscopic tools including macroscopic ones will be used in the course of this project. The whole project's idea is illustrated in a graphical way in figure 50.

In a second step, starting from a fully-characterized Mott ground state our goal will be to metallize it by electron or hole doping using various schemes, in order to induce and characterize unconventional superconductivity, unveiling predicted exotic orders such as chiral d -wave or f -wave symmetry.

Crucial issues to be addressed in the project

I list here the 6 key issues that form the backbone of my scientific project.

1) **The magnetic state, i.e. the spin order, is completely unknown at any temperature** in all α -phase materials. Knowing the spin ordering will enable determining which magnetic state is realized with which symmetry. This piece of information is key to fully characterize the quantum states and the interplay between charge and spin orders. It is particularly crucial in the Mott states of Sn/Si(111), Sn/Ge(111) and Sn/SiC. Various possible magnetic states are predicted on a triangular lattice depending on the ratio between the hopping parameters, U and V : paramagnetic, 120° in-plane antiferromagnetic Néel order, row-wise antiferromagnetic order, non-magnetic insulating spin-liquid states [Balents2010,Li2011,Badrtdinov2016]. The antiferromagnetic ordering energy should be given by $J \sim t^2/U$ [Lee2006] which gives 3 – 5 meV for our materials. These low energy values are consistent with structural transitions observed in Sn/Si(111) and Sn/Ge(111) below 60 K, which could thus present a magnetic state. Experimentally there is a lack of clear-cut experimental results in my opinion: for instance in Sn/Si(111) older low-temperature results reported a band folding by ARPES inconsistent with a pure $\sqrt{3} \times \sqrt{3}$ symmetry possibly induced by an underlying dynamic 3×3 order. More recent results interpret similar data as consistent with a row-wise antiferromagnetic order [Li2013,Jäger2018], while to my opinion a clear symmetry difference between 3×3 and $2\sqrt{3} \times \sqrt{3}$ cannot be made based solely on available results due to a macroscopic contribution from all 3 –fold degenerate orientational domains. Performing STS measurements at $T = 0.3$ K, thus benefiting from a much larger phase coherence length, locally in single magnetic domains using both normal and spin-polarized tips, in combination with quasi-particle interference experiments should enable us to fully resolve this issue and reveal the magnetic ordering and its symmetry if it exists.

2) **The full picture of the various (competing) charge orders** realized in all X/Si(111), X/Ge(111), and X/SiC(111) for X=Pb or Sn, as a function of temperature is missing in order to establish a complete phase diagram. The present α -phase $1/3$ monolayers provide a particularly clean and tunable system with low-disorder and without mixing-in multi-orbitals like in more complicated materials. In contrast our surface materials present a single-orbital character enabling true first-principle treatments which should enable us refining our understanding of competing instabilities in the proximity of different ordering phenomena [Hansmann2016]. This issue is general and occupies a noticeable place for example in the cuprates literature where conflicting interpretations exist about charge-stripe or checkerboard charge ordering, their driving mechanism and implications for superconductivity (see for instance [Julien2015] and references therein).

3) **The role of the electron-lattice coupling** on the various competing orders (charge and spin) is very important in general and particularly for surface systems such as ours. It could favour or act against effects produced by electronic correlations. For instance in Sn/Ge(111) a soft phonon freezes at low temperature stabilizing a 3×3 lattice [Farias2003] while it remains dynamic in Sn/Si(111) [Ortega2002]. In Pb/Si(111) we showed that both electron-phonon and electron-electron interactions act together favouring a 3×3 reconstruction [Tresca2018]. It could be different and act in an opposite way for the remaining systems. A systematic study is lacking for all α -systems as a function of temperature. Experimental results have to be confronted to DFT+U calculations to analyse precisely the electron-phonon contribution to the various instabilities (see [Tresca2018]). This issue is critical for DMFT approaches which cannot handle at present the coupling to lattice degrees of freedom. Nevertheless for some systems this coupling seems not the dominant one (for instance in Sn/Si(111)).

4) **The role of spin-orbit coupling** on the charge and spin ordering, and more generally on the electronic correlations is largely ignored up to now in the α -phase systems. This needs to be investigated in details in the heaviest compounds (Pb), where we have already showed its importance on Si(111) [Tresca2018]. It should have profound effects as well on Ge and SiC substrates, the former to be on the metallic side and the latter on the Mott side. Theoretically, strong SOC is expected to affect largely the physics of correlated electrons [Balents2010], but few detailed studies exist up to now [Brosco2020]. In the α -phase materials SOC effects should nevertheless not be very strong since their energy scale is always (much) smaller than the on-site electron-electron repulsion energy U . In the Sn compounds SOC effects should be much smaller although not negligible [Bardinov2018]. Again the α -phase materials appear as a simple tunable 2D system to probe SOC effects on electronic correlations/Mott physics in a clear way, starting from a single-band system.

5) **Could other 2D surface systems, having a triangular, square or rectangular lattice, be also used to investigate 2D Mott physics as clearly as with the α -phase materials?** The very interesting situation of monolayer transition metal dichalcogenides (TMD), some of which being well-known bulk Mott insulators (for 1T-TaS₂ see [Perfetti2006] and ref therein) or surface Mott insulators (1T-TaSe₂ [Perfetti2003]), deserves our full attention in the framework of this project.

6) **Can unconventional 2D superconductivity be induced from the Mott insulating states of the α -phase surface systems by electron/hole doping, as it is known to occur in several families of materials including the cuprates [Lee2006]?** A recent theoretical work suggests such a possibility and predicts chiral d -wave superconductivity induced by spin and charge fluctuations [Cao2018]. Using $U = 0.7$ eV and $V = 0.2 - 0.3$ eV, which are reasonable parameters for the X/Si(111) compounds as shown previously (see Figure 44b), a superconducting dome is predicted upon hole doping with a high maximum critical temperature $T_c \sim 60$ K at optimal doping as illustrated in Figure 51.

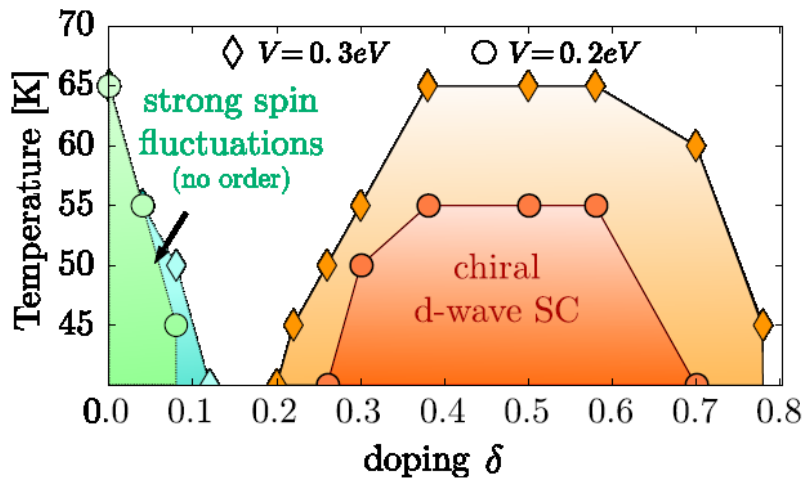


Figure 51: Calculated phase diagram for a single-band Hubbard Hamiltonian describing the α -phase surface materials having long-range Coulomb interactions (V parameter) and on-site energy repulsion $U = 0.7$ eV using the TRILEX approximation. Reproduced after [Cao2018].

This phase diagram resembles the ones where d -wave superconductivity is induced upon electron/hole doping of Mott insulators having a square lattice (case of cuprates [Lee2006]) or triangular lattice (case of organic quasi-2D materials [Kanoda2006]). More exotic orders such as spin-triplet f -wave superconductivity could also be induced if the Fermi surface would present several small pockets [Kuroki2001] or due to the breaking of the inversion symmetry induced by the surface [Smidman2017]. Let us note that a first report of superconductivity induced in the 1/3 ML Sn/Si(111) was done recently using heavily Boron-doped substrates [Wu2020]. It is not clear yet whether this superconductivity is unconventional or not but is very encouraging for our project.

Collaborations

This project is at the interface between surface science, nanoscience, physics of correlated electronic systems, superconductivity, mesoscopic physics and quantum magnetism. The STM/STS local spectroscopy skills are well-mastered in our group, including spin-polarized STS which is very important here. The whole team of our group consisting in the researchers Tristan Cren, Marie Hervé and Marie d'Angelo will participate to this work. The strong technical support of Pascal David and François Debontridder will help us maintaining our set-up and continuing developing new set-up/devices. I plan nevertheless to have several external collaborations to strengthen this project.

Angular resolved photoemission (ARPES) and core level photoemission spectroscopy (PES) experiments

ARPES of the valence states and/or core level PES experiments will be useful to complement STM/STS studies. Among the α -phase systems, I want to probe the occupied states of Pb/Si(111), Pb/Ge(111) and Pb/SiC which were largely unstudied, and investigate their temperature dependence. I also wish to investigate the surface Mott phases. I will do this task in collaboration with Marie d'Angelo (assistant professor in our group). She is specialist of ARPES and Core level PES on 2D materials. We started working together on 1/3 monolayer of Pb/Si(111) [Tresca2018]. The ARPES experiments will be carried out in collaboration with Andres Santander at Paris-Saclay University, who is a specialist of strongly correlated materials. Part of the experiments will be performed at his lab and part applying in synchrotron facilities. Amitayush Thakur, who was master 2 student with me and Matteo Calandra and who is now PhD student with Andres will participate to these measurements.

X-ray magnetic circular or linear dichroism (XMCD-XMLD) experiments

STS measurements done with normal and spin-polarized tips will give us information about the local spin ordering in the Mott insulating state. It will be desirable to have complementary information about the local magnetism using other experimental techniques, in particular to quantify the magnetic moment. This type of measurements can be done using XMCD or XMLD experiments in synchrotron facilities such as at DEIMOS beamline at synchrotron Soleil or ID12 at ESRF. I initiated a collaboration with Danilo Longo, who was our former PhD student and is now post-doc on this beamline. We collaborated together at the DEIMOS beamline to measure the magnetic moments of individual MnPc molecules deposited on various metallic and superconducting monolayers in the framework of another project (ANR [Rodesis](#)). I will take advantage of this collaboration to apply with him for beamtime within this project.

Growth of Transition Metal Dichalcogenides (TMD) materials

The idea here is to study another family of correlated electronic materials on a triangular lattice. The growth and optimization of TMD monolayers (1T-TaSe₂) will be carried out in collaboration with the epitaxy group of my institute (Paola Atkinson, Mahmoud Eddrief). They have a strong experience in molecular beam epitaxy (MBE) growth of topological insulators and are starting to grow TMD materials. A TMD dedicated MBE chamber was set-up in 2020. The samples will be transferred from the MBE to our VT or M3 low-temperature STM using an ultrahigh vacuum suitcase.

Ab initio calculations of 2D materials

This project will highly benefit from a strong coupling between theory and experiment. Modelling the structural and electronic properties, their mutual coupling, using ab initio DFT approaches is very important to furnish a single-particle band picture of our systems. Including spin-orbit coupling and correlation effects in DFT+U and/or using advanced hybrid functionals has revealed to be crucial and efficient [Tresca2018]. I started a close collaboration with Matteo Calandra (CNRS director of research who moved last year to the

University of Trento). He is an internationally recognized expert in DFT calculations, co-developer of the Quantum Espresso worldwide spread code.

Theory of strongly correlated materials

Another theoretical collaboration will exist with a researcher specialist of strongly correlated systems: Prof. Silke Biermann (Ecole Polytechnique). Starting from the single-particle electronic spectrum obtained from DFT methods, Biermann *et al.* could demonstrate the possibility of describing real α -phase materials by solving self-consistently a parameter-free many-body Hamiltonian having both on site U and nearest-neighbour V Coulomb repulsion terms using GW-DMFT [Hansmann2013,Hansmann2016]. Until now only charge orders were addressed without including SOC nor the electron-lattice coupling. Although we have no article in common yet, a close contact has already been established and will be pursued throughout this project. Silke knows well the results of our first study [Tresca2018]. Since my project aims at giving a precise characterization of the various charge and spin orders existing in the α -phase materials at various temperatures and doping levels, this should enable improvements of single-band Hubbard models aiming at describing real correlated 2D materials. This should further put strong constraints on the theoretical models able to describe the microscopic origin of unconventional superconductivity in these systems.

B) Unconventional superconductivity in quasi-1D organic (TMTSF)₂ClO₄

I will end this HDR thesis by presenting a last subject of research dedicated to the study of the electronic properties of quasi-1D organic materials, becoming superconducting under particular physico-chemical conditions. Denis Jérôme, a CNRS researcher from LPS Orsay who is a specialist of the physics of this family of materials and who co-discovered superconductivity in organic materials [Jerome1980], contacted us because he was interested in STM/STS measurements on (TMTSF)₂ClO₄ materials that present a competition between a superconducting and spin-density wave groundstate. This is how I started to study these compounds in 2019-2020 during the master 2 internship of **Mehdi Torkzadeh**. We are now pursuing this work during the PhD thesis of Mehdi. Since this HDR thesis is already rather long, I will be brief on this subject. No publication on this subject has been published yet.

Introduction

There are two kinds of materials that exhibit superconductivity among organic crystals, (TMTSF)₂X or “Bechgaard salts” and the (BEDT-TTF)₂X salts. TMTSF stands for the tetramethyl-tetrafulvalene electron-donor molecule, (BEDT-TTF) is the bisethylenedithio-tetrathiafulvalene and X is a monovalent anion. Bechgaard salts are quasi-one-dimensional systems showing unconventional superconductivity with a competition between a spin-density wave groundstate (having an insulating ground state) and a superconducting state [Jérôme2016].

(TMTSF)₂PF₆ is the prototypical Bechgaard salt. It shows a superconducting behavior under pressure above 9 kbar, the groundstate being a spin density wave (SDW) state at lower pressure [Jerome1980]. The aim of our own study was to probe the low-temperature electronic properties of (TMTSF)₂ClO₄, which is the only ambient pressure superconductor of the (TMTSF)₂X family discovered shortly after (TMTSF)₂PF₆. The crystal structure of (TMTSF)₂ClO₄ is the triclinic space group $P\bar{1}$. The unit cell parameters are $a = 7.27 \text{ \AA}$, $b = 7.7 \text{ \AA}$, $c = 13.28 \text{ \AA}$ and $\alpha = 84.58^\circ$, $\beta = 86.73^\circ$ and $\gamma = 70.43^\circ$ [Pouget2012]. Figure 52 shows a schematic picture of the view perpendicular to the ab plane of this material, i.e. along c^* . The ab plane is the most conducting plane. a is the quasi-1D direction along which the TMTSF molecules are stacked on top of each other forming conducting chains. a is thus the most conducting axis. b is less conducting and the c^* direction is the least conducting axis.

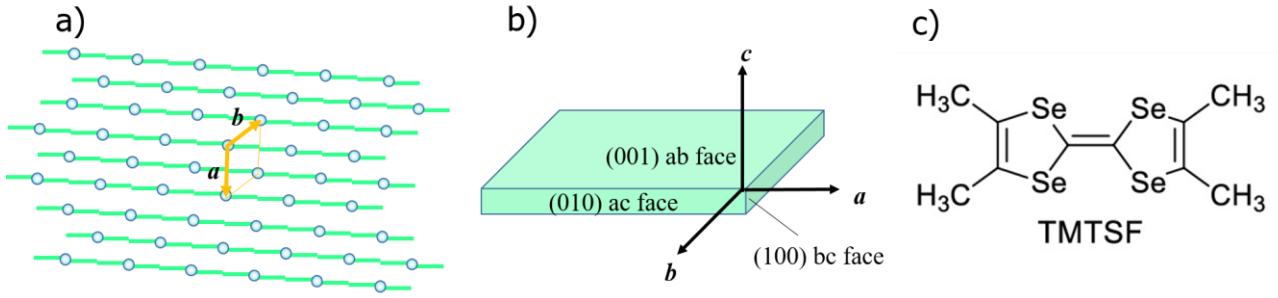


Figure 52: Main structural properties of $(\text{TMTSF})_2\text{ClO}_4$ crystal. a) View normal to the \mathbf{ab} plane, the natural cleavage plane of the surface. Each dot represent a ClO_4 ion. Each green segment represent a TMTSF molecule. The plane of each molecule is locally perpendicular to \mathbf{a} direction. b) Crystal structure main axis. c) TMTSF molecule. Figure from the master thesis of Mehdi Torkzadeh 2019.

We will first introduce the useful basic electronic properties of $(\text{TMTSF})_2\text{PF}_6$ before going to those of $(\text{TMTSF})_2\text{ClO}_4$. As shown in figure 53, the electrical resistivity at ambient pressure in $(\text{TMTSF})_2\text{PF}_6$ is strongly anisotropic with respect to the direction of the applied current. It is minimum along the chain direction, 100 times larger perpendicular to the chain direction in the \mathbf{ab} plane (denoted \mathbf{b}' direction in Figure 53) and 10 000 times larger perpendicular to the \mathbf{ab} planes along \mathbf{c}^* . The transition to a SDW ground state between 10 and 20 K is seen by a large increase of resistivity at lower temperature.

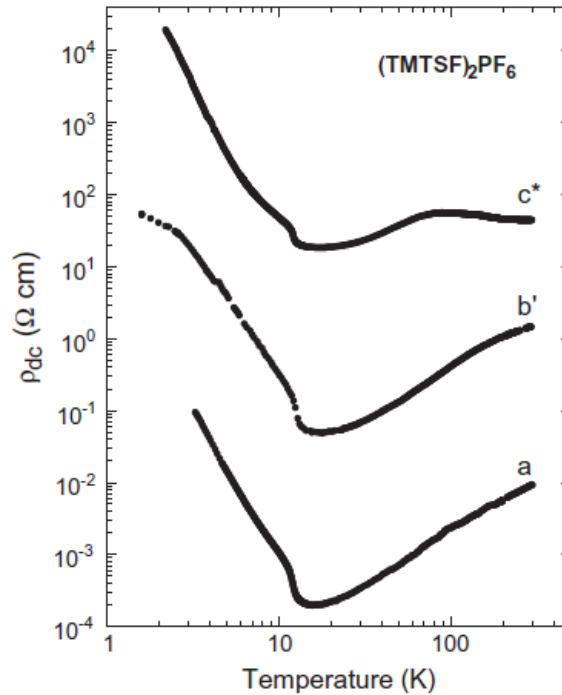


Figure 53: Electrical resistivity measurement along different crystallographic directions of $(\text{TMTSF})_2\text{PF}_6$. Reproduced after [Brown2015].

In the $(\text{TMTSF})_2\text{X}$ family the SDW instability at low temperature can be very-well described by a mean-field 2D model in the \mathbf{ab} plane [Yamaji1986] including the following two main ingredients:

- i) A one-dimensional Fermi surface with a small warping t_b in the direction k_y perpendicular to the 1D direction k_x (see Figure 54a)
- ii) A weak on-site electron-electron repulsion at quarter filling

The quarter filling originates from one electron being taken by the counter-ion (PF_6^- or ClO_4^-) from the two nearest-neighbour TMTSF molecules. The typical resulting quasi-1D Fermi surface is shown on Figure 54a). It explains very well the quasi-1D properties, the SDW vector being naturally the optimum nesting vector:

$$\mathbf{Q}_{SDW} = (2k_F \mathbf{u}_x + \pi/b \mathbf{u}_y)$$

Thus, as long as these good nesting conditions of the quasi-1D Fermi surface will be satisfied, the groundstate will be a Spin-Density Wave (SDW). Applying pressure on $(\text{TMTSF})_2\text{PF}_6$ progressively lowers T_{SDW} the critical temperature of the SDW transition and further induces a superconducting phase. The effect of pressure can be modelled as an effective de-nesting parameter t'_b modulating the Fermi surface along k_y in such a way that it un-nests sufficiently the Fermi surface and restores a metallic state when $t'_b \approx kT_{SDW} \approx 15 - 20$ K. The mechanisms responsible for superconductivity were largely discussed over many years in this family of organic conductors. There is a large number of reliable experimental and theoretical works showing that unconventional superconductivity occurs in these materials. We will not discuss this here in details, but let us mention that proposals like spin-singlet d -wave superconductivity mediated by antiferromagnetic spin fluctuations seems to agree with many observed experimental results and is supported by the renormalization group approach in coherence with the whole phase diagram of the $(\text{TMTSF})_2\text{X}$ family (see [J r me2016] and references therein).

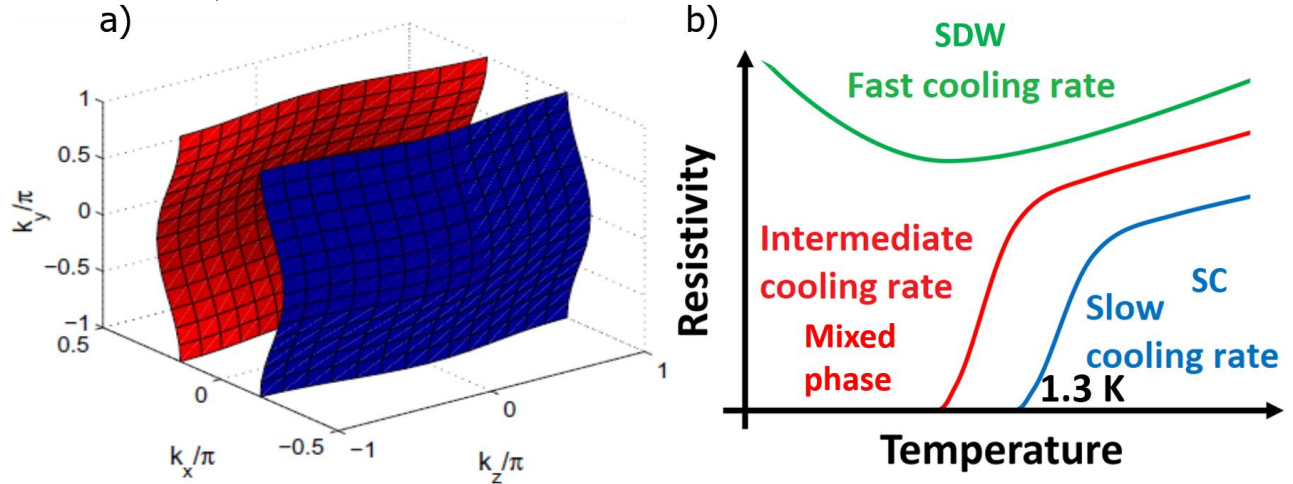


Figure 54: a) Calculated fermi surface of $(\text{TMTSF})_2\text{PF}_6$. Reproduced after [Brown2015]. b) Qualitative behavior of the resistivity in $(\text{TMTSF})_2\text{ClO}_4$ as a function of the cooling rate and corresponding observed phases. The superconducting critical temperature $T_C = 1.3$ K at slow cooling rate is indicated.

There exists a subtle difference among the behaviors of $(\text{TMTSF})_2\text{PF}_6$ and $(\text{TMTSF})_2\text{ClO}_4$. The PF_6^- ion is centrosymmetric while ClO_4^- is non-centrosymmetric. As a result, the ClO_4^- ion can occupy two equivalently stable positions in the crystal structure, while there is only one position for PF_6^- . Thus, at high temperature the ClO_4^- ions switch continuously between these two positions. When cooling the material, the ClO_4^- ions will order around 25 K and choose one particular orientation. The formation of large domains with ordered ions in the same position requires slow cooling [Pouget2012]. On the other hand, it has been shown that fast cooling helps retaining disorder in the anions ordering at low temperatures. The different ordering of the ClO_4^- ions has profound consequences on the groundstate of this material. If $(\text{TMTSF})_2\text{ClO}_4$ is cooled down slowly, it will show unconventional superconductivity below $T_C = 1.3$ K. This is due to the fact that the ions ordering below 25 K strongly dimerizes the TMTSF molecules, doubling the number of bands and thus completely reshaping the Fermi surface. However, when the sample is cooled fast enough at temperatures below 25 K, the material undergoes a SDW state, with an insulating ground state stabilized below 10 – 15 K. In this situation, due to the ions disorder, the bandstructure does not reconstruct and the Fermi surface remains similar to the one shown in Figure 54a). Here the origin of the SDW instability is the same as for the PF_6^- compounds. Figure 54b) shows a schematic picture of the resistivity versus temperature dependence of $(\text{TMTSF})_2\text{ClO}_4$ sample on three cooling rate regimes, slow, intermediate and fast cooling rates.

As a consequence the local electronic properties of the $(\text{TMTSF})_2\text{ClO}_4$ material are expected to change drastically depending on the cooling speed. This means that even for a slow-cooled material one expects to find few regions with disordered ions being thus being insulating. The opposite should also be true: for a fast cooled sample, ordered regions having a superconducting character should also statistically exist. Such a behavior is strongly suggested by a recent study by our colleagues Claire Marrache and Denis J r me [Yonezawa2018]. When increasing the density of disorder (faster cooling) a crossover occurs from an homogeneous superconductivity at low cooling rates to a granular superconductivity at faster cooling rates (intermediate cooling rates). Granular superconductivity means here having superconducting puddles embedded in a normal or badly metallic background that are thus connected through proximity effect.

These facts strongly motivated my work on $(\text{TMTSF})_2\text{ClO}_4$ and the search for inhomogeneous local electronic properties showing the interplay between superconducting, metallic or insulating SDW regions. Because of this kind of phase coexistence, the STM/STS technique is perfectly suited to fulfil this task. Also, the possibility of performing grid spectroscopy to address the symmetry of the unknown superconducting order parameter was a very motivating issue. Moreover, up to now none STM/STS studies was performed under ultrahigh vacuum on this family of compounds and could present reasonable imaging together with spectroscopic properties. This was quite challenging because organic solids are indeed very fragile materials and require a lot of care to be handled for ultrahigh vacuum STM experiment. We used single-crystals synthesized by Cécile Mézières at CNRS Angers in France, and managed to cleave them along the **ab** plane under ultrahigh vacuum. I present in the next section the preliminary experimental results that we obtained.

Phase coexistence of spin-density wave and superconducting regions

We have performed several experiments cooling the sample as slowly as we could (cooling rate about 1.3 K/h) to favor mostly the superconducting phase. We managed to find regions of the sample that were conducting enough to perform low-energy spectroscopy measurements on the surface crystalline plane. Nevertheless many other regions of the sample were found to be insulating at the surface at low-energy, the cleavage process possibly affecting the surface properties of the material in these areas.

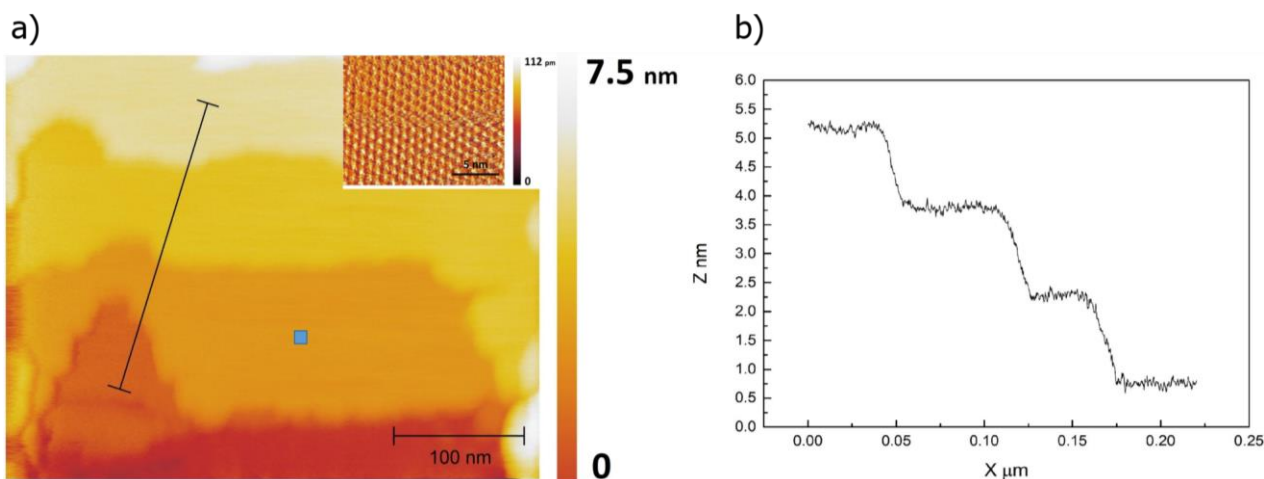


Figure 55: a) Large scale $410 \times 325 \text{ nm}^2$ STM topographic image of the in-situ cleaved $(\text{TMTSF})_2\text{ClO}_4$ single crystal. The top-right inset shows a small-scale area with molecular resolution (the scale bar is 5 nm). Scanning parameters $V = -0.1 \text{ V}$ and $I = 50 \text{ pA}$. b) Variations of height of the STM tip measured along the vertical line shown in the image a).

Figure 55a) shows a large-scale STM image of a nicely cleaved region of the $(\text{TMTSF})_2\text{ClO}_4$ sample surface. It shows several flat atomic planes corresponding to **ab** planes. The variations of height, measured along the vertical line going through 4 successive **ab** atomic planes, is presented in panel b). It is seen that the step height corresponds to the c lattice parameter and agrees with crystallographic data within 10%. Very rarely we could achieve molecular resolution, as is presented in the inset. In this case, the measured a and b parameters were in agreement with crystallographic data within 10%.

Figure 56 presents the first type of excitation spectra measured in nicely cleaved regions such as the one shown in panel 55a). These measurements were carried out in the area indicated by the blue square in panel 55a). The panel 56b) shows that at large-energy scale, the LDOS presents a strong V-shape dependence having a quasi-linear dependence with the excitation energy E . This energy-dependence varies from region to region but always shows a large V-shape depletion. This behavior is consistent with the quasi-1D character of the electronic properties together with weak electron-electron repulsion. It is currently being modelled by our colleagues A. Sedeki and Claude Bourbonnais. The panel 56a) presents the average excitation spectrum measured in the same $8 \times 8 \text{ nm}^2$ region where the measurement shown in panel 56b) was carried out, but at much smaller energy scale and for two temperatures.

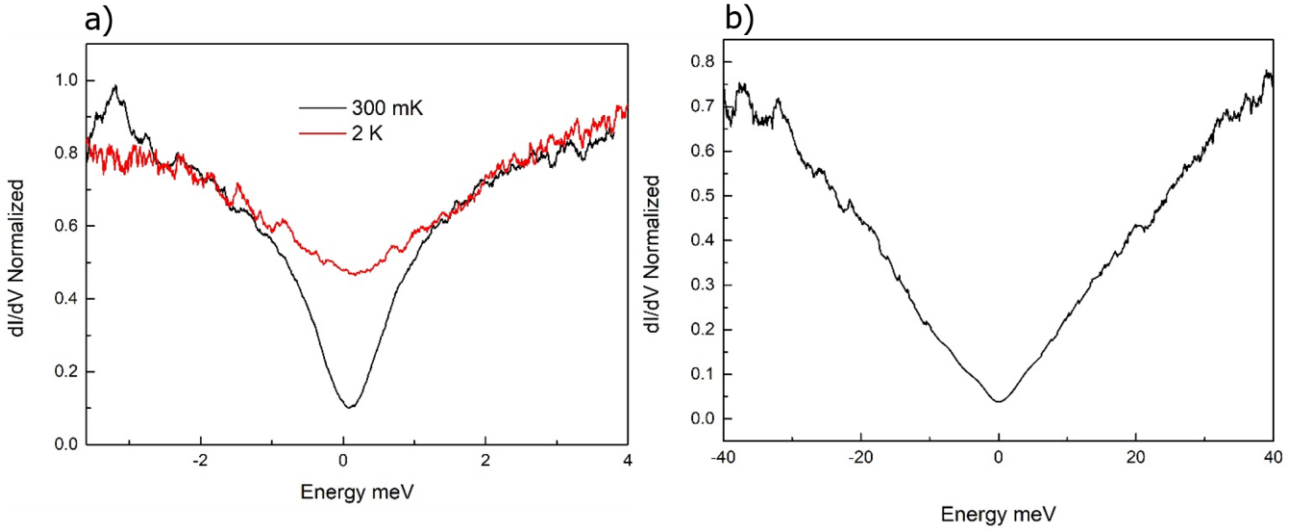


Figure 56: a) Typical excitation spectrum of the in-situ cleaved $(\text{TMTSF})_2\text{ClO}_4$ single crystal measured by STS at $T = 300 \text{ mK}$ and $T = 2 \text{ K}$ in the $8 \times 8 \text{ nm}^2$ area indicated by a blue square in the image 55a). b) Same quantity measured in the same local area but over a larger energy scale.

Considering all of our data, we attribute these spectra to superconducting regions. The bulk superconducting critical temperature T_c is reported to be $T_c = 1.3 \text{ K}$. The black spectrum is associated to the superconducting state while the red one is measured in the normal state. Let us note that in contrast to BCS excitation spectra, we never observed quasiparticle coherence peaks in the excitation spectra. The shape of the spectra that we measured is consistent with other tunneling differential conductance measurements not performed under ultrahigh vacuum reported in the literature. Using perpendicular magnetic field we observed a reduction of the LDOS with the field consistent with a low critical magnetic field along c^* at low temperature (the bulk $H_{c2}^{c^*} \approx 0.2 \text{ T}$).

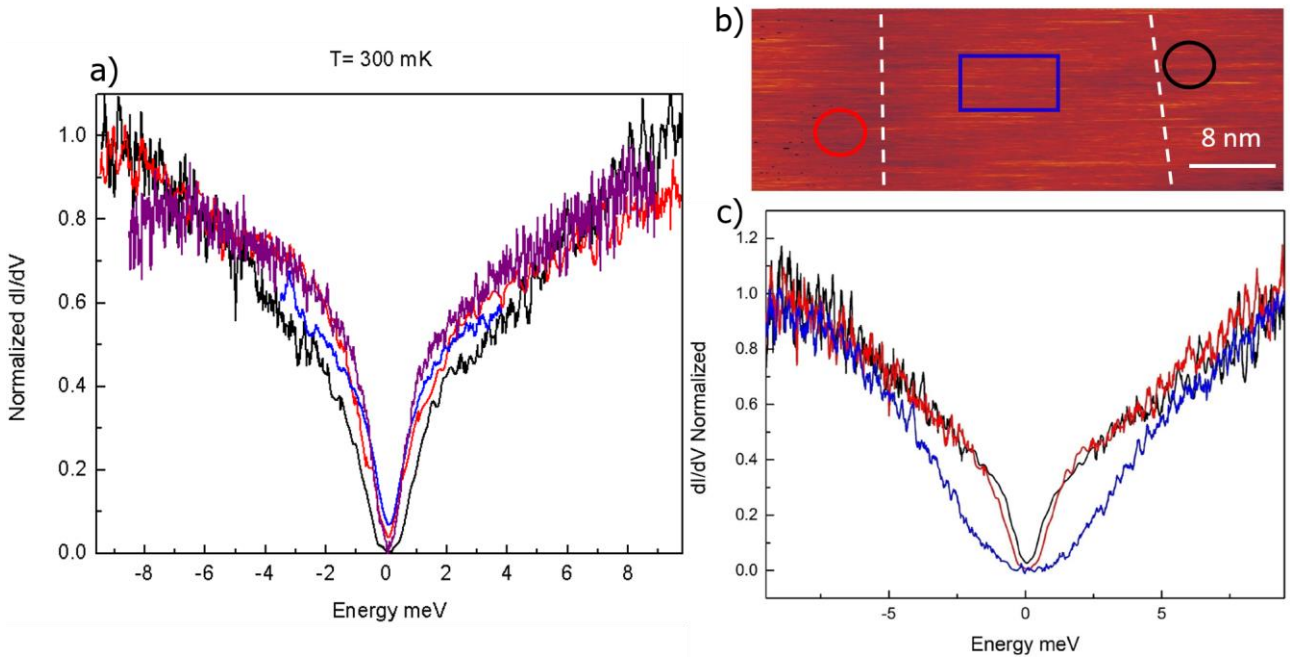


Figure 57: a) Representative excitation spectra of the in-situ cleaved $(\text{TMTSF})_2\text{ClO}_4$ single crystal measured by STS at $T = 300 \text{ mK}$ on several macroscopically distant regions. b) Small scale STM topography of a region of interest presenting superconducting regions (left and right areas from the dashed lines) and a presumably SDW region (central area). c) Excitation spectra measured at 300 mK in the local area seen in panel b). The color of each spectrum is associated to a corresponding circle or rectangle in the area b) where it was measured.

A comparison with other superconducting spectra measured on different macroscopically distant regions of the sample is presented in figure 57a). It is seen that the overall characteristics are similar to the ones presented

in panel 56a). At zero energy, the differential conductance usually does not reach zero and remains finite. This shows that line nodes might exist in this compound and that probably non-magnetic disorder induces pair-breaking filling the spectral gap. These preliminary results are consistent with other previous experimental work reporting a high sensitivity of the superconducting properties to non-magnetic defects rapidly destroying the superconducting phase. The excitation spectra are currently being modelled by A. Sedeki and Claude Bourbonnais.

Interestingly, we frequently observed at $T = 300$ mK regions where the local excitation spectra varied significantly from the superconducting shape presented above. Such an example is seen in panel 57b) and 57c) which shows an insulating region located in-between two superconducting areas. While the black and red spectra are characteristic of the superconducting phase, the blue spectrum might correspond to an area presenting a spin-density wave (SDW) groundstate. It indeed features a broad U-shape depleted LDOS, with an energy scale significantly larger than the one of the superconducting gap and compatible with a 10 – 15 K critical temperature for the SDW ordering. Considering all of our measurements on different samples, we often found areas having characteristics such as the blue spectrum. We also found areas having a metallic behavior, i.e. where the LDOS is not strongly reduced close the Fermi energy as for the superconducting or insulating regions.

At present, our interpretation of these preliminary results is that the cleavage process most probably creates additional disorder in the ClO_4^- anion ordering at the surface. Unfortunately we were not able to obtain a molecular resolution of the surface lattice except in very few cases. We tend to believe that in the local areas where ionic ordering still exists, superconductivity develops and can be measured. In regions where disorder exists, different types of spectra are found: small-gap insulating ones that we interpret as SDW patches to metallic-like ones where non-magnetic disorder destroys almost completely the superconducting phase. More experiments are needed to confirm these results and obtain more statistics. Anyhow, a first partial conclusion is that indeed there is a coexistence of different phases in this material being compatible with superconducting, spin-density wave and metallic areas. Regarding the possibility of addressing the symmetry of the superconducting order parameter using grid spectroscopy measurements in combination with the quasiparticle interference technique, I believe that it will be very difficult. The main reason is that getting and keeping molecular resolution is extremely difficult on these materials, most probably because the tip interacts a lot with the surface in regions that are poorly conducting at the surface, while good surface regions remain scarce. Experiments in magnetic field will also help rationalizing our results as several transitions are predicted to happen and were reported in the bulk material.

Thanks

I would like first to thank the members and reviewers of the Jury to have accepted to review my HDR habilitation thesis. Although my defense was fully on-line due to the covid19 pandemics, I particularly enjoyed the involved and thorough scientific discussion following my Habilitation defense.

I would then like to thank here warmly all the people of our group I had the great pleasure to work with during all these 10 years. We had a very creative and exciting scientific atmosphere. First I sincerely thank my close colleagues with whom most of the presented work was done: Tristan Cren, François Debontridder and Dimitri Roditchev. Then it is my pleasure to thank the other members of the group for a very nice interaction, many of them having joined us later on: Yves Noat, Matteo Calandra, Pascal David, Marie d'Angelo, Marie Hervé.

I also would like to thank warmly all master students, PhD students and post-docs I had the pleasure to work with during these years. Their contribution was essential both scientifically and humanly: Rémi Federicci, Gerbold Ménard, Mathieu Leclerc, Tobias Bilgeri, Raphaël Leriche, Mehdi Torkzadeh, Lise Serrier-Garcia, Clémentine Carbillet, Vasily Stolyarov, Vladimir Cherkez, Danilo Longo, Alexandra Palacio-Morales.

I also thank the numerous colleagues, young and old, with whom I interacted in France or abroad during all these years, which make this job so lively, multicultural and interesting.

I also would like to thank deeply all colleagues of the second floor 22-32 and 22-23 with whom we had plenty of lively scientific discussions and discussions on any subject of interest. I also thank sincerely our colleagues

of the institute from the common services, for the computer support: François Rey, Corinne Poisson, Louis Montclair, Electronic workshop: Francis Breton and Silbe Majrab, Mechanical workshop: Christophe Rafailac and former people. It is my pleasure to thank also all the employees of the helium liquefier: Florin Beuran, David, Richard Sauvage. More generally I would like to thank also the people of the administrative department of our institute who took care of running smoothly our research structure.

Finally I thank very deeply Anna my wife, my kids Sacha, Pierre and Alice, and Ilia and Elena my parents-in-law for their continuous love and support during all these years!

References

HDR References:

- [AbriGork1961] A.A. Abrikosov and L.P. Gor'kov, JETP 12, 1243 (1961)
- [Adler2019] F. Adler et al., Phys. Rev. Lett. 123, 086401 (2019)
- [Altshuler1980] B.L. Altshuler, A.G. Aronov, and P.A. Lee, Phys. Rev. Lett. 44, 1288 (1980)
- [Altshuler1985] B.L. Altshuler and A.G. Aronov, in *Electron-Electron Interactions in Disordered Systems*, edited by A. L. Efros and M. Pollak (North Holland, Amsterdam, 1985)
- [Amundsen2016] M. Amundsen and J. Linder, Scientific Report 6, 22765 (2016)
- [Anderson1959] P.W. Anderson, J. Phys. Chem. Solids 11, 26 (1959)
- [Antonenko2020] D.S. Antonenko and M.A. Skvortsov, JETP Letters 112 (7), 428 (2020)
- [Badrtdinov2016] Badrtdinov et al., Phys. Rev. B 94, 224418 (2016)
- [Balents2010] L. Balents, Nature 464, 199 (2010)
- [Barracough1970] C.G. Barracough et al. J. Chem. Phys. 53, 1643 (1970)
- [Bauer2013] J. Bauer, J.I. Pascual and K. Franke Phys. Rev. B 87, 075125 (2013)
- [Bernevig2013] B.A. Bernevig, T.L.F. Hughes and A. Samarin, *Topological insulators and topological superconductors*. Princeton University Press (2013)
- [Bradlyn2017] Bradlyn *et al.* Nature 547, 298 (2017)
- [Brihuega2005] I. Brihuega et al., Phys. Rev. Lett. 94, 046101 (2005)
- [Brown2015] S. Brown, Physica C 514, 279-289 (2015)
- [Brosco2020] V. Brosco and M. Capone, Phys. Rev. B 101, 235149 (2020)
- [Brun2014] C. Brun, et al. Nat. Phys. 10, 444 (2014)
- [Brun2017] C. Brun, T. Cren, and D. Roditchev, Supercond. Sci. Technol. 30, 013003 (2017)
- [BTK1982] G.E. Blonder, M. Tinkham and T.M. Klapwijk, Phys. Rev. B 25, 4515 (1982)
- [Bulaevskii1985] L.N. Bulaevskii and M.V. Sadvovskii, J. Low Temp. Phys. 59, 89 (1985)
- [Bychkov1984] Yu.A. Bychkov and E.I. Rashba, JETP Lett. 39, 78 (1984)
- [Cao2018] X. Cao et al., Phys. Rev. B 97, 155145 (2018)
- [Carbillet2016] C. Carbillet et al., Phys. Rev. B 93, 144509 (2016)
- [Carbillet2020] C. Carbillet et al., Phys. Rev. B 102, 024504 (2020)
- [Caroli1964] C. Caroli, P.G. de Gennes and J. Matricon, Phys. Lett. 9, 307 (1964)
- [Chand2012] M. Chand et al., Phys. Rev. B 85, 014508 (2012)
- [Chang2007] H.W. Chang et al., J. Appl. Phys. 101, 09D124 (2007)
- [Combescot2015] M. Combescot and S.-Y. Shiao, *Excitons and Cooper pairs*, Oxford graduate texts, Oxford University Press (2015)
- [Cortes2013] R. Cortes et al., Phys. Rev. B 88, 125113 (2013)
- [Cortes2006] R. Cortes et al., Phys. Rev. Lett. 96, 126103 (2006)
- [Crommie1993] M.F. Crommie, C.P. Lutz and D.M. Eigler, Nature 363, 524 (1993)
- [Cren2009] T. Cren et al., Phys. Rev. Lett. 102, 127005 (2009)
- [Dubouchet2019] T. Dubouchet et al., Nat. Phys. 15, 233 (2019)
- [Dutreix2019] C. Dutreix et al., Nature 574, 219 (2019)
- [Farias2003] D. Farias et al., Phys. Rev. Lett. 91, 016103 (2003)
- [Feigelman2010] M.V. Feigel'man, L.B. Ioffe, V.E. Kravtsov and E. Cuevas, Annals of Physics 325, 1390 (2010)
- [Feigelman2012] M.V. Feigel'man and M.A. Skvortsov Phys. Rev. Lett. 109, 147002 (2012)
- [Feigelman2015] M.V. Feigel'man and L.B. Ioffe Phys. Rev. B (R) 92, 100509 (2015)
- [Finkelstein1987] A.M. Finkel'shtein, JETP Lett. 45, 1, 47 (1987)
- [Finkelstein1994] A.M. Finkel'shtein, Physica B 197, 636 (1994)

- [Flores2001] F. Flores et al. *Prog. Surf. Sci.* 67, 299 (2001)
- [Fominov2016] Y.V. Fominov and M.A. Skvortsov, *Phys. Rev. B* 93, 144511 (2016)
- [Franke2011] K.J. Franke, G. Schulze, and J.I. Pascual, *Science* 332, 940 (2011)
- [Fu2007] Y.-S. Fu et al. *Phys. Rev. Lett.* 99, 256601 (2007)
- [Gantmakher2010] V.F. Gantmakher and V.T. Dolgoplov *Physics-Uspekhi* 53, 1-49 (2010)
- [Georges1996] A. Georges et al., *Rev. Mod. Phys.* 68, 13 (1996)
- [Ghosal1998] A. Ghosal, M. Randeria, and N. Trivedi, *Phys. Rev. Lett.* 81, 3940 (1998)
- [Ghosal2001] A. Ghosal, M. Randeria, and N. Trivedi, *Phys. Rev. B* 65, 014501 (2001)
- [Ghosal 2011] K. Bouadim, Y. L. Loh, M. Randeria, and N. Trivedi, *Nat. Phys.* 7, 884 (2011)
- [Glass2015] S. Glass et al., *Phys. Rev. Lett.* 114, 247602 (2015)
- [Gorkov2001] L.P. Gor'kov and E.I. Rashba, *Phys. Rev. Lett.* 87, 037004 (2001)
- [Guéron1996] S. Guéron et al. *Phys. Rev. Lett.* 77, 3025 (1996)
- [Hansmann2013] P. Hansmann et al., *Phys. Rev. Lett.* 110, 166401 (2013)
- [Hansmann2016] P. Hansmann et al., *Sci. Rep.* 6, 19728 (2016)
- [Hatter2015], N. Hatter et al. *Nat. Commun.* 6, 8988 (2015)
- [HupaloDevilStair2003] M. Hupalo, J. Schmalian and M.C. Tringides *Phys. Rev. Lett.* 90, 216106 (2003)
- [Ingold1992] G.-L. Ingold and Yu.V. Nazarov, in *Single Charge Tunneling*, edited by H. Grabert and M. Devoret, NATO ASI, Ser. B Vol. 294 (Plenum, New York, 1992)
- [Ivanov2001] D.A. Ivanov, *Phys. Rev. Lett.* 86, 268 (2001)
- [Ivry2014] Y. Ivry et al. *Phys. Rev. B* 90, 214515 (2014)
- [Jäger2018] M. Jäger et al., *Phys. Rev. B* 98, 165422 (2018)
- [Janod2015] E. Janod et al., *Adv. Funct. Mater.* 25, 6287 (2015)
- [Jerome1980] D. Jérôme et al., *Journal de Physique Lettres*, 41(4), 95 (1980)
- [Jérôme2016] D. Jérôme and S. Yonezawa, *C. R. Physique* 17, 357 (2016)
- [Ji2008] S.-H. Ji et al., *Phys. Rev. Lett.* 100, 226801 (2008)
- [Jo2006] C. Jo et al., *J. Magn. Magn. Mater.* 306, 156–160 (2006)
- [Julien2015] M.H. Julien *Science* 350, 914 (2015)
- [Kamlapure2013] A. Kamlapure et al. *Sci. Rep.* 3, 2979 (2013)
- [Kanoda2006] K. Kanoda, *J. Phys. Soc. Jpn.* 5, 051007 (2006)
- [Kim2010] K.S. Kim et al., *Phys. Rev. Lett.* 104, 246803 (2010)
- [Kim2018] H. Kim et al., *Science Advances*, 4, 5 (2018)
- [Kitaoka2013] Y. Kitaoka et al. *J. Appl. Phys.* 113, 17E130 (2013)
- [Kuroki2001] K. Kuroki et al., *Phys. Rev. B* 63, 174507 (2001)
- [Jäger2018] M. Jäger et al., *Phys. Rev. B* 98, 165422 (2018)
- [Ji2008] S.H. Ji et al. *Phys. Rev. Lett.* 100, 226801 (2008)
- [Lamacraft2000] A. Lamacraft and B. D. Simons, *Phys. Rev. Lett.* 85, 4783 (2000)
- [Larkin1971] A.I. Larkin and Yu.N. Ovchinnikov *JETP* 34, 1144 (1972)
- [LarkinVarlamov2005] A.I. Larkin and A. Varlamov, *Theory of fluctuations in superconductors*, Oxford University Press (2005)
- [Lee2006] P.A. Lee et al., *Rev. Mod. Phys.* 78, 17 (2006)
- [Lesueur2008] H. le Sueur et al., *Phys. Rev. Lett.* 100, 197002 (2008)
- [Li2011] G. Li et al., *Phys. Rev. B* 83, 041104(R) (2011)
- [Li2013] G. Li et al., *Nat. Commun.* 4:1620 doi: 10.1038/ncomms2617 (2013)
- [Longo2020] D. Longo et al., *J. Phys. Chem. C* 124 (36), 19829-19840 (2020)
- [Ma1985] M. Ma and P.A. Lee *Phys. Rev. B* 32, 5658 (1985)
- [Machida2019] T. Machida et al., *Nature Materials* 18, 811 (2019)
- [Mahan2000] G. Mahan, *Many-Particle Physics* (New York: Kluwer Plenum), chapter 4 (2000)
- [Matsuura1977] T. Matsuura, *Prog. Theor. Phys.* 57, 1823 (1977)
- [Matthias1958] B.T. Matthias, H. Suhl and E. Corenzwit, *Phys. Rev. Lett.* 1, 92 (1958)
- [Matveev1998] K.A. Matveev and A.I. Larkin, *Phys. Rev. Lett.* 78, 3749 (1998)
- [Menard2015] G.C. Ménard et al. *Nature Physics* 11, 1013 (2015)
- [Menard2017] G.C. Ménard et al. *Nature communications* 8, 2040, (2017) doi:10.1038/s41467-017-02192-x
- [Menard2019] G.C. Ménard et al. *Nature communications* 10, 2587 (2019) doi:10.1038/s41467-019-10397-5
- [Minamitani2015] E. Minamitani *Phys. Rev. B* 92, 075144 (2015)
- [Ming2017] F. Ming et al., *Phys. Rev. Lett.* 119, 266802 (2017)
- [Modesti2007] S. Modesti et al., *Phys. Rev. Lett.* 98, 126401 (2007)
- [Mourik2012] V. Mourik et al., *Science* 336, 6084 (2012)

- [Nadj-Perge2014] S. Nadj-Perge et al., *Science* 346, 6029 (2014)
 [Noat2013] Y. Noat et al. *Phys. Rev. B* 88, 014503 (2013)
 [Noat2015] Y. Noat et al. *Phys. Rev. B* 92, 134510 (2015)
 [Norman2003] M.R. Norman & C. Pépin, *Rep. Prog. Phys.* 66, 1547 (2003)
 [Odobescu2017] A. B. Odobescu et al., *Phys. Rev. B* 95, 195151 (2017)
 [Ortega2002] J. Ortega et al., *J. Phys.: Condens. Matter* 14, 5979 (2002)
 [Perfetti2003] L. Perfetti et al., *Phys. Rev. Lett.* 90, 166401 (2003)
 [Perfetti2006] L. Perfetti et al., *Phys. Rev. Lett.* 97, 067402 (2006)
 [Pfen2002] O. Pfennigstorf et al., *Phys. Rev. B* 65, 045412 (2002)
 [Pietzsch2004] O. Pietzsch et al., *Phys. Rev. Lett.* 92, 057202 (2004)
 [Pouget2012] J.P. Pouget, *Crystals* 2, 466-520 (2012)
 [Profeta2007] G. Profeta et al., *Phys. Rev. Lett.* 98, 086401 (2007)
 [Qi2011] X.-L. Qi and S.-C. Zhang, *Rev. Mod. Phys.* 83, 1057 (2011)
 [Rahn2012] D.J. Rahn et al., *Phys. Rev. B* 85, 224532 (2012)
 [Reeg2018] C. Reeg et al., *Phys. Rev. B* 97, 165425 (2018)
 [Ren2016] X.-Y. Ren et al., *Phys. Rev. B* 94, 075436 (2016)
 [Rusinov1969] A.I. Rusinov, *JETP Lett.* 9, 85 (1969)
 [Sacepe2008] B. Sacépé et al. *Phys. Rev. Lett.* 101, 157006 (2008)
 [Sacepe2011] B. Sacépé et al. *Nat. Phys.* 7, 239 (2011)
 [Santoro1999] G. Santoro et al. *Phys. Rev. B* 59, 1891 (1999)
 [Semenov2009] A. Semenov et al., *Phys. Rev. B* 80, 054510 (2009)
 [Shiba1968] H. Shiba, *Prog. Theor. Phys.* 40, 435 (1968)
 [Skvortsov2013] M.A. Skvortsov and M.V. Feigel'man *JETP* 117, 487 (2013)
 [Sigrist1991] M. Sigrist and K. Ueda, *Rev. Mod. Phys.* 63, 239 (1991)
 [Simon2011] L. Simon et al., *J. Phys. D: Appl. Phys.* 44, 464010 (2011)
 [Smidman2017] M. Smidman et al., *Rep. Prog. Phys.* 80, 036501 (2017)
 [Stolyarov2018] V.S. Stolyarov et al., *Nature Communications* 9(1), 2277 (2018)
 [Tosatti1974] Tosatti & Anderson, *Jpn. J. Appl. Phys., Suppl.* 2, 381 (1974)
 [Tresca2018] C. Tresca et al., *Phys. Rev. Lett.* 120, 196402 (2018)
 [Tung1992] R.T. Tung, *Materials Chemistry and Physics* 32, 107-133 (1992)
 [Usadel1970] K.D. Usadel, *Phys. Rev. Lett.* 25, 507 (1970)
 [Volovik1999] G.E. Volovik, *JETP Lett.* 70, 792 (1999)
 [Wu2020] X. Wu et al., *Phys. Rev. Lett.* 125, 117001 (2020)
 [Yamada2013] M. Yamada et al., *Phys. Rev. Lett.* 110, 237001 (2013)
 [Yamaji1986] K. Yamaji, *Synthetic Metals*, 13, 29 (1986)
 [Yazani1997] A. Yazdani et al., *Science* 275, 1767 (1997)
 [Yonezawa2018] S. Yonezawa et al., *Phys. Rev. B* 97, 014521 (2018)
 [Yoshizawa2014] S. Yoshizawa, et al. *Phys. Rev. Lett.* 113, 247004 (2014)
 [Yu1965] L. Yu, *Acta, Phys. Sin.* 21, 75 (1965)
 [Zhang2010] T. Zhang et al., *Nat. Phys.* 6 104 (2010)
 [Zhou1998] F. Zhou et al., *Journal of Low Temp. Phys.*, 110, 841 (1998)

Acronyms used in the HDR thesis

ARPES: Angular Resolved Photoemission Spectroscopy
 BCS: Bardeen Cooper Schrieffer
 DFT: Density Functional Theory
 DOS: Density-of-States
 LDOS: Local Density-of-States
 LEED: Low-Energy-Electron Diffraction
 MBE: Molecular Beam Epitaxy
 SOC: Spin-Orbit Coupling
 STM: Scanning Tunnelling Microscopy
 STS: Scanning Tunnelling Spectroscopy
 UHV : Ultrahigh Vacuum

2DEG : Two-Dimensional Electron Gas

T_c : Critical temperature

Δ : Energy gap

$\Phi_0 = h/2e$: flux quantum

e : electronic charge

k_F : Fermi wavevector

λ_F : Fermi wavelength

ϵ_F : Fermi energy

ℓ_e : elastic electronic mean free path

Publication List

At 01.01.2021:

I am co-author of: [link to Google scholar](#)

- ✓ 27 Publications in peer-reviewed journals (including 3 Nature Physics, 7 Physical Review Letters, 4 Nature Communications, 1 Physical Review X, 9 Physical Review B, 2 APL)
- including 16 Publications in journals with impact factor > 7
- ✓ 1 Review paper (Superconductor Science and Technology)
- ✓ 3 Chapters of book (Oxford university press and De Gruyter)
- ✓ 15 Invited presentations to international conferences or workshops
- ✓ 1 Invited lecture to an international advanced school
- ✓ 6 Conference proceedings

PUBLICATION LIST – BOOK CHAPTERS

Co-author of 2 book chapters edited by Oxford University Press (published in 2017) “The Oxford Handbook of small superconductors”, edited by A.V. Narlikar

1. *Local scale spectroscopic studies of vortex organization in mesoscopic superconductor, chapter 2 in “The Oxford Handbook of Small Superconductors”, Ed. by A.V. Narlikar, Oxford University Press, 2017*
D. Roditchev, T. Cren, C. Brun, and M. Milosevic
2. *Proximity effect: a new insight from in-situ fabricated hybrid nanostructures, chapter 4 in “The Oxford Handbook of Small Superconductors”, Ed. by A.V. Narlikar, Oxford University Press, 2017*
J.C. Cuevas, D. Roditchev, T. Cren, C. Brun

Co-author of 1 book chapter edited by De Gruyter (published in 2017) “Superconductors at the Nanoscale From Basic Research to Applications”, edited by R. Wördenweber, V. Moshchalkov, S. Bending and F. Tafuri

3. *STM studies of vortex cores in strongly confined nanoscale superconductors, chapter 3 in “Superconductors at the Nanoscale From Basic Research to Applications”, Ed. by R. Wördenweber, V. Moshchalkov, S. Bending, F. Tafuri, De Gruyter, 2017*
T. Cren, C. Brun, and D. Roditchev

PUBLICATION LIST – PEER-REVIEWED RESEARCH ARTICLES

1. *Misfit Layer Compounds: A Platform for Heavily Doped 2D Transition Metal Dichalcogenides*
R. Leriche, A. Palacio-morales, M. Campetella, C. Tresca, S. Sasaki, C. Brun, F. Debontridder, P. David, I. Arfaoui, O. Šofranko, T. Samuely, G. Kremer, C. Monney, T. Jaouen, L. Cario, M. Calandra, T. Cren, [Adv. Funct. Mater. 2007706 \(2020\)](#)
2. *Surface Phase Nucleation of Lead Monoatomic Layers on Si(111) Induced by Manganese Phthalocyanine Molecules*
D. Longo, M.-L. Bocquet, N. Lorente, H. Cruguel, F. Debontridder, S. Royer, P. David, A. Palacio-Morales, T. Cren, N. Witkowski, C. Brun, [J. Phys. Chem. C 124, 36, 19829 \(2020\)](#)
3. *Unveiling Odd-Frequency Pairing around a Magnetic Impurity in a Superconductor*

- V. Perrin, Flávio L. n. Santos, G. Ménard, C. Brun, T. Cren, M. Civelli, P. Simon, [Phys. Rev. Lett. 125, 117003 \(2020\)](#)
4. *Spectroscopic evidence for strong correlations between local superconducting gap and local Altshuler-Aronov density of states suppression in ultrathin NbN films*
C. Carbillet, V. Cherkez, M.A. Skvortsov, M.V. Feigel'man, F. Debontridder, L.B. Ioffe, V.S. Stolyarov, K. Ilin, M. Siegel, C. Noûs, D. Roditchev, T. Cren, C. Brun, [Phys. Rev. B 102, 024504 \(2020\)](#)
 5. *Isolated pairs of Majorana zero modes in a disordered superconducting lead monolayer*
G. Ménard, A. Mesaros, C. Brun, F. Debontridder, D. Roditchev, P. Simon, T. Cren, [Nature Communications 10, 2587 \(2019\)](#)
 6. *Local Josephson vortex generation and manipulation with a Magnetic Force Microscope*
V.V. Dremov, S.Y. Grebenchuk, A.G. Shishkin, D.S. Baranov, R.A. Hovhannisyan, O.V. Skryabina, N. Lebedev, I.A. Golovchanskiy, V.I. Chichkov, C. Brun, T. Cren, V.M. Krasnov, A.A. Golubov, D. Roditchev, V.S. Stolyarov, [Nature Communications 10, 4009 \(2019\)](#)
 7. *Yu-Shiba-Rusinov bound states versus topological edge states in Pb/Si (111)*
G.C. Ménard, C. Brun, R. Leriche, M. Trif, F. Debontridder, D. Demaille, D. Roditchev, P. Simon, T. Cren, [Eur. Phys. J. Special Topics 227, 2303 \(2019\)](#)
 8. *Chiral Spin Texture in the Charge-Density-Wave Phase of the Correlated Metallic Pb/Si(111) Monolayer*
C. Tresca, C. Brun, T. Bilgeri, G. Menard, V. Cherkez, R. Federicci, D. Longo, F. Debontridder, M. D'angelo, D. Roditchev, G. Profeta, M. Calandra, T. Cren, [Phys. Rev. Lett. 120, 196402 \(2018\)](#)
 9. *Expansion of a superconducting vortex core into a diffusive metal*
V. Stolyarov, T. Cren, C. Brun, I. Golovchanskiy, O. Skryabina, D. Kasatonov, M. Khapaev, M. Kupriyanov, A. Golubov, D. Roditchev, [Nature Communications 9, 2277 \(2018\)](#)
 10. *Two-dimensional topological superconductivity in Pb/Co/Si(111)*
G.C. Ménard, S. Guissart, C. Brun, R.T. Leriche, M. Trif, F. Debontridder, D. Demaille, D. Roditchev, P. Simon and T. Cren, *Nature Communications* 8, 2040 (2017)
doi:10.1038/s41467-017-02192-x
 11. *Review of 2D superconductivity: the ultimate case of epitaxial monolayers*
C. Brun, T. Cren, D. Roditchev, *Supercond. Sci. Technol.* 30, 013003 (2017)
 12. *Confinement of superconducting fluctuations due to emergent electronic inhomogeneities*
C Carbillet, S Caprara, M Grilli, C Brun, T Cren, F Debontridder, B Vignolle, W Tabis, D Demaille, L Largeau, K Ilin, M Siegel, D Roditchev, B Leridon, *Phys. Rev. B* 93, 144509 (2016)
 13. *Coherent long-range magnetic bound states in a superconductor*

- G. Ménard, S. Guissart, C. Brun, S. Pons, V. Stolyarov, F. Debontridder, Matthieu Leclerc, Etienne Janod, Laurent Cario, Dimitri Roditchev, P. Simon and T. Cren, *Nature Physics* 11, 1013 (2015)
14. *Quasiparticle spectra of 2H-NbSe₂: Two-band superconductivity and the role of tunneling selectivity*
Y. Noat, J. A. Silva-Guillen, T. Cren, V. V. Cherkez, C. Brun, S. Pons, F. Debontridder, D. Roditchev, W. Sacks, L. Cario, P. Ordejon, E. Canadell, *Phys. Rev. B* 92, 134510 (2015)
 12. *Direct observation of Josephson vortex cores*
D. Roditchev, C. Brun, L. Serrier-Garcia, J.C. Cuevas, V.H. Loiola Bessa, M.V. Milošević, F. Debontridder, V.S. Stolyarov, and T. Cren, *Nature Physics* 11, 332 (2015)
 13. *Remarkable effects of disorder on superconductivity of single atomic layers of lead on silicon*
C. Brun, T. Cren, V. Cherkez, F. Debontridder, S. Pons, L.B. Ioffe, B.L. Altshuler, D. Fokin, M. C. Tringides, S. Bozhko, and D. Roditchev, *Nature Physics* 10, 444 (2014)
 14. *Ex situ elaborated proximity mesoscopic structures for ultrahigh vacuum scanning tunneling spectroscopy*
V.S. Stolyarov, T. Cren, F. Debontridder, C. Brun, I. S. Veshchunov, O.V. Skryabina, A.Yu. Rusanov, and D. Roditchev, *Appl. Phys. Lett.* 104, 172604 (2014)
 15. *Proximity Effect between two Superconductors Spatially Resolved by Scanning Tunneling Spectroscopy*
V.Cherkez, J. C. Cuevas, C. Brun, T. Cren, G. Ménard, F. Debontridder, V. Stolyarov and D. Roditchev, *Phys. Rev. X* 4, 011033 (2014)
 16. *Coulomb blockade phenomena observed in supported metallic nanoislands*
I-P. Hong, C. Brun, M. Pivetta, F. Patthey, and W.-D. Schneider, *Front.Physics* 1:13. doi: 10.3389/fphy.2013.00013 (2013)
 17. *Scanning Tunneling Spectroscopy Study of the Proximity Effect in a Disordered Two-Dimensional Metal*
L. Serrier-Garcia, J. C. Cuevas, T. Cren, C. Brun, V. Cherkez, F. Debontridder, D. Fokin, F. S. Bergeret, and D. Roditchev, *Phys. Rev. Lett.* 110, 157003 (2013)
 18. *Unconventionnal superconductivity in ultrathin superconducting NbN films studied by scanning tunneling spectroscopy*
Y. Noat, V. Cherkez, C. Brun, T. Cren, C. Carbillet, F. Debontridder, , K. Ilin, M. Siegel, A. Semenov, H.-W. Hübers, D. Roditchev, *Phys. Rev. B* 88, 014503 (2013)
 19. *Dynamical Coulomb blockade Observed in Nanosized Electrical Contacts*
C. Brun, K. Müller, I-P. Hong, F. Patthey, C. Flindt, and W.-D. Schneider, *Phys. Rev. Lett.* 108, 126802 (2012)
 20. *Scanning-Tunneling Microscope Imaging of Single-Electron Solitons in a Material with Incommensurate Charge-Density Waves*

- S. Brazovskii, C. Brun, Z. Z. Wang, and P. Monceau, *Phys. Rev. Lett.* 108, 096801 (2012)
21. *Surface Charge-Density Wave Phase Transition in NbSe₃*
C. Brun, Z. Z. Wang, P. Monceau, and S. Brazovskii, *Phys. Rev. Lett.* 104, 256403 (2010)
22. *Decay Mechanisms of Excited Electrons in Quantum-Well States of Ultrathin Lead Islands Grown on Si(111): Scanning Tunneling Spectroscopy and Theory*
I-P. Hong, C. Brun, F. Patthey, I.Yu. Sklyadneva, X. Zubizarreta, R. Heid, V. M. Silkin, P.M. Echenique, K.P. Bohnen, E.V. Chulkov, and W.-D. Schneider, *Phys. Rev. B Rapid. Comm.* **80**, 081409(R) (2009)
23. *Scanning Tunneling Microscopy at NbSe₃ Surface: Evidence for Interaction between q₁ and q₂ Charge-Density Waves in the Pinned Regime*
C. Brun, P. Monceau, and Z.Z. Wang *Phys. Rev. B* 80, 045423 (2009)
24. *Reduction of the Superconducting Gap of Ultrathin Pb Islands Grown on Si(111)*
C. Brun, I-P. Hong, F. Patthey, I.Yu. Sklyadneva, R. Heid, P.M. Echenique, K.P. Bohnen, E.V. Chulkov, and W.-D. Schneider, *Phys. Rev. Lett.* 102, 207002 (2009)
25. *Local work function changes determined by field emission resonances: NaCl/Ag(100)*
H.-C. Ploigt, C. Brun, M. Pivetta, F. Patthey, and W.-D. Schneider, *Phys. Rev. B*, 76, 195404 (2007)
26. *Analysis of the Scanning Tunneling Microscopy Images of the Charge Density Wave Phase in Quasi-one-dimensional Rb_{0.3}MoO₃*
E. Machado-Charry, P. Ordejon, E. Canadell, C. Brun, Z.Z. Wang, *Phys. Rev. B*, 74, 155123 (2006)
27. *Charge-Density Waves in Rubidium Blue Bronze (Rb_{0.3}MoO₃) observed by Scanning Tunneling Microscopy*
C. Brun, J.C. Girard, Z.Z. Wang, J. Marcus, J. Dumas, C. Schlenker, *Phys. Rev. B*, 72, 235119 (2005)

PUBLICATION LIST – PEER-REVIEWED CONFERENCE PROCEEDINGS

1. *Direct observation of single-electron solitons and Friedel oscillations in a quasi-one dimensional material with incommensurate charge-density waves*
C. Brun, S. Brazovskii, Z.-Z. Wang, P. Monceau, *Physica B: Condensed Matter* 460, 88 (2015)
2. *Charge-density waves studied at the surface and the atomic scale*
C. Brun, Z. Z. Wang, P. Monceau, and S. Brazovskii, *Physica B* 407, 1845 (2012)
3. *Inhomogeneities of the CDW vector at the (-201) surface of Quasi-1D blue bronze Rb_{0.3}MoO₃*
C. Brun, E. Machado-Charry, P. Ordejon, E. Canadell, and Z.Z. Wang, *J. Phys. Conf. Series*, 61, 140 (2007)
4. *“Extraordinary” Surface Phase Transition at (100) Surface of NbSe₃*
C. Brun, and Z.Z. Wang, *J. Phys. Conf. Series*, 61, 147 (2007)

5. *Charge-Density Waves modulation in different chains of NbSe₃*

C. Brun, Z.Z. Wang, P. Monceau, J. Phys. IV France, Proceedings ECRYS 2005, 131, 225 (2005)

6. *STM observation of CDW on cleaved (-201) surface of Rb_{0.3}MoO₃*

C. Brun, J.C. Girard, Z.Z. Wang, J. Marcus, J. Dumas, C. Schlenker, J. Phys. IV France, Proceedings ECRYS 2005, 131, 203 (2005)

Invited Talks

At 07.01.2020:

- ✓ 18 Invited conferences in International Conferences or Workshops - 1 Invited lecture in an International Advanced School – 3 Invited talks in National Meetings

INVITED TALKS IN INTERNATIONAL CONFERENCES OR WORKSHOPS

PRESENTED BY TOPIC

- i) *Mott physics in a single atomic plane*
 - 1) 2019: [SUPERSTRIPES 2019](#), International conference on quantum physics in complex matter: superconductivity, magnetism and ferroelectricity, Ischia, Italy
 - 2) 2019: [SOIG 2019](#), International workshop on Spin-orbit interaction and G-factor
- ii) *Two-dimensional topological superconductivity in Pb/Co/Si(111)*
 - 3) 2019: Workshop on The challenge of 2-Dimensional Superconductivity, Leiden, Netherlands
 - 4) 2018: Workshop on Superconductor-insulator transition and low-dimensional superconductors, Villars-de-Lans, France
 - 5) 2018: Workshop on New platforms for topological superconductivity with magnetic atoms, Dresden, Germany
 - 6) 2017: [Workshop on Multifunctional Dirac materials](#), Stockholm, Sweden
 - 7) 2017: [SUPERSTRIPES 2017](#), International conference on quantum physics in complex matter: superconductivity, magnetism and ferroelectricity, Ischia, Italy
- iii) *Proximity and Josephson vortices observed by scanning tunnelling spectroscopy*
 - 8) 2019: Rencontres de Moriond 2019, La Thuile, Italy
 - 9) 2016: 5th International conference on superconductivity and magnetism (ICSM2016), Fethiye, Turkey
- iv) *Remarkable effects of disorder on superconductivity of single atomic layers of lead on silicon*
 - 10) 2015: [International symposium](#) on low dimensional order mediated by interfaces, Hannover, Germany
 - 11) 2015: [American March meeting](#), San Antonio, USA – Focus session on 2D superconductivity
 - 12) 2014: 10th intern. workshop on nanomagnetism and superconductivity at the nanoscale, Coma-ruga, Spain
 - 13) 2014: European workshop on statistical physics and low dimensional systems SPLDS-2014, Nancy
- v) *Break-up of long-range coherence due to phase fluctuations in ultrathin superconducting NbN films*
 - 14) 2012: [CECAM Workshop](#), control and enhancement of superconductivity in conventional and high T_c nanostructures, Lausanne, Switzerland – Internationally recognized leading scientists present
- vi) *Charge Density Waves studied at the surface and at the local scale*
 - 15) 2014: International school and workshop on electronic crystals [ECRYS 2014](#), Cargèse, France
 - 16) 2011: International workshop on electronic crystals [ECRYS 2011](#), Cargèse, France
- vii) *Decay mechanisms of quantum-well states and Superconductivity in ultrathin Pb/Si(111) islands*
 - 17) 2011: European workshop on statistical physics and low dimensional systems SPLDS11, Nancy
- viii) *Thin superconducting lead islands studied by low-temperature scanning tunneling microscopy*
 - 18) 2008: European workshop on statistical physics and low dimensional systems SPLDS08, Nancy

INVITED TALKS IN INTERNATIONAL ADVANCED SCHOOL

Lecturer of a Mesoscopic Superconductivity Course at the Mesoscopic Physics School of the GdR Méso – 2016, November, Cargèse, France

INVITED TALKS IN NATIONAL CONFERENCES OR WORKSHOPS

PRESENTED BY TOPIC

Workshop – GdR MEETIC session superconductivity – 2017, March, Bordeaux, France
Two-dimensional topological superconductivity in Pb/Co/Si(111)

Workshop –JSI- Surfaces-Interfaces – 2017, January, Rennes, France
Remarkable properties of superconducting single atomic layers of lead on silicon

Workshop – GdR Méso session plénière – 2014, December, Aussois, France
Remarkable effects of disorder on superconductivity of single atomic layers of lead on silicon